

Effects of heavy Higgs bosons in the hadronic production of top-quark pairs including QCD corrections

DISSERTATION

zur Erlangung des akademischen Grades
doctor rerum naturalium
(Dr. rer. nat.)
im Fach Physik
Spezialisierung: Theoretische Physik

eingereicht an der
Mathematisch-Naturwissenschaftlichen Fakultät
der Humboldt-Universität zu Berlin

von

Herrn Dipl.-Phys. Peter Galler

Präsidentin der Humboldt-Universität zu Berlin

Prof. Dr.-Ing. Dr. Sabine Kunst

Dekan der Mathematisch-Naturwissenschaftlichen Fakultät

Prof. Dr. Elmar Kulke

Gutachter:	1. Prof. Dr. Peter Uwer 2. Prof. Dr. Christophe Grojean 3. Prof. Dr. Tilman Plehn
eingereicht am:	09.11.2017
Tag der mündlichen Prüfung:	15.01.2018

Selbstständigkeitserklärung

Ich erkläre, dass ich die Dissertation selbstständig und nur unter Verwendung der von mir gemäß §7 Abs. 3 der Promotionsordnung der Mathematisch-Naturwissenschaftlichen Fakultät, veröffentlicht im Amtlichen Mitteilungsblatt der Humboldt-Universität zu Berlin Nr. 126/2014 am 18.11.2014 angegebenen Hilfsmittel angefertigt habe.

Peter Galler

Berlin, den 09.11.2017

Abstract

With the discovery of the Higgs boson in the year 2012 the standard model of particle physics (SM) seems to be experimentally confirmed within measurement uncertainties. However there are, for example, astronomical and cosmological observations for which the SM does not provide an explanation. Furthermore, there are also theoretical considerations that lead to the conclusion that the SM needs to be extended. Hence, a large effort in theoretical and experimental particle physics is put into the search for physics beyond the SM. The Higgs discovery is also the discovery of a new kind of elementary particle: a scalar. Considering the fact that the SM describes many different types of fermions and gauge bosons but only one type of scalar and in the light of the need for a SM extension the question whether additional elementary scalars or pseudoscalars exist in nature is interesting.

This question is studied in this thesis within the two-Higgs doublet extension of the SM which introduces a second Higgs doublet giving rise to several new spin-0 bosons in addition to the scalar that has been discovered already. In particular, these additional Higgs bosons are assumed to be massive enough to decay into top-quark pairs such that their phenomenological signatures can be studied with collider observables related to top-quark pair production. Specifically, the resonant production of heavy Higgs bosons and their decay into top-quark pairs is calculated up to next-to-leading order in the QCD coupling constant retaining the full spin information of the top-quark pair. The interference between the resonant heavy Higgs contribution and the nonresonant QCD background has to be taken into account because it gives a large contribution to the process. Furthermore, the available spin information allows for the construction of spin dependent observables such as top-quark polarization and top-antitop spin correlations. While the effects of heavy Higgs bosons on top-quark polarization are rather small spin correlations can increase the sensitivity to heavy Higgs boson effects in the top-quark pair decay channel significantly when compared to spin independent observables. This is especially the case when these top-spin observables are measured in relevant regions of the phase space of the top and antitop momenta. In this thesis a method is presented that can be used to construct the spin correlation which is most sensitive to heavy Higgs effects. Furthermore, it is shown that the next-to-leading order corrections are required to construct observables which entail robust predictions. The results for the next-to-leading order in the QCD coupling constant presented in this work were the first ones given for resonant heavy Higgs production and decay into top-quark pairs.

Keywords: Higgs sector extension, two-Higgs-doublet model, next-to-leading order corrections, spin correlations

Zusammenfassung

Durch die Entdeckung des Higgsbosons im Jahr 2012 wurde das Standardmodell der Elementarteilchenphysik (SM) im Rahmen der Messunsicherheiten experimentell bestätigt. Dennoch gibt es, zum Beispiel, astronomische und kosmologische Beobachtungen, für die das SM keine Erklärung liefert. Auch aus theoretischer Sicht gibt es Überlegungen, die den Schluss zulassen, dass es einer Erweiterung des SM bedarf. Ein großer Teil der experimentellen und theoretischen Hochenergiephysik ist deshalb der Suche nach neuer Physik gewidmet. Die Entdeckung des Higgsbosons ist auch gleichzeitig die Entdeckung einer zuvor nicht beobachteten Art von Elementarteilchen: Skalare. Unter dem Gesichtspunkt dass das SM viele verschiedene Arten von Fermionen und Eichbosonen beschreibt aber nur eine Art von Skalaren und im Lichte der Notwendigkeit das SM zu erweitern, ist die Frage interessant, ob möglicherweise weitere elementare Skalare oder Pseudoskalare in der Natur existieren.

Dieser Frage wird in der vorliegenden Dissertation im Rahmen der Zwei-Higgs-Duplet-Erweiterung (2HDM) des SM nachgegangen. Das 2HDM führt ein zweites Higgsduplet ein, welches mehrere Spin-0 Bosonen zusätzlich zum Higgsboson generiert. In dieser Arbeit wird von der Annahme ausgegangen, dass die zusätzlichen Higgsbosonen schwer genug sind um in ein Top-Antitop-Paar zu zerfallen. Somit können die experimentellen Signaturen dieser neuen Teilchen mit Hilfe von Observablen der Topquarkpaarproduktion untersucht werden. Dazu wird die resonante Erzeugung von schweren Higgsbosonen und deren Zerfall in Topquarkpaare bis einschließlich der nächst-zu-führenden Ordnung in der QCD-Kopplungskonstanten berechnet. Dabei wird die volle Spininformation des Top-Antitop-Paares beibehalten. Die Interferenz zwischen der resonanten Higgsproduktion und dem QCD-Untergrund, welche in früheren experimentellen Analysen vernachlässigt wurde, muss jedoch in diesem Prozess aufgrund ihres signifikanten Beitrags berücksichtigt werden. Weiterhin erlaubt die verfügbare Spininformation die Untersuchung spinabhängiger Observablen. Es stellt sich dabei heraus, dass die Effekte schwerer Higgsbosonen auf die Topquarkpolarisation sehr klein sind, währendem Top-Antitop-Spinkorrelationen wesentlich sensitiver auf diese Effekte sein können, insbesondere im Vergleich zu spinunabhängigen Observablen. Die Sensitivität von spinabhängigen Observablen kann zudem noch durch entsprechende Schnitte auf den Phasenraum von Top- und Antitopquark verstärkt werden. In der vorliegenden Arbeit wird ein Verfahren vorgestellt, mit dessen Hilfe sich die Spinkorrelationen identifizieren lassen, welche die größte Sensitivität auf die Effekte schwerer Higgsbosonen aufweisen. Außerdem wird durch die Berechnung der Beiträge zur nächst-zu-führenden Ordnung u.a. gezeigt, dass diese Beiträge wichtig sind um aussagekräftige und robuste Observablen zu definieren. Die Ergebnisse der nächst-zu-führenden Ordnung, die in dieser Arbeit vorgestellt werden, sind die ersten ihrer Art für die resonante Erzeugung von schweren Higgsbosonen und deren Zerfall nach Topquarkpaaren.

Schlagwörter: Higgssektorerweiterung, Zwei-Higgs-Duplet-Modell, Korrekturen nächst-zu-führender Ordnung, Spinkorrelationen

Acknowledgements

For all the support and advice received during my PhD studies from numerous people I am very grateful. In particular, I would like to thank my PhD advisor Peter Uwer for his continued support and effort as well as for his valuable advice and inspiring discussions. Special thanks also goes to Werner Bernreuther, Clemens Mellein and Zong-Guo Si with whom I had the pleasure to work and publish results that were developed in the course of this PhD project. In particular, I would like to thank Clemens Mellein for independently cross checking numerical results. The members of the particle phenomenology group at the Humboldt-Universität zu Berlin have made my life as a PhD student a diverse, interesting and memorable time and I enjoyed the pleasant working environment within this group. In particular, my thanks goes to Bas Tausk with whom I had many interesting and helpful discussions. During my PhD studies I was a member of the Research Training Group “Mass, Spectrum, Symmetry: Particle Physics in the Era of the Large Hadron Collider” which is funded by the Deutsche Forschungsgemeinschaft through grand no. GRK 1504. I enjoyed interesting discussions with fellow PhD students and principle investigators initiated through biannual meetings and I am grateful for the financial support as well as for the scientific training received through this research training group.

I would like to express my warmhearted thanks to my family for its continued support and encouragement which in fact reaches back to my very first memories and beyond. I am especially indebted to my wife for her understanding and support throughout my PhD studies and in particular during the final writing phase of this thesis.

Contents

1. Introduction	1
1.1. The standard model of particle physics	2
1.1.1. Quantum chromo dynamics	4
1.1.2. The standard model of particle physics Higgs boson	5
1.1.3. The top quark	7
1.2. Physics beyond the standard model	9
1.3. Outline of this thesis	12
2. The two-Higgs-doublet model	15
2.1. The scalar potential and the Higgs mass eigenstates	15
2.2. Gauge-Higgs coupling	21
2.3. Yukawa couplings	23
2.4. Parameters	25
2.5. Theoretical constraints	28
2.6. Decay widths	29
2.7. The alignment limit	36
3. Spin density matrix formalism	41
3.1. Spin density matrix	41
3.2. Production density matrix	42
3.3. Spin correlation vs. angular correlation	45
3.4. Spin dependent matrix element	48
4. Heavy Higgs effects in top-quark pair production at leading order in α_s	53
4.1. Analytic results	55
4.2. Phenomenology	57
4.2.1. Top-antitop invariant mass distribution	58
4.2.2. Higgs-Higgs interference effects	60
4.2.3. Longitudinal top-quark polarization	63
4.2.4. Spin correlations	66
5. Heavy Higgs effects in top-quark pair production at next-to-leading order in α_s	77
5.1. Introduction	77
5.2. Computational methods	78
5.2.1. Large top mass limit	78
5.2.2. Treatment of unstable particles	80
5.2.3. Soft gluon approximation	82

Contents

5.2.4. Virtual corrections	85
5.2.5. Real corrections	97
5.2.6. Catani–Seymour dipole subtraction	100
5.3. Analytical results	102
5.4. Phenomenological results	107
5.4.1. Spin independent observables	107
5.4.2. Spin dependent observables	120
6. Summary and Conclusions	139
A. Trilinear couplings among the Higgs bosons of the 2HDM	143
B. Theoretical constraints on the 2HDM from stability, unitarity and perturbativity	145
B.1. Boundedness of the potential from below	145
B.2. Unitarity	147
B.3. Perturbativity	148
C. On-shell decay of the top-quark pair system	151
C.1. Factorization of top-quark pair production and decay	151
C.2. Leading order master formula for top-quark pair production and dileptonic decay	152
C.3. Double differential distribution	154
C.4. Opening angle distribution	156
D. Discrete symmetries of the production density matrix and top-quark polarization in the 2HDM	157
E. Optimal spin correlations	161
F. Cancellation of real and virtual nonfactorizable corrections in the soft gluon approximation	165
G. Top quark pair invariant mass distribution for scenarios Ia–Ic	167
H. Numerical results for C_{hel}, C_{nn}, C_{rr} and D in scenarios Ia–Ic	169
Bibliography	173

List of Figures

2.1. Comparison of the decay widths of neutral Higgs bosons to bottom quarks and top quarks.	31
2.2. Relative contribution of the bottom quark to the decay of a Higgs boson (h , H , A) into two gluons in the 2HDM.	33
2.3. Higgs production with full top and bottom mass dependence at NLO QCD compared to the approximated result.	34
2.4. Partial decay width of neutral Higgs bosons (H, A) into two gluons at NLO QCD in the large top-mass limit as a function of the respective Higgs mass.	35
4.1. Feynman diagrams for $t\bar{t}$ production at leading order.	53
4.2. Sample Feynman diagrams for the nonresonant heavy Higgs contributions to the gluon fusion channel of $t\bar{t}$ production.	55
4.3. Sample Feynman diagrams for the two-loop corrections to $t\bar{t}$ production involving two heavy Higgs propagators.	55
4.4. $M_{t\bar{t}}$ distribution of scenario 1 at LO for $\sqrt{S_{\text{had}}} = 13\text{TeV}$	59
4.5. $M_{t\bar{t}}$ distribution of scenario 2 at LO for $\sqrt{S_{\text{had}}} = 13\text{TeV}$	59
4.6. Maximal relative contribution of the Higgs-Higgs interference with respect to the single Higgs contribution to the $t\bar{t}$ cross section as a function of the heavy Higgs masses.	62
4.7. Partonic cross sections σ_{int} , σ_2 and σ_3 as a function of the partonic center of mass energy \sqrt{s} for $m_\phi = 500, 700, 900\text{GeV}$, $\tan\beta = 1$ and $\alpha_i = \alpha_i^{\text{max}}$, $i = 1, 2, 3$	63
4.8. Maximal longitudinal (anti)top-quark polarization as a function of m_2 for $\tan\beta = 1$ and $\sqrt{S_{\text{had}}} = 8\text{TeV}$	64
4.9. Maximal longitudinal (anti)top-quark polarization as a function of m_2 for $\tan\beta = 0.7, 1, 1.5$ and $\sqrt{S_{\text{had}}} = 13\text{TeV}$	66
4.10. Contour plots in θ - φ space for the signal-to-background ratio $\delta C_{\theta,\varphi}$ and the absolute size of the spin correlation $ C_{\theta,\varphi}^{\text{QCD}+2\text{HDM}} $	69
4.11. Maximum signal-to-background ratio of the optimal $t\bar{t}$ spin correlation C_{max} as a function of m_2	70
4.12. Spin correlation $C_{\theta,\varphi}^{M_{t\bar{t}}}$ as a function of $M_{t\bar{t}}$	72
4.13. Comparison of the maximal signal-to-background ratio of spin correlations with and without $M_{t\bar{t}}$ cut and the $M_{t\bar{t}}$ distribution for discrete values of m_2 using an $M_{t\bar{t}}$ bin width of 50 GeV.	73
4.14. Comparison of the maximal signal-to-background ratio of spin correlations with and without $M_{t\bar{t}}$ cut and the $M_{t\bar{t}}$ distribution for discrete values of m_2 using an $M_{t\bar{t}}$ bin width of 80 GeV.	74

List of Figures

4.15. Comparison of the maximal signal-to-background ratio of spin correlations with and without $M_{t\bar{t}}$ cut and the $M_{t\bar{t}}$ distribution for discrete values of m_2 using an $M_{t\bar{t}}$ bin width of 100 GeV.	74
5.1. Example Feynman diagram for an NLO two-loop contribution to $t\bar{t}$ production involving heavy Higgs bosons.	77
5.2. Dyson summation for the Higgs propagator.	80
5.3. Example Feynman diagrams for factorizable, nonfactorizable resonant and non-factorizable nonresonant contributions.	83
5.4. Factorizable contributions in the gg channel.	85
5.5. Example Feynman diagrams for nonfactorizable contributions in the gg channel.	86
5.6. Example Feynman diagram for nonfactorizable nonresonant contribution in the $q\bar{q}$ channel.	86
5.7. Born-like heavy Higgs contribution from the $\mathcal{O}(\alpha_s^2)$ term $f_{S,P}^{(1)}$ of the effective $gg\phi$ coupling.	87
5.8. Leading order heavy Higgs exchange diagram in the heavy top mass limit.	87
5.9. Example QCD Feynman diagrams contributing to the Higgs-QCD interference at NLO.	88
5.10. Example counterterm Feynman diagrams.	95
5.11. Example Feynman diagrams for real corrections to $t\bar{t}$ production involving heavy Higgs bosons.	98
5.12. Example Feynman diagrams for the pure QCD real corrections to $t\bar{t}$ production.	98
5.13. Example Feynman diagram for nonresonant real corrections in the gg channel.	99
5.14. Interference Feynman diagrams for nonfactorizable contributions.	99
5.15. Distribution of the $t\bar{t}$ invariant mass for scenario 1 at NLO.	113
5.16. Distribution of the $t\bar{t}$ invariant mass for scenario 2 at NLO.	114
5.17. Distribution of the $t\bar{t}$ invariant mass for scenario 3 at NLO.	114
5.18. Comparison between the top-quark rapidity distribution in scenario 1 with and without $M_{t\bar{t}}$ cut at NLO.	115
5.19. Top quark rapidity distribution for scenario 1 at NLO evaluated for selected $M_{t\bar{t}}$ windows.	116
5.20. Top quark rapidity distribution for scenario 2 at NLO evaluated for selected $M_{t\bar{t}}$ windows.	117
5.21. Top quark rapidity distribution for scenario 3 at NLO evaluated for selected $M_{t\bar{t}}$ windows.	117
5.22. Distribution of the cosine of the Collins–Soper angle for scenario 1 at NLO evaluated for selected $M_{t\bar{t}}$ windows.	118
5.23. Distribution of the cosine of the Collins–Soper angle for scenario 2 at NLO evaluated for selected $M_{t\bar{t}}$ windows.	119
5.24. Distribution of the cosine of the Collins–Soper angle for scenario 3 at NLO evaluated for selected $M_{t\bar{t}}$ windows.	119
5.25. Normalized distribution of the CP -sensitive observable ϕ_{CP}^* for scenarios 1a–1c in selected regions of $M_{t\bar{t}}$	126
5.26. Results for the spin correlation observables C_{hel} , C_{nn} , C_{rr} and D evaluated in the lower and upper $M_{t\bar{t}}$ bin for scenario 1a.	128
5.27. Results for the spin correlation observables C_{hel} , C_{nn} , C_{rr} and D evaluated in the lower and upper $M_{t\bar{t}}$ bin for scenario 1b.	129
5.28. Results for the spin correlation observables C_{hel} , C_{nn} , C_{rr} and D evaluated in the lower and upper $M_{t\bar{t}}$ bin for scenario 1c.	130
5.29. Unnormalized spin correlation observables binned in $M_{t\bar{t}}$ for scenario 1a.	131

5.30. Data-to-background ratio of the $M_{t\bar{t}}$ distribution as determined by an ATLAS analysis compared to the signal-to-background ratio in scenario II. 133

5.31. Results for $C_{\text{hel}}^{M_{t\bar{t}}}$ in scenario II. 135

5.32. Results for $C_{\text{nn}}^{M_{t\bar{t}}}$ in scenario II. 135

C.1. Schematic Feynman amplitude for $t\bar{t}$ production with subsequent decay of the (anti)top into W^+b ($W^-\bar{b}$). 151

F.1. Example for the cancellation of real and virtual contributions in the SGA. The red dotted cut corresponds to the real correction and the blue dotted cut corresponds to the virtual correction. 165

G.1. Distribution of the $t\bar{t}$ invariant mass for scenario 1a at NLO. 167

G.2. Distribution of the $t\bar{t}$ invariant mass for scenario 1b at NLO. 168

G.3. Distribution of the $t\bar{t}$ invariant mass for scenario 1c at NLO. 168

List of Tables

1.1. Fermions in the SM and their interaction with gauge bosons.	3
2.1. Possible couplings between Higgs and gauge bosons in the CP conserving and CP violating 2HDM.	22
2.2. Reduced scalar and pseudoscalar Yukawa couplings of the neutral Higgs bosons in the 2HDM.	25
2.3. Number of independent parameters in the Higgs potential V_Φ for different symmetries imposed on V_Φ	25
2.4. Parametrizations of the Higgs Potential V_Φ for different symmetries imposed on V_Φ	28
2.5. Reduced scalar and pseudoscalar Yukawa couplings of the neutral Higgs bosons in the alignment limit of the 2HDM.	37
5.1. Values of the reduced Yukawa couplings to the third-generation fermions and couplings to gauge bosons $V = W^\pm, Z$ of the neutral Higgs bosons ϕ_j in scenarios 1 and 2.	108
5.2. Dominant partial decay widths and the total widths of the two heavy, neutral Higgs bosons ϕ_2 and ϕ_3 in scenario 1.	109
5.3. Dominant partial decay widths and total widths of the two heavy, neutral Higgs bosons ϕ_2 and ϕ_3 in scenario 2.	109
5.4. Values of the reduced Yukawa couplings and couplings to gauge bosons $V = W^\pm, Z$ of the neutral Higgs bosons ϕ_j for scenario 3.	110
5.5. Dominant partial decay widths and total widths of the two heavy, neutral Higgs bosons ϕ_2 and ϕ_3 in scenario 3.	110
5.6. Inclusive $t\bar{t}$ production cross sections in different type-II 2HDM scenarios at NLO.	112
5.7. $M_{t\bar{t}}$ windows used in the computation of the y_t and $\cos\theta_{CS}$ distributions.	115
5.8. Input values for the type-II 2HDM parameters for scenarios Ia–Ic and II.	121
5.9. Reduced scalar and pseudoscalar Yukawa couplings and couplings to weak gauge bosons for scenarios Ia–Ic and II.	121
5.10. Dominant two-body partial widths and total decay width of ϕ_2 and ϕ_3 in scenarios Ia–Ic.	121
5.11. Dominant two-body partial width and total decay width of ϕ_2 and ϕ_3 in scenario II.	122
5.12. R -ratios and K -factors for C_{hel} , C_{nn} , C_{rr} and D in the lower and upper $M_{t\bar{t}}$ bin for scenarios Ia–Ic.	132
5.13. Results for the expectation value of the triple correlation $\langle O_{CP} \rangle$ for scenario Ic within selected $M_{t\bar{t}}$ bins and inclusively in $M_{t\bar{t}}$	136

List of Tables

5.14. Results for the top-quark polarization coefficient $B_1(\hat{\mathbf{k}})$ for selected $M_{t\bar{t}}$ bins and inclusively in $M_{t\bar{t}}$	137
D.1. Transformation properties of the production density matrix coefficients in the gg channel.	158
E.1. Spin correlation binned in $M_{t\bar{t}}$ with a maximal signal-to-background ratio for an $M_{t\bar{t}}$ bin width of 50 GeV.	162
E.2. Spin correlation binned in $M_{t\bar{t}}$ with a maximal signal-to-background ratio for an $M_{t\bar{t}}$ bin width of 80 GeV.	163
E.3. Spin correlation binned in $M_{t\bar{t}}$ with a maximal signal-to-background ratio for an $M_{t\bar{t}}$ bin width of 100 GeV.	164
H.1. Spin correlations in scenario Ia.	170
H.2. Spin correlations in scenario Ib.	171
H.3. Spin correlations in scenario Ic.	172

List of Abbreviations

2HDM	two-Higgs-doublet model
BSM	beyond the standard model
CKM	Cabbibo-Kobayashi-Maskawa
cms	center of mass system
CPC	CP conserving / conservation
CPV	CP violating / violation
FCNC	flavor changing neutral current
GCP	general CP
H.c.	Hermitian conjugate
HF	Higgs family
LHC	Large Hadron Collider
lhs	left hand side
LO	leading order
NLO	next-to-leading order
PDF	parton distribution function
QCD	quantum chromo dynamics
rhs	right hand side
SGA	soft gluon approximation
SM	standard model of particle physics
SUSY	supersymmetry
$t\bar{t}$	top-antitop
vev	vacuum expectation value

Introduction

Since the experimental discovery of the electron in 1897 by Emil Wiechert and almost simultaneously by Joseph John Thomson 120 years have passed. In this time the field of particle physics has come a long way in its quest to identify and characterize the most fundamental constituents of nature and the interactions between them. Since the theoretical formulation of the *standard model of particle physics (SM)* in the 1960-70's [1–5] many aspects of the phenomenology of the basic building blocks of nature can actually be described by this theory. This is exemplified by a plethora of theoretical predictions that meet experimental results for all different kinds of processes and experiments to high accuracy. But the SM goes beyond a pure description and reveals a fundamental symmetry that underlies elementary particles and their interactions: gauge symmetry. The triumph of the SM cumulated in the discovery [6, 7] of a 125 GeV resonance in 2012 which is now believed to be a spin-0 boson with the properties [8, 9] of the so-called SM *Higgs* boson. Having found this last missing piece, the existence of which was predicted [10–12] already 53 years ago, the consistency and solidness of the SM would seem more impenetrable than ever.

The many experimental results that are in agreement with the SM can, however, not hide the fact that there are also experimental observations for which the SM gives either a wrong prediction, e.g. when it comes to the baryon asymmetry in the universe, or none at all, e.g. regarding dark matter. There are also theoretical considerations that mark the SM as incomplete the most prominent aspect being the fact that only three of the four fundamental interactions (forces) in nature are described by the SM.

Still, these issues seem not to have any measurable impact on the predictive power of the SM for example for high energy collider experiments where no significant deviations from the SM have been detected so far. But the high energy physics community has only begun to exploit the full potential of the Large Hadron Collider (LHC) which is anticipated to run until 2035 [13]. After the discovery of the Higgs boson one goal of the LHC is to measure the properties of the Higgs boson as precise as possible. Furthermore the experiments will continue searching for deviations from the predictions that hint towards a possible extension of the SM.

This dissertation is dedicated to the phenomenological study of a SM extension in the Higgs sector featuring, additional heavy Higgs bosons. In particular, the impact of these additional Higgs bosons on hadron collider observables related to the production of top-quark pairs is investigated in detail. Hence, particles of particular significance for this work are the Higgs boson or rather its heavy companions in the model studied here and the top quark.

In this introductory chapter a short overview over the SM is given in Sec. 1.1 including a more detailed description of the SM Higgs boson (Sec. 1.1.2) and the top quark (Sec. 1.1.3).

1. Introduction

The motivation to study physics beyond the standard model in general is discussed in Sec. 1.2 and an outline of this thesis is given in Sec. 1.3.

1.1. The standard model of particle physics

It is beyond the scope of this work to give a complete account of the SM in all its details but some important aspects are covered in this section. For more details and comprehensive introductions see for example Ref. [14, 15].

The SM classifies all known fundamental particles and describes the strong, weak and electromagnetic interactions between them. The structure of the SM is founded on the principle of gauge symmetry. All fermions in the SM are representation of the gauge group $G_{\text{SM}} = SU(3)_c \times SU(2)_L \times U(1)_Y$ and the bosons are the corresponding gauge fields mediating the interactions between the fermions¹. The gauge group and the choice of representations of this group therefore determine the whole coupling structure of the SM.

G_{SM} is a product of three Lie groups each representing a fundamental interaction and associated gauge fields. The gauge bosons of the electromagnetic force are called *photons* (γ). The weak force mediating, for example, the radioactive β -decay, is represented by three kinds of gauge bosons: W^+ , W^- and Z . The third fundamental interaction in the SM is the strong force which is mediated by eight different bosons called *gluons* (g). While the gauge bosons have spin 1 there is another type of boson with spin 0: the Higgs boson (h). It is not associated to a gauge symmetry but plays an integral part in the SM as will be explained below.

The fermions can be divided into two groups according to their interactions. The first group consists of *quarks* which interact via all three forces described by the SM. The quarks come in six variants called *flavors*: up (u), down (d), strange (s), charm (c), bottom (b) and top (t). The so-called *up-type quarks* (u , c , t) have the same quantum numbers but different masses. The other three quark flavors are called *down-type quarks* (d , s , b) which also have the same quantum numbers but different masses. The second group of fermions in the SM consists of *leptons* which interact only via the weak and electromagnetic forces. Among the leptons one can further distinguish two groups: electrically charged leptons (ℓ^\pm) and electrically neutral leptons called *neutrinos* (ν). The charged leptons come in three different flavors: electron (e^-), muon (μ^-) and tau (τ^-) which have different mass but are otherwise identical. There exist also three neutrino flavors which are associated to the lepton flavors: electron-neutrino (ν_e), muon-neutrino (ν_μ) and tau-neutrino (ν_τ). Here only the fermions have been listed but additionally there is an antifermion associated with each fermion in the SM.

The SM fermions of left-handed chirality transform as doublets under the $SU(2)_L$ gauge group while right-handed fermions transform as singlets under this group. The left-handed quark doublets consist of an up-type quark and a down-type quark while the left-handed lepton doublets consist of a lepton and the associated neutrino.

The different flavors of the fermions in the SM can be grouped into three so-called *families* or *generations*. Fermions of the same type (up-type, down-type, charged lepton) which are members of different families have the same quantum numbers but different masses. The SM fermions are listed in Tab. 1.1 together with their representations with respect to the gauge group, their electrical charge quantum number and the interaction with gauge bosons. In the original SM the neutrinos were assumed to be massless. Hence, a right-handed neutrino for generating neutrino masses was not needed. Due to the gauge structure of the SM the right-handed neutrino does not interact via any of the three forces since it has no electrical

¹In the case of nonabelian gauge fields the bosons also interact with each other.

Table 1.1.: Fermions in the SM and their interaction with gauge bosons. The subscript L (R) denotes left-handed (right-handed) fermions. The representation of the fermions with respect to the gauge group is indicated in the third column. Q denotes the electrical charge. The last column indicates the gauge boson couplings of the respective fermions.

Family	Fermion type			$SU(3)_c \times SU(2)_L \times U(1)_Y$	Q	Gauge interaction
	I	II	III			
Quarks	$Q_L = \begin{pmatrix} u_L \\ d_L \end{pmatrix}, \begin{pmatrix} c_L \\ s_L \end{pmatrix}, \begin{pmatrix} t_L \\ b_L \end{pmatrix}$			$(3, 2, \frac{1}{6})$	$\frac{2}{3}$	γ, W^\pm, Z, g
	$u_R,$	$c_R,$	t_R		$-\frac{1}{3}$	
	$d_R,$	$s_R,$	b_R	$(3, 1, \frac{2}{3})$	$\frac{2}{3}$	
Leptons	$L_L = \begin{pmatrix} \nu_{e,L} \\ e_L^- \end{pmatrix}, \begin{pmatrix} \nu_{\mu,L} \\ \mu_L^- \end{pmatrix}, \begin{pmatrix} \nu_{\tau,L} \\ \tau_L^- \end{pmatrix}$			$(1, 2, -\frac{1}{2})$	0	W^\pm, Z
	$e_R^-,$	$\mu_R^-,$	τ_R^-		$(3, 1, -\frac{1}{3})$	$-\frac{1}{3}$
				$(1, 1, -1)$	-1	W^\pm, Z, γ

charge and transforms as singlet under $SU(3)_c$ and $SU(2)_L$. Hence, a right-handed neutrino is not listed in Tab. 1.1. However, through experimental evidence [16–18] it is now established that at least two of the three neutrinos have masses. This aspect will be briefly discussed in Sec. 1.2.

The conceptual and mathematical foundation of the SM is based on a renormalizable quantum gauge field theory. For a few well-known examples of the vast literature on the topic of quantum field theories see Refs. [19–23]. According to Weinberg quantum field theory “is the only way to reconcile the principles of quantum mechanics [...] with those of special relativity” [21]. It also resolves the long-standing particle-wave dualism by the unified description of fundamental particles as quantum fields. In most cases quantum field theories are defined in terms of Lagrangian densities \mathcal{L} which is most convenient in the quantization of the classical fields using the path integral formalism or action principle. Hence, elementary particles can be identified with the fields that appear in the Lagrangian as opposed to composite particles which are not present in the Lagrangian [24].

The kinds of terms that appear in the Lagrangian are restricted by Lorentz symmetry, gauge symmetry and renormalizability. Imposing Lorentz invariance is just another way of saying that the terms in the Lagrangian have to be Lorentz scalars. Local gauge symmetry implies the existence of additional bosonic gauge fields that are coupled to fermions in a specific way. This is necessary because the kinetic term for fermions $\bar{\psi}\not{\partial}\psi$ is in general not invariant under local gauge transformations. Consider, for example, the $SU(N)$ gauge transformation

$$\psi \rightarrow U(x)\psi, \quad U(x) = e^{-igt^a\chi^a(x)}, \quad (1.1)$$

where t^a are the generators of the $SU(N)$ with $a = 1, \dots, N^2 - 1$ and $\chi^a(x)$ are arbitrary functions

1. Introduction

of x . Gauge invariance can be achieved by coupling gauge bosons A_μ^a to the fermions ψ via the covariant derivative

$$\bar{\psi}\not{D}\psi, \quad D_\mu = \partial_\mu - igt^a A_\mu^a(x), \quad (1.2)$$

where $t^a A_\mu^a(x)$ transforms as [23]

$$t^a A_\mu^a(x) \rightarrow U(x) \left[t^a A_\mu^a(x) + \frac{i}{g} \partial_\mu \right] U^{-1}(x) \quad (1.3)$$

under the $SU(N)$ gauge transformation. Hence, imposing local gauge invariance under a certain gauge group introduces as many gauge bosons as there are generators of the respective group. Therefore, with respect to the SM gauge group $SU(3)_c \times SU(2)_L \times U(1)_Y$ we expect $8+3+1 = 12$ gauge bosons. Indeed, as outlined above, there are eight gluons, three gauge bosons of the weak force and the photon in the SM.

Renormalizability as a principle to restrict the allowed terms in the Lagrangian permits only operators of mass dimension four or less. However, from a modern point of view this principle is less relevant if the SM is considered as an effective field theory. The topic of renormalization is discussed for the process studied in this work in Sec. 5.2.4.

The Lagrangian (without gauge fixing and ghost terms) of the SM is given by [25]

$$\begin{aligned} \mathcal{L}_{\text{SM}} = & - \frac{1}{4} G_{\mu\nu}^a G^{a\mu\nu} - \frac{1}{4} W_{\mu\nu}^a W^{a\mu\nu} - \frac{1}{4} B_{\mu\nu}^a B^{a\mu\nu} \\ & + \sum_{q=d,u,s,c,b,t} i\bar{q}\not{D}q + \sum_{\psi_L} i\bar{\psi}_L\not{D}\psi_L + \sum_{\psi_R} i\bar{\psi}_R\not{D}\psi_R \\ & - \left[y_{ij}^\ell \bar{L}_{iL} \Phi \ell_{jR} + y_{ij}^d \bar{Q}_{iL} \Phi d_{jR} + y_{ij}^u \bar{Q}_{iL} \tilde{\Phi} u_{jR} + \text{h.c.} \right] \\ & + (D_\mu \Phi)(D^\mu \Phi)^\dagger + \mu|\Phi|^2 - \lambda|\Phi|^4. \end{aligned} \quad (1.4)$$

We do not want to go into the details of the whole SM Lagrangian. In Eq. (1.4) the notation of Ref. [25] has been used where further details regarding each term in the Lagrangian can be found. Here we focus only on some aspects of \mathcal{L}_{SM} which are of particular interest for this work.

1.1.1. Quantum chromo dynamics

The Lagrangian of quantum chromo dynamics (QCD), the strong interaction, is given by

$$\mathcal{L}_{\text{SM}} \supset \mathcal{L}_{\text{QCD}} = -\frac{1}{4} G_{\mu\nu}^a G^{a\mu\nu} + \sum_{q=d,u,s,c,b,t} \bar{q}[i\not{D} - m_q]q \quad (1.5)$$

with the gluon field strength tensor

$$G_{\mu\nu}^a = \partial_\mu G_\nu^a - \partial_\nu G_\mu^a - g_s f^{abc} G_\mu^b G_\nu^c \quad (1.6)$$

and the covariant derivative

$$D_\mu = \partial_\mu + ig_s t^a G_\mu^a. \quad (1.7)$$

The quark masses are denoted by m_q in \mathcal{L}_{QCD} . The $SU(3)_c$ generators of the fundamental representation are denoted by t^a , $a = 1, \dots, 8$ and the generators of the adjoint representation—the structure functions—by f^{abc} . The $SU(3)_c$ coupling constant is denoted by g_s . In the following chapters we will often refer to

$$\alpha_s = \frac{g_s^2}{4\pi} \quad (1.8)$$

as the *coupling constant of the strong interaction*. The first term in \mathcal{L}_{QCD} includes the kinetic term for the gluon fields and gives rise to gluon self interactions, namely three- and four-gluon vertices. The second term contains the kinetic term for the quarks and describes the interaction between quarks and gluons. The gauge fixing and ghost terms in \mathcal{L}_{QCD} have been omitted in Eq. (1.5) although they are necessary for a consistent theory. Here we do not want to go into the detail of these terms. Instead Eq. (1.5) is given to motivate the coupling structure of QCD which is of particular importance for top-antitop ($t\bar{t}$) production considered in this work. Furthermore, contributions from ghosts are absent in this process and at the perturbative order considered here.

1.1.2. The standard model of particle physics Higgs boson

The contribution from the SM Higgs $SU(2)_L$ -doublet Φ to \mathcal{L}_{SM} is given by the last two lines in Eq. (1.4). The last two terms in \mathcal{L}_{SM} represent the Higgs potential

$$V_H = -\mu^2|\Phi|^2 + \lambda|\Phi|^4. \quad (1.9)$$

For $\mu^2, \lambda > 0$ this potential has a minimum and the Higgs doublet acquires a nonzero vacuum expectation value (vev) at

$$\langle \Phi \rangle = \frac{1}{\sqrt{2}} \begin{pmatrix} 0 \\ v \end{pmatrix}, \quad (1.10)$$

where $v = \sqrt{\mu^2/\lambda} = 246$ GeV. By an appropriate gauge transformation (unitary gauge) the Higgs doublet can be written as

$$\Phi = \frac{1}{\sqrt{2}} \begin{pmatrix} 0 \\ v + h(x) \end{pmatrix}, \quad (1.11)$$

where $h(x)$ is an excitation around the ground state, the vacuum, and is referred to as the Higgs boson [10–12]. Feeding Eq. (1.11) back into Eq. (1.9) yields a relation between the parameter μ and the Higgs boson mass m_h at tree level

$$m_h^2 = 2\mu^2. \quad (1.12)$$

The ground state of the Higgs field as given in Eq. (1.10) breaks $SU(2)_L \times U(1)_Y$ gauge symmetry. However, a particular combination of generators still leaves this state invariant such that the vacuum is symmetric under $U(1)_Q$. Breaking the gauge symmetry in this way generates masses for three of the four gauge bosons involved. Furthermore, the $SU(2)_L$ gauge bosons W_μ^a and the $U(1)_Y$ gauge boson B_μ mix with each other to form the massive W^\pm and Z bosons as well as the massless photon which corresponds to the unbroken $U(1)_Q$ gauge symmetry. This process of going from an $SU(2)_L \times U(1)_Y$ gauge symmetry over to a $U(1)_Q$ gauge symmetry in the SM is called *spontaneous electroweak symmetry breaking* or *Higgs mechanism*. Even though the Lagrangian in Eq. (1.4) is invariant under the SM gauge group G_{SM} the ground state partially breaks this symmetry generating masses for three gauge bosons. In Sec. 2.2 a few more details are given concerning the mass generation of the electroweak gauge bosons for the case of an extended Higgs sector. Furthermore, the kinetic term with the covariant derivative in the last line of Eq. (1.4) also gives rise to the coupling between the Higgs boson and gauge bosons, an aspect which is also considered for an extended Higgs sector in Sec. 2.2.

The third line in Eq. (1.4) describes the Yukawa interaction between the SM Higgs doublet and the fermions. Consider, as an example, the term describing the coupling to up-type quarks such as the top quark

$$y_{ij}^u \bar{Q}_{iL} \tilde{\Phi} u_{jR}, \quad (1.13)$$

1. Introduction

where y_{ij}^u is the Yukawa coupling matrix for up-type quarks and $i, j = 1, 2, 3$ are family indices. Q_{iL} denotes the left-handed quark doublet of the i th family and u_{jR} denotes the right-handed quark of the j th family and $\tilde{\Phi} = i\sigma_2\Phi^*$, where σ_2 is the second Pauli-matrix. Inserting the vev (1.10) into the Yukawa term (1.13) generates terms that are bilinear in the quark fields. They can be interpreted as mass terms if these terms are diagonal in the family indices. The general complex 3×3 Yukawa matrix y_{ij}^u can be diagonalized by two unitary transformations V_L^u and V_R^u

$$\frac{v}{\sqrt{2}}V_L^u y^u (V_R^u)^\dagger = M_u = \text{diag}(m_u, m_c, m_t), \quad (1.14)$$

where m_u, m_c and m_t are the masses of the up, charm and top quark. The mass basis (primed) is therefore given by

$$u'_L = V_L^u u_L, \quad u'_R = V_R^u u_R \quad (1.15)$$

and analogously for the down-type quarks

$$d'_L = V_L^d d_L, \quad d'_R = V_R^d d_R. \quad (1.16)$$

These are the d, u, s, c, b and t quarks with definite masses mentioned in the beginning of this section. The family-nondiagonal mixing of quark flavors in the mass basis leads to interactions with W^\pm bosons that are flavor changing across families and that are determined by the so-called *Cabbibo-Kobayashi-Maskawa (CKM) matrix* $V = V_L^u (V_L^d)^\dagger$.

The Yukawa interaction Lagrangian (third line in Eq. (1.4)) is gauge invariant. However, this invariance is spontaneously broken by the Higgs vev which generates $SU(2)_L$ -violating mass terms for the fermions. The generation of fermion masses through spontaneous electroweak symmetry breaking, in which the Higgs boson acquires a nonzero vev, is also referred to as *Higgs mechanism*. In fact the generation of gauge boson and fermion masses, respectively, can be seen as two kinds of Higgs mechanisms. In the mass basis the Yukawa interaction with the Higgs boson becomes also diagonal with respect to the families because the Higgs coupling to fermions is proportional to the fermion mass (1.14). Hence, flavor changing neutral currents (FCNCs) are absent in in the SM Higgs sector. In Sec. 2.3 it is shown that in the presence of a second $SU(2)_L$ Higgs doublet the Yukawa interaction becomes more complicated and in particular, the absence of FCNCs at tree-level is in general not guaranteed.

The theoretical concept of spontaneous breaking of gauge symmetry and therefore the foundations of the Higgs mechanism in the SM were already developed in 1964 in several papers published in *Physical Review Letters* by Brout and Englert [10], Higgs [11] and Guralnik, Hagen, Kibble [12]. Even though all these, and maybe even more, authors contributed to the understanding of spontaneous gauge symmetry breaking and predicted the existence of a corresponding spin-0 boson the literature today often refers to only one of these authors by calling the spin-0 boson in the SM *Higgs boson*. For brevity and in alignment with the conventions used in the literature this work is also referring to the spin-0 boson in the SM as “Higgs boson”. This nomenclature should not in any way diminish the achievements and contributions of other physicists involved in the development of the theory of the Higgs boson. In the following chapters we refer also to non-SM spin-0 bosons as “Higgs bosons”.

In this thesis phenomenological aspects of an extended Higgs sector are discussed. Therefore, it is appropriate to first give a brief account of where we stand with the SM Higgs boson from an experimental point of view. In 2012 a resonance with a mass of 125 GeV was discovered at the LHC [6, 7]. Until now subsequent measurements have confirmed, within experimental uncertainties, the hypothesis that this is the SM Higgs. The spin (J) and parity (P) of the Higgs boson in the SM are given by $J^P = 0^+$. In Refs. [26, 27] the hypothesis of a SM

Higgs boson has been tested against several alternatives² such as non-SM spin-0 couplings, e.g. odd parity, and spin-2 models. All alternative hypotheses were excluded with a confidence level of 99% or higher. With the available data collected so far it was also possible to measure production and decay rates of the Higgs boson and constrain its couplings. In Ref. [29] the combination of results for the Higgs production and decay rates and constraints on the Higgs couplings from analyses of the LHC run I data are presented. The combined signal strength of all measurements is given by $\mu = 1.09 \pm 0.11$ with respect to the SM expectation, which shows a very good agreement with the SM. All measurements of the 5 fb⁻¹ of data collected at $\sqrt{s}_{\text{had}} = 7$ TeV and 20 fb⁻¹ at $\sqrt{s}_{\text{had}} = 8$ TeV as analysed in Ref. [29] are consistent with the SM predictions. A recent analysis [30] of the run II data bases on 36.1 fb⁻¹ of data at $\sqrt{s}_{\text{had}} = 13$ TeV studies Higgs boson production and decay in the $H \rightarrow ZZ^* \rightarrow 4\ell$ and $H \rightarrow \gamma\gamma$ decay channels. The total cross section is measured to be consistent with the SM prediction at 13 TeV and the global signal strength measured by Ref. [30] is again in agreement with the SM prediction: $\mu = 1.09 \pm 0.12$. Also an interpretation of the data in terms of coupling modifiers and ratios thereof yields no significant deviation from the SM. There are also attempts to measure the total decay width Γ_h of the SM Higgs boson which is predicted to be $\Gamma_h \approx 4$ MeV. A dedicated analysis [31] determined an upper limit of $\Gamma_h < 26$ MeV and $\Gamma_h < 66$ MeV for the gluon fusion process and vector boson fusion process, respectively. For completeness we also give the combination of results [32] for the Higgs boson mass obtained for measurements at 7 and 8 TeV: $m_h = 125.09 \pm 0.24$ GeV. Even though there are constraints on the Higgs mass (for example from Large Electron-Positron Collider (LEP) data [33]) the exact value is not predicted by the SM and therefore has to be measured. The results of these very precise measurements are consistent with the constraints on the Higgs mass in the SM.

The analyses listed above are only examples for some of the more recent measurements that are representative for the overall consistent picture that the results are in agreement with the hypothesis of a SM Higgs boson with a mass of 125 GeV. However, the uncertainties of the measurements still leave room for deviations from the SM, in particular with respect to Higgs couplings. Therefore, in the future more precise measurements of the Higgs boson's properties at the LHC based on larger statistics could reveal a nonstandard nature of the discovered spin-0 boson.

But even if the properties of this 125 GeV resonance are measured to be SM-like to high precision there is still the possibility that additional Higgs bosons may exist. In the following chapters this will be mainly the school of thought on which this thesis is based.

1.1.3. The top quark

The top quark stands out among the SM fermions. It takes a unique position in the SM as the heaviest know elementary particle which is almost as heavy as a gold atom ($m_t = 0.94m_{\text{AU}}$). Since the mass is related to the Yukawa interaction the top quark's coupling to the Higgs is the strongest among the SM fermions and it is therefore also considered as a sensitive probe to study the mechanism of electroweak symmetry breaking. Furthermore, the top quark has some unique properties that are particularly beneficial for the phenomenological studies carried out in this thesis. Hence, it is used in this work as a probe to study new physics in the Higgs sector. In the following a brief overview is given over the properties of the top quark. For more detailed reviews of top-quark physics see for example Refs. [34–38].

As outlined above the top quark, as all the other quarks in the SM, transforms as a triplet under the $SU(3)_c$ gauge group. The left-handed top quark with a hypercharge of $Y = 1/6$ is the $I_3 = 1/2$ weak-isospin partner of the left-handed bottom quark. The right-handed top quark has

²The spin-1 scenario is excluded by the Yang theorem [28].

1. Introduction

a hypercharge of $Y = 2/3$. Therefore, the top quark is electrically charged: $Q = I_3 + Y = +2/3$. These quantum numbers indicate that the top quark is charged with respect to all three gauge groups of the SM, i.e. it interacts via the strong, weak and electromagnetic forces.

The world combination of measurements of the top-quark mass [39] yields

$$m_t = 173.34 \pm 0.76 \text{ GeV}. \quad (1.17)$$

which has an accuracy of 0.4%. However, as discussed for example in Ref. [40] this measured quantity is related to a parameter in the Monte Carlo generators [41] used to extract this result rather than being related to a parameter in the Lagrangian. Hence, this quantity is subject to tunings and calibrations of these generators and the relation to a mass definition in perturbative quantum field theory is not known. While other measurements based on theoretically computable observables with a top mass definition in a well defined renormalization scheme have been proposed [42, 43] and measured (for an overview see Ref. [44]) the so far achieved accuracy is not as high as in (1.17). However, these results are in agreement with the world combination. Thus, for the phenomenological studies in this thesis the experimental result given in Eq. (1.17) is interpreted as the top-quark pole mass.

In the SM the only possible two-body decays of the top quark are mediated via the weak force

$$t \rightarrow qW^+, \quad (1.18)$$

where q denotes a general down-type quark, i.e. $q = d, s, b$. Due to the large top-quark mass the decay into an on-shell W boson with $m_W = 80.385 \text{ GeV}$ [45] is possible. The W^+ boson, for example, decays further either into leptons ($\ell^+ \nu_\ell$) or quarks ($q\bar{q}'$). The decay rate is proportional to the square of the CKM matrix element $|V_{tq}|^2$. Since $|V_{tb}|^2 \approx 1$ [46, 47] assuming unitarity of the CKM matrix ($|V_{tu}|^2 + |V_{ts}|^2 + |V_{tb}|^2 = 1$) yields $|V_{ts}|^2, |V_{td}|^2 \ll |V_{tb}|^2$. Therefore, the top-quark decays almost exclusively into W^+b , with a branching fraction given by [45]

$$\frac{\Gamma(Wb)}{\Gamma(Wq(q = b, s, d))} = 0.957 \pm 0.034. \quad (1.19)$$

In the Born approximation the decay rate of the top quark to a W boson and a b quark is given by

$$\Gamma_t = \Gamma(t \rightarrow Wb) = \frac{1}{16\pi} \frac{m_t^3}{v^2} |V_{tb}|^2 \left(1 - \frac{m_W^2}{m_t^2}\right)^2 \left(1 + 2 \frac{m_W^2}{m_t^2}\right). \quad (1.20)$$

Inserting the values for m_t (1.17) and m_W and setting $|V_{tb}|^2 = 1$ gives

$$\Gamma_t = 1.5 \text{ GeV}. \quad (1.21)$$

The top-quark width is relatively narrow with respect to the mass of the top quark

$$\frac{\Gamma_t}{m_t} = 0.009. \quad (1.22)$$

Hence, it is possible to consider the decay of the top quark in the so-called *narrow width approximation* where the top-quark decays on-shell³. In this approximation top-quark pair production and the subsequent decay can be factorized into two processes.

The decay width in (1.21) corresponds to a top-quark lifetime of

$$\tau_t = \frac{1}{\Gamma_t} \approx 5 \times 10^{-25} \text{ s}. \quad (1.23)$$

³For certain observables and regions of phase space off-shell effects can become important [48, 49].

This very short lifetime leads to a unique property of the top quark: Comparing τ_t to the average hadronization time [36] $\tau_{\text{had}} = 1/\Lambda_{\text{QCD}} \approx 3 \times 10^{-24} \text{s}$ shows that the top-quark decays before it can take part in the hadron forming process. Therefore, the spin information of the top quark is not diluted by hadronization but instead is passed to the decay products of the top quark. The decay via the P violating weak interaction translates this spin information into angular correlations of the top quark's decay products. This thesis makes use of this property by studying spin dependent observables that are sensitive to top-quark polarization and $t\bar{t}$ spin correlations.

At the LHC top quarks are mainly produced in top-antitop pairs with a measured cross section of $\sigma_{t\bar{t}} = 818 \pm 36 \text{ pb}^4$ [50] at 13 TeV while single tops are produced less often with a cross section of $\sigma_t = 154 \pm 22 \text{ pb}$ [51] at 13 TeV in the t channel. This happens mainly because $t\bar{t}$ production is mediated via the strong interaction while single top production proceeds via the weak interaction. The experimental results for the cross section are in agreement with the theoretical expectation of the SM of $\sigma_{t\bar{t}} = 832_{-46}^{+40} \text{ pb}$ [52] (at next-to-next-to-leading order and including next-to-next-to-leading logarithmic corrections in QCD) and $\sigma_t = 136.0_{-2.9}^{+4.1} \text{ pb}$ [53,54] (at next-to-leading order (NLO) QCD).

1.2. Physics beyond the standard model

As already mentioned above the SM was so far successful in describing particle physics experiments at lepton and hadron colliders to high accuracy. Still, there are some experimental observations that are in disagreement with theoretical predictions derived within the SM. The investigation of these kinds of discrepancies between observation and theory is what we call the *phenomenologically motivated search for physics beyond the SM*. Apart from this motivation bases on experimental observation there is another equally well-tread path in the quest for new physics namely the *theoretically motivated search for physics beyond the SM*. In the following both of these avenues are discussed briefly.

Let us consider first which experimental observations show clear indications and evidence for the existence of physical phenomena that are not described by the SM. The strongest hints for new physics comes from astronomical and cosmological observations:

- The matter density ρ_m of the universe relative to the critical energy density ρ_{crit} (which corresponds to the total energy density of a universe with zero curvature) is measured to be [55] $\Omega_m = \rho_m/\rho_{\text{crit}} = 0.308 \pm 0.012$. However, baryonic matter, i.e. matter that is described by the SM, accounts only for about 17% of the matter density (5% of the total energy density) in the universe. The remaining contribution to the matter density is of unknown origin and does not emit any kind of electromagnetic radiation. Hence, it is referred to as *dark matter* [45]. The existence of dark matter is only inferred from its gravitational effects over a wide range of astronomical and cosmological observables. However, so far, dark matter has evaded direct detection e.g. through nuclear recoil or indirect detection through radiation from dark matter annihilation processes. Furthermore, there has been no evidence for dark matter particles created at the LHC.
- Surveys of distant supernovae [56, 57] revealed an accelerated expansion of the universe which corresponds to a nonvanishing positive cosmological constant. The contribution of the cosmological constant to the total energy density of the universe (which coincides with the critical energy density) is measured as [55] $\Omega_\Lambda = 0.6911 \pm 0.0062$. This drives the accelerated expansion of the universe and is also called *dark energy* [45]. While

⁴ Statistical and systematic uncertainties were added in quadrature.

1. Introduction

it is easy to incorporate this contribution into the Einstein equations of gravitation a quantum field theoretical description of the cosmological constant faces the so-called *cosmological constant problem* [58].

In regard of these experimental observations it becomes clear that while the SM is very successful in describing baryonic matter it is completely ignorant about 95% of the energy density of the universe.

- In the context of a modern understanding of the evolution of the universe the domination of matter over antimatter observed today, also referred to as *baryon asymmetry* [59], has to be generated dynamically and cannot be attributed to certain initial conditions. In Ref. [60] the three *necessary* conditions have been identified which have to be fulfilled in order to yield an asymmetry between baryons and antibaryons: 1.) baryon number violation, 2.) C and CP violation and 3.) a deviation from thermal equilibrium. All of these conditions are fulfilled in the SM. In particular, condition three could be realized by the electroweak phase transition from the phase with vanishing Higgs vev v to the phase where $v \neq 0$. However, as it turns out the necessary first order phase transition only occurs for Higgs masses $m_h < 72$ GeV [61–63]. In combination with theoretical predictions indicating that the effects of CP violation in the SM are not sufficiently strong [64–66] the SM seems to fail in explaining the observed baryon asymmetry in the universe.
- In order to explain seemingly acausal temperature fluctuations in the cosmic microwave background so-called *inflation* (see Ref. [45] for a review) was proposed. It involves a phase of exponentially rapid expansion of the universe in the very early stages of its evolution. In the SM there is neither a candidate for a quantum field that could drive inflation nor is the SM providing an alternative explanation for the almost uniform cosmic microwave background.

With another set of observations [16–18] neutrino oscillations have been discovered which indicate that neutrinos have mass while in the SM they are assumed to be massless. A simple extension of the SM to massive neutrinos via the Higgs mechanism is possible. However, neutrinos are the only kind of fermions in the SM that are electrically neutral and could therefore be their own antiparticles, i.e. Majorana fermions. A gauge invariant Majorana mass term in the Lagrangian is a nonrenormalizable dimension-five operator which would indicate the existence of a mass scale at which new physics is to be expected.

There are also several theoretical considerations that motivate the search for new physics.

- The most obvious flaw of the SM is the fact that one of the fundamental forces, the gravitational interaction, is not described at all because so far there exist no complete quantum theory of gravitation. Attempts to remedy this have been undertaken but it might be still a long way to go.
- If the SM is considered as an effective theory of a more complete one at much higher energy scales Λ then there is the question of how the Higgs mass m_h is stabilized against that larger energy scale. The Higgs mass squared should receive quantum corrections $\delta m_h^2 \sim \mathcal{O}(\Lambda^2)$ such that in order to arrive at the renormalized Higgs mass of $m_h^2 = m_{h,B}^2 + \delta m_h^2$ there is either a finely tuned (for a large Λ) cancellation between the bare mass $m_{h,B}$ and the quantum corrections or the Higgs mass is 'protected' by a so far undiscovered symmetry, e.g. supersymmetry (SUSY). The second conclusion directly leads to new physics and in fact the search for SUSY is largely motivated by this mass scale problem

which is also referred to as *the hierarchy problem*. However, the seriousness of the hierarchy problem and fine tuning arguments in general are debated in the literature.

- Another interesting aspect of the SM is the concept of flavor and the existence of three fermion families. The underlying theoretical foundation from which the SM flavor structure arises is, until now, unknown. In particular, it is not clear why the Higgs boson couples so distinctively to the different flavors in the SM giving rise to fermion masses which spread over six orders of magnitude from 173 GeV for the top quark to 0.5 MeV for the electron⁵. Furthermore, a fundamental understanding of the mixing pattern of fermions and how it might be related to the hierarchy of masses is absent. The SM has, in this regard, only descriptive power but lacks any explanation of what kind of mathematical structure underlies the concept of flavor.
- The SM does also not explain the origin of the gauge group $SU(3)_c \times SU(2)_L \times U(1)_Y$ nor does it predict the representations of these groups realized by the SM fermions. The quantum numbers of leptons and quarks are determined through experimental input. Hence, the SM provides a flexible structure in terms of a gauge theory which has to be 'filled' by experimental input.
- There is an additional term that contributes to \mathcal{L}_{QCD} (1.5), namely

$$\mathcal{L}_\theta = \theta \frac{\alpha_s}{32\pi^2} \epsilon_{\mu\nu\rho\sigma} G^{\mu\nu a} G^{\rho\sigma a} \quad (1.24)$$

which gives rise to CP violating effects in QCD. In particular, it generates an electric dipole moment of the neutron d_n . However, experimental measurements have put strong constraints on this effect in terms of an upper limit: $d_n < 3.6 \times 10^{-26} e\text{cm}$ (95% CL) [67]. This in turn yields an upper limit for the θ -term of $\theta \lesssim 10^{-10}$ [68–71]. The question why this parameter is so small or maybe even vanishing is known as the *strong CP problem*. Again, the SM does not deliver an answer to this question. Attempts of resolving this problem have lead to the introduction of a new type of particle, the *axion*.

This is of course only a subset of theoretical questions about the SM that are unresolved at the moment. A common theme of all the theoretical considerations above is the question whether there exists a more fundamental theory that can predict at least some of the parameters of the SM that, for now, have to be determined experimentally. Thus, providing some kind of explanation for structures in the SM that seem somewhat arbitrary such as the different fermion flavors or families.

While astronomical and cosmological observations and the observation of neutrino oscillations indicate the existence of physics beyond the SM they do not directly hint on how this new physics is realized. In light of this lack of direct evidence for new physics, e.g. in terms of new particles, theoretical considerations of the kind discussed above could serve as a starting point in the search for directions where to look for new physics.

From a phenomenological point of view there are several tools and methods used to approach the study of beyond the standard model (BSM) effects in collider physics. In principle they can be divided into model independent approaches, studies within concrete UV-complete models and some hybrid of the former two. The model independent approach which has gained increased attention over the last years as a tool in collider phenomenology is effective field theory, in particular the so-called *standard model effective field theory*. This is basically an expansion of the Lagrangian in terms of operators of mass dimension $D > 4$ which are

⁵Including the neutrinos with $m_\nu \sim 0.1$ eV yields a fermion mass range of 11 orders of magnitude.

1. Introduction

suppressed by factors of Λ^{4-D} where Λ is the energy scale of the new physics. These operators correspond to new types of interactions with new coupling constants (Wilson coefficients) that parametrize the low-energy behaviour of a theory involving energy scales of order Λ . The advantage of this method is that one can parametrize BSM contributions in a largely model independent, systematic and most importantly gauge invariant way. In this respect effective field theory supersedes the framework of anomalous couplings where, for example, gauge interactions are extended by additional terms in the Lagrangian parametrizing new physics. However, in applying this method of effective field theory to extract bounds on the Wilson coefficients from experimental data one makes implicit assumptions about the energy scale of the new physics. In cases where this method is not applicable, e.g. when searching for high-mass resonances at the LHC, the use of so-called *simplified models* has been advocated. These models have the advantage of capturing certain phenomenological key features under investigation, e.g. resonances, while at the same time being conceptually and computationally simple. However, they are not always gauge invariant but their completion to gauge invariant theories can have phenomenologically relevant effects [72]. As a third path to physics beyond the SM UV-complete, gauge invariant theories can be considered. The disadvantage of this approach is the fact that these theories can be complicated from a computational and conceptual point of view as well as involve many parameters making straightforward interpretations of experimental results difficult. In these cases usually some additional assumptions are made in order to restrict the parameter space and reduce the number of parameters. Furthermore, the fact that in this approach only one specific model is studied can be regarded as a disadvantage considering that at the moment it is not clear where to look for new physics. However, the advantage of studying concrete models is that they can be applied to collider phenomenology without any restrictions on the phase space, higher order corrections can be systematically calculated in a gauge invariant way and all phenomenological effects of this model can be taken consistently into account.

This dissertation is implementing the third method of studying physics beyond the SM described above by investigating phenomenological aspects of the renormalizable and gauge invariant two-Higgs-doublet model (2HDM) extension of the SM (Chap. 2).

1.3. Outline of this thesis

The aim of this dissertation is to study the impact of heavy non-SM Higgs bosons on the production of $t\bar{t}$ pairs in proton-proton collisions at the LHC. While the existence of a spin-0 boson with properties of the SM Higgs boson is experimentally established the existence of other heavier Higgs bosons is not completely ruled out yet. The scalar sector could be much richer than predicted by the SM involving several scalars and/or pseudoscalars. This thesis is focused on spin-0 bosons in addition to the SM Higgs boson with masses large enough to decay into $t\bar{t}$ pairs leaving their “footprint” in collider observables related to $t\bar{t}$ production. Several of these observables are studied and compared with respect to their sensitivity to the contributions of heavy Higgs bosons in order to identify those kinds of measurements that probe the parameters of the Higgs sector extension further.

Some parts of the results presented in this work could be applied quite generally to new physics models featuring heavy Higgs bosons which couple to top quarks. In particular, the analytical results and the numerical setup to generate the phenomenological predictions are given in terms of reduced Yukawa couplings, masses and decay widths of the heavy Higgs bosons. The choice of a specific model relates these input parameters, e.g. the decay width depends on the couplings and masses. Hence, for a consistent unitary description the choice of a specific model is in order. Here the extended Higgs sector is studied in terms of the

so-called 2HDM. A detailed account of this model with respect to its properties relevant for $t\bar{t}$ production is given in Chap. 2. There are several theoretical motives to study this model the most prominent being SUSY. If SUSY is an underlying symmetry of nature two Higgs doublets are required to generate masses for up-type and down-type quarks and to guarantee anomaly cancellation. But even in the absence of experimental confirmation of SUSY the 2HDM remains an interesting model because it could provide a source of CP violation in addition to the one already present in the SM to explain the observed baryon asymmetry in the universe [73, 74]. Furthermore, the 2HDM is also discussed in the literature, e.g. in Ref. [75], as a portal connecting the SM with dark matter. Another theoretically attractive property of the 2HDM is the fact that it presents a consistent, renormalizable extension of the SM without adding more than just the one additional Higgs doublet. It is therefore conceptionally a rather simple extension of the SM and can be seen as one of the first steps in probing nature beyond the SM going from simple to more complicated models.

In principle one could study the 2HDM within a parameter region where the additional Higgs bosons decay predominantly into final states other than top quarks. However, from an experimental point of view top quarks are abundantly produced at a pp collider such that the LHC is often referred to as a “top-quark factory” [36, 76]. Hence, top quarks are produced as a statistically large sample needed for precision analyses. On the theoretical side $t\bar{t}$ production in the SM is very well understood including QCD corrections up to next-to-next-to-leading order and next-to-next-to-leading logarithmic corrections. The ability to perform precision physics with $t\bar{t}$ production both on the experimental and theoretical side, makes it possible to detect even small deviations from the SM. Furthermore, from a phenomenological point of view, due to the top quark’s properties described in Sec. 1.1.3 $t\bar{t}$ production is a very good testing laboratory for new physics effects. In particular, through the experimental accessibility of spin effects such as top-quark polarization and $t\bar{t}$ spin correlations, we have a set of observables at our disposal that have the potential to significantly increase the sensitivity to the effects of heavy Higgs bosons. The theoretical formalism used to extract this spin information and to construct spin dependent observables is described in Chap. 3.

The resonant production of heavy Higgs bosons and their decay into $t\bar{t}$ pairs at the LHC within the 2HDM is considered at leading order (LO) in the QCD coupling constant α_s in Chap. 4 and at NLO in Chap. 5. The discussion at LO introduces the main phenomenological features of this process. The analytical results are presented taking into account the full spin dependence by using the formalism introduced in Chap. 3. The presentation of the analytical results in this form allows a straight forward interpretation in terms of the phenomenological features of the process under consideration. This is illustrated using the top-quark polarization as an example. In general, specific terms in the analytical results can be directly related to spin independent and spin dependent observables. These observables are investigated in detail at LO QCD in Chap. 4 to assess their sensitivity to the effects of heavy Higgs bosons in $t\bar{t}$ production.

In Chap. 5 the computational methods used to obtain the analytical results at NLO QCD are presented and certain approximations applied to this calculation are discussed. Furthermore, analytical results are given in terms of virtual and real corrections. The discussion of phenomenological results is divided into two parts concerning spin independent and spin dependent observables, respectively. These observables are used to study several representative parameter scenarios within the 2HDM. In particular, the effect of NLO corrections on these observables and on their sensitivity to heavy Higgs effects is discussed. Most of the results presented in Chap. 5 are published in Refs. [77] (spin independent results) and [78] (spin dependent results) which were the first studies of heavy Higgs bosons in $t\bar{t}$ production performed

1. Introduction

at NLO QCD.

The results of this thesis are summarized in Chap. 6 where also a conclusion and outlook is given. The appendices contain supplemental material to support arguments in the main text, provide additional material such as figures, tables and formulas and give further explanations.

The two-Higgs-doublet model

The effects of heavy Higgs bosons in $t\bar{t}$ production are investigated in this work within the so-called 2HDM. This model introduces a second Higgs $SU(2)_L$ -doublet in addition to the one already present in the SM. Formally one can think of the doublet extension as adopting the family pattern of the fermion sector in the SM also in the Higgs sector and consider the two Higgs doublets as two 'families'. The model is not only interesting as a Higgs sector extension per se but it is for example also motivated by SUSY which requires two Higgs doublets for consistency and it can provide additional CP violation which is needed to explain the observed baryon asymmetry. More recently it has been considered as a possibility to mediate interactions between SM particles and dark matter [75].

As already mentioned in Chap. 1 the study of contributions from additional heavy neutral Higgs bosons to $t\bar{t}$ production could be kept rather general and this analysis could be adapted also to other extensions of the SM which involve heavy spin-0 bosons that couple to $t\bar{t}$. However, to obtain phenomenological predictions one has to choose the number of Higgs bosons that take part in the process under consideration. Furthermore, the decay widths of the heavy Higgs bosons have to be specified. These are model dependent and affect the phenomenology of $t\bar{t}$ production. In order to take the decay widths into account in a consistent way that respects unitarity the choice of one particular model is necessary. In this work the 2HDM of type II is chosen.

In this chapter the model and its features that are particularly relevant for the study of heavy Higgs bosons in $t\bar{t}$ production are outlined. In particular, we collect relevant formulae that relate the parameters of the Lagrangian with phenomenological parameters of the model such as the Higgs boson masses and the angles describing the mixing between the Higgs bosons. In the following chapters we will mostly refer to the phenomenological parameter set, e.g. when defining certain parameter scenarios. A comprehensive review on the 2HDM can be found in Ref. [79].

2.1. The scalar potential and the Higgs mass eigenstates

The full Lagrangian of the model can be split up into the contribution from the SM without the Higgs sector and the contribution from the 2HDM

$$\mathcal{L} = \mathcal{L}_{\text{SM}} + \mathcal{L}_{\text{2HDM}}, \quad (2.1)$$

with

$$\mathcal{L}_{\text{2HDM}} = \mathcal{L}_{\Phi, \text{kin}} + \mathcal{L}_{\text{Yuk}} - V_{\Phi}(\Phi_1, \Phi_2), \quad (2.2)$$

2. The two-Higgs-doublet model

where $\mathcal{L}_{\Phi, \text{kin}}$ is the kinetic term for the two Higgs doublets, \mathcal{L}_{Yuk} describes the Yukawa interaction of the two Higgs doublets to quarks and leptons and V_{Φ} is the scalar potential. The most general gauge invariant, Hermitian, renormalizable scalar potential of the 2HDM may be written as [80]

$$\begin{aligned} V(\Phi_1, \Phi_2) &= m_{11}^2 \Phi_1^\dagger \Phi_1 + m_{22}^2 \Phi_2^\dagger \Phi_2 - (m_{12}^2 \Phi_1^\dagger \Phi_2 + \text{H.c.}) \\ &+ \frac{\lambda_1}{2} (\Phi_1^\dagger \Phi_1)^2 + \frac{\lambda_2}{2} (\Phi_2^\dagger \Phi_2)^2 + \lambda_3 (\Phi_1^\dagger \Phi_1) (\Phi_2^\dagger \Phi_2) + \lambda_4 (\Phi_1^\dagger \Phi_2) (\Phi_2^\dagger \Phi_1) \\ &+ \left[\frac{\lambda_5}{2} (\Phi_1^\dagger \Phi_2)^2 + \lambda_6 (\Phi_1^\dagger \Phi_1) (\Phi_1^\dagger \Phi_2) + \lambda_7 (\Phi_2^\dagger \Phi_2) (\Phi_1^\dagger \Phi_2) + \text{H.c.} \right], \end{aligned} \quad (2.3)$$

where m_{11} , m_{22} , λ_1 , λ_2 , λ_3 and λ_4 are real parameters and m_{12} , λ_5 , λ_6 and λ_7 are in general complex parameters. The two complex $SU(2)_L$ -Higgs doublets can be parametrized as follows

$$\Phi_1 = \begin{pmatrix} \xi_1^+ \\ \frac{1}{\sqrt{2}} (v_1 + \varphi_1 + i\chi_1) \end{pmatrix}, \quad \Phi_2 = \begin{pmatrix} \xi_2^+ \\ \frac{1}{\sqrt{2}} (v_2 + \varphi_2 + i\chi_2) \end{pmatrix}, \quad (2.4)$$

where v_1 and v_2 are the two vevs of the Higgs doublets Φ_1 and Φ_2 , respectively. A relative phase between the vevs would lead to spontaneous CP violation. However, here we do not consider this possibility and assume both vevs to be real. The doublets have hypercharge $Y = +1/2$ such that the complex scalars ξ_i^+ in the upper components (with $I_3 = +1/2$) of Φ_i have electrical charge $Q = Y + I_3 = 1$ while φ_i and χ_i are electrically neutral ($Q = 0$) and real.

Since the 2HDM extension of the SM must reproduce the observed structure of the electro-weak SM in particular the vevs of the Higgs doublets must be nonvanishing and the potential must assume a minimum at these values. The *minimization condition*

$$\text{Re} \left[\frac{\partial V}{\partial \Phi_i} \Big|_{\substack{\Phi_1 = \langle \Phi_1 \rangle \\ \Phi_2 = \langle \Phi_2 \rangle}} \right] = 0, \quad \text{Im} \left[\frac{\partial V}{\partial \Phi_i} \Big|_{\substack{\Phi_1 = \langle \Phi_1 \rangle \\ \Phi_2 = \langle \Phi_2 \rangle}} \right] = 0, \quad i = 1, 2 \quad (2.5)$$

with

$$\langle \Phi_1 \rangle = \frac{1}{\sqrt{2}} \begin{pmatrix} 0 \\ v_1 \end{pmatrix}, \quad \langle \Phi_2 \rangle = \frac{1}{\sqrt{2}} \begin{pmatrix} 0 \\ v_2 \end{pmatrix} \quad (2.6)$$

leads to the following equations

$$m_{11}^2 = \frac{v_2}{v_1} \text{Re}(m_{12}^2) - \frac{1}{2} \left[\text{Re} \left(v_2^2 \lambda_5 + 3v_1 v_2 \lambda_6 + \frac{v_2^3}{v_1} \lambda_7 \right) + v_1^2 \lambda_1 + v_2^2 (\lambda_3 + \lambda_4) \right], \quad (2.7)$$

$$m_{22}^2 = \frac{v_1}{v_2} \text{Re}(m_{12}^2) - \frac{1}{2} \left[\text{Re} \left(v_1^2 \lambda_5 + \frac{v_1^3}{v_2} \lambda_6 + 3v_1 v_2 \lambda_7 \right) + v_2^2 \lambda_2 + v_1^2 (\lambda_3 + \lambda_4) \right], \quad (2.8)$$

$$\text{Im}(m_{12}^2) = \frac{1}{2} \left[v_1 v_2 \text{Im}(\lambda_5) + v_1^2 \text{Im}(\lambda_6) + v_2^2 \text{Im}(\lambda_7) \right]. \quad (2.9)$$

Equations (2.7)–(2.9) can be used to eliminate m_{11}^2 , m_{22}^2 and the imaginary part of m_{12}^2 from the scalar potential (2.3). Then after inserting the explicit form of the two doublets (2.4) one reads off the mass (bilinear) terms from the scalar potential. The part of the potential which determines the mass eigenstates of the charged Higgs bosons reads¹

$$\mathcal{L}_{m_{H^\pm}} = \begin{pmatrix} \xi_1^- & \xi_2^- \end{pmatrix} M_+ \begin{pmatrix} \xi_1^+ \\ \xi_2^+ \end{pmatrix}, \quad (2.10)$$

¹Note that for complex scalars ϕ_i the mass term in the Lagrangian reads $\mathcal{L}_m = \sum_i m_i^2 |\phi_i|^2$.

2.1. The scalar potential and the Higgs mass eigenstates

where

$$M_+ = \left(\text{Re}(m_{12}^2) - \frac{1}{2} [(\lambda_4 + \text{Re}(\lambda_5)) v_1 v_2 + \text{Re}(\lambda_6) v_1^2 + \text{Re}(\lambda_7) v_2^2] \right) \begin{pmatrix} \frac{v_2}{v_1} & -1 \\ -1 & \frac{v_1}{v_2} \end{pmatrix} \quad (2.11)$$

and $\xi_i^- = (\xi_i^+)^*$. Diagonalizing the mass matrix M_+ gives:

$$\begin{aligned} M_+^D &= S^{-1} M_+ S \\ &= \left(\text{Re}(m_{12}^2) - \frac{1}{2} [(\lambda_4 + \text{Re}(\lambda_5)) v_1 v_2 + \text{Re}(\lambda_6) v_1^2 + \text{Re}(\lambda_7) v_2^2] \right) \begin{pmatrix} 0 & 0 \\ 0 & \frac{v_1^2 + v_2^2}{v_1 v_2} \end{pmatrix} \end{aligned} \quad (2.12)$$

with the transformation matrix

$$S = \begin{pmatrix} \frac{v_1}{v} & -\frac{v_2}{v} \\ \frac{v_2}{v} & \frac{v_1}{v} \end{pmatrix} \quad (2.13)$$

and $v^2 = v_1^2 + v_2^2$. From (2.12) we see immediately that there is a zero-mass eigenstate. This is the Goldstone boson G^\pm associated with the W^\pm gauge boson. The second mass eigenstate is the charged Higgs boson H^\pm .

The orthogonal matrix S (2.13) can be parametrized in terms of one rotation angle β

$$S = \begin{pmatrix} \cos\beta & -\sin\beta \\ \sin\beta & \cos\beta \end{pmatrix} \quad (2.14)$$

with

$$v_1 = v \cos\beta, \quad v_2 = v \sin\beta. \quad (2.15)$$

The mass of the charged Higgs boson then reads

$$m_{H^\pm}^2 = \frac{\text{Re}(m_{12}^2)}{\cos\beta \sin\beta} - \frac{v^2}{2} [\lambda_4 + \text{Re}(\lambda_5) + \text{Re}(\lambda_6) \cot\beta + \text{Re}(\lambda_7) \tan\beta]. \quad (2.16)$$

and the charged Higgs boson and Goldstone boson mass eigenstates are given by

$$\begin{pmatrix} G^+ \\ H^+ \end{pmatrix} = S^{-1} \begin{pmatrix} \xi_1^+ \\ \xi_2^+ \end{pmatrix} = \begin{pmatrix} \xi_1^+ \cos\beta + \xi_2^+ \sin\beta \\ -\xi_1^+ \sin\beta + \xi_2^+ \cos\beta \end{pmatrix}. \quad (2.17)$$

The remaining degrees of freedom in the Higgs sector are neutral Higgs bosons and the Goldstone boson associated with the Z gauge boson. Assuming that all the parameters of the scalar potential are real such that CP symmetry is not violated by the potential one finds the neutral Goldstone boson G^0 and the pseudoscalar Higgs boson A to be mixtures of the χ_i components of the two doublets

$$G^0 = \chi_1 \cos\beta + \chi_2 \sin\beta, \quad (2.18)$$

$$A = -\chi_1 \sin\beta + \chi_2 \cos\beta, \quad (2.19)$$

where G^0 is massless and the mass of A is given by

$$m_A^2 = \frac{m_{12}^2}{\cos\beta \sin\beta} - \frac{v^2}{2} (2\lambda_5 + \lambda_6 \cot\beta + \lambda_7 \tan\beta). \quad (2.20)$$

In the more general case where m_{12} , $\lambda_{5,6,7}$ are complex and the potential violates CP the neutral Higgs boson mass eigenstates are not CP eigenstates. In particular the pseudoscalar A is not

2. The two-Higgs-doublet model

a mass eigenstate but instead mixes with the scalar degrees of freedom φ_1 and φ_2 . The mass term for the neutral Higgs bosons in the CP violating (CPV) case reads²

$$\mathcal{L}_{\text{neutral}} = \frac{1}{2}(\varphi_1, \varphi_2, A) \begin{pmatrix} M_{11} & M_{12} & M_{13} \\ M_{12} & M_{22} & M_{23} \\ M_{13} & M_{23} & M_{33} \end{pmatrix} \begin{pmatrix} \varphi_1 \\ \varphi_2 \\ A \end{pmatrix} \quad (2.21)$$

with the entries of the mass matrix M

$$M_{11} = \text{Re}(m_{12}^2) \tan \beta + \frac{v^2}{2} (2\lambda_1 \cos^2 \beta + 3\text{Re}(\lambda_6) \sin \beta \cos \beta - \text{Re}(\lambda_7) \tan \beta \sin^2 \beta), \quad (2.22)$$

$$M_{12} = \frac{v^2}{2} (2 \sin \beta \cos \beta \lambda_{345} + 3\text{Re}(\lambda_6) \cos^2 \beta + 3\text{Re}(\lambda_7) \sin^2 \beta) - \text{Re}(m_{12}^2), \quad (2.23)$$

$$M_{13} = -\frac{v^2}{2} (\text{Im}(\lambda_5) \sin \beta + 2\text{Im}(\lambda_6) \cos \beta), \quad (2.24)$$

$$M_{22} = \text{Re}(m_{12}^2) \cot \beta + \frac{v^2}{2} (2\lambda_2 \sin^2 \beta - \text{Re}(\lambda_6) \cot \beta \cos^2 \beta + 3\text{Re}(\lambda_7) \sin \beta \cos \beta), \quad (2.25)$$

$$M_{23} = -\frac{v^2}{2} (\text{Im}(\lambda_5) \cos \beta + 2\text{Im}(\lambda_7) \sin \beta), \quad (2.26)$$

$$M_{33} = \frac{\text{Re}(m_{12}^2)}{\sin \beta \cos \beta} - \frac{v^2}{2} (2\text{Re}(\lambda_5) + \text{Re}(\lambda_6) \cot \beta + \text{Re}(\lambda_7) \tan \beta), \quad (2.27)$$

where $\lambda_{345} = \lambda_3 + \lambda_4 + \text{Re}(\lambda_5)$. In the following we derive the relations between parameters of the Higgs potential and the Higgs boson masses and mixing angles. Therefore, we define the matrix R as the rotation matrix that transforms the CP basis $\{\varphi_1, \varphi_2, A\}$ into the mass basis $\{\phi_1, \phi_2, \phi_3\}$

$$\begin{pmatrix} \phi_1 \\ \phi_2 \\ \phi_3 \end{pmatrix} = R \begin{pmatrix} \varphi_1 \\ \varphi_2 \\ A \end{pmatrix} \quad (2.28)$$

such that

$$RMR^T = \begin{pmatrix} m_1^2 & 0 & 0 \\ 0 & m_2^2 & 0 \\ 0 & 0 & m_3^2 \end{pmatrix} \equiv M_D. \quad (2.29)$$

The general rotation matrix $R(\alpha_1, \alpha_2, \alpha_3)$ is constructed from three rotations involving the Euler angles α_1 , α_2 and α_3

$$\begin{aligned} R(\alpha_1, \alpha_2, \alpha_3) &= \begin{pmatrix} 1 & 0 & 0 \\ 0 & \cos \alpha_3 & \sin \alpha_3 \\ 0 & -\sin \alpha_3 & \cos \alpha_3 \end{pmatrix} \begin{pmatrix} \cos \alpha_2 & 0 & \sin \alpha_2 \\ 0 & 1 & 0 \\ -\sin \alpha_2 & 0 & \cos \alpha_2 \end{pmatrix} \begin{pmatrix} \cos \alpha_1 & \sin \alpha_1 & 0 \\ -\sin \alpha_1 & \cos \alpha_1 & 0 \\ 0 & 0 & 1 \end{pmatrix} \\ &= \begin{pmatrix} c_1 c_2 & c_2 s_1 & s_2 \\ -c_3 s_1 - c_1 s_2 s_3 & c_1 c_3 - s_1 s_2 s_3 & c_2 s_3 \\ -c_1 c_3 s_2 + s_1 s_3 & -c_3 s_1 s_2 - c_1 s_3 & c_2 c_3 \end{pmatrix} \end{aligned} \quad (2.30)$$

with $s_i = \sin \alpha_i$ and $c_i = \cos \alpha_i$. The matrix R obeys certain symmetries [81] which can be used to restrict the range of angles to $-\pi/2 < \alpha_i \leq \pi/2$.

²Note that for real spin-0 bosons ϕ_i the mass term in the Lagrangian reads $\mathcal{L}_m = \sum_i \frac{1}{2} m_i^2 \phi_i^2$

2.1. The scalar potential and the Higgs mass eigenstates

Solving the system of seven equations (2.16) and (2.22) - (2.27) gives

$$\lambda_1 = \left(\frac{M_{11}}{v^2 \sin^2 \beta} - \eta - \frac{3}{2} \text{Re}(\lambda_6) \cot \beta + \frac{1}{2} \text{Re}(\lambda_7) \tan \beta \right) \tan^2 \beta, \quad (2.31)$$

$$\lambda_2 = \left(\frac{M_{22}}{v^2 \cos^2 \beta} - \eta + \frac{1}{2} \text{Re}(\lambda_6) \cot \beta - \frac{3}{2} \text{Re}(\lambda_7) \tan \beta \right) \cot^2 \beta, \quad (2.32)$$

$$\lambda_3 = \frac{M_{12}}{v^2 \cos \beta \sin \beta} + \frac{2m_{H^+}^2}{v^2} - \eta - \frac{1}{2} (\text{Re}(\lambda_6) \cot \beta + \text{Re}(\lambda_7) \tan \beta), \quad (2.33)$$

$$\lambda_4 = \frac{M_{33} - 2m_{H^+}^2}{v^2} + \eta - \frac{1}{2} (\text{Re}(\lambda_6) \cot \beta + \text{Re}(\lambda_7) \tan \beta), \quad (2.34)$$

$$\text{Re}(\lambda_5) = \eta - \frac{M_{33}}{v^2} - \frac{1}{2} (\text{Re}(\lambda_6) \cot \beta + \text{Re}(\lambda_7) \tan \beta), \quad (2.35)$$

$$\text{Im}(\lambda_5) = -\frac{2M_{23}}{v^2 \cos \beta} - 2\text{Im}(\lambda_7) \tan \beta, \quad (2.36)$$

$$\text{Im}(\lambda_6) = \left(\frac{M_{23}}{v^2 \cos \beta} - \frac{M_{13}}{v^2 \sin \beta} + \text{Im}(\lambda_7) \tan \beta \right) \tan \beta, \quad (2.37)$$

where M_{ij} according to (2.29) is given by

$$M_{ij} = \sum_{k,l=1}^3 R_{ki} (M_D)_{kl} R_{lj} = \sum_{k,l=1}^3 m_k^2 R_{kj} \delta_{kl} R_{li} = \sum_{k=1}^3 m_k^2 R_{ki} R_{kj} \quad (2.38)$$

and

$$\eta = \frac{\text{Re}(m_{12}^2)}{v^2 \sin \beta \cos \beta}. \quad (2.39)$$

Hence, in Eqs. 2.31–2.37 we have expressed most of the parameters of the Higgs potential in terms of the phenomenological parameters m_1 , m_2 , m_3 , m_{H^+} , α_1 , α_2 , α_3 , $\tan \beta$ and v . In general not all parameters in the potential can be expressed in terms of phenomenological parameters. In the equations above the parameters $\text{Re}(\lambda_6)$, λ_7 and m_{12}^2 (η) have to be given in addition to the phenomenological parameters to specify the general Higgs potential. In Sec. 2.4 the parameters of the 2HDM are discussed in detail, in particular, with respect to certain symmetries applied to the Lagrangian.

We turn now to the case in which the scalar potential is CP conserving (CPC) and all its parameters are real. In this case the neutral Higgs mass eigenstates are also CP eigenstates, i.e. states which transform differently under CP cannot mix. This can be easily seen from Eq. (2.24) and Eq. (2.26): If all parameters in the potential are real (in particular λ_5 , λ_6 and λ_7) M_{13} and M_{23} vanish and the mass matrix M (2.21) becomes block diagonal

$$\mathcal{L}_{\text{neutral}} = \frac{1}{2} (\varphi_1, \varphi_2, A) \begin{pmatrix} (M_\varphi)_{11} & (M_\varphi)_{12} & 0 \\ (M_\varphi)_{12} & (M_\varphi)_{22} & 0 \\ 0 & 0 & m_A^2 \end{pmatrix} \begin{pmatrix} \varphi_1 \\ \varphi_2 \\ A \end{pmatrix} \quad (2.40)$$

with

$$(M_\varphi)_{11} = m_{12}^2 \tan \beta + \frac{v^2}{2} (2\lambda_1 \cos^2 \beta + 3\lambda_6 \cos \beta \sin \beta - \lambda_7 \tan \beta \sin^2 \beta), \quad (2.41)$$

$$(M_\varphi)_{22} = m_{12}^2 \cot \beta + \frac{v^2}{2} (2\lambda_2 \sin^2 \beta - \lambda_6 \cot \beta \cos^2 \beta + 3\lambda_7 \cos \beta \sin \beta), \quad (2.42)$$

$$(M_\varphi)_{12} = -m_{12}^2 + \frac{v^2}{2} (2\lambda_{345} \cos \beta \sin \beta + 3\lambda_6 \cos^2 \beta + 3\lambda_7 \sin^2 \beta). \quad (2.43)$$

2. The two-Higgs-doublet model

The mass eigenstates are obtained by diagonalizing the mass matrix M_φ

$$H = \varphi_1 \cos \alpha + \varphi_2 \sin \alpha, \quad (2.44)$$

$$h = -\varphi_1 \sin \alpha + \varphi_2 \cos \alpha, \quad (2.45)$$

where the angle α that parametrizes the mixing between φ_1 and φ_2 was introduced. Often the angle α is used in the literature that considers only the CPC 2HDM. However, the mixing between the neutral scalars φ_1 and φ_2 in the CPC case can also be parametrized using the general matrix $R(\alpha_1, \alpha_2, \alpha_3)$ (2.30) by setting $\alpha_1 = \alpha + \pi/2$, $\alpha_2 = \alpha_3 = 0$

$$\begin{pmatrix} h \\ -H \\ A \end{pmatrix} = R(\alpha + \pi/2, 0, 0) \begin{pmatrix} \varphi_1 \\ \varphi_2 \\ A \end{pmatrix} = \begin{pmatrix} -\sin \alpha & \cos \alpha & 0 \\ -\cos \alpha & -\sin \alpha & 0 \\ 0 & 0 & 1 \end{pmatrix} \begin{pmatrix} \varphi_1 \\ \varphi_2 \\ A \end{pmatrix}. \quad (2.46)$$

The mass eigenvalues of the CP -even Higgs bosons are given by

$$m_{H,h}^2 = \frac{1}{2} \left\{ (M_\varphi)_{11} + (M_\varphi)_{22} \pm \sqrt{((M_\varphi)_{11} - (M_\varphi)_{22})^2 + 4(M_\varphi)_{12}^2} \right\}. \quad (2.47)$$

In order to determine the mass eigenstates we have studied the bilinear terms in the potential. The trilinear and quartic terms determine the interaction among the Higgs bosons. For the purpose of calculating the two-body decay widths of the Higgs bosons we need the trilinear couplings between the Higgs bosons. Since these terms are rather lengthy they are presented in appendix A.

To summarize this section the two complex Higgs doublets Φ_1 and Φ_2 of the 2HDM give rise to five physical Higgs bosons: three neutral and two charged (H^\pm) ones. When the scalar potential is CPC (and there is no spontaneous CP breaking) then the electrically neutral Higgs bosons have definite CP and one can separate them into the scalars h and H ($m_h < m_H$) and a pseudoscalar A . The scalar mass eigenstates are mixtures of the doublet components φ_1 and φ_2 parametrized by the mixing angle α . In the case of CP violation (or spontaneous CP breaking) the neutral Higgs boson mass eigenstates ϕ_1 , ϕ_2 and ϕ_3 are mixtures of the scalars φ_1 , φ_2 and the pseudoscalar A parametrized by the mixing angles α_1 , α_2 and α_3 . Thus a distinction of ϕ_1 , ϕ_2 and ϕ_3 into scalars and pseudoscalars is not possible. Besides the five physical Higgs bosons there remain three more degrees of freedom generated by the two complex Higgs doublets. These states are the Goldstone bosons G^\pm and G^0 which mix with the $SU(2)_L$ -gauge field W^μ and the $U(1)_Y$ -gauge field B^μ to provide (in the unitary gauge) the longitudinal polarizations of the massive gauge bosons W^\pm and Z . In this way the 2HDM provides the same spontaneous symmetry breaking mechanism to generate massive gauge bosons as in the SM. In the next section we will see that the masses of the gauge bosons in the SM are as well reproduced by the 2HDM.

Finally we can express the two Higgs doublets (2.4) in terms of the mass eigenstates

$$\Phi_1 = \begin{pmatrix} G^+ \cos \beta - H^+ \sin \beta \\ \frac{1}{\sqrt{2}} [v_1 + iG^0 \cos \beta + \sum_j \phi_j (R_{j1} - iR_{j3} \sin \beta)] \end{pmatrix}, \quad (2.48)$$

$$\Phi_2 = \begin{pmatrix} G^+ \sin \beta + H^+ \cos \beta \\ \frac{1}{\sqrt{2}} [v_2 + iG^0 \sin \beta + \sum_j \phi_j (R_{j2} + iR_{j3} \cos \beta)] \end{pmatrix}. \quad (2.49)$$

In the CPC case where $\alpha_2 = \alpha_3 = 0$ the doublets can be expressed in terms of the mass and

CP eigenstates h , H and A

$$\Phi_1 = \begin{pmatrix} G^+ \cos \beta - H^+ \sin \beta \\ \frac{1}{\sqrt{2}} [v_1 + h \cos \alpha_1 + H \sin \alpha_1 + i(G^0 \cos \beta - A \sin \beta)] \end{pmatrix}, \quad (2.50)$$

$$\Phi_2 = \begin{pmatrix} G^+ \sin \beta + H^+ \cos \beta \\ \frac{1}{\sqrt{2}} [v_2 + h \sin \alpha_1 - H \cos \alpha_1 + i(G^0 \sin \beta + A \cos \beta)] \end{pmatrix}, \quad (2.51)$$

where

$$\alpha_1 = \alpha + \frac{\pi}{2}. \quad (2.52)$$

2.2. Gauge-Higgs coupling

The gauge boson masses and the couplings between gauge and Higgs bosons are derived from the kinetic part of the 2HDM Lagrangian (2.2)

$$\mathcal{L}_{\Phi, \text{kin}} = (D_\mu \Phi_1)^\dagger (D^\mu \Phi_1) + (D_\mu \Phi_2)^\dagger (D^\mu \Phi_2) \quad (2.53)$$

with

$$D_\mu = \partial_\mu - i \frac{g}{\sqrt{2}} (W_\mu^+ T^+ + W_\mu^- T^-) - i \frac{1}{\sqrt{g^2 + g'^2}} Z_\mu \left(g^2 T^3 - g'^2 \frac{Y}{2} \right) - ie Q A_\mu, \quad (2.54)$$

where

$$T^\pm = T^1 \pm iT^2, \quad T^i = \frac{\sigma^i}{2}, \quad (2.55)$$

σ^i are the Pauli-matrices and g and g' are the $SU(2)_L$ and $U(1)_Y$ gauge couplings, respectively. The covariant derivative in matrix form reads

$$D_\mu = \begin{pmatrix} \partial_\mu - i\kappa_{z,1} Z_\mu - ieA_\mu & -i\kappa_w W_\mu^+ \\ -i\kappa_w W_\mu^- & \partial_\mu - i\kappa_{z,2} Z_\mu \end{pmatrix} \quad (2.56)$$

with

$$\kappa_{z,1} = \frac{1}{2} \frac{g^2 - g'^2}{\sqrt{g^2 + g'^2}}, \quad \kappa_{z,2} = -\frac{\sqrt{g^2 + g'^2}}{2}, \quad \kappa_w = \frac{g}{\sqrt{2}}. \quad (2.57)$$

Acting with D_μ on the doublets in Eq. (2.53) evaluated at the vacuum expectation values (2.6) gives the masses of the W^\pm and Z bosons

$$\begin{aligned} \mathcal{L}_{Z,W, \text{mass}} &= \mathcal{L}_{\Phi, \text{kin}} \Big|_{\substack{\Phi_1 = \langle \Phi_1 \rangle \\ \Phi_2 = \langle \Phi_2 \rangle}} = \frac{v_1^2 + v_2^2}{2} (\kappa_w^2 W_\mu^+ W^{-\mu} + \kappa_{z,2}^2 Z_\mu Z^\mu) \\ &= m_W^2 W_\mu^+ W^{-\mu} + \frac{m_Z^2}{2} Z_\mu Z^\mu. \end{aligned} \quad (2.58)$$

Thus the gauge boson masses

$$m_W = g \frac{v}{2}, \quad m_Z = \sqrt{g^2 + g'^2} \frac{v}{2} \quad (2.59)$$

are identical to those of the SM for $v = \sqrt{v_1^2 + v_2^2} = 246 \text{ GeV}$.

Using Eq. (2.48) and Eq. (2.49) the Lagrangian in Eq. (2.53) can be expressed in terms of Higgs mass eigenstates to determine the couplings of the Higgs bosons with the gauge bosons. All possible couplings in the CPV and CPC case are listed schematically in Tab. 2.1.

2. The two-Higgs-doublet model

Table 2.1.: Possible couplings between Higgs and gauge bosons in the CPC and CPV 2HDM. The bracket notation is to be understood as follows: $ZZ(h, H) = ZZh, ZZH$. The numbers in square brackets refer to the respective equations in the text.

coupling pattern	CPC 2HDM	CPV 2HDM
$V\phi\phi$	$W^\pm H^\mp(h, H, A)$ $Z(hA, HA, H^+H^-)$ [2.62] γH^+H^-	$W^\pm H^\mp\phi_j$ $Z(\phi_1\phi_2, \phi_1\phi_3, \phi_2\phi_3, H^+H^-)$ [2.60] γH^+H^-
$VV\phi$	$WW(h, H), ZZ(h, H)$ [2.63]	$WW\phi_j, ZZ\phi_j$ [2.61]
$VV'\phi$	—	—
$VV\phi\phi$	$W^+W^-(hh, HH, AA, H^+H^-)$ $ZZ(hh, HH, AA, H^+H^-)$ $\gamma\gamma H^+H^-$	$W^+W^-(\phi_j\phi_k, H^+H^-)$ $ZZ(\phi_j\phi_k, H^+H^-)$ $\gamma\gamma H^+H^-$
$VV'\phi\phi$	$W^\pm ZH^\mp(h, H, A)$ $W^\pm\gamma H^\mp(h, H, A)$ $Z\gamma H^+H^-$	$W^\pm ZH^\mp\phi_j$ $W^\pm\gamma H^\mp\phi_j$ $Z\gamma H^+H^-$

The corresponding expressions in the Lagrangian are here only given for the couplings that are relevant for the two-body decays of the neutral Higgs bosons. There are two types of interactions between the neutral Higgs bosons and gauge bosons that contribute to two-body decays: $VV\phi$ and $V\phi\phi$ couplings

$$\begin{aligned} \mathcal{L}_{Z\Phi\Phi} &= \sum_{j < k=1}^3 \frac{m_Z}{v} (\phi_j \partial_\mu \phi_k - \phi_k \partial_\mu \phi_j) \\ &\times \left[(R_{j2}R_{k3} - R_{j3}R_{k2}) \cos\beta + (R_{j3}R_{k1} - R_{j1}R_{k3}) \sin\beta \right] Z^\mu \\ &+ i\kappa_{z,1} (H^- \partial_\mu H^+ - H^+ \partial_\mu H^-) Z^\mu, \end{aligned} \quad (2.60)$$

$$\mathcal{L}_{VV\Phi} = \sum_{j=1}^3 (R_{j1} \cos\beta + R_{j2} \sin\beta) \left[\frac{2m_W^2}{v} W_\mu^+ W^{-\mu} + \frac{m_Z^2}{v} Z_\mu Z^\mu \right] \phi_j. \quad (2.61)$$

In the CPC case the general expressions in Eqs. 2.60 and 2.61 simplify to

$$\begin{aligned} \mathcal{L}_{Z\Phi\Phi} &= \frac{m_Z}{v} \left\{ \left[h(\partial_\mu A) - A(\partial_\mu h) \right] \sin(\alpha_1 - \beta) \right. \\ &\quad \left. + \left[H(\partial_\mu A) - A(\partial_\mu H) \right] \cos(\alpha_1 - \beta) \right\} Z^\mu \\ &+ i\kappa_{z,1} (H^- \partial_\mu H^+ - H^+ \partial_\mu H^-) Z^\mu, \end{aligned} \quad (2.62)$$

$$\mathcal{L}_{VV\Phi} = (h \cos(\alpha_1 - \beta) + H \sin(\alpha_1 - \beta)) \left[\frac{2m_W^2}{v} W_\mu^+ W^{-\mu} + \frac{m_Z^2}{v} Z_\mu Z^\mu \right]. \quad (2.63)$$

In this work the decays $\phi_j \rightarrow W^\pm H^\mp$ are not considered because $m_{H^+} > m_j$ is assumed.

2.3. Yukawa couplings

The couplings of Higgs bosons to fermions are determined by the Yukawa-interaction part \mathcal{L}_{Yuk} of the Lagrangian. In its most general form it can be written as

$$\mathcal{L}_{\text{Yuk}} = -\bar{Q}'_L \left[(\lambda'_{d,1} \Phi_1 + \lambda'_{d,2} \Phi_2) d'_R + (\lambda'_{u,1} \tilde{\Phi}_1 + \lambda'_{u,2} \tilde{\Phi}_2) u'_R \right] - \bar{L}'_L (\lambda'_{l,1} \Phi_1 + \lambda_{l,2} \Phi_2) l'_R + \text{H.c.}, \quad (2.64)$$

where

$$\bar{Q}_L = \begin{pmatrix} u \\ d \end{pmatrix} \quad \text{and} \quad \bar{L}_L = \begin{pmatrix} \nu_l \\ l^- \end{pmatrix} \quad (2.65)$$

are the left-handed quark and lepton $SU(2)_L$ doublets with u , d , ν_l and l^- denoting up-type quarks, down-type quarks, neutrinos with lepton flavor l and negatively charged leptons. The right-handed up-type quark, down-type quark and lepton singlets are denoted by u_R , d_R and l_R . Furthermore

$$\tilde{\Phi}_j = i\sigma_2 \Phi_j^*, \quad (2.66)$$

where σ_2 is the second Pauli-matrix. $\lambda'_{f,j}$, $f = d, u, l$ are the Yukawa matrices for the coupling of down-type quarks, up-type quarks and leptons to the j th Higgs doublet. Flavor indices have been suppressed. Primed quantities denote the flavor basis. Without imposing any additional symmetries $\lambda'_{f,j}$ are arbitrary complex-valued matrices. Let us assume that in the quark and lepton mass basis the Yukawa matrices $\lambda_{f,1}$ (unprimed quantities denote the fermion mass basis) are real and diagonal. Then there are only flavor-diagonal couplings between the fermion mass eigenstates and Φ_1 . However, $\lambda_{f,2}$ do not need to be diagonal such that flavor-off-diagonal couplings between fermions and Φ_2 were possible³. In other words the Lagrangian in Eq. (2.64) with general Yukawa matrices introduces FCNCs at tree level. This kind of interaction is experimentally very well constrained, hence a mechanism is needed to avoid these FCNCs.

There are two methods commonly used to ensure that Higgs-mediated FCNCs are absent at tree level: *Yukawa alignment* [82] and *imposing a Z_2 symmetry* [83–86]. In case of Yukawa alignment the matrices $\lambda_{f,1}$ and $\lambda_{f,2}$ are proportional such that they can be diagonalized simultaneously. However, due to higher order corrections the matrices $\lambda_{f,1}$ and $\lambda_{f,2}$ can mix under renormalization. In Ref. [87] it has been shown that the Yukawa matrices remain proportional under renormalization if and only if *fermions with the same charge couple only to one Higgs doublet*. This brings us to the second possibility of avoiding FCNCs. This method imposes a Z_2 symmetry under which the Higgs doublets and the fermions transform such that one type of fermion (up-type, down-type, lepton) can only couple to one Higgs doublet. There are four different possibilities to realize such a coupling pattern. In this work the so-called *type II* is implemented

$$\text{type II:} \quad \lambda_2^d = \lambda_2^l = 0, \quad \lambda_1^u = 0, \quad (2.67)$$

i.e. right-handed down-type quarks and leptons couple to Φ_1 and right-handed up-type quarks couple to Φ_2 . This coupling structure can be realized by imposing the following Z_2 symmetry transformations

$$\Phi_1 \rightarrow \Phi_1, \quad d_R \rightarrow d_R, \quad l_R \rightarrow l_R, \quad (2.68)$$

$$\Phi_2 \rightarrow -\Phi_2, \quad u_R \rightarrow -u_R \quad (2.69)$$

³In the SM there is only one Higgs doublet and therefore only three Yukawa matrices for up-type quarks, down-type quarks and leptons. These can all individually be diagonalized by transformation into the fermion mass basis. Hence in the SM there is no problem with flavor changing neutral currents in the Yukawa sector.

2. The two-Higgs-doublet model

and demanding that the Lagrangian is invariant under this Z_2 symmetry. Besides generating the desired Yukawa couplings the exact symmetry also constrains the Higgs potential such that

$$m_{12}^2 = \lambda_6 = \lambda_7 = 0. \quad (2.70)$$

Due to Eq. (2.67) the type-II 2HDM Yukawa Lagrangian \mathcal{L}_{Yuk} in Eq. (2.64) simplifies to the form

$$\mathcal{L}_{\text{Yuk}} = -\bar{Q}'_L \left[\lambda'_d \Phi_1 d'_R + \lambda'_u \tilde{\Phi}_2 u'_R \right] - \bar{L}'_L \lambda'_l \Phi_1 l'_R + \text{H.c.}, \quad (2.71)$$

where $\lambda'_d \equiv \lambda_{d,1}$, $\lambda'_u \equiv \lambda'_{u,2}$ and $\lambda'_l \equiv \lambda'_{l,1}$. After electro-weak symmetry breaking and rotating to the mass basis where the Yukawa matrices are diagonal the Lagrangian in Eq. (2.71) generates the following mass terms

$$\mathcal{L}_{\text{mass}} = -\frac{\lambda_d^{ij}}{\sqrt{2}} v_1 \bar{d}_i d_j - \frac{\lambda_u^{ij}}{\sqrt{2}} v_2 \bar{u}_i u_j - \frac{\lambda_l^{ij}}{\sqrt{2}} v_1 \bar{l}_i l_j, \quad (2.72)$$

where i, j are family indices and $\lambda_f = \text{diag}(y_{f,1}, y_{f,2}, y_{f,3})$. From Eq. (2.72) we read off the fermion masses

$$m_d = \frac{y_d v \cos \beta}{\sqrt{2}}, \quad m_u = \frac{y_u v \sin \beta}{\sqrt{2}}, \quad m_l = \frac{y_l v \cos \beta}{\sqrt{2}}, \quad (2.73)$$

where the family indices have been omitted and the subscripts d, u and l denote down-type quarks, up-type quarks and leptons.

The Yukawa interaction between fermion and Higgs mass eigenstates can be read off Eq. (2.71) after rotating to the fermion mass basis and using Eqs. (2.48) and (2.49)

$$\begin{aligned} \mathcal{L}_{\text{Yuk}} = & -\frac{m_u}{v} \bar{u} \left[\frac{R_{j2}}{\sin \beta} - i \frac{R_{j3} \cos \beta}{\sin \beta} \gamma_5 \right] u \phi_j + y_u \cos \beta \left[H^+ V_{ud} \bar{u}_R d_L + H^- V_{ud}^* \bar{d}_L u_R \right] \\ & -\frac{m_d}{v} \bar{d} \left[\frac{R_{j1}}{\cos \beta} - i \frac{R_{j3} \sin \beta}{\cos \beta} \gamma_5 \right] d \phi_j + y_d \sin \beta \left[H^+ V_{ud} \bar{u}_L d_R + H^- V_{ud}^* \bar{d}_R u_L \right] \\ & -\frac{m_l}{v} \bar{l} \left[\frac{R_{j1}}{\cos \beta} - i \frac{R_{j3} \sin \beta}{\cos \beta} \gamma_5 \right] l \phi_j + y_l \sin \beta \left[H^+ (\bar{\nu}_l)_L l_R + H^- \bar{l}_R (\nu_l)_L \right], \end{aligned} \quad (2.74)$$

where summation over $j = 1, 2, 3$ is implied. The general form of the Yukawa couplings of the neutral Higgs bosons in \mathcal{L}_{Yuk} can be parametrized as follows

$$\mathcal{L}_{\text{Yuk,neutral}} = -\frac{m_f}{v} \bar{f} (a_{fj} - i b_{fj} \gamma_5) f \phi_j, \quad (2.75)$$

where a_{fj} (b_{fj}) denote the reduced scalar (pseudoscalar) Yukawa couplings to up-type quarks ($f = u, c, t$), down-type quarks ($f = d, s, b$) and leptons ($f = e, \mu, \tau$), respectively. The reduced Yukawa couplings of the neutral Higgs bosons in the 2HDM are summarized in Tab. 2.2. The reduced Yukawa couplings in the CPC case are also presented in Tab. 2.2. They are obtained by setting $\alpha_2 = \alpha_3 = 0$ in the rotation matrix R and identifying $\phi_1 = h$, $\phi_2 = -H$ and $\phi_3 = A$.

We close this section with some remarks on Z_2 symmetry breaking [88]. Z_2 symmetry is realized when the Z_2 violating terms in the Lagrangian are absent ($m_{12}^2 = \lambda_6 = \lambda_7 = 0$). There are two stages of Z_2 breaking. The first stage, “soft Z_2 breaking”, occurs when $m_{12}^2 \neq 0$ (but $\lambda_6 = \lambda_7 = 0$). This type of Z_2 violation respects the symmetry at high scales where the transition amplitudes $\Phi_1 \leftrightarrow \Phi_2$ are suppressed but breaks Z_2 at low scales, which gives this kind of breaking its name. In general the term “soft” is attributed to symmetry breaking caused by operators of mass dimension two in the Lagrangian because these operators become dominant at energy scales that are low compared to the mass coefficient of these operators. If Z_2 is broken softly and fermions of the same type (u, d, l) can couple to only one Higgs doublet then Z_2 remains softly broken even when radiative corrections are taken into account [89, 90]. Hence, the absence of FCNC can be guaranteed also in the case of softly broken Z_2 . If $m_{12}^2 \neq 0$, $\lambda_6 \neq 0$ and/or $\lambda_7 \neq 0$ one speaks of “hard” Z_2 breaking. In this case FCNC are not forbidden (at least not because of Z_2 symmetry) even at tree-level.

Table 2.2.: Reduced scalar (a_{fj}) and pseudoscalar (b_{fj}) Yukawa couplings of the neutral Higgs bosons in the CPC case (h, H, A) and the CPV case (ϕ_1, ϕ_2, ϕ_3). The subscripts u, d and l denote the coupling to up-type quarks, down-type quarks and leptons, respectively. Furthermore $c_j = \cos \alpha_j$ and $s_j = \sin \alpha_j$, $j = 1, 2, 3$.

	a_{uj}	b_{uj}	a_{dj}, a_{lj}	b_{dj}, b_{lj}
ϕ_1	$\frac{s_1 c_2}{\sin \beta}$	$s_2 \cot \beta$	$\frac{c_1 c_2}{\cos \beta}$	$s_2 \tan \beta$
h	$\frac{s_1}{\sin \beta}$	0	$\frac{c_1}{\cos \beta}$	0
ϕ_2	$\frac{c_1 c_3 - s_1 s_2 s_3}{\sin \beta}$	$c_2 s_3 \cot \beta$	$-\frac{s_1 c_3 + c_1 s_2 s_3}{\cos \beta}$	$c_2 s_3 \tan \beta$
H	$-\frac{c_1}{\sin \beta}$	0	$\frac{s_1}{\cos \beta}$	0
ϕ_3	$-\frac{s_1 s_2 c_3 + c_1 s_3}{\sin \beta}$	$c_2 c_3 \cot \beta$	$\frac{s_1 s_3 - c_1 s_2 c_3}{\cos \beta}$	$c_2 c_3 \tan \beta$
A	0	$\cot \beta$	0	$\tan \beta$

Table 2.3.: Number of independent parameters in the Higgs potential V_Φ for different symmetries imposed on V_Φ . The numbers in brackets refer to the case when the minimization conditions (Eqs. 2.7–2.9) have not been applied to the potential.

symmetry	no. of parameters in the potential V_Φ
none	13 (14)
CP	10
Z_2^{SB}	9 (10)
Z_2	8
CP and Z_2^{SB}	8
CP and Z_2	7

2.4. Parameters

This section gives a summary and overview of the 2HDM model parameters introduced in Sec. 2.1. In general there are 14 parameters⁴ in the scalar potential (2.3) which determine the couplings among the Higgs bosons as well as the couplings to gauge bosons (Sec. 2.2) and fermions (Sec. 2.3). By imposing certain symmetries on the general scalar potential the number of parameters can be reduced as shown in Tab. 2.3. If the potential is invariant under CP transformations

$$\Phi_a \rightarrow \Phi'_a = e^{i\xi} \Phi_a^*, \quad a = 1, 2 \quad (2.76)$$

it is possible to find a basis $\{\Phi_1, \Phi_2\}$ (by unitary rotations in the Φ_1 - Φ_2 -space) in which all parameters of the Higgs potential are real [91]. Since there are four complex parameters ($m_{12}^2, \lambda_5, \lambda_6, \lambda_7$) the number of independent parameters reduces by four when imposing CP symmetry on the Higgs potential. Imposing in addition a softly broken Z_2 (Z_2^{SB}) symmetry ($\lambda_6 = \lambda_7 = 0$, see also Sec. 2.3) reduces the number of parameters further by two. If CP

⁴Real and imaginary parts of the complex parameters are counted separately.

2. The two-Higgs-doublet model

and exact Z_2 symmetry ($m_{12}^2 = \lambda_6 = \lambda_7 = 0$) are simultaneously imposed there are only seven independent parameters. CP and Z_2 symmetry are in fact special cases of two kinds of more general symmetries that leave the kinetic term in the Lagrangian invariant [79]. The first kind of symmetry is related to the following transformation

$$\Phi_a \rightarrow \Phi'_a = S_{ab}\Phi_b, \quad (2.77)$$

where S is an arbitrary unitary matrix. This kind of symmetries are called Higgs family (HF) symmetries. They are unitary transformations among the Higgs doublets. The Z_2 symmetry ($\Phi_1 \rightarrow \Phi_1, \Phi_2 \rightarrow -\Phi_2$) is a special case of a HF symmetry with

$$S_{Z_2} = \begin{pmatrix} 1 & 0 \\ 0 & -1 \end{pmatrix}. \quad (2.78)$$

The second kind of general transformation can be written as

$$\Phi_a \rightarrow \Phi'_a = X_{ab}\Phi_b^*, \quad (2.79)$$

where X is an arbitrary unitary matrix. It is a generalization of the CP symmetry called general CP (GCP) transformation. In particular, one recovers the ordinary CP symmetry in Eq. (2.76) by setting

$$X = \begin{pmatrix} e^{i\xi} & 0 \\ 0 & e^{i\xi} \end{pmatrix}. \quad (2.80)$$

Even though one can combine different HF and GCP symmetries (e.g. Tab. 2.3) it has been shown in Refs. [92, 93] that there exist only six classes of HF/GCP symmetry-constrained potentials for the 2HDM. Despite these general considerations this work is restricted to cases listed in Tab. 2.3, in particular, the combination of Z_2^{SB} and CP symmetry. A motivation for considering a Z_2 symmetry is given in Sec. 2.3. The soft breaking of the Z_2 leaves the model more flexible due to the additional parameter m_{12}^2 . In particular, it allows one to evade rather strong constraints [94] on the Higgs boson masses imposed by stability and unitarity of the 2HDM that are present when imposing exact Z_2 symmetry.

In the following we discuss if the parameters of the Higgs potential V_Φ (2.3) can be expressed in terms of phenomenological parameters when certain symmetries are imposed on V_Φ . We define the set of phenomenological parameters as

$$v, \tan\beta, \eta, m_1, m_2, m_3, m_{H^+}, \alpha_1, \alpha_2, \alpha_3. \quad (2.81)$$

Recall that η is related to m_{12}^2 by Eq. (2.39). Initially there are 14 parameters in the Higgs potential:

$$m_{11}^2, m_{22}^2, \text{Re}(m_{12}^2), \text{Im}(m_{12}^2), \\ \lambda_1, \lambda_2, \lambda_3, \lambda_4, \text{Re}(\lambda_5), \text{Re}(\lambda_6), \text{Re}(\lambda_7), \text{Im}(\lambda_5), \text{Im}(\lambda_6), \text{Im}(\lambda_7). \quad (2.82)$$

The minimization conditions Eqs. (2.7)–(2.9) are used to rewrite m_{11}^2 and m_{22}^2 in terms of v and $\tan\beta$ and $\text{Im}(m_{12}^2)$ in terms of $\text{Im}(\lambda_5)$, $\text{Im}(\lambda_6)$ and $\text{Im}(\lambda_7)$ such that the number of independent parameters is reduced by one. Hence one is left with 13 parameters in the scalar potential of which ten can be expressed in terms of the phenomenological parameters in Eq. (2.81) by applying the minimization conditions and Eqs. (2.31)–(2.37). Hence, we are left with the following complete set of 13 parameters

$$v, \tan\beta, m_1, m_2, m_3, m_{H^+}, \eta, \alpha_1, \alpha_2, \alpha_3, \text{Im}(\lambda_6), \text{Re}(\lambda_7), \text{Im}(\lambda_7). \quad (2.83)$$

Imposing Z_2^{SB} symmetry ($\lambda_6 = \lambda_7 = 0$) the number of potential parameters reduces from 13 to nine. The number of phenomenological parameters given in Eq. (2.81) is also reduced by one [95]: In the case where $\lambda_6 = \lambda_7 = 0$ the two entries M_{13} (2.24) and M_{23} (2.26) are very similar

$$M_{13} = -\frac{v^2 \text{Im}(\lambda_5)}{2} \sin \beta, \quad (2.84)$$

$$M_{23} = -\frac{v^2 \text{Im}(\lambda_5)}{2} \cos \beta \quad (2.85)$$

such that the following relation holds

$$\tan \beta = \frac{M_{13}}{M_{23}} = \frac{m_1^2 R_{11} R_{13} + m_2^2 R_{21} R_{23} + m_3^2 R_{31} R_{33}}{m_1^2 R_{12} R_{13} + m_2^2 R_{22} R_{23} + m_3^2 R_{32} R_{33}}, \quad (2.86)$$

where Eq. (2.38) was used. Equation (2.86) states that $\tan \beta$, α_i and m_i are not independent. One can, for example, eliminate the mass m_3 in favor of the other parameters

$$m_3^2 = \frac{m_1^2 R_{13} (R_{12} \tan \beta - R_{11}) + m_2^2 R_{23} (R_{22} \tan \beta - R_{21})}{R_{33} (R_{31} - R_{32} \tan \beta)}. \quad (2.87)$$

The set of nine independent phenomenological parameters is then given by

$$v, \tan \beta, \eta, m_1, m_2, m_{H^+}, \alpha_1, \alpha_2, \alpha_3. \quad (2.88)$$

Thus, in the case of softly broken Z_2 all nine independent parameters of the Higgs potential can be written in term of the parameters in Eq. (2.88) such that the Higgs potential is uniquely determined by the phenomenological parameters only. In addition to the Z_2^{SB} symmetry one can impose CP invariance on the Higgs potential which restricts all parameters in the potential to be real and reduces the number of potential parameters from nine (under Z_2^{SB}) to eight

$$m_{11}^2, m_{22}^2, m_{12}^2, \lambda_1, \lambda_2, \lambda_3, \lambda_4, \lambda_5, \quad (2.89)$$

where m_{12}^2 is real due to CPC. Now Eq. (2.86) does not hold any longer because in the CP conserving case $M_{13} = M_{23} = 0$. However, the number of mixing angles is reduced, since $\alpha_2 = \alpha_3 = 0$ if CP is conserved. Hence, imposing Z_2^{SB} and CP symmetries simultaneously leaves eight phenomenological parameters

$$v, \tan \beta, \eta, m_h, m_H, m_A, m_{H^+}, \alpha_1. \quad (2.90)$$

Again, all eight parameters in the Higgs potential (2.89) can be expressed in terms of phenomenological parameters.

If the Lagrangian is invariant under CP the vacuum can still violate CP spontaneously if there is a relative phase between the two vacuum expectation values v_1 and v_2 . Here we have chosen them to be real such that there is no spontaneous CP violation. More general constraints under which the vacuum is CP conserving are given in Ref. [91] and are reproduced here for convenience

$$m_{12}^2 - \frac{1}{2} \lambda_6 v_1^2 - \frac{1}{2} \lambda_7 v_2^2 \geq \lambda_5 v_1 v_2 \quad \text{for } \lambda_5 > 0, \quad (2.91)$$

$$m_{12}^2 - \frac{1}{2} \lambda_6 v_1^2 - \frac{1}{2} \lambda_7 v_2^2 \geq 0 \quad \text{for } \lambda_5 \leq 0. \quad (2.92)$$

2. The two-Higgs-doublet model

Table 2.4.: Parametrizations of the Higgs potential V_Φ for different symmetries imposed on V_Φ . The potential parametrization (second column) uses the parameters introduced in Eq. (2.3) whereas the phenomenological parametrization uses the parameters given in the third column. The fourth column indicates where the phenomenological parameters are not sufficient to fully parametrize the potential. The choice of which parameters of the potential remain unconstrained after setting the phenomenological parameters to specific values is of course arbitrary. In the fourth column one choice is given as an example.

symmetry	potential param.	pheno. param.	unconstrained
none	$m_{11}^2, m_{22}^2, \text{Re}(m_{12}^2), \lambda_{1,2,3,4}$ $\text{Re}(\lambda_{5,6,7}), \text{Im}(\lambda_{5,6,7})$	$v, \tan\beta, \eta, \alpha_1, \alpha_2, \alpha_3$ m_1, m_2, m_3, m_{H^+}	$\text{Im}(\lambda_6), \text{Re}(\lambda_7), \text{Im}(\lambda_7)$
Z_2^{SB}	$m_{11}^2, m_{22}^2, \text{Re}(m_{12}^2), \lambda_{1,2,3,4}$ $\text{Re}(\lambda_5), \text{Im}(\lambda_5)$	$v, \tan\beta, \eta, \alpha_1, \alpha_2, \alpha_3$ m_1, m_2, m_{H^+}	—
Z_2^{SB} and CP	$m_{11}^2, m_{22}^2, \text{Re}(m_{12}^2), \lambda_{1,2,3,4,5}$	$v, \tan\beta, \eta, \alpha_1,$ m_1, m_2, m_3, m_{H^+}	—

Due to the fact that (2.91) and (2.92) are inequalities they restrict the parameter space but do not reduce the number of parameters. For example, for a CP conserving potential obeying Z_2^{SB} and $\lambda_5 > 0$ the ground state is CP conserving under the condition $m_{12}^2 \geq \lambda_5 v_1 v_2$.

Table 2.4 summarizes the independent parameters in the potential and the phenomenological parametrization under the assumption of different symmetries. In this work we will either consider a CP conserving potential with Z_2^{SB} or a CP violating potential were $\lambda_6 \neq 0$ and $\lambda_7 \neq 0$ such that all masses m_i , mixing angles α_i and $\tan\beta$ are independent parameters.

2.5. Theoretical constraints

There are several theoretical constraints on the 2HDM that need to be taken into account for consistency of the theory. First, the Higgs potential has to be bounded from below in order to yield a stable ground state. Second, scattering amplitudes involving the Higgs bosons of the 2HDM have to obey unitarity. Third, couplings among the Higgs bosons given by the parameters in the potential should not exceed certain boundaries in order to guarantee that perturbation theory is still applicable (perturbativity). These three aspects constrain the valid parameter space of the 2HDM. However, in this work the choice of parameter scenarios is guided by phenomenological aspects rather than these theoretical constraints. For example, when estimating the maximal top-quark polarization for a certain class of scenarios in Sec. 4.2.3 some region of the parameter space might be excluded by one or more of these theoretical constraints. Mostly these constraints come from perturbativity when, roughly speaking, the mass separation between the heavy Higgs bosons is too large. Tools to check these bounds, e.g. 2HDMC [96] (only for CPC 2HDM) use tree-level information to obtain the theoretical bounds which therefore are to be understood as estimates rather than rigorous constraints. Furthermore, when estimating an upper bound for the maximal polarization of the top quark the constraints would lead to a reduction in the polarization. Thus, by neglecting the theoretical

bounds the polarization is not underestimated.

The theoretical constraints on the 2HDM do not play an important role in the following analyses. Still, constraining the parameter space of the 2HDM from purely theoretical considerations is interesting and often discussed in the literature. That is why a brief account of the constraints from stability, unitarity and perturbativity on the 2HDM are discussed in Appendix B.

2.6. Decay widths

In this section the analytic expressions of the partial two-body decay widths of the neutral Higgs bosons in the 2HDM are presented. Besides the direct decays

$$\phi_j \rightarrow q\bar{q}, VV, \phi_k Z, \phi_k \phi_l \quad (2.93)$$

that occur at tree-level and correspond to the respective interaction terms in the Lagrangian discussed in Secs. 2.1–2.3 there exist also the loop-mediated decays

$$\phi_j \rightarrow gg, \gamma\gamma. \quad (2.94)$$

The decay $\phi_j \rightarrow \gamma\gamma$ is compared to the other decay channels negligible for the purpose of this work and is not further considered.

We begin with the direct decays in Eq. (2.93). The partial decay width of a (pseudo) scalar Higgs boson into a quark-antiquark pair including NLO QCD corrections was calculated in Refs. [97] and [98] and is reproduced here using the conventions and notation of this work

$$\Gamma(\phi_j \rightarrow Q\bar{Q}) = \frac{C_{Am_Q^2}}{8\pi v^2} m_j \beta_{Qj} \left[a_{Qj}^2 \beta_{Qj}^2 \left(1 + \frac{\alpha_s(\mu)}{\pi} C_F \Delta_S^{Qj} \right) + b_{Qj}^2 \left(1 + \frac{\alpha_s(\mu)}{\pi} C_F \Delta_P^{Qj} \right) \right] \quad (2.95)$$

with

$$\Delta_S^{Qj} = \frac{A(\beta_{Qj})}{\beta_{Qj}} + \frac{1}{16\beta_{Qj}^3} (3 + 34\beta_{Qj}^2 - 13\beta_{Qj}^4) \ln \frac{1 + \beta_{Qj}}{1 - \beta_{Qj}} + \frac{3}{8\beta_{Qj}^2} (-1 + 7\beta_{Qj}^2), \quad (2.96)$$

$$\Delta_P^{Qj} = \frac{A(\beta_{Qj})}{\beta_{Qj}} + \frac{1}{16\beta_{Qj}} (19 + 2\beta_{Qj}^2 + 3\beta_{Qj}^4) \ln \frac{1 + \beta_{Qj}}{1 - \beta_{Qj}} + \frac{3}{8} (7 - \beta_{Qj}^2), \quad (2.97)$$

$$\begin{aligned} A(\beta_{Qj}) &= (1 + \beta_{Qj}^2) \left[4\text{Li}_2 \left(\frac{1 - \beta_{Qj}}{1 + \beta_{Qj}} \right) + 2\text{Li}_2 \left(-\frac{1 - \beta_{Qj}}{1 + \beta_{Qj}} \right) - 3 \ln \frac{2}{1 + \beta_{Qj}} \ln \frac{1 + \beta_{Qj}}{1 - \beta_{Qj}} \right. \\ &\quad \left. - 2 \ln \beta_{Qj} \ln \frac{1 + \beta_{Qj}}{1 - \beta_{Qj}} \right] - 3\beta_{Qj} \ln \frac{4}{1 - \beta_{Qj}^2} - 4\beta_{Qj} \ln \beta_{Qj}, \end{aligned} \quad (2.98)$$

$$\beta_{Qj} = \sqrt{1 - \frac{4m_Q^2}{m_j^2}}. \quad (2.99)$$

$\text{Li}_2(z)$ denotes the dilogarithm defined as

$$\text{Li}_2(z) = - \int_0^z \frac{dt}{t} \ln(1 - t). \quad (2.100)$$

The Higgs bosons couple to all quarks. However, due to the small masses of the quarks in the first and second family the couplings to these quarks are strongly suppressed with respect to the couplings to quarks of the third family (bottom and top quark). The couplings to light quarks can therefore be safely neglected. In the following we investigate if the contributions

2. The two-Higgs-doublet model

from the Yukawa coupling to the bottom quark can be neglected as well when compared to the contribution from the top quark.

In Fig. 2.1 the ratio $\Gamma(\phi \rightarrow b\bar{b})/\Gamma(\phi \rightarrow t\bar{t})$ is shown for $\phi = h, H, A$ and different values of $\tan\beta$. The following parameters⁵ have been used to in Fig. 2.1:

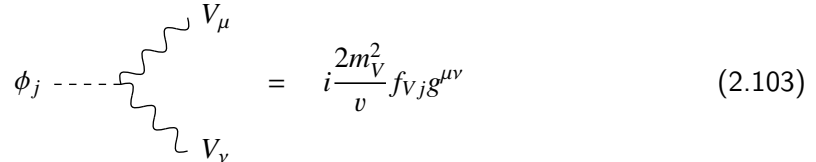
$$\begin{aligned} m_t &= 173.34\text{GeV}, & m_b &= 5\text{GeV}, & \alpha_s(\mu_R) &= \alpha_s(m_\phi), \\ \tan\beta &= 0.7, 1, 2, 5, & \alpha_1 &= \beta, & \alpha_2 &= \alpha_3 = 0. \end{aligned} \quad (2.101)$$

The reduced Yukawa couplings (Tab. 2.2) corresponding to the parameter choice in Eq. (2.101) are given by

$$\begin{aligned} a_{ht} &= 1, & a_{hb} &= 1, & a_{Ht} &= -\cot\beta, & a_{Hb} &= \tan\beta, & b_{At} &= \cot\beta, & b_{Ab} &= \tan\beta, \\ b_{ht} &= b_{hb} = b_{Ht} = b_{Hb} = a_{At} = a_{Ab} &= 0. \end{aligned} \quad (2.102)$$

The parameter setting $\alpha_1 = \beta$ and $\alpha_2 = \alpha_3 = 0$ ensures that the mass eigenstate h has the same couplings to fermions and vector bosons as the SM Higgs boson (alignment limit, see also Sec. 2.7) and, simultaneously, the Yukawa couplings of H and A are maximal (with respect to the variation of α_3). In particular, the Yukawa couplings of h are independent of $\tan\beta$ as can be seen from Eq. (2.102). Figure 2.1 illustrates that even the partial decay width into bottom quarks is strongly suppressed with respect to the partial decay width into top quarks as long as $\tan\beta$ is not too large ($\tan\beta \leq 2$) and $m_\phi \gtrsim 400\text{GeV}$. Since in this work we are interested in heavy Higgs bosons decaying into top quarks we focus on a parameter region where $\tan\beta \sim 1$. Thus, it is well justified to neglect the partial decay width into all quark flavors except the top quark.

As seen in Sec. 2.2 there exists a rich gauge-Higgs coupling sector in the 2HDM. However, among all the possible coupling listed in Tab. 2.1 only the couplings $VV\phi_j$ ($V = W^\pm, Z$) and $Z\phi_j\phi_k$ are relevant for the two-body decay width of the neutral Higgs bosons ϕ_j (assuming $m_{H^\pm} > m_j$). The Feynman rule for the $VV\phi_j$ vertex can be read off from the Lagrangian in Eq. (2.61)



$$\phi_j \text{ --- } \begin{array}{c} \text{---} \\ \text{---} \end{array} \begin{array}{c} \text{---} \\ \text{---} \end{array} = i \frac{2m_V^2}{v} f_{Vj} g^{\mu\nu} \quad (2.103)$$

with

$$f_{Vj} = (R_{j1} \cos\beta + R_{j2} \sin\beta). \quad (2.104)$$

The decay matrix element $|\mathcal{M}_{\phi_j VV}|^2$ summed over the polarizations of the final state particles V is given by

$$|\mathcal{M}_{\phi_j VV}|^2 = \frac{f_{Vj}^2 m_j^4}{v^2} (1 - 4x_{Vj}^2 + 12x_{Vj}^4), \quad (2.105)$$

where the mass ratios

$$x_{ab} = \frac{m_a}{m_b} \quad (2.106)$$

have been introduced. The decay width for $\phi_j \rightarrow VV$ is obtained as

$$\Gamma(\phi_j \rightarrow VV) = m_j \frac{f_{Vj}^2}{16\pi} \left(\frac{m_j}{v} \right)^2 C_V \beta_{Vj} (1 - 4x_{Vj}^2 + 12x_{Vj}^4), \quad (2.107)$$

⁵For the on-shell bottom-quark mass m_b the result of Ref. [99] was used. For the coupling of the strong force $\alpha_s(\mu)$ the value provided by the parton distribution function CT10n1o [100] via the LHAPDF [101, 102] library was used.

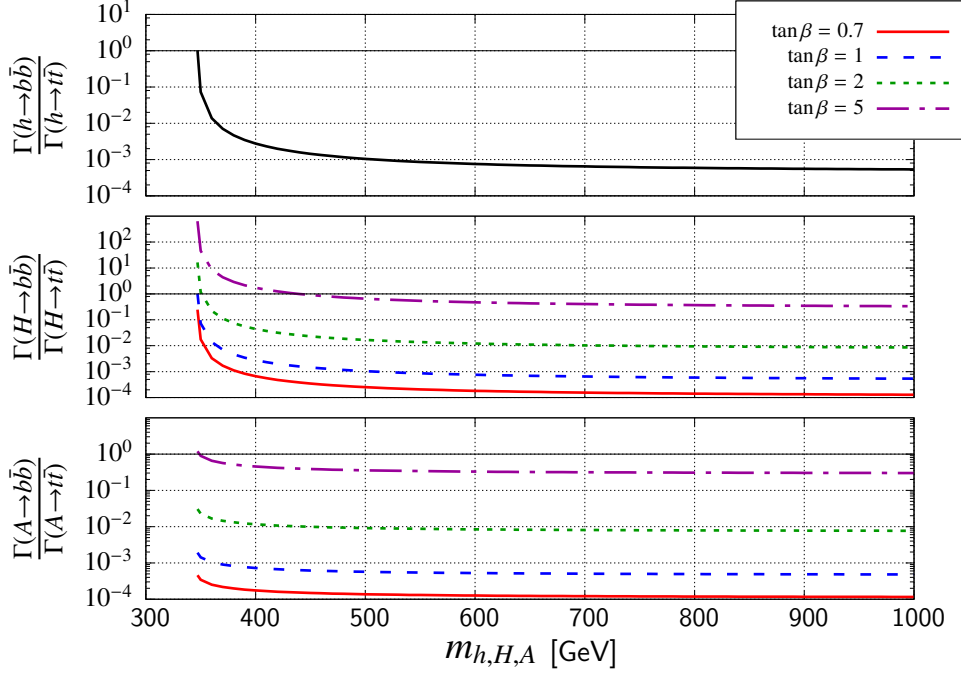


Figure 2.1.: Ratio of the decay width $\Gamma(\phi \rightarrow b\bar{b})$ with respect to $\Gamma(\phi \rightarrow t\bar{t})$ as a function of m_ϕ and $\tan\beta$ for $\phi = h$ (top plot), $\phi = H$ (center plot) and $\phi = A$ (bottom plot). Due to the choice of parameters ($\alpha_1 = \beta$) the ratio in the top plot is independent of $\tan\beta$.

where $\beta_{Vj} = \sqrt{1 - \frac{4m_V^2}{m_j^2}}$ and C_V is a symmetry factor

$$C_V = \begin{cases} 1 & V = W^\pm \\ \frac{1}{2} & V = Z \end{cases} \quad (2.108)$$

which accounts for indistinguishable particles in the final state in the case of $\phi_j \rightarrow ZZ$.

Another two-body decay channel of the neutral Higgs bosons relevant for this work is $\phi_j \rightarrow \phi_k Z$. For the calculation of the corresponding decay width one can read off the Feynman rule for the $Z\phi\phi$ vertex from the Lagrangian in Eq. (2.60)

$$\begin{array}{c} \phi_k \\ \nearrow p_k \\ \phi_j \text{---} p_j \text{---} \\ \searrow \\ Z \end{array} = \frac{m_Z}{v} (p_j^\mu - p_k^\mu) f_{jkZ} \quad (2.109)$$

with

$$f_{jkZ} = R_{j3}(R_{k1} \sin\beta - R_{k2} \cos\beta) - R_{k3}(R_{j1} \sin\beta - R_{j2} \cos\beta). \quad (2.110)$$

The decay matrix element summed over the polarizations of the decay products reads

$$|\mathcal{M}_{\phi_j\phi_k Z}|^2 = f_{jkZ}^2 \frac{m_j^4}{v^2} \lambda(1, x_{kj}^2, x_{Zj}^2), \quad (2.111)$$

where

$$\lambda(x, y, z) = x^2 + y^2 + z^2 - 2xy - 2xz - 2yz. \quad (2.112)$$

2. The two-Higgs-doublet model

The decay width for $\phi_j \rightarrow \phi_k Z$ is then given by

$$\Gamma(\phi_j \rightarrow \phi_k Z) = m_j \frac{f_{jkZ}^2}{16\pi} \left(\frac{m_j}{v}\right)^2 \lambda^{3/2}(1, x_{kj}^2, x_{Zj}^2). \quad (2.113)$$

As mentioned in Sec. 2.1 the Higgs potential (2.3) describes the self-interaction between the Higgs bosons in the 2HDM. The terms trilinear in the Higgs fields are relevant for the two-body decays of the Higgs bosons and yield the following Feynman rules

$$\begin{array}{c} \phi_k \\ \text{---} \\ \phi_j \text{---} \\ \text{---} \\ \phi_l \end{array} = i v f_{jkl}, \quad (2.114)$$

where f_{jkl} is given in appendix A. The decay matrix element for the decay $\phi_j \rightarrow \phi_k \phi_l$ is trivial

$$|\mathcal{M}_{\phi_j \phi_k \phi_l}|^2 = v^2 f_{jkl}^2 \quad (2.115)$$

and the decay width is given by

$$\Gamma(\phi_j \rightarrow \phi_k \phi_l) = v \frac{f_{jkl}^2}{16\pi m_j} \left(1 - \frac{\delta_{kl}}{2}\right) \lambda^{1/2}(1, x_{kj}^2, x_{lj}^2), \quad (2.116)$$

where the factor $1 - \delta_{kl}/2$ accounts for indistinguishable final state particles.

We turn now to the loop-mediated decay $\phi_j \rightarrow gg$. The partial decay width of a (pseudo) scalar Higgs boson into gluons including NLO QCD corrections can be found in [103] and is reproduced here using the conventions and notations of this work

$$\Gamma(\phi_j \rightarrow gg) = \frac{C_A C_F m_j^3}{2\pi} \left[\left(|F_j^S|^2 + \frac{\alpha_s(\mu)}{\pi} |F_j^{S,\infty}|^2 E_{Sj}^\infty \right) + 4 \left(|F_j^P|^2 + \frac{\alpha_s(\mu)}{\pi} |F_j^{P,\infty}|^2 E_{Pj}^\infty \right) \right] \quad (2.117)$$

with

$$E_{Sj}^\infty = \frac{95}{4} - \frac{7}{6} N_f + 2\beta_0 \ln \frac{\mu^2}{m_j^2}, \quad (2.118)$$

$$E_{Pj}^\infty = \frac{97}{4} - \frac{7}{6} N_f + 2\beta_0 \ln \frac{\mu^2}{m_j^2}, \quad (2.119)$$

where

$$\beta_0 = \frac{1}{2} \left(\frac{11}{6} C_A - \frac{2}{3} T_R N_f \right) \quad (2.120)$$

denotes the leading coefficient of the QCD β -function. N_f is the number of active quark flavors and

$$C_F = \frac{N_c^2 - 1}{2N_c} = 4/3, \quad C_A = N_c = 3. \quad (2.121)$$

The superscript ∞ in Eq. (2.117) denotes the large top mass limit ($m_t \rightarrow \infty$). The form factors for scalar and pseudoscalar couplings are given by

$$F_j^S = \frac{\alpha_s a_{tj}}{8\pi v} \tau_j [1 - (1 - \tau_j) f(\tau_j)], \quad F_j^{S,\infty} = \lim_{\tau_j \rightarrow \infty} F_j^S = \frac{\alpha_s a_{tj}}{12\pi v}, \quad (2.122)$$

$$F_j^P = \frac{\alpha_s b_{tj}}{16\pi v} \tau_j f(\tau_j), \quad F_j^{P,\infty} = \lim_{\tau_j \rightarrow \infty} F_j^P = -\frac{\alpha_s b_{tj}}{16\pi v}, \quad (2.123)$$

$$f(\tau_j) = \begin{cases} \frac{1}{4} \left[\ln \left(\frac{1 + \sqrt{1 - \tau_j}}{1 - \sqrt{1 - \tau_j}} \right) - i\pi \right]^2 & \tau_j < 1 \\ -\arcsin^2 \left(\sqrt{\frac{1}{\tau_j}} \right) & \tau_j \geq 1 \end{cases}, \quad \tau_j = \frac{4m_t^2}{m_j^2}. \quad (2.124)$$

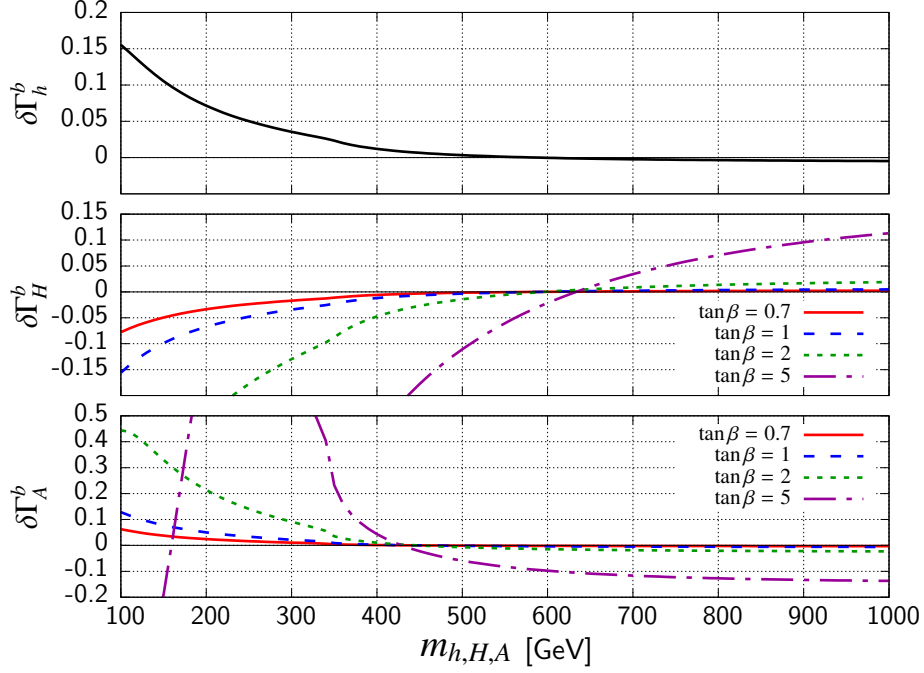


Figure 2.2.: Relative contribution of the bottom quark to the decay of a Higgs boson (h , H , A) into two gluons in the 2HDM. The parameters used to generate this plot are given in Eq. (2.101). Because of the choice $\alpha_1 = \beta$ the decay width of the mass eigenstate h is independent of $\tan\beta$.

The bottom quark contributions to F_{Sj} and F_{Pj} are neglected because they are suppressed with respect to the top-quark contribution if $\tan\beta < 2$ and $m_\phi \geq 400$ GeV. Figure 2.2 illustrates this suppression by showing the ratio

$$\delta\Gamma_\phi^b = \frac{\Gamma_{\text{LO}}(\phi \rightarrow gg) - \Gamma_{\text{LO}}^b(\phi \rightarrow gg)}{\Gamma_{\text{LO}}^b(\phi \rightarrow gg)}, \quad (2.125)$$

where $\Gamma_{\text{LO}}^b(\phi \rightarrow gg)$ denotes the partial decay width of the Higgs boson ϕ ($\phi = h, H, A$) to two gluons including the contributions from the bottom quark loop at leading order and $\Gamma_{\text{LO}}(\phi \rightarrow gg)$ denotes the leading order contribution of the partial decay width given in Eq. (2.117) which does not include the b -quark contribution. The plots in Fig. 2.2 have been generated using the parameters given in Eq. (2.101). The values of the Yukawa couplings corresponding to this particular choice of $\tan\beta$ and α_i are listed in Eq. (2.102). Figure 2.2 shows that the b -quark contribution depends on the mass m_ϕ of the Higgs boson. Furthermore $\delta\Gamma_H^b$ and $\delta\Gamma_A^b$ depend on $\tan\beta$ while $\delta\Gamma_h^b$ is independent of $\tan\beta$ which is a consequence of the choice $\alpha_1 = \beta$. When increasing $\tan\beta$ the bottom-quark Yukawa couplings of H and A increase and the top-quark Yukawa couplings decrease which in total increases the relative contribution of the bottom quark loop to the decay $\phi \rightarrow gg$. In this work we focus on $\tan\beta \sim 1$. In this case Fig. 2.2 shows that for masses $m_\phi > 100\text{GeV}$ the bottom quark contribution does not exceed 15%. For masses that are larger than the $t\bar{t}$ threshold $m_\phi > 2m_t$ the bottom-quark contribution is well below 5% and for $500\text{GeV} \leq m_\phi \leq 1000\text{GeV}$ it even drops below 1%. This shows that for heavy Higgs bosons that can decay on-shell into top quarks the bottom-quark contribution to the loop in the decay to gluons is negligible given that $\tan\beta < 2$.

Besides neglecting the bottom quark contribution another approximation is made in Eq. (2.117):

2. The two-Higgs-doublet model

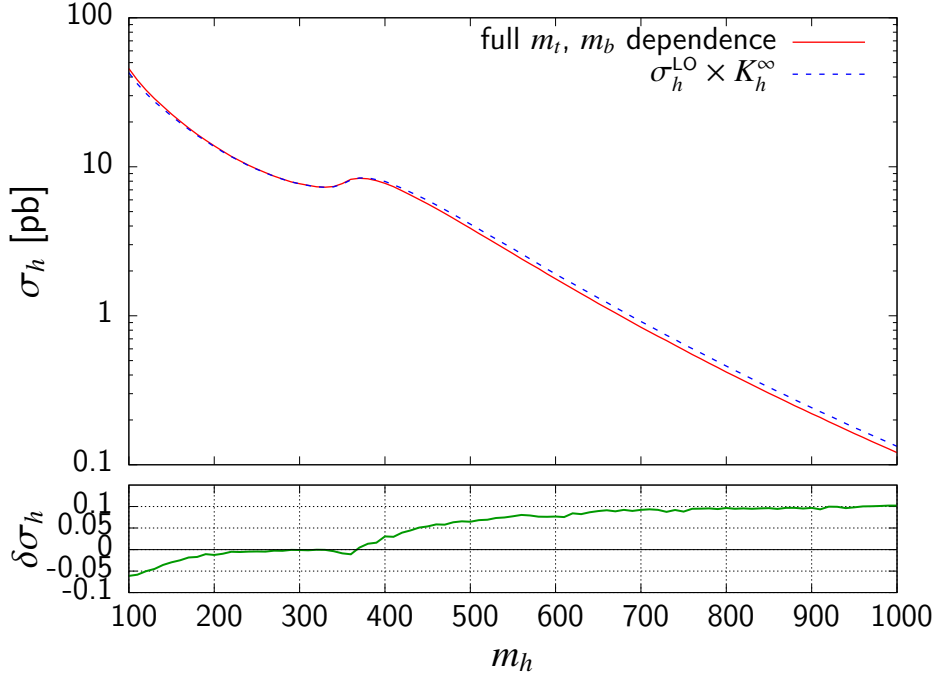


Figure 2.3.: Upper plot: Higgs production cross section $\sigma_h = \sigma(gg \rightarrow h)$ with full top and bottom mass dependence at NLO QCD (red solid curve) and approximated (blue dashed curve) according to Eq. (2.126). This plot was extracted from Ref. [104] using the tool EasyNData [105]. Lower plot: Relative deviation $\delta\sigma_h$ of the approximated cross section from the exact result.

The NLO corrections are given in the large top-mass limit. This limit is strictly only valid as long as the expansion parameter $\tau^{-1} = \frac{m_\phi^2}{4m_t^2}$ is small. For Higgs bosons decaying on-shell into top quarks this condition is not fulfilled. In Ref. [104] it was shown for Higgs production via gluon fusion (the inverse process of $\phi \rightarrow gg$) that the validity of this approximation can be extended to higher Higgs masses by applying a rescaling factor to the NLO correction in the large top mass limit

$$\tilde{\sigma}_H \equiv \sigma_h^{(0)} + \frac{\sigma_h^{(0)}}{\sigma_h^{\infty,(0)}} \sigma_h^{\infty,(1)} = \sigma_h^{(0)} K_H^\infty, \quad (2.126)$$

where $\tilde{\sigma}_H$ denotes the approximated rescaled cross section. $\sigma_h^{(0)}$ represents the LO cross section with the full m_t dependence and $\sigma_h^{\infty,(1)}$ denotes the NLO QCD correction in the limit $m_t \rightarrow \infty$. The rescaling factor $\sigma_h^{(0)}/\sigma_h^{\infty,(0)}$ is the ratio of the LO cross sections with the full m_t dependence with respect to the LO cross section in the large top mass limit $\sigma_h^{\infty,(0)}$. The K -factor K_H^∞ is defined as

$$K_H^\infty = \frac{\sigma_h^{\infty,(0)} + \sigma_h^{\infty,(1)}}{\sigma_h^{\infty,(0)}} = \frac{\sigma_h^{\infty,\text{NLO}}}{\sigma_h^{\infty,\text{LO}}}. \quad (2.127)$$

Figure 2.3 shows how well this approximation of the Higgs production cross section via gluon fusion performs with respect to the cross section including the full m_t (and m_b) dependence. For Higgs boson masses $m_h > 450\text{GeV}$ the relative deviation $\delta\sigma_h$ between the exact and the approximated rescaled cross section exceeds 5% but stays below 10% almost up to $m_h = 1000\text{GeV}$. A pseudoscalar Higgs boson A shows similar behavior [104].

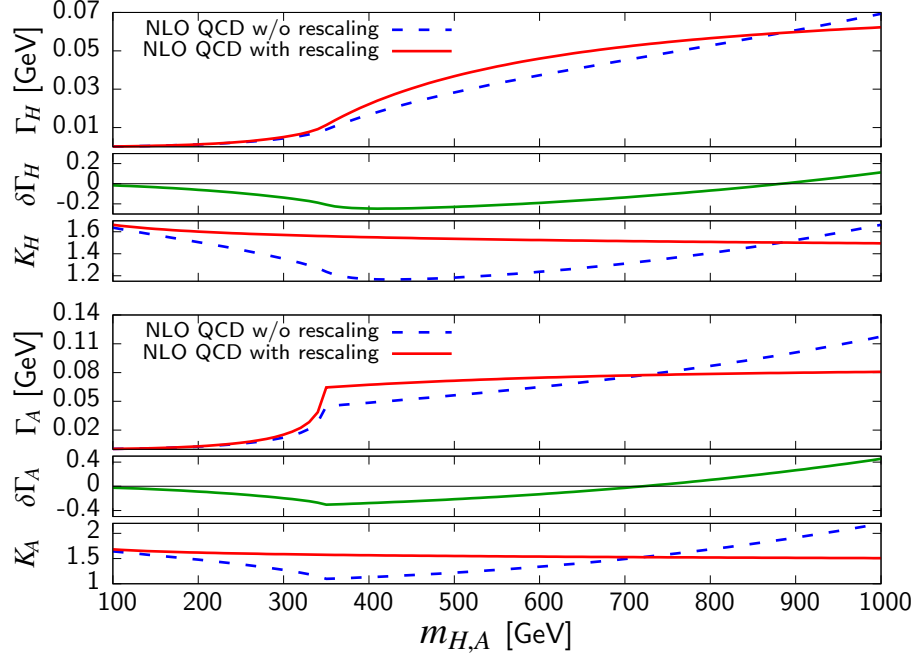


Figure 2.4.: Partial decay width of neutral Higgs bosons (H,A) into two gluons at NLO QCD in the large top-mass limit as a function of the respective Higgs mass. The upper plots show the result for the decay width $\Gamma(\phi \rightarrow gg)$ without rescaling (blue dashed curve) (2.117) and with rescaling (red solid curve) (2.128). The center plots show the relative deviation $\delta\Gamma_\phi$ of the unrescaled decay width with respect to the rescaled one. The lower plots show the K -factor (ratio between NLO and LO result) for the decay widths without rescaling (blue dashed curve) and with rescaling (red solid curve).

Observing that this rescaling procedure performs so well up to Higgs masses as high as 1TeV one should apply this prescription also to Eq. (2.117)

$$\Gamma(\phi_j \rightarrow gg) = \frac{C_A C_F m_j^3}{2\pi} \left[|F_{Sj}|^2 \left(1 + \frac{\alpha_s(\mu)}{\pi} E_{Sj}^\infty \right) + 4|F_{Pj}|^2 \left(1 + \frac{\alpha_s(\mu)}{\pi} E_{Pj}^\infty \right) \right]. \quad (2.128)$$

The two expressions (2.117) and (2.128) for the partial decay width $\Gamma(\phi \rightarrow gg)$ are compared in Fig. 2.4 for $\phi = H$ and $\phi = A$. The case $\phi = h$ is identical to $\phi = H$ because of the choice of parameters in Eq. (2.101) where $\tan\beta = 1$ in Fig. 2.4. In the upper plots the partial decay widths including the rescaling (2.128) (red solid curve) and without rescaling (2.117) (blue dashed curve) are displayed. From the center plots one can read off the relative deviation $\delta\Gamma_\phi$, $\phi = H, A$ (green solid curve) of the nonrescaled decay width with respect to the rescaled version. It shows that deviations can become as large as 20% for Γ_H and 40% for Γ_A . The lower plots present the K -factors for the rescaled decay width (red solid curve) and the nonrescaled width (blue dashed curve). They are defined as the ratio of the (non-)rescaled width in Eq. (2.128) (Eq. (2.117)) with respect to the decay width at LO. The K -factors of the rescaled decay widths are essentially flat (apart from a slight tilt) whereas the K -factors of nonrescaled decay width have a much stronger dependence on the Higgs mass. In addition to the fact that the rescaling prescription shows only moderate deviation from the full result

2. The two-Higgs-doublet model

even for large Higgs masses⁶ the stability of the K -factor as illustrated in Fig. 2.4 is another argument for favoring Eq. (2.128) over Eq. (2.117).

A final remark on the $\phi \rightarrow gg$ decay: The partial decay width for $\phi \rightarrow gg$ is compared to other decay channels of the Higgs bosons very small such that any uncertainty (e.g. resulting from the rescaling procedure) is suppressed accordingly.

2.7. The alignment limit

In this section a special limit of the general 2HDM is discussed, the so-called (*SM*) *alignment limit* which is not to be confused with the Yukawa alignment mentioned in Sec. 2.3. The term alignment limit stands for a region of parameter space of the general 2HDM in which one of the neutral Higgs mass eigenstate (here ϕ_1) has SM couplings to fermions and gauge bosons as well as SM self-couplings at tree-level and can therefore be identified with the SM Higgs boson. This limit is particularly interesting because it allows for a consistent extension of the SM given that the experimental results on the 125GeV resonance discovered in 2012 [6, 7] so far are in agreement [8, 9] with the SM hypothesis (within the experimental and theoretical uncertainties). The condition for ϕ_1 to have SM Yukawa, gauge and self-couplings restricts the allowed parameter region of the 2HDM increasing its predictive power and its experimental compatibility with respect to the results of the Higgs measurements⁷ at the LHC.

To ensure SM couplings to fermions one needs to inspect the Yukawa couplings of ϕ_1 . In the SM the reduced Yukawa couplings (see Sec. 2.3, Tab. 2.2) assume the following values

$$a_{u1} = 1, \quad a_{d1} = 1, \quad b_{u1} = b_{d1} = 0. \quad (2.129)$$

One therefore obtains the following system of equations

$$a_{u1} = \frac{\sin \alpha_1 \cos \alpha_2}{\sin \beta} = 1, \quad (2.130)$$

$$a_{d1} = \frac{\cos \alpha_1 \cos \alpha_2}{\cos \beta} = 1, \quad (2.131)$$

$$b_{u1} = \sin \alpha_2 \cot \beta = 0, \quad (2.132)$$

$$b_{d1} = \sin \alpha_2 \tan \beta = 0. \quad (2.133)$$

Under the assumption that $\tan \beta > 0$ Eqs. (2.132) and (2.133) constrain the angle α_2 : $\sin \alpha_2 = 0$. Since $-\pi/2 < \alpha_2 \leq \pi/2$ (see Sec. 2.1) it follows that

$$\alpha_2 = 0. \quad (2.134)$$

Equations (2.130) and (2.131) then lead to

$$\alpha_1 = \beta. \quad (2.135)$$

The two conditions in Eqs. (2.134) and (2.135) also fix the Yukawa couplings of the heavy Higgs bosons ϕ_2 and ϕ_3 . For convenience all Yukawa couplings using $\alpha_1 = \beta$ and $\alpha_2 = 0$ are presented in Tab. 2.5. Since the alignment limit only fixes α_1 and α_2 the mixing angle α_3 remains a free parameter in this limit. From Tab. 2.5 it is obvious that the absolute reduced Yukawa couplings $|a_{fj}|, |b_{fj}|$ of the heavy Higgs bosons $j = 2, 3$ are maximal for $\alpha_3 = 0$ or

⁶In Fig. 2.3 this is shown for the cross section of Higgs production via gluon fusion. The decay $\phi_j \rightarrow gg$ is just the inverse process.

⁷There are of course other experimental constraints (e.g. the electric dipole moment of the neutron) that constrain the parameter space further.

Table 2.5.: Reduced scalar (a_{fj}) and pseudoscalar (b_{fj}) Yukawa couplings of the neutral Higgs bosons in the 2HDM alignment limit. The subscripts u , d and l denote the coupling to up-type quarks, down-type quarks and leptons, respectively.

	a_{uj}	b_{uj}	a_{dj}, a_{lj}	b_{dj}, b_{lj}
h	1	0	1	0
ϕ_2	$\cot\beta \cos\alpha_3$	$\sin\alpha_3 \cot\beta$	$-\tan\beta \cos\alpha_3$	$\sin\alpha_3 \tan\beta$
ϕ_3	$-\cot\beta \sin\alpha_3$	$\cos\alpha_3 \cot\beta$	$\tan\beta \sin\alpha_3$	$\cos\alpha_3 \tan\beta$

$\alpha_3 = \pi/2$. In both cases the scalar potential is CP conserving and the neutral Higgs boson mass eigenstates are CP eigenstates

$$\begin{aligned} \alpha_3 = 0 & : \phi_2 = -H, \quad \phi_3 = A \\ \alpha_3 = \pi/2 & : \phi_2 = A, \quad \phi_3 = H. \end{aligned} \quad (2.136)$$

So far we have established the constraints on the parameters for which the Yukawa couplings of ϕ_1 have SM values. In the alignment limit the couplings of ϕ_1 to gauge bosons should be the same as in the SM as well. Inserting the conditions (2.134) and (2.135) into the expression for the couplings f_{Vj} (2.104) yields

$$f_{V1} = R_{11} \cos\beta + R_{12} \sin\beta = \cos^2\beta + \sin^2\beta = 1 \quad (2.137)$$

which is equal to the SM coupling between the Higgs boson $\phi_1 = h$ and two vector bosons $V = Z, W^\pm$. For $\alpha_1 = \beta, \alpha_2 = 0$ the couplings f_{jkZ} (2.110) vanish for the mass eigenstate ϕ_1

$$\begin{aligned} f_{1kZ} = f_{k1Z} & = R_{13}(R_{k1} \sin\beta - R_{k2} \cos\beta) - R_{k3}(R_{11} \sin\beta - R_{12} \cos\beta) \\ & = 0 \cdot (R_{k1} \sin\beta - R_{k2} \cos\beta) - R_{k3}(\cos\beta \sin\beta - \sin\beta \cos\beta) = 0. \end{aligned} \quad (2.138)$$

Additionally all other nonstandard couplings to gauge bosons

$$\phi_1 H^\pm W^\mp, \quad \phi_1 \phi_j W^+ W^-, \quad \phi_1 \phi_j ZZ, \quad \phi_1 H^\pm W^\mp Z, \quad \phi_1 H^\pm W^\mp \gamma \quad (2.139)$$

vanish in the alignment limit as well. This shows that the constraints $\alpha_1 = \beta$ and $\alpha_2 = 0$ as derived from the Yukawa couplings also yield the SM couplings of ϕ_1 to the gauge bosons.

Finally we turn to the Higgs self-interactions. The trilinear self-coupling f_{111} of ϕ_1 in the

2. The two-Higgs-doublet model

general 2HDM is given by (see also Appendix A)

$$\begin{aligned}
f_{111} = 3 \left\{ & -2R_{11}R_{12}R_{13} \left[\text{Im}(\lambda_5) + \sin\beta \cos\beta (\text{Im}(\lambda_6) + \text{Im}(\lambda_7)) \right] \right. \\
& + \frac{1}{2}R_{13}^3 \left[\text{Im}(\lambda_5) \sin(2\beta) + \cos(2\beta) (\text{Im}(\lambda_6) - \text{Im}(\lambda_7)) - \text{Im}(\lambda_6) - \text{Im}(\lambda_7) \right] \\
& + R_{11}^2 R_{13} \left[-\text{Im}(\lambda_5) \sin\beta \cos\beta - \text{Im}(\lambda_6) (\cos(2\beta) + 2) \right] \\
& + R_{12}^2 R_{13} \left[\text{Im}(\lambda_7) (\cos(2\beta) - 2) - \text{Im}(\lambda_5) \sin\beta \cos\beta \right] \\
& + R_{11}^3 \left[\lambda_1 \cos\beta + \text{Re}(\lambda_6) \sin\beta \right] \\
& + R_{11}^2 R_{12} \left[\lambda_{345} \sin\beta + 3\text{Re}(\lambda_6) \cos\beta \right] \\
& + R_{11} R_{12}^2 \left[\lambda_{345} \cos\beta + 3\text{Re}(\lambda_7) \sin\beta \right] \\
& + R_{11} R_{13}^2 \left[\lambda_{345}^- \cos^3\beta + \sin^2\beta \cos\beta (\lambda_1 - 2\text{Re}(\lambda_5)) + \text{Re}(\lambda_6) \sin^3\beta \right. \\
& \quad \left. + \sin\beta \cos^2\beta (\text{Re}(\lambda_7) - 2\text{Re}(\lambda_6)) \right] \\
& + R_{12}^3 \left[\lambda_2 \sin\beta + \text{Re}(\lambda_7) \cos\beta \right] \\
& \left. + R_{12} R_{13}^2 \left[\lambda_{345}^- \sin^3\beta + \sin\beta \cos^2\beta (\lambda_2 - 2\text{Re}(\lambda_5)) \right. \right. \\
& \quad \left. \left. + \sin^2\beta \cos\beta (\text{Re}(\lambda_6) - 2\text{Re}(\lambda_7)) + \text{Re}(\lambda_7) \cos^3\beta \right] \right\}.
\end{aligned} \tag{2.140}$$

This expression simplifies enormously in the alignment limit

$$f_{111}(\alpha_1 = \beta, \alpha_2 = 0) = 3 \left(\frac{m_1}{v} \right)^2. \tag{2.141}$$

The same holds for the quartic self coupling

$$\begin{aligned}
f_{1111} = 3 \left\{ & \lambda_1 R_{11}^4 + 4R_{11}^3 R_{12} \text{Re}(\lambda_6) + R_{11}^2 R_{12}^2 (2\lambda_3 + 2\lambda_4 + 2\text{Re}(\lambda_5)) \right. \\
& \left. + 4R_{11} R_{12}^3 \text{Re}(\lambda_7) + \lambda_2 R_{12}^4 \right\},
\end{aligned} \tag{2.142}$$

where f_{1111} is defined via the self-interaction term in the Lagrangian

$$\mathcal{L}_{\phi_1^4} = \frac{f_{1111}}{4!} \phi_1^4. \tag{2.143}$$

In the alignment limit f_{1111} simplifies to

$$f_{1111}(\alpha_1 = \beta, \alpha_2 = 0) = 3 \left(\frac{m_1}{v} \right)^2. \tag{2.144}$$

The values of the trilinear (2.141) and quartic (2.143) couplings in the alignment limit are equal to the respective SM values. However, while all nonstandard couplings between ϕ_1 and the gauge bosons vanish in the alignment limit this is not the case for the couplings to the other scalars of the 2HDM. There still exist nonstandard couplings to other Higgs bosons that are not present in the SM (since there are no additional Higgs bosons). The nonstandard trilinear interactions between ϕ_1 and $\phi_{2,3}$ in the alignment limit are

$$f_{122}(\alpha_1 = \beta, \alpha_2 = 0) = \frac{m_1^2 + 2m_2^2}{v^2} - 2\eta, \tag{2.145}$$

$$f_{133}(\alpha_1 = \beta, \alpha_2 = 0) = \frac{m_1^2 + 2m_3^2}{v^2} - 2\eta, \tag{2.146}$$

where η is defined in Eq. (2.39). The other nonstandard trilinear couplings among the neutral Higgs bosons involving ϕ_1 vanish in the alignment limit

$$f_{112} = f_{113} = f_{123} = 0. \quad (2.147)$$

Furthermore there is an interaction between ϕ_1 and H^\pm

$$\mathcal{L}_{\phi_1 H^+ H^-} = f_{144} \phi_1 H^+ H^-, \quad (2.148)$$

where f_{144} is given by

$$f_{144}(\alpha_1 = \beta, \alpha_2 = 0) = \frac{m_1^2 + 2m_{H^+}^2}{v^2} - 2\eta \quad (2.149)$$

in the alignment limit. Among the quartic Higgs interactions the following nonstandard couplings involving ϕ_1 remain different from zero in the alignment limit

$$\phi_1^2 \phi_2^2, \quad \phi_1^2 \phi_2 \phi_3, \quad \phi_1^2 \phi_3^2, \quad \phi_1 \phi_2^3, \quad \phi_1 \phi_2^2 \phi_3, \quad \phi_1 \phi_2 \phi_3^2, \quad \phi_1 \phi_3^2 \quad (2.150)$$

while the following couplings vanish in the alignment limit

$$f_{1112} = f_{1113} = 0. \quad (2.151)$$

Even though in the alignment limit there are nonstandard interactions between ϕ_1 and the other Higgs bosons this does not affect the decay width of ϕ_1 at tree-level as long all other Higgs mass eigenstates are heavier. However, in a situation where ϕ_1 is not the lightest Higgs boson, decays such as $\phi_1 \rightarrow \phi_2 \phi_2$ are possible and would lead to a deviation of the total decay width of ϕ_1 with respect to the SM value. In this work it is always assumed that ϕ_1 is the lightest Higgs boson mass eigenstate.

In summary, the SM alignment limit of the 2HDM can be reached from the general 2HDM by setting the mixing angles $\alpha_1 = \beta$ and $\alpha_2 = 0$. This ensures that the lightest neutral Higgs boson ϕ_1 has SM Yukawa, gauge and self-couplings. In particular, ϕ_1 is a scalar in this limit while ϕ_2 and ϕ_3 are in general CP mixtures. In the case where $\alpha_3 = 0$ or $\alpha_3 = \pi/2$ the mass eigenstates $\phi_{2,3}$ are also CP eigenstates, one being a scalar and the other a pseudoscalar.

Spin density matrix formalism

As discussed in Sec. 1.1.3 the properties of the top quark are particularly well suited for investigating spin effects at hadron colliders. In this respect, among others, the top quark takes a unique position among all quarks. Due to the presence and experimental accessibility of top-quark polarization and $t\bar{t}$ spin correlations it is possible to study the underlying interaction that produced the top quarks in a complementary way to the investigation of spin independent observables. In this work, it will be shown that spin dependent observables can lead to an increased sensitivity to new physics effects in $t\bar{t}$ production. The method used in this work to extract spin information from the $t\bar{t}$ final state is the so-called *spin density matrix formalism* [106]. This chapter reviews this formalism in the context of $t\bar{t}$ production.

3.1. Spin density matrix

The quantum mechanical density operator ρ , also called *density matrix*, describes the statistical ensemble of a quantum system of mixed states

$$\rho = \sum_i p_i |\psi_i\rangle \langle \psi_i|, \quad (3.1)$$

where p_i is the probability to observe the ensemble in the quantum state $|\psi_i\rangle$. The density matrix is Hermitian and has trace one

$$\rho^\dagger = \rho, \quad \text{Tr}[\rho] = 1. \quad (3.2)$$

Expectation values of observables represented by operators O acting on the Hilbert space of the respective ensemble are calculated by taking the trace

$$\langle O \rangle = \text{Tr}[\rho O]. \quad (3.3)$$

As is well known the density matrix of a spin-1/2 system is given by

$$\rho = \frac{1}{2} (\mathbb{1} + \mathbf{b} \cdot \boldsymbol{\sigma}), \quad (3.4)$$

where \mathbf{b} is the polarization of the ensemble, i.e. $\mathbf{b} = \langle \mathbf{P} \rangle = \langle \boldsymbol{\sigma} \rangle$. Since we are interested in top-quark pair production we consider the density matrix for the $t\bar{t}$ pair

$$\rho_{t\bar{t}} = \frac{1}{4} [\mathbb{1} \otimes \mathbb{1} + \mathbf{b}^+ \cdot \boldsymbol{\sigma} \otimes \mathbb{1} + \mathbb{1} \otimes \boldsymbol{\sigma} \cdot \mathbf{b}^- + c_{ij} \sigma_i \otimes \sigma_j], \quad (3.5)$$

3. Spin density matrix formalism

where \mathbf{b}^+ (\mathbf{b}^-) is the polarization of the ensemble of (anti)top quarks, i.e.

$$\mathbf{b}^+ = \langle \mathbf{P}_t \rangle = \langle 2\mathbf{S}_t \rangle = \langle \boldsymbol{\sigma} \otimes \mathbb{1} \rangle, \quad (3.6)$$

$$\mathbf{b}^- = \langle \mathbf{P}_{\bar{t}} \rangle = \langle 2\mathbf{S}_{\bar{t}} \rangle = \langle \mathbb{1} \otimes \boldsymbol{\sigma} \rangle. \quad (3.7)$$

The spin operators of top and antitop quark are defined as

$$\mathbf{S}_t = \frac{1}{2}(\boldsymbol{\sigma} \otimes \mathbb{1}) \quad \text{and} \quad \mathbf{S}_{\bar{t}} = \frac{1}{2}(\mathbb{1} \otimes \boldsymbol{\sigma}). \quad (3.8)$$

The relation between the coefficients c_{ij} in Eq. (3.5) and $t\bar{t}$ spin correlations in general can be derived by actually calculating spin correlations using the general definition

$$\text{corr}(X, Y) = \frac{\langle XY \rangle - \langle X \rangle \langle Y \rangle}{\sqrt{\langle X^2 \rangle - \langle X \rangle^2} \sqrt{\langle Y^2 \rangle - \langle Y \rangle^2}} \quad (3.9)$$

and replacing $X = \mathbf{S}_t \cdot \hat{\mathbf{a}}_1$ and $Y = \mathbf{S}_{\bar{t}} \cdot \hat{\mathbf{a}}_2$ where $\hat{\mathbf{a}}_1$ and $\hat{\mathbf{a}}_2$ are arbitrary unit three-vectors (reference axes):

$$\text{corr}(\mathbf{S}_t \cdot \hat{\mathbf{a}}_1, \mathbf{S}_{\bar{t}} \cdot \hat{\mathbf{a}}_2) = \frac{c_{ij} \hat{a}_1^i \hat{a}_2^j - (\mathbf{b}^+ \cdot \hat{\mathbf{a}}_1)(\mathbf{b}^- \cdot \hat{\mathbf{a}}_2)}{\sqrt{[1 - (\mathbf{b}^+ \cdot \hat{\mathbf{a}}_1)^2][1 - (\mathbf{b}^- \cdot \hat{\mathbf{a}}_2)^2]}}. \quad (3.10)$$

In the absence of polarization $\mathbf{b}^+ = 0$ and $\mathbf{b}^- = 0$ Eq. (3.10) simplifies to

$$\text{corr}(\mathbf{S}_t \cdot \hat{\mathbf{a}}_1, \mathbf{S}_{\bar{t}} \cdot \hat{\mathbf{a}}_2) = 4\langle (\mathbf{S}_t \cdot \hat{\mathbf{a}}_1)(\mathbf{S}_{\bar{t}} \cdot \hat{\mathbf{a}}_2) \rangle = c_{ij} \hat{a}_1^i \hat{a}_2^j. \quad (3.11)$$

In the case where the polarization is very small $|\mathbf{b}^\pm| = b \ll 1$ Eq. (3.11) is still a good approximation receiving corrections at $O(b^2)$. On the other side Eq. (3.10) shows that c_{ij} can be nonvanishing even when there is no spin correlation, $\text{corr}(\mathbf{S}_t \cdot \hat{\mathbf{a}}_1, \mathbf{S}_{\bar{t}} \cdot \hat{\mathbf{a}}_2) = 0$. In that case c_{ij} receives only the uncorrelated contribution from the polarization of top and antitop.

3.2. Production density matrix

As we have seen (and is well known) the spin density matrix $\rho_{t\bar{t}}$ describes (anti)top-quark polarization and $t\bar{t}$ spin correlations of the $t\bar{t}$ ensemble. However, $\rho_{t\bar{t}}$ carries no information about how this ensemble of quantum states was prepared. Since we are interested in the spin properties of $t\bar{t}$ pairs produced in hadronic collisions we make use of the so-called *production density matrix* [106] where the production process of $t\bar{t}$ pairs is taken into account. One can write the final state $|f\rangle$ of the collision process in terms of the initial state $|i\rangle$ using the T matrix

$$|f\rangle = T |i\rangle. \quad (3.12)$$

This makes it possible to construct the production density matrix

$$R^{i \rightarrow f} = |f\rangle \langle f| = T |i\rangle \langle i| T^\dagger. \quad (3.13)$$

Note that there is a difference between R and the general density matrix ρ described in Sec. 3.1. In particular, $\text{Tr}[\rho] = 1$ while $\text{Tr}[R] \neq 1$ because if we start from the density matrix of the initial state $\rho_i = |i\rangle \langle i|$ then $\text{Tr}[R^{i \rightarrow f}] = \text{Tr}[T^\dagger T \rho_i] \neq 1$ because T is not unitary. The production density matrix in spin space for the production of top quarks

$$a(p_a), b(p_b) \rightarrow t(k_t), \bar{t}(k_{\bar{t}}) \quad (3.14)$$

is given by [106]

$$R_{\alpha_1\alpha_2,\beta_1\beta_2}^{ab\rightarrow t\bar{t}}(\mathbf{k}, \mathbf{p}) = \frac{1}{N_{ab}} \sum_{\lambda_a, \lambda_b, \text{col.}} \langle t, \alpha_1, k_t; \bar{t}, \beta_1, k_{\bar{t}} | T | a, \lambda_a, p_a; b, \lambda_b, p_b \rangle \times \langle t, \alpha_2, k_t; \bar{t}, \beta_2, k_{\bar{t}} | T | a, \lambda_a, p_a; b, \lambda_b, p_b \rangle^*, \quad (3.15)$$

where α_i and β_i are the spin states of the top and antitop, respectively and a and b denote the initial state partons ($ab = q\bar{q}, gg$). In the partonic center of mass system (cms) $\mathbf{p}_a = -\mathbf{p}_b = \mathbf{p}$ and likewise $\mathbf{k}_t = -\mathbf{k}_{\bar{t}} = \mathbf{k}$. Here only hadronic collisions are considered where the initial particles are unpolarized, hence the polarizations λ_a, λ_b in the initial state are summed. Furthermore specific color states can experimentally neither be generated in the initial state nor be detected in the final state such that the sum also goes over color in the initial and final state. The factor $1/N_{ab}$ takes care of the averaging of the spins and colors in the initial state

$$N_{gg} = 4(N_c^2 - 1)^2, \quad N_{q\bar{q}} = 4N_c^2. \quad (3.16)$$

The matrix $R^{ab\rightarrow t\bar{t}}$ has the same decomposition as the spin density matrix discussed above

$$R_{\alpha_1\alpha_2,\beta_1\beta_2}^{ab\rightarrow t\bar{t}} = A^{ab} \delta_{\alpha_1\alpha_2} \delta_{\beta_1\beta_2} + \mathbf{B}_i^{ab,+} \sigma_{\alpha_1\alpha_2}^i \delta_{\beta_1\beta_2} + \mathbf{B}_i^{ab,-} \delta_{\alpha_1\alpha_2} \sigma_{\beta_1\beta_2}^i + C_{ij}^{ab} \sigma_{\alpha_1\alpha_2}^i \sigma_{\beta_1\beta_2}^j \quad (3.17)$$

or written in matrix notation

$$\mathbf{R}^{ab\rightarrow t\bar{t}} = A^{ab} \mathbb{1} \otimes \mathbb{1} + \mathbf{B}^{ab,+} \cdot \boldsymbol{\sigma} \otimes \mathbb{1} + \mathbb{1} \otimes \boldsymbol{\sigma} \cdot \mathbf{B}^{ab,-} + C_{ij}^{ab} \sigma_i \otimes \sigma_j. \quad (3.18)$$

The coefficient of the spin density matrix are process dependent as indicated by the superscript ab . In the following this superscript will be dropped and the dependence is to be understood implicitly. The normalization of $R^{ab\rightarrow t\bar{t}}$ is obtained by taking the trace

$$\text{Tr}[R^{ab\rightarrow t\bar{t}}] = 4A = \frac{1}{N_{ab}} \sum_{\substack{s_a, s_b, \text{col.}, \\ \alpha\beta}} \langle t, \alpha; \bar{t}, \beta | T | ab \rangle \langle t, \alpha; \bar{t}, \beta | T | ab \rangle^* = |\overline{\mathcal{M}}(ab \rightarrow t\bar{t})|^2, \quad (3.19)$$

where for the first equal sign Eq. (3.18) and $\text{Tr}[\boldsymbol{\sigma} \otimes \mathbb{1}] = \text{Tr}[\mathbb{1} \otimes \boldsymbol{\sigma}] = \text{Tr}[\sigma_i \otimes \sigma_j] = 0$ was used. For the second and third equal sign the definition of the trace as sum over diagonal elements ($\alpha_1 = \alpha_2$ and $\beta_1 = \beta_2$) and the definition of the spin and color averaged T -matrix element $|\overline{\mathcal{M}}|^2$ were used. The relation between the differential partonic cross section in the cms and $|\overline{\mathcal{M}}|^2$

$$\left(\frac{d\sigma_{ab\rightarrow t\bar{t}}}{d\cos\theta} \right)_{\text{cms}} = \frac{\beta_t}{32\pi s} |\overline{\mathcal{M}}(ab \rightarrow t\bar{t})|^2 \quad (3.20)$$

can be used to express the coefficient A in Eq. (3.18) as follows

$$A = \frac{8\pi s}{\beta_t} \left(\frac{d\sigma_{ab\rightarrow t\bar{t}}}{d\cos\theta} \right)_{\text{cms}}, \quad (3.21)$$

where $\beta_t = \sqrt{1 - 4m_t^2/s}$, $\cos\theta = \hat{\mathbf{k}} \cdot \hat{\mathbf{p}}$ with $\hat{\mathbf{k}} = \mathbf{k}/|\mathbf{k}|$, $\hat{\mathbf{p}} = \mathbf{p}/|\mathbf{p}|$ and s is the center-of-mass energy squared.

The coefficients \mathbf{B}^\pm in Eq. (3.18) are related to the polarization of top and antitop in hadronic collisions. A precise relation is given in Appendix C and Sec. 4.2.3. Since the scattering process is independent of the choice of the orientation of the reference frame, i.e. invariant under rotation of all momenta (\mathbf{k}, \mathbf{p}) it is possible to decompose the \mathbf{B}^\pm in terms of $\hat{\mathbf{k}}, \hat{\mathbf{p}}$ and ϵ_{ijl}

$$B_i^\pm = b_1^\pm \hat{p}_i + b_2^\pm \hat{k}_i + b_3^\pm \epsilon_{ijl} \hat{p}_j \hat{k}_l \quad (3.22)$$

3. Spin density matrix formalism

the b_i^\pm are scalar functions of z and s .

The coefficients C_{ij} are directly related to $t\bar{t}$ spin correlations in the case where both t and \bar{t} are unpolarized otherwise C_{ij} receives uncorrelated contributions from the polarization of top and antitop. By the same arguments of rotational invariance used above C_{ij} has to transform as a rank two tensor under rotations. The most general rank two tensor that can be constructed out of $\hat{\mathbf{k}}$, $\hat{\mathbf{p}}$, δ_{ij} and ϵ_{ijl} is given by¹

$$C_{ij} = c_0\delta_{ij} + c_1\epsilon_{ijl}\hat{p}_l + c_2\epsilon_{ijl}\hat{k}_l + c_3(\hat{p}_i\hat{k}_j - \hat{k}_i\hat{p}_j) + c_4\hat{p}_i\hat{p}_j + c_5\hat{k}_i\hat{k}_j + c_6(\hat{p}_i\hat{k}_j + \hat{k}_i\hat{p}_j) + c_7(p_i\epsilon_{jlm}p_lk_m + p_j\epsilon_{ilm}p_lk_m) + c_8(k_i\epsilon_{jlm}p_lk_m + k_j\epsilon_{ilm}p_lk_m). \quad (3.23)$$

\mathbf{B}^\pm and C_{ij} can be rewritten by introducing the unit three-vector $\hat{\mathbf{n}} = \hat{\mathbf{p}} \times \hat{\mathbf{k}}$ as follows² [107]

$$B_i^\pm = b_1^\pm \hat{p}_i + b_2^\pm \hat{k}_i + b_3^\pm \hat{n}_i, \quad (3.24)$$

$$C_{ij} = c_0\delta_{ij} + c_1\epsilon_{ijl}\hat{p}_l + c_2\epsilon_{ijl}\hat{k}_l + c_3\epsilon_{ijl}\hat{n}_l + c_4\hat{p}_i\hat{p}_j + c_5\hat{k}_i\hat{k}_j + c_6(\hat{p}_i\hat{k}_j + \hat{k}_i\hat{p}_j) + c_7(\hat{p}_i\hat{n}_j + \hat{n}_i\hat{p}_j) + c_8(\hat{k}_i\hat{n}_j + \hat{n}_i\hat{k}_j). \quad (3.25)$$

So far the expectation values that have been considered were calculated with respect to the spin space. Since we study hadronic collision processes we evaluate expectation values of observables also with respect to the phase space. In general the expectation value is defined as

$$\langle O \rangle = \frac{\int d\sigma O}{\int d\sigma} = \frac{1}{\sigma} \int d\sigma O \quad (3.26)$$

which represents a weighted average of the phase space dependent observable O with weights $d\sigma/\sigma$ where σ is the total hadronic cross section. In analogy to this expression the expectation value of an operator \hat{O} that represents the observable O can be written in terms of the production density matrix

$$\langle \hat{O} \rangle = \frac{1}{\sigma} \sum_{a,b} \int dx_1 dx_2 d\Phi_{t\bar{t}} f_{p,a}(x_1, \mu_F) f_{p,b}(x_2, \mu_F) \text{Tr}[R^{ab \rightarrow t\bar{t}} \hat{O}], \quad (3.27)$$

where x_1 and x_2 are the momentum fractions of the proton momentum carried by parton a and b , respectively. $f_{p,a}$ ($f_{p,b}$) is the parton distribution function (PDF) for parton a (b) in a proton. It is a measure of the probability to find parton a (b) with momentum $p_a \in [x_1P, x_1P + dx_1]$ ($p_b \in [x_2P, x_2P + dx_2]$) in a proton with momentum P . The convolution with the PDFs therefore takes into account that in a hadronic collision the partonic initial states do not have sharp momenta. In Eq. (3.27) $d\Phi_{t\bar{t}}$ denotes the phase space measure including the delta function for energy momentum conservation and the flux factor

$$d\Phi_{t\bar{t}} = \frac{1}{2s} \frac{d^3k_t}{(2\pi)^3 2E_1} \frac{d^3k_{\bar{t}}}{(2\pi)^3 2E_2} (2\pi)^4 \delta^{(4)}(p_a + p_b - k_t - k_{\bar{t}}) \theta(s - 4m_t^2), \quad (3.28)$$

where $s = x_1x_2S_{\text{had}}$ and S_{had} is the hadronic center of mass energy squared.

¹There are nine free parameters c_0, \dots, c_8 for the real 3×3 matrix C_{ij} . Note also that the antisymmetric (in ij) combination $\hat{k}_i\epsilon_{jlm}p_lk_m - \hat{k}_j\epsilon_{ilm}p_lk_m = \epsilon_{ijl}\hat{p}_l - z\epsilon_{ijl}\hat{k}_l$ and is therefore represented by a linear combination of the c_1 and c_2 terms. A similar relation holds for $\hat{p}_i\epsilon_{jlm}p_lk_m - \hat{p}_j\epsilon_{ilm}p_lk_m$.

²Note that the $\epsilon_{ijl}\hat{n}_l = \hat{p}_i\hat{k}_j - \hat{k}_i\hat{p}_j$ and $n_i n_j = -\hat{k}_i\hat{k}_j - \hat{p}_i\hat{p}_j + z(\hat{p}_i\hat{k}_j + \hat{k}_i\hat{p}_j) + \delta_{ij}(1 - z^2)$. Hence the antisymmetric structure $\hat{k}_i\hat{p}_j - \hat{p}_i\hat{k}_j$ in Eq. (3.23) and the symmetric structure $n_i n_j$ are covered by Eq. (3.25).

3.3. Spin correlation vs. angular correlation

This section illustrates the relation between spin dependent observables defined at the level of stable $t\bar{t}$ pairs and angular correlations of the $t\bar{t}$ decay products.

As an example we consider the expectation value $\langle(\mathbf{S}_t \cdot \hat{\mathbf{k}}_t)(\mathbf{S}_{\bar{t}} \cdot \hat{\mathbf{k}}_{\bar{t}})\rangle = -\langle(\mathbf{S}_t \cdot \hat{\mathbf{k}})(\mathbf{S}_{\bar{t}} \cdot \hat{\mathbf{k}})\rangle$. According to Eq. (3.27) the trace has to be evaluated

$$\text{Tr}[R^{ab \rightarrow t\bar{t}}(\mathbf{S}_t \cdot \hat{\mathbf{k}}_t)(\mathbf{S}_{\bar{t}} \cdot \hat{\mathbf{k}}_{\bar{t}})] = -\frac{1}{4}\text{Tr}[R^{ab \rightarrow t\bar{t}}(\sigma_i \otimes \sigma_j)\hat{k}_i\hat{k}_j] = -C_{ij}k_ik_j. \quad (3.29)$$

Using the decomposition of C_{ij} in Eq. (3.25) gives

$$\text{Tr}[R^{ab \rightarrow t\bar{t}}(\mathbf{S}_t \cdot \hat{\mathbf{k}}_t)(\mathbf{S}_{\bar{t}} \cdot \hat{\mathbf{k}}_{\bar{t}})] = -(c_0 + c_1 + z^2c_2 + 2zc_6). \quad (3.30)$$

Inserting Eq. (3.30) into Eq. (3.27) yields

$$\langle(\mathbf{S}_t \cdot \hat{\mathbf{k}}_t)(\mathbf{S}_{\bar{t}} \cdot \hat{\mathbf{k}}_{\bar{t}})\rangle = -\frac{1}{\sigma_{t\bar{t}}} \sum_{ab} \int_{4m_t^2}^{S_{\text{had}}} ds L_{ab}(S_{\text{had}}, s) \frac{\beta_t}{32\pi s} \int dz (c_0 + c_1 + z^2c_2 + 2zc_6), \quad (3.31)$$

where $\sigma_{t\bar{t}}$ denotes the hadronic cross section for $t\bar{t}$ production and where the luminosity function

$$L_{ab}(S_{\text{had}}, s) = \frac{1}{S_{\text{had}}} \int_{\eta}^1 \frac{d\xi}{\xi} f_{p,a}(\xi, \mu_F) f_{p,b}(\eta/\xi, \mu_F), \quad \eta = \frac{s}{S_{\text{had}}} \quad (3.32)$$

was introduced.

Expectation values of spin operators at the level of stable top quarks such as in Eq. (3.31) are directly related to angular correlations of the decay products of the $t\bar{t}$ pair. For example, in the dileptonic decay channel

$$pp \rightarrow t(k_t) + \bar{t}(k_{\bar{t}}) \rightarrow \ell^+(q_{\ell^+}) + \ell^-(q_{\ell^-}) + X \quad (3.33)$$

by replacing

$$\mathbf{S}_t \rightarrow \hat{\mathbf{q}}_{\ell^+} \quad \text{and} \quad \mathbf{S}_{\bar{t}} \rightarrow \hat{\mathbf{q}}_{\ell^-} \quad (3.34)$$

the correspondence

$$\langle(\mathbf{S}_t \cdot \hat{\mathbf{k}}_t)(\mathbf{S}_{\bar{t}} \cdot \hat{\mathbf{k}}_{\bar{t}})\rangle_{t\bar{t}} \longleftrightarrow \langle(\hat{\mathbf{q}}_{\ell^+} \cdot \hat{\mathbf{k}}_t)(\hat{\mathbf{q}}_{\ell^-} \cdot \hat{\mathbf{k}}_{\bar{t}})\rangle_{\ell\ell} = \langle\cos\theta_+ \cos\theta_-\rangle_{\ell\ell} \quad (3.35)$$

can be obtained, where $\hat{\mathbf{q}}_{\ell^+} \cdot \hat{\mathbf{k}}_t = \cos\theta_+$ and $\hat{\mathbf{q}}_{\ell^-} \cdot \hat{\mathbf{k}}_{\bar{t}} = \cos\theta_-$ have been defined.

In order to derive the relation between $\langle(\mathbf{S}_t \cdot \hat{\mathbf{k}}_t)(\mathbf{S}_{\bar{t}} \cdot \hat{\mathbf{k}}_{\bar{t}})\rangle_{t\bar{t}}$ and $\langle\cos\theta_+ \cos\theta_-\rangle_{\ell\ell}$ we consider the decay of the $t\bar{t}$ pair. In analogy to the production density matrix R the so-called *decay density matrix* D can be defined. For example the decay density matrix for $t \rightarrow b\ell^+\nu$ is given by [108]

$$D_{\alpha\beta}^{t \rightarrow b\ell^+\nu} = \sum_{b, \ell^+, \nu \text{ spins}} \langle b\ell^+\nu | T | t, \alpha \rangle \langle t, \beta | T^\dagger | b\ell^+\nu \rangle. \quad (3.36)$$

$D^{t \rightarrow b\ell^+\nu}$ has the same structure as the spin density matrix discussed in Sec. 3.1

$$D^{t \rightarrow b\ell^+\nu} = G_t(\mathbb{1} + \kappa_t \hat{\mathbf{q}}_{\ell^+} \cdot \boldsymbol{\sigma}), \quad (3.37)$$

where $\hat{\mathbf{q}}_{\ell^+}$ is the direction of flight of the antilepton ℓ^+ in the top quark rest frame. The coefficient κ_f is called the *spin analyzing power* of the top decay product f . The lepton ($f = \ell$) has the maximum value $\kappa_\ell = 1$ at tree level. For the antitop-quark decay $\bar{t} \rightarrow \bar{b}\ell^-\bar{\nu}$ the decay density matrix is given by

$$D^{\bar{t} \rightarrow \bar{b}\ell^-\bar{\nu}} = G_{\bar{t}}(\mathbb{1} - \kappa_{\bar{t}} \hat{\mathbf{q}}_{\ell^-} \cdot \boldsymbol{\sigma}), \quad (3.38)$$

3. Spin density matrix formalism

where $\hat{\mathbf{q}}_{\ell^-}$ is the direction of the lepton (ℓ^-) momentum in the top quark rest frame. In the narrow width approximation for the W boson propagator G_t and $G_{\bar{t}}$ are defined as

$$G_t = \Gamma_t \text{BR}(t \rightarrow b\ell^+\nu) \frac{1536\pi^3 m_t}{(1-\omega)^2(1+2\omega)} (1-x_+) x_+ \delta((q_{\ell^+} + q_\nu)^2 - m_W^2), \quad (3.39)$$

$$G_{\bar{t}} = \Gamma_{\bar{t}} \text{BR}(\bar{t} \rightarrow \bar{b}\ell^-\bar{\nu}) \frac{1536\pi^3 m_t}{(1-\omega)^2(1+2\omega)} (1-x_-) x_- \delta((q_{\ell^-} + q_{\bar{\nu}})^2 - m_W^2), \quad (3.40)$$

where $x_\pm = \frac{2E_\pm}{m_t}$ are the normalized energies of the positively and negatively charged lepton in the top and antitop rest frame, respectively. Γ_t denotes the total top-quark decay width, BR is the branching ratio of the respective top-quark decay mode and $\omega = \frac{m_W^2}{m_t^2}$. q_{ℓ^+} , q_ν denote the four-momenta of the antilepton and the neutrino in the top-quark rest frame and q_{ℓ^-} and $q_{\bar{\nu}}$ denote the four-momenta of the lepton and the antineutrino in the antitop-quark rest frame. In the case where the decay of the W boson is not further considered and the b quark is used as the spin analyzer of the top quark the decay density matrix is given by

$$D^{t \rightarrow Wb} = \tilde{G}_t (\mathbb{1} + \kappa_b \hat{\mathbf{q}}_b \cdot \boldsymbol{\sigma}), \quad (3.41)$$

where $\hat{\mathbf{q}}_b$ is the direction of the bottom quark momentum in the top-quark rest frame and

$$\kappa_b = \frac{2m_W^2 - m_t^2}{2m_W^2 + m_t^2}. \quad (3.42)$$

Using $m_t = 173\text{GeV}$ and $m_W = 80\text{GeV}$ in Eq. (3.42) $\kappa_b \approx 0.4$ which is lower than the analyzing power of the lepton. Hence, the leptonic decay of the (anti)top quark is best suited for the study of spin dependent observables.

In the narrow width approximation for the top and antitop quark the process

$$ab \rightarrow t(k_t) \bar{t}(p_{\bar{t}}) \rightarrow b(q_b) \bar{b}(q_{\bar{b}}) \ell^+(q_{\ell^+}) \ell^-(q_{\ell^-}) \nu(q_\nu) \bar{\nu}(q_{\bar{\nu}}) \quad (3.43)$$

factorizes into the production of $t\bar{t}$ and the decay of t and \bar{t} . The corresponding matrix element can then be written in terms of the production density matrix of $t\bar{t}$ production and the decay density matrices of top and antitop quark (see also Appendix C.1)

$$|\mathcal{M}(ab \rightarrow t\bar{t} \rightarrow b\bar{b}\ell^+\ell^-\nu\bar{\nu})|^2 = \frac{\pi^2}{(m_t \Gamma_t)^2} \delta(k_t^2 - m_t^2) \delta(k_{\bar{t}}^2 - m_t^2) \text{Tr}[R^{ab \rightarrow t\bar{t}} D^{t \rightarrow b\ell^+\nu} \otimes D^{\bar{t} \rightarrow \bar{b}\ell^-\bar{\nu}}], \quad (3.44)$$

where the factor in front of the trace on the right hand side (rhs) is due to the narrow width approximation of the top and antitop propagators. The general structure of the matrix element for the process in (3.43) can then be expressed by the coefficients of $R^{ab \rightarrow t\bar{t}}$, $D^{t \rightarrow b\ell^+\nu}$ and $D^{\bar{t} \rightarrow \bar{b}\ell^-\bar{\nu}}$

$$\begin{aligned} |\mathcal{M}(ab \rightarrow t\bar{t} \rightarrow b\bar{b}\ell^+\ell^-\nu\bar{\nu})|^2 &= 4G_t G_{\bar{t}} \frac{\pi^2}{(m_t \Gamma_t)^2} \delta(k_t^2 - m_t^2) \delta(k_{\bar{t}}^2 - m_t^2) \\ &\times \left(A + \kappa_t \hat{\mathbf{q}}_{\ell^+} \cdot \mathbf{B}^+ - \kappa_{\bar{t}} \hat{\mathbf{q}}_{\ell^-} \cdot \mathbf{B}^- - \kappa_{\bar{t}}^2 C_{ij} q_{\ell^+}^i q_{\ell^-}^j \right), \end{aligned} \quad (3.45)$$

where $k_t = q_{\ell^+} + q_b + q_\nu$ and $p_{\bar{t}} = q_{\ell^-} + q_{\bar{b}} + q_{\bar{\nu}}$. Inserting the decomposition of \mathbf{B}^\pm (3.24) and

C_{ij} (3.25) gives

$$\begin{aligned}
 |\mathcal{M}(ab \rightarrow t\bar{t} \rightarrow b\bar{b}\ell^+\ell^-\nu\bar{\nu})|^2 &= 4G_t G_{\bar{t}} \frac{\pi^2}{(m_t \Gamma_t)^2} \delta(k_t^2 - m_t^2) \delta(k_{\bar{t}}^2 - m_t^2) \\
 &\times \left\{ A + \kappa_\ell \left[b_1^+ (\hat{\mathbf{k}} \cdot \hat{\mathbf{q}}_{\ell^+}) + b_2^+ (\hat{\mathbf{p}} \cdot \hat{\mathbf{q}}_{\ell^+}) + b_3^+ (\hat{\mathbf{n}} \cdot \hat{\mathbf{q}}_{\ell^+}) \right] - \kappa_\ell \left[b_1^- (\hat{\mathbf{k}} \cdot \hat{\mathbf{q}}_{\ell^-}) + b_2^- (\hat{\mathbf{p}} \cdot \hat{\mathbf{q}}_{\ell^-}) + b_3^- (\hat{\mathbf{n}} \cdot \hat{\mathbf{q}}_{\ell^-}) \right] \right. \\
 &- \kappa_\ell^2 \left[c_0 (\hat{\mathbf{q}}_{\ell^+} \cdot \hat{\mathbf{q}}_{\ell^-}) + c_1 (\hat{\mathbf{k}} \cdot \hat{\mathbf{q}}_{\ell^+}) (\hat{\mathbf{k}} \cdot \hat{\mathbf{q}}_{\ell^-}) + c_2 (\hat{\mathbf{p}} \cdot \hat{\mathbf{q}}_{\ell^+}) (\hat{\mathbf{p}} \cdot \hat{\mathbf{q}}_{\ell^-}) + c_3 [\hat{\mathbf{k}} \cdot (\hat{\mathbf{q}}_{\ell^+} \times \hat{\mathbf{q}}_{\ell^-})] \right. \\
 &+ c_4 [\hat{\mathbf{p}} \cdot (\hat{\mathbf{q}}_{\ell^+} \times \hat{\mathbf{q}}_{\ell^-})] + c_5 [\hat{\mathbf{n}} \cdot (\hat{\mathbf{q}}_{\ell^+} \times \hat{\mathbf{q}}_{\ell^-})] + c_6 [(\hat{\mathbf{k}} \cdot \hat{\mathbf{q}}_{\ell^+}) (\hat{\mathbf{p}} \cdot \hat{\mathbf{q}}_{\ell^-}) + (\hat{\mathbf{k}} \cdot \hat{\mathbf{q}}_{\ell^-}) (\hat{\mathbf{p}} \cdot \hat{\mathbf{q}}_{\ell^+})] \\
 &\left. \left. + c_7 [(\hat{\mathbf{k}} \cdot \hat{\mathbf{q}}_{\ell^+}) (\hat{\mathbf{n}} \cdot \hat{\mathbf{q}}_{\ell^-}) + (\hat{\mathbf{k}} \cdot \hat{\mathbf{q}}_{\ell^-}) (\hat{\mathbf{n}} \cdot \hat{\mathbf{q}}_{\ell^+})] + c_8 [(\hat{\mathbf{p}} \cdot \hat{\mathbf{q}}_{\ell^+}) (\hat{\mathbf{n}} \cdot \hat{\mathbf{q}}_{\ell^-}) + (\hat{\mathbf{p}} \cdot \hat{\mathbf{q}}_{\ell^-}) (\hat{\mathbf{n}} \cdot \hat{\mathbf{q}}_{\ell^+})] \right] \right\}. \quad (3.46)
 \end{aligned}$$

Equation (3.46) shows how the top-quark decay (in this case the dileptonic decay) ‘‘analyzes’’ the spin structures of the $t\bar{t}$ system: The coefficients b_i^\pm , c_j of the production density matrix are related to angular distributions of the charged leptons. Hence, these angular correlations can be directly related to spin observables sensitive to (anti)top-quark polarization and $t\bar{t}$ spin correlations.

With Eq. (3.46) we can proceed with deriving a relation between $\langle (\mathbf{S}_t \cdot \hat{\mathbf{k}}_t) (\mathbf{S}_{\bar{t}} \cdot \hat{\mathbf{k}}_{\bar{t}}) \rangle_{t\bar{t}}$ and $\langle \cos \theta_+ \cos \theta_- \rangle_{\ell\ell} = \langle (\hat{\mathbf{k}}_t \cdot \hat{\mathbf{q}}_{\ell^+}) (\hat{\mathbf{k}}_{\bar{t}} \cdot \hat{\mathbf{q}}_{\ell^-}) \rangle_{\ell\ell}$. Since $(\hat{\mathbf{k}}_t \cdot \hat{\mathbf{q}}_{\ell^+}) (\hat{\mathbf{k}}_{\bar{t}} \cdot \hat{\mathbf{q}}_{\ell^-}) = -(\hat{\mathbf{k}} \cdot \hat{\mathbf{q}}_{\ell^+}) (\hat{\mathbf{k}} \cdot \hat{\mathbf{q}}_{\ell^-})$ is bilinear in $\hat{\mathbf{q}}_{\ell^+}$ and $\hat{\mathbf{q}}_{\ell^-}$ the only terms in Eq. (3.46) that can contribute to this structure are c_j . To determine which of these terms in fact contribute one has to take into account that $\hat{\mathbf{p}}$ and $\hat{\mathbf{q}}_{\ell^\pm}$ have a component in the direction of $\hat{\mathbf{k}}$

$$\hat{\mathbf{p}} = \hat{\mathbf{p}}^\perp + z\hat{\mathbf{k}}, \quad \hat{\mathbf{p}}^\perp \cdot \hat{\mathbf{k}} = 0 \quad (3.47)$$

$$\hat{\mathbf{q}}_{\ell^\pm} = \hat{\mathbf{q}}_{\ell^\pm}^\perp + (\hat{\mathbf{k}} \cdot \hat{\mathbf{q}}_{\ell^\pm})\hat{\mathbf{k}}, \quad \hat{\mathbf{q}}_{\ell^\pm}^\perp \cdot \hat{\mathbf{k}} = 0 \quad (3.48)$$

Collecting all terms involving $\cos \theta_+ \cos \theta_-$ in Eq. (3.46) yields

$$|\mathcal{M}(ab \rightarrow t\bar{t} \rightarrow b\bar{b}\ell^+\ell^-\nu\bar{\nu})|^2 \sim \kappa_\ell^2 \left[c_0 + c_1 + z^2 c_2 + 2zc_6 \right] \cos \theta_+ \cos \theta_- + \dots, \quad (3.49)$$

where the dots represent terms that do not depend on $\cos \theta_+ \cos \theta_-$. The linear combination of c 's in Eq. (3.49) is exactly the same that we encountered in Eq. (3.31) when evaluating the expectation value $\langle (\mathbf{S}_t \cdot \hat{\mathbf{k}}_t) (\mathbf{S}_{\bar{t}} \cdot \hat{\mathbf{k}}_{\bar{t}}) \rangle_{t\bar{t}}$ which has to be compared with $\langle \cos \theta_+ \cos \theta_- \rangle$. Using Eq. (3.26) yields

$$\begin{aligned}
 \langle \cos \theta_+ \cos \theta_- \rangle_{\ell\ell} &= \frac{\text{BR}(t \rightarrow b\ell^+\nu) \text{BR}(\bar{t} \rightarrow \ell^-\bar{\nu})}{\sigma} \\
 &\times \sum_{ab} \int dx_1 dx_2 f_{p,a}(x_1, \mu_F) f_{p,b}(x_2, \mu_F) \theta(s - 4m_t^2) \\
 &\times \frac{\beta_t}{16\pi^2 s} \int \frac{d\Omega_+}{4\pi} \frac{d\Omega_-}{4\pi} d\Omega_t (\kappa_\ell^2 C(s, z) \cos^2 \theta_+ \cos^2 \theta_-), \quad (3.50)
 \end{aligned}$$

where $C(s, z) = c_0 + c_1 + z^2 c_2 + 2zc_6$ and where the terms of the matrix element indicated by the dots in Eq. (3.49) were omitted because they vanish after phase space integration. In Eq. (3.50)

$$s = x_1 x_2 S_{\text{had}}, \quad d\Omega_\pm = d \cos \theta_\pm d\varphi_\pm, \quad d\Omega_t = dz d\varphi_t. \quad (3.51)$$

Performing the integration over $d\Omega_\pm$ and $d\varphi_t$ yields

$$\begin{aligned}
 \langle \cos \theta_+ \cos \theta_- \rangle_{\ell\ell} &= \frac{\text{BR}(t \rightarrow b\ell^+\nu) \text{BR}(\bar{t} \rightarrow \ell^-\bar{\nu})}{\sigma} \\
 &\times \sum_{ab} \int_{4m_t^2}^{S_{\text{had}}} ds L_{ab}(S_{\text{had}}, s) \frac{\beta_t}{32\pi s} \int dz \left(\frac{4}{9} C(s, z) \right). \quad (3.52)
 \end{aligned}$$

3. Spin density matrix formalism

Further, using the relation

$$\sigma = \sigma_{t\bar{t}} \text{BR}(t \rightarrow b\ell^+\nu) \text{BR}(\bar{t} \rightarrow \ell^-\bar{\nu}) \quad (3.53)$$

in Eq. (3.52) and comparing to Eq. (3.31) one can derive the following result

$$\langle \cos \theta_+ \cos \theta_- \rangle_{\ell\bar{\ell}} = -\kappa_\ell^2 \frac{4}{9} \langle (\mathbf{S}_t \cdot \hat{\mathbf{k}}_t)(\mathbf{S}_{\bar{t}} \cdot \hat{\mathbf{k}}_{\bar{t}}) \rangle_{t\bar{t}} = \kappa_\ell^2 \frac{4}{9} \langle (\mathbf{S}_t \cdot \hat{\mathbf{k}})(\mathbf{S}_{\bar{t}} \cdot \hat{\mathbf{k}}) \rangle_{t\bar{t}}. \quad (3.54)$$

Of course the relation (3.54) is only valid as long as no acceptance cut on the leptons are applied because these cuts are not defined in the $t\bar{t}$ phase space. However, as can be seen from Eqs. (3.52) and (3.31) cuts on the $t\bar{t}$ invariant mass $M_{t\bar{t}}$ are allowed.

3.4. Spin dependent matrix element

In this section the spin dependent matrix element is introduced, starting with its definition and how to calculate it explicitly. Two applications of the spin dependent matrix element are presented. One is a method how to include the decay of the $t\bar{t}$ pair by generating the matrix element for $t\bar{t}$ production and decay from the spin dependent matrix element. The second application is the calculation of expectation values such as for example in Eq. (3.31) using the spin dependent matrix element.

In Sec. 3.2 it was shown that the trace over the production density matrix gives the spin averaged matrix element

$$\text{Tr}[R^{ab \rightarrow t\bar{t}}] = |\overline{\mathcal{M}}(ab \rightarrow t\bar{t})|^2. \quad (3.55)$$

The spin dependent matrix element is obtained by projecting onto an arbitrary spin state using the projection operator

$$\frac{1}{2}(\mathbb{1} + \boldsymbol{\sigma} \cdot \hat{\mathbf{s}}_t) \otimes \frac{1}{2}(\mathbb{1} + \boldsymbol{\sigma} \cdot \hat{\mathbf{s}}_{\bar{t}}), \quad (3.56)$$

where $\hat{\mathbf{s}}_t$ ($\hat{\mathbf{s}}_{\bar{t}}$) is the spin three-vector (spin quantization axis) of the (anti)top quark in the respective rest frame. The spin dependent matrix element is then given by taking the trace

$$|\mathcal{M}(\hat{\mathbf{s}}_t, \hat{\mathbf{s}}_{\bar{t}})|^2 = \frac{1}{4} \text{Tr}[R^{ab \rightarrow t\bar{t}}(\mathbb{1} + \boldsymbol{\sigma} \cdot \hat{\mathbf{s}}_t)(\mathbb{1} + \boldsymbol{\sigma} \cdot \hat{\mathbf{s}}_{\bar{t}})] = A + \mathbf{B}^+ \cdot \hat{\mathbf{s}}_t + \mathbf{B}^- \cdot \hat{\mathbf{s}}_{\bar{t}} + C_{ij} \hat{s}_t^i \hat{s}_{\bar{t}}^j. \quad (3.57)$$

It can be calculated by using the following spinor relations

$$u(k, s)\bar{u}(k, s) = \frac{1}{2}(1 + \gamma_5 \not{s})(\not{k} + m) \quad \text{and} \quad v(k, s)\bar{v}(k, s) = \frac{1}{2}(1 + \gamma_5 \not{s})(\not{k} - m), \quad (3.58)$$

where $u(k, s)$ ($v(k, s)$) denotes the spinor of a (anti)particle with momentum k and spin four-vector s . Applying Eq. (3.58) to the calculation of the matrix element of $t\bar{t}$ production yields

$$|\mathcal{M}(s_t, s_{\bar{t}})|^2 = A + \widetilde{B}_\mu^+ s_t^\mu + \widetilde{B}_\mu^- s_{\bar{t}}^\mu + \widetilde{C}_{\mu\nu} s_t^\mu s_{\bar{t}}^\nu, \quad (3.59)$$

where s_t and $s_{\bar{t}}$ are the spin four-vectors of the top and antitop quark, respectively. \widetilde{B}^\pm and \widetilde{C} are functions of s and $z = \hat{\mathbf{k}} \cdot \hat{\mathbf{p}}$.

The structure of the spin dependent matrix element in Eq. (3.59) is at first given by the fact that the spinor products in Eq. (3.58) generate terms that contain one scalar product with a spin vector (\widetilde{B}^\pm), terms with two scalar products involving s_t and $s_{\bar{t}}$ (\widetilde{C}) and terms without any spin vector (A). The term

$$A = \frac{1}{4} |\overline{\mathcal{M}}(ab \rightarrow t\bar{t})|^2 \quad (3.60)$$

3.4. Spin dependent matrix element

is in fact the same as in $R^{ab \rightarrow t\bar{t}}$ (cf. Eq. (3.19)). The relations between \widetilde{B}^\pm , \widetilde{C} and the coefficients of $R^{ab \rightarrow t\bar{t}}$ are given by

$$\mathbf{B}^+ \cdot \hat{\mathbf{s}}_t = \widetilde{B}_\mu^+ s_t^\mu, \quad \mathbf{B}^- \cdot \hat{\mathbf{s}}_{\bar{t}} = \widetilde{B}_\mu^- s_{\bar{t}}^\mu, \quad C_{ij} \hat{s}_t^i \hat{s}_{\bar{t}}^j = \widetilde{C}_{\mu\nu} s_t^\mu s_{\bar{t}}^\nu, \quad (3.61)$$

where the explicit form of the spin four-vectors s_t and $s_{\bar{t}}$ is needed. In the top and antitop rest frame they are given by

$$s_t = (0, \hat{\mathbf{s}}_t)^T \quad \text{and} \quad s_{\bar{t}} = (0, \hat{\mathbf{s}}_{\bar{t}})^T. \quad (3.62)$$

If the external momenta are given in the $t\bar{t}$ rest frame then in Eq. (3.59) the spin four-momenta are also given in this frame. Boosting s_t and $s_{\bar{t}}$ in Eq. (3.62) into the $t\bar{t}$ rest frame gives

$$s_t = \begin{pmatrix} \beta_t \gamma_t (\hat{\mathbf{k}} \cdot \hat{\mathbf{s}}_t) \\ \hat{\mathbf{s}}_t + (\gamma_t - 1) (\hat{\mathbf{k}} \cdot \hat{\mathbf{s}}_t) \hat{\mathbf{k}} \end{pmatrix}, \quad (3.63)$$

$$s_{\bar{t}} = \begin{pmatrix} -\beta_t \gamma_t (\hat{\mathbf{k}} \cdot \hat{\mathbf{s}}_{\bar{t}}) \\ \hat{\mathbf{s}}_{\bar{t}} + (\gamma_t - 1) (\hat{\mathbf{k}} \cdot \hat{\mathbf{s}}_{\bar{t}}) \hat{\mathbf{k}} \end{pmatrix} \quad (3.64)$$

with $\gamma_t = E_t/m_t$, $\beta_t = \sqrt{1 - m_t^2/E_t^2}$. E_t denotes the top-quark energy in the $t\bar{t}$ rest frame. $\hat{\mathbf{s}}_t$ ($\hat{\mathbf{s}}_{\bar{t}}$) is the spin quantization axis in the (anti)top-quark rest frame (as in Eq. (3.57)) and $\hat{\mathbf{k}}$ is the direction of the top-quark momentum in the $t\bar{t}$ rest frame. While in LO compact results for the coefficients of $R^{ab \rightarrow t\bar{t}}$ can be derived, including NLO corrections leads to cumbersome expressions rendering this approach less useful.

In the following it is shown how the spin dependent matrix element can be used to calculate expectation values of operators without extracting the production density matrix. As an example the operator $(\mathbf{S}_t \cdot \hat{\mathbf{a}}_1)(\mathbf{S}_{\bar{t}} \cdot \hat{\mathbf{a}}_2)$ is considered with

$$\text{Tr}[R^{ab \rightarrow t\bar{t}}(\mathbf{S}_t \cdot \hat{\mathbf{a}}_1)(\mathbf{S}_{\bar{t}} \cdot \hat{\mathbf{a}}_2)] = C_{ij} \hat{a}_1^i \hat{a}_2^j. \quad (3.65)$$

In the spin dependent matrix element this corresponds to the term $C_{ij} \hat{s}_t^i \hat{s}_{\bar{t}}^j$ which can be projected out by the following linear combination of spin dependent matrix elements with flipped spins

$$\text{Tr}[R^{ab \rightarrow t\bar{t}}(\mathbf{S}_t \cdot \hat{\mathbf{a}}_1)(\mathbf{S}_{\bar{t}} \cdot \hat{\mathbf{a}}_2)] = \frac{1}{4} \left[|\mathcal{M}(\hat{\mathbf{a}}_1, \hat{\mathbf{a}}_2)|^2 - |\mathcal{M}(\hat{\mathbf{a}}_1, -\hat{\mathbf{a}}_2)|^2 - |\mathcal{M}(-\hat{\mathbf{a}}_1, \hat{\mathbf{a}}_2)|^2 + |\mathcal{M}(-\hat{\mathbf{a}}_1, -\hat{\mathbf{a}}_2)|^2 \right]. \quad (3.66)$$

Hence, in order to calculate the trace in Eq. (3.65) the spin dependent matrix element has to be evaluated four times using different combinations of spin vectors $\hat{\mathbf{s}}_t = \pm \hat{\mathbf{a}}_1$ and $\hat{\mathbf{s}}_{\bar{t}} = \pm \hat{\mathbf{a}}_2$ in the top and antitop rest frame. For the spin four-vectors, e.g. in Eq. (3.59), this means

$$s_t = (0, \hat{\mathbf{a}}_1)^T, \quad s_{\bar{t}} = (0, \hat{\mathbf{a}}_2)^T \quad (3.67)$$

in the top and antitop-quark rest frame and

$$s_t = \begin{pmatrix} \varkappa_t (\hat{\mathbf{k}} \cdot \hat{\mathbf{a}}_1) \\ \hat{\mathbf{a}}_1 + \lambda_t (\hat{\mathbf{k}} \cdot \hat{\mathbf{a}}_1) \hat{\mathbf{k}} \end{pmatrix}, \quad s_{\bar{t}} = \begin{pmatrix} -\varkappa_{\bar{t}} (\hat{\mathbf{k}} \cdot \hat{\mathbf{a}}_2) \\ \hat{\mathbf{a}}_2 + \lambda_{\bar{t}} (\hat{\mathbf{k}} \cdot \hat{\mathbf{a}}_2) \hat{\mathbf{k}} \end{pmatrix}, \quad \varkappa_t = \beta_t \gamma_t, \quad \lambda_t = (\gamma_t - 1) \quad (3.68)$$

in the $t\bar{t}$ rest frame. After the trace has been determined by this method it can be integrated over the $t\bar{t}$ phase space (Eq. (3.27)) to obtain the expectation value $\langle (\mathbf{S}_t \cdot \hat{\mathbf{a}}_1)(\mathbf{S}_{\bar{t}} \cdot \hat{\mathbf{a}}_2) \rangle$. This procedure is also applicable for more complicated operators, e.g.

$$\begin{aligned} & \text{Tr}[R^{ab \rightarrow t\bar{t}}(\mathbf{S}_t \cdot \mathbf{S}_{\bar{t}})] \\ &= \frac{1}{4} \left\{ |\mathcal{M}(\hat{\mathbf{d}}^{(1)}, \hat{\mathbf{d}}^{(1)})|^2 - |\mathcal{M}(\hat{\mathbf{d}}^{(1)}, -\hat{\mathbf{d}}^{(1)})|^2 - |\mathcal{M}(-\hat{\mathbf{d}}^{(1)}, \hat{\mathbf{d}}^{(1)})|^2 + |\mathcal{M}(-\hat{\mathbf{d}}^{(1)}, -\hat{\mathbf{d}}^{(1)})|^2 \right. \\ &+ |\mathcal{M}(\hat{\mathbf{d}}^{(2)}, \hat{\mathbf{d}}^{(2)})|^2 - |\mathcal{M}(\hat{\mathbf{d}}^{(2)}, -\hat{\mathbf{d}}^{(2)})|^2 - |\mathcal{M}(-\hat{\mathbf{d}}^{(2)}, \hat{\mathbf{d}}^{(2)})|^2 + |\mathcal{M}(-\hat{\mathbf{d}}^{(2)}, -\hat{\mathbf{d}}^{(2)})|^2 \\ &+ \left. |\mathcal{M}(\hat{\mathbf{d}}^{(3)}, \hat{\mathbf{d}}^{(3)})|^2 - |\mathcal{M}(\hat{\mathbf{d}}^{(3)}, -\hat{\mathbf{d}}^{(3)})|^2 - |\mathcal{M}(-\hat{\mathbf{d}}^{(3)}, \hat{\mathbf{d}}^{(3)})|^2 + |\mathcal{M}(-\hat{\mathbf{d}}^{(3)}, -\hat{\mathbf{d}}^{(3)})|^2 \right\} \quad (3.69) \end{aligned}$$

3. Spin density matrix formalism

or

$$\begin{aligned}
& \text{Tr}[R^{ab \rightarrow \bar{t}\bar{t}}(\mathbf{S}_t \times \mathbf{S}_{\bar{t}}) \cdot \hat{\mathbf{k}}] \\
&= \frac{1}{4} \left\{ (\hat{\mathbf{d}}^{(1)} \cdot \hat{\mathbf{k}}) \left[|\mathcal{M}(\hat{\mathbf{d}}^{(2)}, \hat{\mathbf{d}}^{(3)})|^2 - |\mathcal{M}(\hat{\mathbf{d}}^{(2)}, -\hat{\mathbf{d}}^{(3)})|^2 - |\mathcal{M}(-\hat{\mathbf{d}}^{(2)}, \hat{\mathbf{d}}^{(3)})|^2 + |\mathcal{M}(-\hat{\mathbf{d}}^{(2)}, -\hat{\mathbf{d}}^{(3)})|^2 \right. \right. \\
&\quad \left. \left. - |\mathcal{M}(\hat{\mathbf{d}}^{(3)}, \hat{\mathbf{d}}^{(2)})|^2 + |\mathcal{M}(\hat{\mathbf{d}}^{(3)}, -\hat{\mathbf{d}}^{(2)})|^2 + |\mathcal{M}(-\hat{\mathbf{d}}^{(3)}, \hat{\mathbf{d}}^{(2)})|^2 - |\mathcal{M}(-\hat{\mathbf{d}}^{(3)}, -\hat{\mathbf{d}}^{(2)})|^2 \right] \right. \\
&\quad + (\hat{\mathbf{d}}^{(2)} \cdot \hat{\mathbf{k}}) \left[|\mathcal{M}(\hat{\mathbf{d}}^{(3)}, \hat{\mathbf{d}}^{(1)})|^2 - |\mathcal{M}(\hat{\mathbf{d}}^{(3)}, -\hat{\mathbf{d}}^{(1)})|^2 - |\mathcal{M}(-\hat{\mathbf{d}}^{(3)}, \hat{\mathbf{d}}^{(1)})|^2 + |\mathcal{M}(-\hat{\mathbf{d}}^{(3)}, -\hat{\mathbf{d}}^{(1)})|^2 \right. \\
&\quad \left. \left. - |\mathcal{M}(\hat{\mathbf{d}}^{(1)}, \hat{\mathbf{d}}^{(3)})|^2 + |\mathcal{M}(\hat{\mathbf{d}}^{(1)}, -\hat{\mathbf{d}}^{(3)})|^2 + |\mathcal{M}(-\hat{\mathbf{d}}^{(1)}, \hat{\mathbf{d}}^{(3)})|^2 - |\mathcal{M}(-\hat{\mathbf{d}}^{(1)}, -\hat{\mathbf{d}}^{(3)})|^2 \right] \right. \\
&\quad \left. + (\hat{\mathbf{d}}^{(3)} \cdot \hat{\mathbf{k}}) \left[|\mathcal{M}(\hat{\mathbf{d}}^{(1)}, \hat{\mathbf{d}}^{(2)})|^2 - |\mathcal{M}(\hat{\mathbf{d}}^{(1)}, -\hat{\mathbf{d}}^{(2)})|^2 - |\mathcal{M}(-\hat{\mathbf{d}}^{(1)}, \hat{\mathbf{d}}^{(2)})|^2 + |\mathcal{M}(-\hat{\mathbf{d}}^{(1)}, -\hat{\mathbf{d}}^{(2)})|^2 \right. \right. \\
&\quad \left. \left. - |\mathcal{M}(\hat{\mathbf{d}}^{(2)}, \hat{\mathbf{d}}^{(1)})|^2 + |\mathcal{M}(\hat{\mathbf{d}}^{(2)}, -\hat{\mathbf{d}}^{(1)})|^2 + |\mathcal{M}(-\hat{\mathbf{d}}^{(2)}, \hat{\mathbf{d}}^{(1)})|^2 - |\mathcal{M}(-\hat{\mathbf{d}}^{(2)}, -\hat{\mathbf{d}}^{(1)})|^2 \right] \right\}, \tag{3.70}
\end{aligned}$$

where $\{\hat{\mathbf{d}}^{(1)}, \hat{\mathbf{d}}^{(2)}, \hat{\mathbf{d}}^{(3)}\}$ is an arbitrary orthonormal basis (e.g. $\hat{\mathbf{d}}^{(i)} = \hat{\mathbf{e}}^{(i)} = (\delta_{1i}, \delta_{2i}, \delta_{3i})^T$).

Furthermore, inserting Eq. (3.66) into Eq. (3.27) yields the so-called *double spin asymmetry*

$$4\langle (\mathbf{S}_t \cdot \hat{\mathbf{a}}_1)(\mathbf{S}_{\bar{t}} \cdot \hat{\mathbf{a}}_2) \rangle = \frac{1}{\sigma_{t\bar{t}}} (\sigma_{t\bar{t}}(\uparrow\uparrow) + \sigma_{t\bar{t}}(\downarrow\downarrow) - \sigma_{t\bar{t}}(\uparrow\downarrow) - \sigma_{t\bar{t}}(\downarrow\uparrow)), \tag{3.71}$$

where $\sigma_{t\bar{t}}$ is the hadronic $t\bar{t}$ production cross section. The first arrow denotes the spin state of the top quark and the second arrow the spin state of the antitop quark. Thus Eq. (3.71) relates the expectation value $4\langle (\mathbf{S}_t \cdot \hat{\mathbf{a}}_1)(\mathbf{S}_{\bar{t}} \cdot \hat{\mathbf{a}}_2) \rangle$ with the production cross section of the polarized top-quark pairs.

Note, that it is of course also possible to project out the polarization coefficients \mathbf{B}^\pm using

$$\mathbf{B}^+ \cdot \hat{\mathbf{a}}_1 = \frac{1}{2} [|\mathcal{M}(\hat{\mathbf{a}}_1, 0)|^2 - |\mathcal{M}(-\hat{\mathbf{a}}_1, 0)|^2] \quad \text{and} \quad \mathbf{B}^- \cdot \hat{\mathbf{a}}_2 = \frac{1}{2} [|\mathcal{M}(0, \hat{\mathbf{a}}_2)|^2 - |\mathcal{M}(0, -\hat{\mathbf{a}}_2)|^2], \tag{3.72}$$

in order to calculate polarization related observables.

In the above considerations it has been explicitly shown that the spin dependent matrix element is in fact sufficient to calculate expectation values of operators. In the following it will be shown that the on-shell decay of the $t\bar{t}$ pair can be implemented via the spin dependent matrix element. In order to see this one has to compare the matrix element for $t\bar{t}$ production and decay, e.g. into leptons, Eq. (3.45)

$$\begin{aligned}
|\mathcal{M}(ab \rightarrow t\bar{t} \rightarrow b\bar{b}\ell^+\ell^-\nu\bar{\nu})|^2 &= 4G_t G_{\bar{t}} \frac{\pi^2}{(m_t \Gamma_t)^2} \delta(k_t^2 - m_t^2) \delta(k_{\bar{t}}^2 - m_{\bar{t}}^2) \\
&\times \left(A + \kappa_\ell \hat{\mathbf{q}}_{\ell^+} \cdot \mathbf{B}^+ - \kappa_\ell \hat{\mathbf{q}}_{\ell^-} \cdot \mathbf{B}^- - \kappa_\ell^2 C_{ij} q_{\ell^+}^i q_{\ell^-}^j \right) \tag{3.73}
\end{aligned}$$

with the spin dependent matrix element Eq. (3.57)

$$|\mathcal{M}(\hat{\mathbf{s}}_t, \hat{\mathbf{s}}_{\bar{t}})|^2 = A + \mathbf{B}^+ \cdot \hat{\mathbf{s}}_t + \mathbf{B}^- \cdot \hat{\mathbf{s}}_{\bar{t}} + C_{ij} \hat{s}_t^i \hat{s}_{\bar{t}}^j \tag{3.74}$$

from which the following relation can be derived

$$|\mathcal{M}(ab \rightarrow t\bar{t} \rightarrow b\bar{b}\ell^+\ell^-\nu\bar{\nu})|^2 = 4G_t G_{\bar{t}} \frac{\pi^2}{(m_t \Gamma_t)^2} \delta(k_t^2 - m_t^2) \delta(k_{\bar{t}}^2 - m_{\bar{t}}^2) |\mathcal{M}(\kappa_\ell \hat{\mathbf{q}}_{\ell^+}, -\kappa_\ell \hat{\mathbf{q}}_{\ell^-})|^2, \tag{3.75}$$

3.4. Spin dependent matrix element

where $\hat{\mathbf{q}}_{\ell^+}$ ($\hat{\mathbf{q}}_{\ell^-}$) is the direction of the momentum of the positively (negatively) charged lepton in the (anti)top-quark rest frame. k_t is the top-quark momentum with $k_t = k_b + q_{\ell^+} + k_\nu$ and $p_{\bar{t}}$ is the antitop-quark momentum with $p_{\bar{t}} = k_{\bar{b}} + q_{\ell^-} + k_{\bar{\nu}}$. This means the on-shell top-quark decay can be implemented through the spin dependent matrix element by setting

$$s_t = (0, \kappa_{\ell} \hat{\mathbf{q}}_{\ell^+})^T, \quad s_{\bar{t}} = (0, -\kappa_{\ell} \hat{\mathbf{q}}_{\ell^-})^T \quad (3.76)$$

in the top and antitop-quark rest frames or equivalently

$$s_t = \kappa_{\ell} \begin{pmatrix} \varkappa_t(\hat{\mathbf{k}} \cdot \hat{\mathbf{q}}_{\ell^+}) \\ \hat{\mathbf{q}}_{\ell^+} + \lambda_t(\hat{\mathbf{k}} \cdot \hat{\mathbf{q}}_{\ell^+})\hat{\mathbf{k}} \end{pmatrix}, \quad s_{\bar{t}} = -\kappa_{\ell} \begin{pmatrix} -\varkappa_t(\hat{\mathbf{k}} \cdot \hat{\mathbf{q}}_{\ell^-}) \\ \hat{\mathbf{q}}_{\ell^-} + \lambda_t(\hat{\mathbf{k}} \cdot \hat{\mathbf{q}}_{\ell^-})\hat{\mathbf{k}} \end{pmatrix} \quad (3.77)$$

in the $t\bar{t}$ rest frame and multiplying the matrix element with the respective functions on the rhs of Eq. (3.75).

In this section it was shown that the spin dependent matrix element has versatile applications. In particular, we have seen that spin dependent matrix elements provide a method for the numerical calculation of expectation values of spin operators. This is particularly useful when considering NLO corrections where the analytical expressions for the coefficient of the production density matrix are rather cumbersome. However, with respect to an analytical calculation there is the disadvantage of multiple matrix element evaluations per phase space point. This drawback can be partially compensated by separating the kinematical part from the spin dependent part such that only the spin dependent part has to be reevaluated, which saves computational time. Besides expectation values we have also seen how the spin dependent matrix element can be applied to generate the on-shell decay of the $t\bar{t}$ pair.

While the spin dependent matrix elements can be calculated as discussed in the beginning of this section it is also possible to obtain them using the so-called *spinor helicity formalism* (see e.g. Refs. [109, 110]). In this approach the massive spinor of top quark with momentum k_t can be constructed as a sum of two massless spinors with momenta p_1 and p_2 such that $k_t = p_1 + p_2$. The difference of the massless momenta is then the spin four-vector [109] $s_t = (p_1 - p_2)/m_t$ of the top quark. In the top-quark rest frame s_t is given by the reference axis $\hat{\mathbf{a}}_1$ as $s_t = (0, \hat{\mathbf{a}}_1)^T$. Analogous relations hold for the antitop quark.

Heavy Higgs effects in top-quark pair production at leading order in α_s

In this chapter the effects of heavy Higgs bosons on $t\bar{t}$ production at $\mathcal{O}(\alpha_s^2)$ (LO) in the QCD coupling constant α_s are discussed. First a precise account is given of the contributions that are considered for $t\bar{t}$ production. Furthermore, analytical results as well as a discussion of phenomenological aspects is presented. This chapter serves as a detailed introduction into the considered process of heavy Higgs boson production and decay into top-quark pairs discussing the most prominent phenomenological aspects and the observables used to study them.

Feynman diagrams considered at LO are displayed in Fig. 4.1. The diagrams in Fig. 4.1a represent the QCD contribution to $t\bar{t}$ production in the gluon fusion channel. The amplitude given by the sum of the Feynman diagrams in Fig. 4.1a is denoted by $\mathcal{A}_{\text{QCD}}^{gg,(0)}$. The diagram in Fig. 4.1b shows the QCD contribution in the quark annihilation channel and the respective amplitude is denoted by $\mathcal{A}_{\text{QCD}}^{q\bar{q},(0)}$. The diagrams in Fig. 4.1c represent the contribution from the heavy Higgs bosons to $t\bar{t}$ production in the gluon fusion channel. In this work the extended Higgs sector with new heavy Higgs bosons is provided by the 2HDM which features three neutral Higgs bosons ϕ_j , $j = 1, 2, 3$. One of which (ϕ_1) is assumed to be the Higgs discovered at the LHC [6,7] and the other two are the heavy Higgs bosons ϕ_2 and ϕ_3 . Since we assume the additional charged Higgs boson as very heavy in all phenomenological studies presented in this work (also at NLO) it plays effectively no role. Each of the heavy neutral Higgs bosons gives

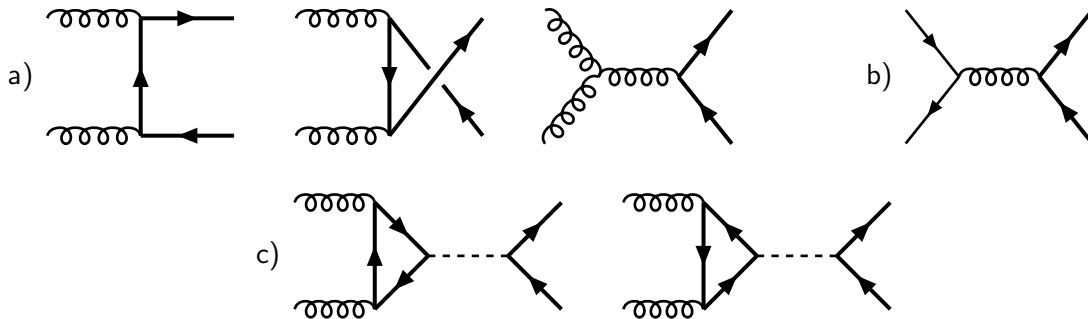


Figure 4.1.: Feynman diagrams for $t\bar{t}$ production at leading order. a) QCD contribution to the gluon fusion channel, b) quark annihilation channel, c) heavy Higgs contribution to the gluon fusion channel.

4. Heavy Higgs effects in top-quark pair production at leading order in α_s

a contribution as displayed in Fig. 4.1c. The corresponding amplitudes are denoted by $\mathcal{A}_{\phi_j}^{gg,(0)}$ with $j = 2, 3$. In case of the quark-antiquark channel there is no contribution from (heavy) Higgs bosons when setting the couplings to light quarks to zero and neglecting the coupling to the bottom quark. Hence, at LO the quark-antiquark channel is not sensitive to the heavy Higgs bosons. From this point on we will drop the superscript gg and refer exclusively to the gg channel if not stated otherwise. For the gluon fusion channel the full amplitude squared is denoted by $|\mathcal{M}^{(0)}|^2$. From here on \mathcal{M} always includes the average over spin and color degrees of freedom (dof) of the initial state particles and summation over color dof of the final state particles. $|\mathcal{M}^{(0)}|^2$ can be decomposed into

$$|\mathcal{M}^{(0)}|^2 = |\mathcal{M}_{\text{QCD}}^{(0)}|^2 + \mathcal{M}_{\phi, \text{QCD}}^{(0)} + |\mathcal{M}_{\phi}^{(0)}|^2 \quad (4.1)$$

where

$$\begin{aligned} |\mathcal{M}_{\text{QCD}}^{(0)}|^2 &= \frac{1}{N_{gg}} \sum_{\text{spin, col.}} \mathcal{A}_{\text{QCD}}^{(0)} (\mathcal{A}_{\text{QCD}}^{(0)})^*, \\ \mathcal{M}_{\phi, \text{QCD}}^{(0)} &= \sum_{j=2,3} \mathcal{M}_{\phi_j, \text{QCD}}^{(0)}, & \mathcal{M}_{\phi_j, \text{QCD}}^{(0)} &= \frac{1}{N_{gg}} \sum_{\text{spin, col.}} 2\text{Re} \left[\mathcal{A}_{\phi_j}^{(0)} (\mathcal{A}_{\text{QCD}}^{(0)})^* \right], \\ |\mathcal{M}_{\phi}^{(0)}|^2 &= \sum_{j=2,3} |\mathcal{M}_{\phi_j}^{(0)}|^2 + \mathcal{M}_{\phi_{2,3}}^{(0)}, \\ |\mathcal{M}_{\phi_j}^{(0)}|^2 &= \frac{1}{N_{gg}} \sum_{\text{spin, col.}} \mathcal{A}_{\phi_j}^{(0)} (\mathcal{A}_{\phi_j}^{(0)})^*, & \mathcal{M}_{\phi_{2,3}}^{(0)} &= \frac{1}{N_{gg}} \sum_{\text{spin, col.}} 2\text{Re} \left[\mathcal{A}_{\phi_2}^{(0)} (\mathcal{A}_{\phi_3}^{(0)})^* \right], \end{aligned} \quad (4.2)$$

where $N_{gg} = 4(N_c^2 - 1)^2$. The matrix element $|\mathcal{M}_{\text{QCD}}^{(0)}|^2$ denotes the pure QCD contribution to $t\bar{t}$ production at LO. In this work terms in the matrix element that are of $\mathcal{O}(\alpha_s^n y_t^4)$ are called the *signal amplitude squared* (at LO: $|\mathcal{M}_{\phi}^{(0)}|^2$), where α_s is the coupling constant of the strong force and y_t is the top-quark Yukawa coupling. Terms in the matrix element that are of $\mathcal{O}(\alpha_s^n y_t^2)$ are called *Higgs-QCD interference* or *signal-background interference* (at LO: $\mathcal{M}_{\phi, \text{QCD}}^{(0)}$).

Making α_s and y_t explicit Eq. (4.1) reads

$$|\mathcal{M}^{(0)}|^2 = \alpha_s^2 (|\mathcal{M}_{\text{QCD}}^{(0)'}|^2 + y_t^2 \mathcal{M}_{\phi, \text{QCD}}^{(0)'} + y_t^4 |\mathcal{M}_{\phi}^{(0)'}|^2), \quad (4.3)$$

where the prime denotes the matrix elements with coupling constants removed. In fact there are more contributions to the second and third term in Eq. (4.3) than shown in Fig. 4.1c. The second term receives contribution from the interference of the QCD tree level amplitude displayed in Fig. 4.1a and Yukawa corrections to $t\bar{t}$ production of the type shown exemplary in Fig. 4.2. However, the focus of this work is on the *resonant* production of spin-0 bosons and their decay into top-quark pairs. In the resonant region the four-momentum squared of the Higgs boson propagator is close to the Higgs boson's mass. The contributions shown in Fig. 4.2 are nonresonant and are therefore negligible in the resonance region. The third term in Eq. (4.3) receives also contributions from the interference of the amplitudes shown in Fig. 4.1c and Fig. 4.2 as well as contributions from the interference of the amplitudes in Fig. 4.1a and those of Fig. 4.3. However, these contributions are suppressed by an extra loop factor of $1/(16\pi^2)$ and are therefore not considered at LO in the QCD coupling constant. Furthermore Yukawa corrections to the quark annihilation channel which contribute to $\mathcal{O}(\alpha_s^2 y_t^2)$ and $\mathcal{O}(\alpha_s^2 y_t^4)$ are negligible in the resonance region and are not taken into account.

As indicated in Eq. (4.2) for the amplitude in Fig. 4.1c only the contributions from the heavy Higgs bosons ϕ_2, ϕ_3 are considered. The contribution from the SM-like Higgs boson is attributed to the weak corrections to $t\bar{t}$ production and is included using existing results from the literature [111–113] when the NLO corrections are studied in Chap. 5. Since the SM Higgs

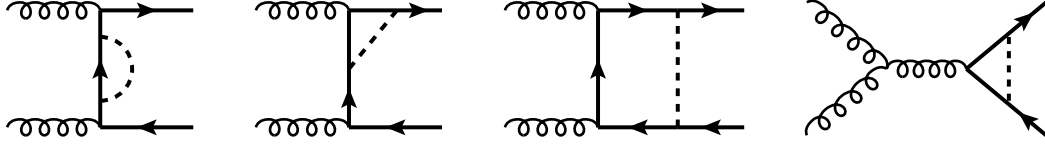


Figure 4.2.: Sample Feynman diagrams for the nonresonant heavy Higgs contributions to the gluon fusion channel of $t\bar{t}$ production.

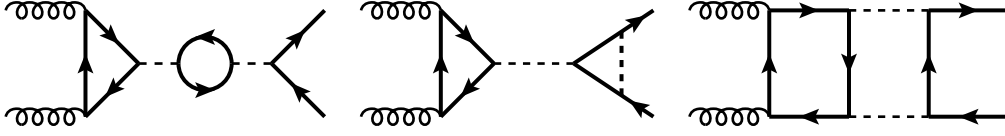


Figure 4.3.: Sample Feynman diagrams for the two-loop corrections to $t\bar{t}$ production involving two heavy Higgs propagators.

boson mass $m_h = m_{\phi_1} = 125\text{GeV} < 2m_t$ the impact of the light Higgs boson is small¹ and does not matter from a phenomenological point of view. Hence, the SM Higgs boson's contribution to the amplitude shown in Fig. 4.1c is neglected in this chapter and is only included when we discuss the NLO corrections in Chap. 5.

4.1. Analytic results

Having defined $t\bar{t}$ production including QCD and Higgs contributions at LO this section presents the analytical results for the matrix elements defined in Eq. (4.2). Since top-quark spin effects such as polarization and correlation may provide an enhanced sensitivity to new physics effects the full spin information of the matrix elements is taken into account. To allow an easy interpretation we use the production density matrix formalism introduced in Sec. 3.2.

The matrix element squared of the Higgs boson contributions in Fig. 4.1c is comprised of two components: The contribution of each heavy Higgs boson ϕ_j squared $|\mathcal{M}_{\phi_j}^{(0)}|^2$ is given by

$$|\mathcal{M}_{\phi_j}^{(0)}(\hat{\mathbf{s}}_t, \hat{\mathbf{s}}_{\bar{t}})|^2 = A_{\phi_j} + \mathbf{B}_{\phi_j}^+ \cdot \hat{\mathbf{s}}_t + \mathbf{B}_{\phi_j}^- \cdot \hat{\mathbf{s}}_{\bar{t}} + C_{\phi_j}^{mn} \hat{s}_t^m \hat{s}_{\bar{t}}^n, \quad (4.4)$$

where

$$N_{\phi_j} = \frac{m_t^2 s^3}{2C_{FV}^2} G_{jj}, \quad (4.5)$$

$$A_{\phi_j} = N_{\phi_j} (a_{tj}^2 \beta_t^2 + b_{tj}^2), \quad (4.6)$$

$$b_{\phi_j,1}^\pm = b_{\phi_j,2}^\pm = b_{\phi_j,3}^\pm = 0, \quad (4.7)$$

$$c_{\phi_j,0} = N_{\phi_j} (a_{tj}^2 \beta_t^2 - b_{tj}^2), \quad (4.8)$$

$$c_{\phi_j,2} = 2N_{\phi_j} \beta_t a_{tj} b_{tj}, \quad (4.9)$$

$$c_{\phi_j,5} = -2N_{\phi_j} \beta_t^2 a_{tj}^2, \quad (4.10)$$

$$c_{\phi_j,1,3,4,6,7,8} = 0. \quad (4.11)$$

¹The SM Higgs boson is far off-shell.

4. Heavy Higgs effects in top-quark pair production at leading order in α_s

with

$$G_{ij} = \widetilde{F}_i^S (\widetilde{F}_j^S)^* + 4\widetilde{F}_i^P (\widetilde{F}_j^P)^* , \quad (4.12)$$

$$\widetilde{F}_j^{S,P} = \frac{F_j^{S,P}}{s - m_{\phi_j}^2 + i\Gamma_{\phi_j} m_{\phi_j}} . \quad (4.13)$$

The form factors $F_i^S = F_i^S(\tau)$ and $F_i^P = F_i^P(\tau)$ are defined in Eqs. (2.122)–(2.124). However, contrary to Eq. (2.124) τ is defined here as

$$\tau = 1 - \beta_t^2 = \frac{4m_t^2}{s} . \quad (4.14)$$

The definition of the reduced Yukawa couplings a_{tj} and b_{tj} is given in Eq. (2.75). The contribution from the interference between the Higgs bosons $\mathcal{M}_{\phi_{2,3}}^{(0)}$ is given by

$$\mathcal{M}_{\phi_{2,3}}^{(0)}(\hat{\mathbf{s}}_t, \hat{\mathbf{s}}_{\bar{t}}) = A_{\phi_{2,3}} + \mathbf{B}_{\phi_{2,3}}^+ \cdot \hat{\mathbf{s}}_t + \mathbf{B}_{\phi_{2,3}}^- \cdot \hat{\mathbf{s}}_{\bar{t}} + C_{\phi_{2,3}}^{mn} \hat{s}_t^m \hat{s}_{\bar{t}}^n , \quad (4.15)$$

where

$$N_{\phi_{2,3}} = \frac{m_t^2 s^3}{2C_F v^2} , \quad (4.16)$$

$$A_{\phi_{2,3}} = 2N_{\phi_{2,3}} (a_{t2} a_{t3} \beta_t^2 + b_{t2} b_{t3}) \text{Re}[G_{23}] , \quad (4.17)$$

$$b_{\phi_{2,3},2}^\pm = \mp 2N_{\phi_{2,3}} \beta_t (a_{t2} b_{t3} - a_{t3} b_{t2}) \text{Im}[G_{23}] , \quad (4.18)$$

$$b_{\phi_{2,3},1}^\pm = b_{\phi_{2,3},3}^\pm = 0 , \quad (4.19)$$

$$c_{\phi_{2,3},0} = 2N_{\phi_{2,3}} (a_{t2} a_{t3} \beta_t^2 - b_{t2} b_{t3}) \text{Re}[G_{23}] , \quad (4.20)$$

$$c_{\phi_{2,3},2} = N_{\phi_{2,3}} (a_{t2} b_{t3} + a_{t3} b_{t2}) \text{Re}[G_{23}] , \quad (4.21)$$

$$c_{\phi_{2,3},5} = -4N_{\phi_{2,3}} \beta_t^2 a_{t2} a_{t3} \text{Re}[G_{23}] , \quad (4.22)$$

$$c_{\phi_{2,3},1,3,4,6,7,8} = 0 . \quad (4.23)$$

Equations (4.17)–(4.23) show that the interference of the two Higgs bosons is only nonzero in the CP violating case. In this case the neutral Higgs bosons mass eigenstates are mixtures of scalar *and* pseudoscalar components. In Eqs. (4.17)–(4.23) the reduced Yukawa couplings occur in the combination $a_{t2} a_{t3}$ and $b_{t2} b_{t3}$ either directly or through the form factor term G_{23} . If both scalars are CP eigenstates (i.e. in the CP conserving case) these products of Yukawa couplings vanish and there is no interference between the Higgs bosons.

In Ref. [107] the properties of the production density matrix coefficients b_1, \dots, b_3 and c_0, \dots, c_8 under discrete symmetry transformations have been investigated in detail. For convenience Tab 1 in Ref. [107] which lists the transformation properties of the coefficients is reproduced in Appendix D in Tab. D.1. Bose symmetry of the initial gg state, for example, determines if the coefficients are even or odd functions of z . For the exchange of a spin-0 boson the matrix element does not depend on z . Hence all coefficients that are odd functions of z must vanish: $b_1, b_3, c_1, c_3, c_6, c_8 = 0$. This can immediately be verified from Eqs. (4.6)–(4.11) and Eqs. (4.17)–(4.23). In Appendix D we give some further details of the transformation properties of b_2^\pm , which are related to top and antitop-quark polarization, and argue why this coefficients vanish in $|\mathcal{M}_{\phi_j}^{(0)}|^2$ but are nonzero in $\mathcal{M}_{\phi_{2,3}}^{(0)}$. The contribution from the Higgs-Higgs interference ($\mathcal{M}_{\phi_{2,3}}^{(0)}$) can, therefore, contribute to the polarization of top and antitop quarks already at LO.

The matrix element representing the interference between the Higgs amplitude (Fig. 4.1b) and the QCD amplitude (Fig. 4.1a) is given by

$$\mathcal{M}_{\phi_j, \text{QCD}}^{(0)}(\hat{\mathbf{s}}_t, \hat{\mathbf{s}}_{\bar{t}}) = A_{\text{int},j} + \mathbf{B}_{\text{int},j}^+ \cdot \hat{\mathbf{s}}_t + \mathbf{B}_{\text{int},j}^- \cdot \hat{\mathbf{s}}_{\bar{t}} + C_{\text{int},j}^{mn} \hat{s}_t^m \hat{s}_{\bar{t}}^n, \quad (4.24)$$

where

$$N_{\text{int}} = -\frac{g_s^2 m_t^2}{C_A C_F v (1 - \beta_t^2 z^2)}, \quad (4.25)$$

$$A_{\text{int},j} = N_{\text{int}} s (a_{tj} \beta_t^2 \text{Re}[\tilde{F}_j^S] - 2b_{tj} \text{Re}[\tilde{F}_j^P]), \quad (4.26)$$

$$b_{\text{int},2j}^\pm = \mp N_{\text{int}} s \beta_t (2a_{tj} \text{Im}[\tilde{F}_j^P] + b_{tj} \text{Im}[\tilde{F}_j^S]), \quad (4.27)$$

$$b_{\text{int},1j}^\pm = b_{\text{int},3j}^\pm = 0, \quad (4.28)$$

$$c_{\text{int},0j} = N_{\text{int}} s (a_{tj} \beta_t^2 \text{Re}[\tilde{F}_j^S] + 2b_{tj} \text{Re}[\tilde{F}_j^P]), \quad (4.29)$$

$$c_{\text{int},2j} = -N_{\text{int}} s \beta_t (2a_{tj} \text{Re}[\tilde{F}_j^P] - b_{tj} \text{Re}[\tilde{F}_j^S]), \quad (4.30)$$

$$c_{\text{int},5j} = -2N_{\text{int}} s \beta_t^2 a_{tj} \text{Re}[\tilde{F}_j^S], \quad (4.31)$$

$$c_{\text{int},1,3,4,6,7,8j} = 0. \quad (4.32)$$

Regarding the coefficients $b_{\text{int},2j}^\pm$ only the CP -odd part $b_{\text{int},2j}^{CP\text{-odd}} = 1/2(b_{\text{int},2j}^+ - b_{\text{int},2j}^-)$ is nonzero and is proportional to the imaginary part of \tilde{F}_j^S and \tilde{F}_j^P . This is similar to the case of $b_{\phi_{2,3,2}}^\pm$ which is explained in detail in Appendix D. In the case of CP conservation the contributions $b_{\text{int},2j}^\pm$ vanish. This can also be seen from the structure of the reduced Yukawa couplings which occur in the combination $a_{tj} b_{tj}$ in $b_{\text{int},2j}^\pm$ in Eq. (4.27). In the case where the Higgs boson mass eigenstates are CP eigenstates $a_{tj} b_{tj} = 0$ such that $b_{\text{int},2j}^\pm$ vanish.

Hence, if CP is violated in the Higgs sector longitudinal polarization of the top and antitop quark is already generated at LO through interference among the heavy Higgs bosons ($b_{\phi_{2,3}}^{CP\text{-odd}}$) and interference between the QCD and heavy Higgs contributions ($b_{\text{int},2j}^{CP\text{-odd}}$). This is particularly interesting because the (anti)top-quark polarization is zero at LO in the SM. Therefore, we expect an enhanced sensitivity to the effects of CPV heavy Higgs boson contributions to $t\bar{t}$ production when studying observables that are sensitive to (anti)top-quark polarization. Additionally, in the following section we also study observables that are sensitive to $t\bar{t}$ spin correlations.

4.2. Phenomenology

In this section some phenomenological aspect of heavy Higgs boson production and decay to $t\bar{t}$ in the 2HDM based on the LO results are discussed. We start with the $t\bar{t}$ invariant mass distribution to establish some basic features of this process. We investigate the contribution of the Higgs-Higgs interference to the cross section in CP violating scenarios to answer the question whether these interference effects are phenomenologically relevant. A large part of this section is dedicated to spin dependent observables. We discuss (anti)top-quark spin polarization and determine an estimate of the maximal size of the polarization in CP violating 2HDM scenarios. Spin correlations between top and antitop are investigated as well and we define an observable with maximal sensitivity to the effects of heavy Higgs bosons on $t\bar{t}$ spin correlations.

4. Heavy Higgs effects in top-quark pair production at leading order in α_s

4.2.1. Top-antitop invariant mass distribution

The differential cross section $d\sigma/dM_{t\bar{t}}$ also called the $t\bar{t}$ invariant mass distribution is a priori a useful observable to study resonances decaying into $t\bar{t}$ pairs. $M_{t\bar{t}}$ is defined as

$$M_{t\bar{t}} = \sqrt{(k_t + k_{\bar{t}})^2}, \quad (4.33)$$

where k_t and $k_{\bar{t}}$ are the four-momenta of the top and antitop quark. As can be seen from the Feynman diagrams in Fig. 4.1c the 2HDM contribution to $t\bar{t}$ production is an s -channel process such that the heavy Higgs bosons with $m_{2,3} > 2m_t$ should be visible as resonances in the $M_{t\bar{t}}$ distribution. However, the interference of the amplitudes in Fig. 4.1a and Fig. 4.1c distorts the usual peak of the resonance leading, for example, to a peak dip structure. In the following this is illustrated by two example scenarios:

$$\begin{aligned} \alpha_1 &= \beta, & \alpha_2 &= 0, & \alpha_3 &= 0, & \tan\beta &= 1, \\ m_1 &= 125\text{GeV}, & m_{H^+} &= 1050\text{GeV}, & \eta &= 0, & v &= 246\text{GeV} \end{aligned} \quad (4.34)$$

$$\text{scenario 1: } \quad m_2 = m_H = 500\text{GeV}, \quad m_3 = m_A = 550\text{GeV} \quad (4.35)$$

$$\text{scenario 2: } \quad m_2 = m_H = 500\text{GeV}, \quad m_3 = m_A = 800\text{GeV} \quad (4.36)$$

The parameter set in Eq. (4.34) is common for both scenarios which live in the CP conserving alignment limit of the 2HDM. The difference between both scenarios is the choice of heavy Higgs boson masses. While scenario 1 features a small mass difference $\Delta m = m_3 - m_2 = 50\text{GeV}$ in scenario 2 the masses are well-separated ($\Delta m = 300\text{GeV}$).

The $M_{t\bar{t}}$ distributions for scenario 1 and 2 are displayed in Figs. 4.4 and 4.5. They have been generated for $\sqrt{S_{\text{had}}} = 13\text{TeV}$ using the PDF set CT10n1o [100]. The upper plots show in black the $M_{t\bar{t}}$ distribution for QCD and the sum of QCD and 2HDM contributions in red. Furthermore, the residual scale dependence of the $M_{t\bar{t}}$ distribution is shown as blue band where μ_R and μ_F have been varied simultaneously by a factor of two around the central value $\mu_R = \mu_F = \mu_0 = (m_2 + m_3)/4$. The inlay plot in Fig. 4.5 represents a detailed view of the resonance region of ϕ_3 with $m_3 = 800\text{GeV}$. The signal-to-background ratio (S/B) is displayed in the center plots of Figs. 4.4 and 4.5. Instead of a resonance peak the 2HDM contribution generates for example a peak-dip structure in the $M_{t\bar{t}}$ spectrum which is due to the interference with the QCD background. This is illustrated in the lower plots of Figs 4.4 and 4.5 where the green distribution shows the contribution from the heavy Higgs amplitudes squared and the blue histogram represents the contribution from the interference between the heavy Higgs amplitude and the nonresonant QCD background. The scale uncertainty due to renormalization scale μ_R cancels completely in the ratio (at LO). The remaining uncertainty due to μ_F is so small that it is not visible in the plots. The bin widths in both figures are 10GeV which are chosen for illustrative purposes. The experimental minimum bin width is more likely about 40GeV (see e.g. [114,115]) for the low-mass range of the $t\bar{t}$ invariant mass distribution. The following conclusions can be drawn from Figs. 4.4 and 4.5:

1. The Higgs-QCD interference is of the same order of magnitude as the contribution from the Higgs amplitude squared and can therefore not be neglected. It changes the shape of the $M_{t\bar{t}}$ distribution significantly and distorts the resonance peak. In the case of scenario 2 the contribution from ϕ_3 even generates a dip instead of a peak. The kind of distortion is not unique and different possibilities depending on the choice of parameters have been investigated for example in Ref. [116].

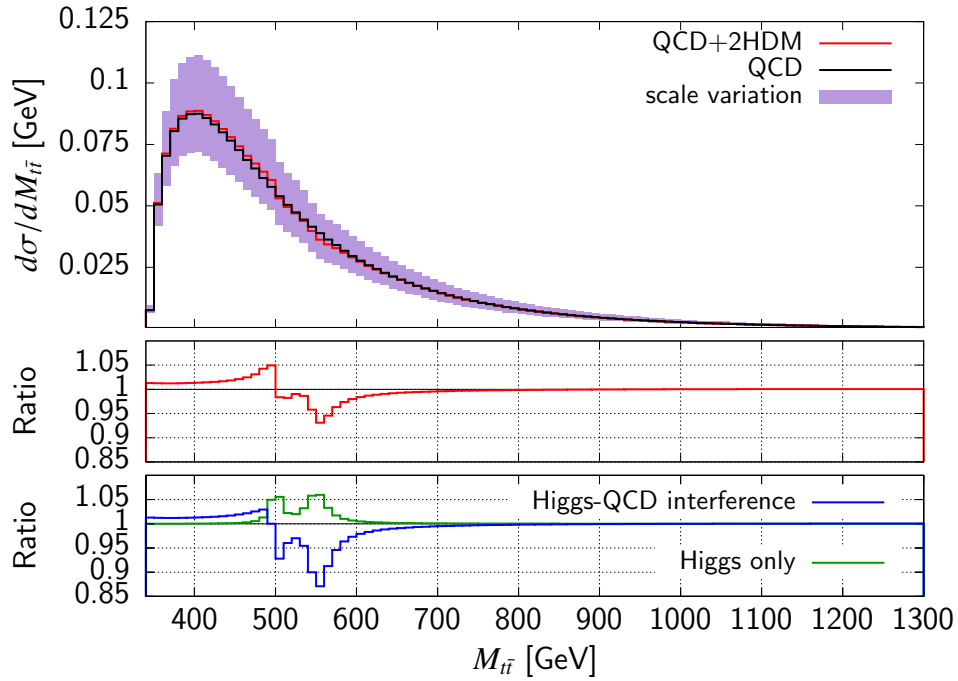


Figure 4.4.: $M_{i\bar{i}}$ distribution of scenario 1 at LO for $\sqrt{s}_{\text{had}} = 13\text{TeV}$. The upper plot shows the $M_{i\bar{i}}$ distribution for QCD only (black) and QCD+2HDM (red) as well as the scale uncertainty. The center plot displays the ratio (QCD+2HDM)/QCD and the lower plot shows the two contributions to this ratio.

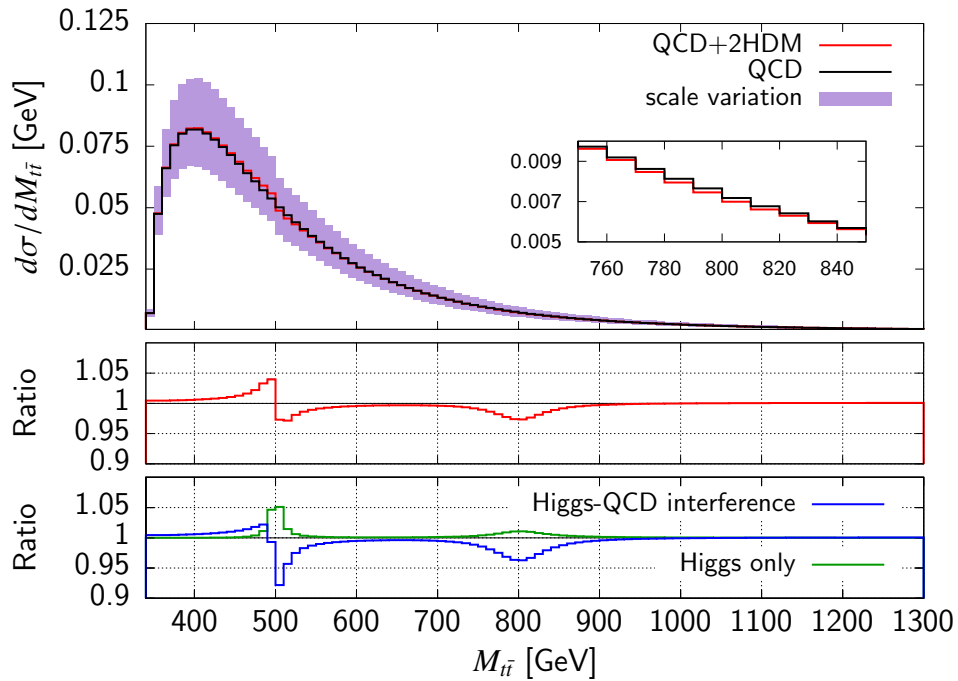


Figure 4.5.: Same as Fig. 4.4 but for scenario 2. The inlay plot displays a detailed view of the resonance region of ϕ_3 .

4. Heavy Higgs effects in top-quark pair production at leading order in α_s

2. The dominant contribution from heavy Higgs bosons is localized to approximately

$$m_{2,3} - 100\text{GeV} \leq M_{t\bar{t}} \leq m_{2,3} + 100\text{GeV}. \quad (4.37)$$

Outside this resonance region the contribution from the 2HDM to $t\bar{t}$ production is very small.

These are two important aspects of this process that will guide the NLO calculations in the next chapter. Figures 4.4 and 4.5 also show that it is in principle possible to detect heavy Higgs bosons by measuring the $M_{t\bar{t}}$ distribution. However, when using more realistic bin widths the S/B is reduced such that it becomes harder to detect the resonance in the $M_{t\bar{t}}$ spectrum. Furthermore, the larger the Higgs mass and the larger the mass separation Δm the smaller the S/B as can be seen when comparing Fig. 4.4 (scenario 1) with Fig. 4.5 (scenario 2).

4.2.2. Higgs-Higgs interference effects

In this subsection we consider the interference of the two heavy Higgs bosons in the CP violating case and study the size of the spin independent contribution in Eq. (4.17)

$$A_{\phi_{2,3}} = 2N_{\phi_{2,3}} (a_{t2}a_{t3}\beta_t^2 + b_{t2}b_{t3}) \text{Re}[G_{23}]. \quad (4.38)$$

In particular, we shall address the question how large the Higgs-Higgs interference can get given the experimental constraints on the mixing angles α_i , $i = 1, 2, 3$. The term $A_{\phi_{2,3}}$ is dominated by $\text{Re}[G_{23}]$ which contains the product of the propagator of ϕ_2 and the complex conjugate of the Propagator of ϕ_3 . Therefore $\text{Re}[G_{2,3}]$ has a ‘‘double Breit-Wigner’’-like form

$$\text{Re}[G_{2,3}] \sim \frac{1}{\left[(s - m_2^2)^2 + m_2^2\Gamma_2^2\right] \left[(s - m_3^2)^2 + m_3^2\Gamma_3^2\right]} \quad (4.39)$$

which completely dominates the functional dependence of $\text{Re}[G_{2,3}]$ on s . Hence, the largest possible interference between the heavy neutral Higgs bosons for a given set of mixing angles and $\tan\beta$ occurs when their masses are degenerate $m_2 = m_3$. If the masses are not equal the Breit-Wigner peak of one of the propagators is suppressed by the Breit-Wigner tail of the other propagator and vice versa. In order to assess the maximal possible Higgs-Higgs interference the mass degenerate case is assumed. The model parameters that are kept fixed are given by

$$\begin{aligned} m_1 &= 125\text{GeV}, & m_{H^+} &= 1050\text{GeV}, & \eta &= 0, & v &= 246\text{GeV}, \\ \text{Re}(\lambda_6) &= 0, & \lambda_7 &= 0. \end{aligned} \quad (4.40)$$

Since $\alpha_1, \alpha_2, \alpha_3$ are varied in the following study we include parameter regions with a CPV Higgs potential. In order to keep the parameters $m_1, m_2, m_3, \alpha_1, \alpha_2, \alpha_3, \tan\beta$ independent of each other (cf. Sec. 2.4) we do not enforce softly broken Z_2 symmetry ($\lambda_6 = \lambda_7 = 0$). Instead, $\text{Im}(\lambda_6) \neq 0$ for the choice in Eq. (4.40) and can be calculated from the other parameters (cf. Eq. (2.37)). Experimental limits on $\alpha_1, \alpha_2, \alpha_3, \tan\beta$ have been derived and summarized for example in Ref. [117]. The limits are given for specific values of Higgs boson masses ($m_2 = 400\text{GeV}$, $m_3 = 450\text{GeV}$ and $m_2 = 550\text{GeV}$, $m_3 = 600\text{GeV}$). The allowed parameter space depends on the masses of the neutral Higgs bosons but for simplicity here only one set of constraints is used for the whole mass range $m_2, m_3 \in [400, 1000]\text{GeV}$:

$$\beta - 0.1 \leq \alpha_1 \leq \beta + 0.1, \quad -0.05 \leq \alpha_2 \leq 0.05, \quad -\frac{\pi}{2} \leq \alpha_3 \leq \frac{\pi}{2} \quad (4.41)$$

which is compatible with the limits given for the two mentioned mass sets at $\tan\beta = 1$. For $\tan\beta = \{0.7, 1.5\}$ the limit on α_2 is tighter: $|\alpha_2| \leq \{0.025, 0.01\}$. Since the neutral heavy Higgs

interference term $A_{\phi_{2,3}}$ has a Breit-Wigner structure as discussed above its maximum value is reached for $s = m_\phi = m_2 = m_3$. Hence, we evaluate the partonic cross section for the interference between the two heavy Higgs bosons

$$\sigma_{\text{int}}(s) = \frac{\beta_t}{4\pi s} A_{\phi_{2,3}}(s) \quad (4.42)$$

at $s = m_\phi$ and compare to the contribution from ϕ_2 and ϕ_3 only

$$\sigma_j(s) = \frac{\beta_t}{4\pi s} A_{\phi_j}(s), \quad j = 2, 3. \quad (4.43)$$

Specifically, we consider the ratio

$$\mathcal{R}_{\text{int}}(m_\phi) = \max \left\{ \frac{\sigma_{\text{int}}(m_\phi)}{\max[\sigma_2(m_\phi), \sigma_3(m_\phi)]} \right\} = \max \{ \min[\mathcal{R}_2, \mathcal{R}_3] \} \quad (4.44)$$

with $\mathcal{R}_2 = \sigma_{\text{int}}/\sigma_2$ and $\mathcal{R}_3 = \sigma_{\text{int}}/\sigma_3$. This ratio provides a kind of upper limit on the size of the interference contribution with respect to the largest contribution from each individual heavy Higgs boson.² For example, if $\mathcal{R}_{\text{int}} = 1$ and $\sigma_2 > \sigma_3$ then the interference contribution is as large as σ_2 . By determining this ratio we try to answer the question whether this interference effect can in general be neglected with respect to the single Higgs contributions. \mathcal{R}_{int} is evaluated for a $10 \times 10 \times 10$ grid of $\alpha_1, \alpha_2, \alpha_3$ in the range specified in Eq. (4.41). For each grid point the decay widths of the heavy Higgs bosons have to be calculated since they also depend on the mixing angles (see Sec. 2.6). This effect can not be neglected so it is not possible to use one constant width for each Higgs boson for the entire grid. Once a configuration of mixing angles $\alpha_1^{\text{max}}, \alpha_2^{\text{max}}, \alpha_3^{\text{max}}$ that maximizes the ratio \mathcal{R}_{int} is found α_3^{max} is varied again within $\alpha_3^{\text{max}} - \pi/10 \leq \alpha_3 \leq \alpha_3^{\text{max}} + \pi/10$ with 100 steps to obtain a more accurate result³ for the ratio \mathcal{R}_{int} . This procedure is repeated for each value of m_ϕ . The result is shown in Fig. 4.6 for different values of $\tan\beta$. The dash-dotted curve in Fig. 4.6 represents \mathcal{R}_{int} in the alignment limit and is independent of the choice of $\tan\beta$. The reason for this is the following: In the alignment limit ($\alpha_1 = \beta, \alpha_2 = 0$) and at the resonance ($s = m_\phi^2$) \mathcal{R}_2 and \mathcal{R}_3 take a simple form

$$\mathcal{R}_2 = \frac{\sin^2(2\alpha_3)}{2(w_1 + \sin^2(\alpha_3))(w_2 + \sin^2(\alpha_3))} \frac{\Gamma_{\phi_2}(\alpha_3, \beta)}{\Gamma_{\phi_3}(\alpha_3, \beta)}, \quad (4.45)$$

$$\mathcal{R}_3 = \frac{\sin^2(2\alpha_3)}{2(w_1 + \cos^2(\alpha_3))(w_2 + \cos^2(\alpha_3))} \frac{\Gamma_{\phi_3}(\alpha_3, \beta)}{\Gamma_{\phi_2}(\alpha_3, \beta)}, \quad (4.46)$$

where w_1 and w_2 in general depend on s . For $s = m_\phi^2$

$$w_1 = \frac{\beta_t^2}{1 - \beta_t^2}, \quad w_2 = \frac{|\hat{F}_S|^2}{4|\hat{F}_P|^2 - |\hat{F}_S|^2}. \quad (4.47)$$

The form factors \hat{F}_S and \hat{F}_P are independent of the 2HDM model parameters and are defined by

$$F_j^S = a_{tj} \hat{F}_S \quad \text{and} \quad F_j^P = b_{tj} \hat{F}_P, \quad (4.48)$$

²When maximizing only \mathcal{R}_2 one ends up with configurations where $\sigma_{\text{int}}(m_\phi) \sim \sigma_2(m_\phi)$ but $\sigma_{\text{int}}(m_\phi), \sigma_2(m_\phi) \ll \sigma_3(m_\phi)$. Then the interference effect would still be small and could be neglected. However, to be consistent in these cases also the σ_2 contribution should as well be neglected. Analogous statements hold for the case when only \mathcal{R}_3 is maximized.

³In principle a fine scan in α_1 and α_2 could also be performed but it has been checked that the fine scan in α_3 is sufficient.

4. Heavy Higgs effects in top-quark pair production at leading order in α_s

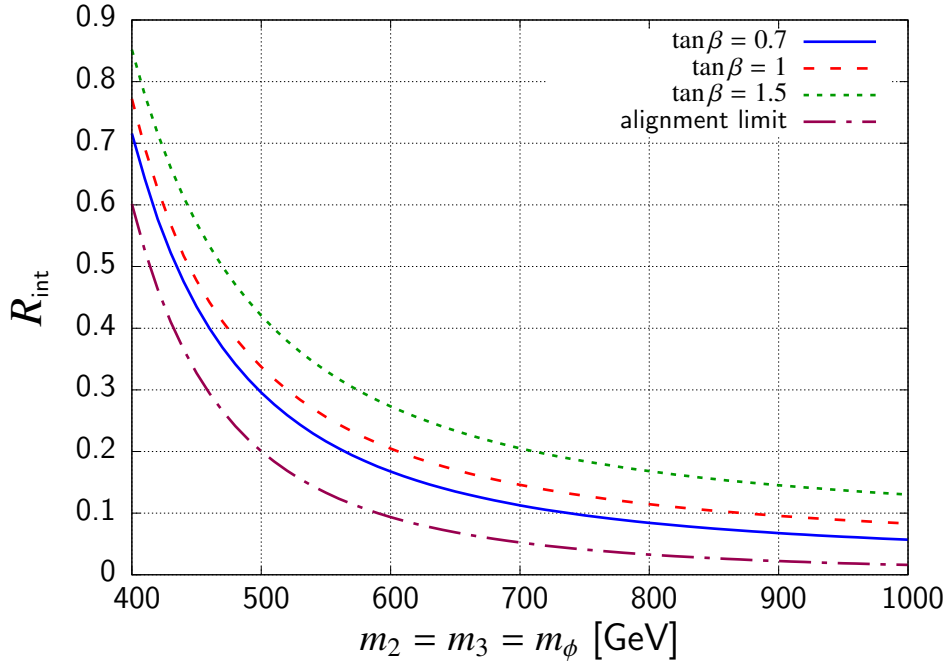


Figure 4.6.: Maximal relative contribution \mathcal{R}_{int} of the Higgs-Higgs interference with respect to the single Higgs contribution to the $t\bar{t}$ cross section as a function of the heavy Higgs masses $m_\phi = m_2 = m_3$.

where F_j^S and F_j^P are defined in Eq. (2.122) and Eq. (2.123), respectively. As can be seen from Eqs. (4.45) and (4.46) the dependence of \mathcal{R}_2 and \mathcal{R}_3 on β enters only via the decay widths. However, in the alignment limit $\min(\mathcal{R}_2, \mathcal{R}_3)$ is maximal for $\alpha_3 = \pi/4$ where $\Gamma_{\phi_2} = \Gamma_{\phi_3}$ because $|a_{t2}| = |a_{t3}| = |b_{t2}| = |b_{t3}|$ and the couplings to W and Z as well as to hh are zero in the alignment limit. Hence, for $\alpha_3 = \pi/4$ the decay widths cancel and the dependence on β drops out such that \mathcal{R}_{int} in the alignment limit (dash-dotted curve in Fig. 4.6) is independent of $\tan\beta$.

Figure 4.6 shows that the Higgs-Higgs interference can not be neglected in general because there are combinations of mixing angles that can lead to sizable effects especially in the low-mass region. In the alignment limit the maximal interference effects drop below 10% already at $m_\phi = 600\text{GeV}$ whereas if all mixing angles are allowed to vary in the range specified in Eq. (4.41) the interference effects are still larger than 10% for $m_\phi = 1\text{TeV}$ and $\tan\beta = 1.5$. As an example Fig. 4.7 shows the partonic cross sections σ_{int} , σ_2 and σ_3 for configurations where $\min(\mathcal{R}_2, \mathcal{R}_3)$ is maximal for $m_\phi = 500\text{GeV}, 700\text{GeV}, 900\text{GeV}$ and $\tan\beta = 1$. Maximizing the relative contribution of the interference with respect to the single Higgs contribution leads to configurations where the contribution from ϕ_2 is approximately as large as the contribution from ϕ_3 such that $\mathcal{R}_2 \approx \mathcal{R}_3$.

Note that the result in Fig. 4.6 is only an upper limit. For $m_2 \neq m_3$ the interference effects are strongly reduced depending on how large the mass separation is. Furthermore, \mathcal{R}_{int} should be seen as an estimate of the largest interference effects because to determine the exact interference strength with respect to the single Higgs contributions the hadronic cross section is needed. However, the peak behaviour of $\sigma_{\text{int}}(s)$, $\sigma_2(s)$ and $\sigma_3(s)$ at $s = m_\phi^2$ filters out the resonance region in the convolution with the PDFs such that \mathcal{R}_{int} which is evaluated at the resonance $s = m_\phi^2$ should give a good approximation to the hadronic case depending on the

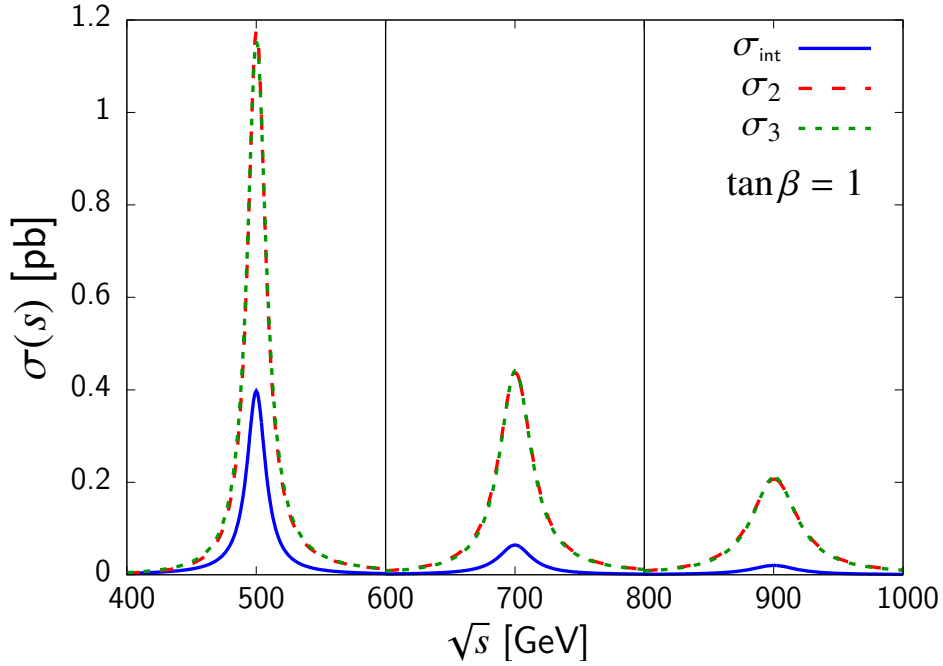


Figure 4.7.: Partonic cross sections σ_{int} , σ_2 and σ_3 as a function of the partonic center of mass energy \sqrt{s} for $m_\phi = 500, 700, 900\text{GeV}$, $\tan\beta = 1$ and $\alpha_i = \alpha_i^{\text{max}}$, $i = 1, 2, 3$.

width of ϕ_2 and ϕ_3 .

4.2.3. Longitudinal top-quark polarization

While it is interesting to study the contribution from Higgs-Higgs interference to the $t\bar{t}$ cross section this question remains rather academic since the interference itself is not an observable. The longitudinal top-quark polarization on the other hand is an observable and is directly related to CP violation in the heavy Higgs contributions to $t\bar{t}$ production. Furthermore one contribution to the top-quark polarization comes from the interference of the two heavy Higgs bosons. In the following we give an estimate of the largest possible longitudinal top-quark polarization induced by heavy Higgs bosons given the experimental constraints on the mixing angles that have been already applied in Sec. 4.2.2 (Eq. (4.41)). The (anti)top-quark polarization is directly related to the B_1 (B_2) coefficient of the double differential distribution (Appendix C, Eqs. (C.33) and (C.34))

$$\begin{aligned} B_1(\hat{\mathbf{a}}_1) &= \kappa_\ell \langle P_t(\hat{\mathbf{a}}_1) \rangle = \kappa_\ell \langle 2\mathbf{S}_t \cdot \hat{\mathbf{a}}_1 \rangle \\ &= \frac{\kappa_\ell}{\sigma_{t\bar{t}}} \int dx_a dx_b f_{p,a}(x_a, \mu_F) f_{p,b}(x_b, \mu_F) dz \frac{\beta_t}{8\pi s} (\mathbf{B}^+ \cdot \hat{\mathbf{a}}_1), \end{aligned} \quad (4.49)$$

$$\begin{aligned} B_2(\hat{\mathbf{a}}_2) &= -\kappa_\ell \langle P_{\bar{t}}(\hat{\mathbf{a}}_2) \rangle = \kappa_\ell \langle -2\mathbf{S}_{\bar{t}} \cdot \hat{\mathbf{a}}_2 \rangle \\ &= -\frac{\kappa_\ell}{\sigma_{t\bar{t}}} \int dx_a dx_b f_{p,a}(x_a, \mu_F) f_{p,b}(x_b, \mu_F) dz \frac{\beta_t}{8\pi s} (\mathbf{B}^- \cdot \hat{\mathbf{a}}_2), \end{aligned} \quad (4.50)$$

where κ_ℓ is the lepton spin analyzing power (which is $\kappa_\ell = 1$ at LO) and $\langle P_t(\hat{\mathbf{a}}_1) \rangle$ ($\langle P_{\bar{t}}(\hat{\mathbf{a}}_2) \rangle$) is the expectation value of the (anti)top-quark polarization with respect to the reference axis $\hat{\mathbf{a}}_1$ ($\hat{\mathbf{a}}_2$). Since \mathbf{B}^\pm can be decomposed (Eq. (3.24)) as follows

$$B_i^\pm = b_1^\pm \hat{p}_i + b_2^\pm \hat{k}_i + b_3^\pm \hat{n}_i \quad (4.51)$$

4. Heavy Higgs effects in top-quark pair production at leading order in α_s

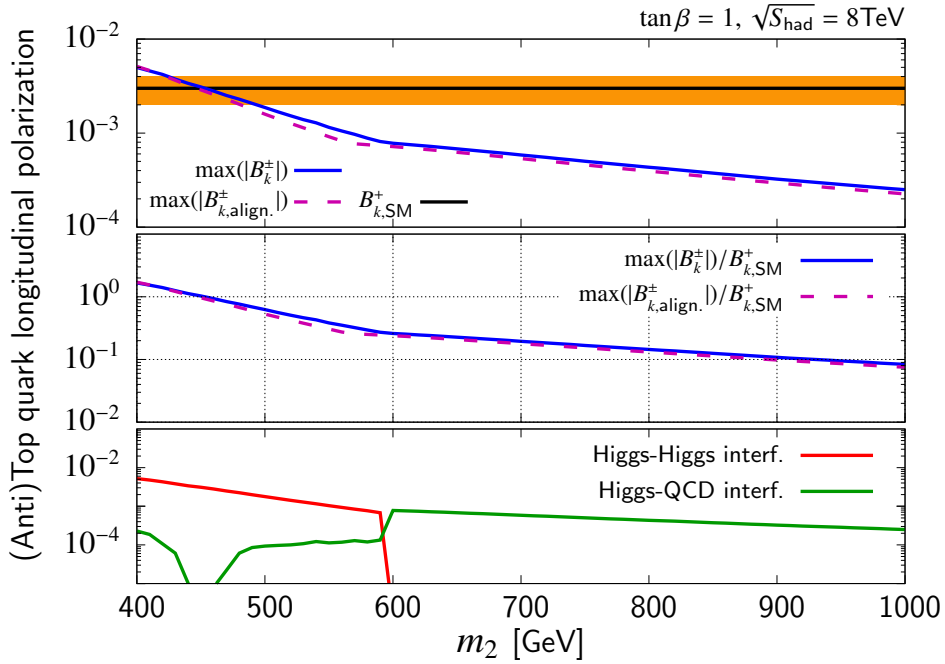


Figure 4.8.: Maximal longitudinal (anti)top-quark polarization as a function of m_2 for $\tan\beta = 1$ and $\sqrt{S_{\text{had}}} = 8\text{TeV}$ using the PDF set CT10n1o [100]. Top plot: Maximal polarization when α_i are free to vary (solid blue) and in the alignment limit (dashed purple). The SM theoretical value is shown as black line and the uncertainty is indicated by the orange band. Center plot: Relative maximal polarization with respect to the SM value. Bottom plot: Contributions from the Higgs-Higgs interference (red) and Higgs-QCD interference to the maximal (anti)top-quark polarization.

and because

$$b_{\phi_{2,3},1}^\pm = b_{\phi_{2,3},3}^\pm = 0 \quad \text{and} \quad b_{\text{int},1j}^\pm = b_{\text{int},3j}^\pm = 0 \quad (4.52)$$

there is no transversal polarization but the (anti)top quarks can be polarized in the direction of their momenta⁴. In the following we determine the maximum of the expectation values $B_k^+ = \langle 2\mathbf{S}_t \cdot \hat{\mathbf{k}} \rangle$ and $B_k^- = \langle 2\mathbf{S}_{\bar{t}} \cdot \hat{\mathbf{k}} \rangle$ by a similar procedure as for the Higgs-Higgs interference. For a grid of $10 \times 10 \times 10$ points in $(\alpha_1, \alpha_2, \alpha_3)$ -parameter space first the corresponding decay widths of the heavy Higgs bosons are generated and then B_k^\pm is calculated. The major difference to the procedure in Sec. 4.2.2 is the calculation of the expectation value of the longitudinal top-quark polarization at the hadron level, i.e. by convoluting with the PDFs according to Eqs. (4.49) and (4.50). Furthermore the maximum is determined for $m_2 \in [400, 1000]\text{GeV}$. As opposed to the Higgs-Higgs interference contribution to the cross section here the polarization is not maximal for $m_2 = m_3$. Hence, a scan over $m_3 \in [m_2, m_2 + 1000]\text{GeV}$ is performed as well. The upper boundary ($m_2 + 1000\text{GeV}$) is chosen because for mass separations $\Delta m = m_3 - m_2 > 1000\text{GeV}$ the width of the Higgs bosons becomes very large ($\frac{\Gamma}{m} > 0.6$). The choice for the parameters that are kept fixed is given in Eq. (4.40).

The results for $\sqrt{S_{\text{had}}} = 8\text{TeV}$ and $\tan\beta = 1$ are shown in Fig. 4.8. The upper plot shows the maximum of the absolute longitudinal polarization of the top ($|B_k^+|$) and antitop ($|B_k^-|$) as a function of m_2 (blue, solid). The parameters $\alpha_1, \alpha_2, \alpha_3$ and m_3 were allowed to vary in the range given above. The dashed curve represents the maximal polarization in the alignment

⁴The polarization with respect to the beam axis $\hat{\mathbf{p}}$ vanishes when integrated over z in Eqs. (4.49) and (4.50).

limit $\max(B_{k,\text{align}}^\pm)$. In the alignment limit $\alpha_1 = \beta$, $\alpha_2 = 0$, such that

$$b_{\phi_{2,3},2}^\pm = \mp N_{\phi_{2,3}} \beta_t \cot^4 \beta \sin(2\alpha_3) (4|\hat{F}_P|^2 - |\hat{F}_S|^2) \text{Im}[P_{23}], \quad (4.53)$$

$$b_{\text{int},2j}^\pm = \mp N_{\text{int}} s \beta_t \left(\frac{1}{2} - \delta_{3j} \right) \cot^2 \beta \sin(2\alpha_3) \text{Im} \left[\frac{\hat{F}_S + 2\hat{F}_P}{s - m_j^2 + i\Gamma_j m_j} \right]. \quad (4.54)$$

Due to the factor $\sin(2\alpha_3)$ in both contributions the polarization in the alignment limit becomes maximal for $\alpha_3 = \pi/4$ and we need to scan only over the masses m_2 and m_3 and not over α_3 . Figure 4.8 shows that the maximal polarization in the alignment limit is only slightly smaller than in the general case because the constraints on α_1 and α_2 allow only for a small deviation from the alignment limit (see Eq. (4.41)). The theoretical prediction [118] for the longitudinal polarization of the top quark in the SM ($B_{k,\text{SM}}^+ = 0.003 \pm 0.001$) is indicated by the black solid line and the orange bar in the plot. In the SM at LO $t\bar{t}$ production proceeds via the CP conserving interactions of QCD. Hence, the top quarks are not polarized. When including corrections due to the parity violating weak interactions a tiny longitudinal polarization is generated. For low masses m_2 of the heavy Higgs boson ϕ_2 the longitudinal top-quark polarization can be as large as the polarization in the SM. But for masses $m_2 > 950\text{GeV}$ the polarization due to CP violation in the extended Higgs sector of the 2HDM drops below 10% of the SM value (middle plot in Fig. 4.8) which is below the theoretical uncertainty of $B_{k,\text{SM}}^+$. The experimental results [119]

$$B_k^+ = -0.044 \pm 0.038 \quad \text{and} \quad B_k^- = -0.064 \pm 0.040 \quad (4.55)$$

are compatible with the SM prediction as well as vanishing longitudinal polarization at a level of less than two standard deviations. Hence, due to the small contribution from the 2HDM to the polarization and the large experimental uncertainties the measurement in Ref. [119] cannot discriminate between the SM and the 2HDM in this observable even if the maximal polarization (compatible with the limits on mixing angles) is assumed. The NLO contribution does not change this picture and an example will be given in the next chapter. However, the contribution of the heavy Higgs bosons to the polarization can be enhanced by applying appropriate cuts in the $t\bar{t}$ invariant mass $M_{t\bar{t}}$. This aspect will also be discussed in the next chapter.

The uncertainties of B_k^\pm due to variations in the renormalization and factorization scales μ_R and μ_F , respectively, are very small at leading order because $\alpha_s(\mu_R)$ cancels in these observables leaving only a residual dependence on μ_F through the PDFs which also cancels to some extent. When varying $\mu_R = \mu_F = \mu_0 = (m_2 + m_3)/4$ by a factor of two ($2\mu_0, \mu_0/2$) the resulting curves lie within the line thickness of the curves in Fig. 4.8 such that the variation is not visible in the plots. The apparent accuracy is of course misleading. Due to the cancellation of the μ_R dependence the variation of the renormalization and factorization scales is not a reliable method to estimate the uncertainty due to missing higher orders.

The maximal polarization (blue curve in the upper plot of Fig. 4.8) as a function of m_2 features a kink at about $m_2 = 600\text{GeV}$. The origin for this kink is illustrated in the lower plot where the absolute values of the contribution from the Higgs-Higgs interference (red) and the interference between Higgs contribution and the QCD background (green) are shown⁵. For masses $m_2 < 600\text{GeV}$ the contribution from the Higgs-Higgs interference is dominant while for $m_2 \geq 600\text{GeV}$ the interference with the background is larger. Since these two contributions have different slopes the total maximal polarizations exhibits a kink at $m_2 = 600\text{GeV}$.

In Fig. 4.9 the maximal longitudinal (anti)top-quark polarization as a function of m_2 is displayed for $\tan\beta = 0.7, 1, 1.5$ at a hadronic center of mass energy of $\sqrt{S_{\text{had}}} = 13\text{TeV}$. The

⁵The red and green curves in the lower plot of Fig. 4.8 also exhibit kinks because they result from the

4. Heavy Higgs effects in top-quark pair production at leading order in α_s

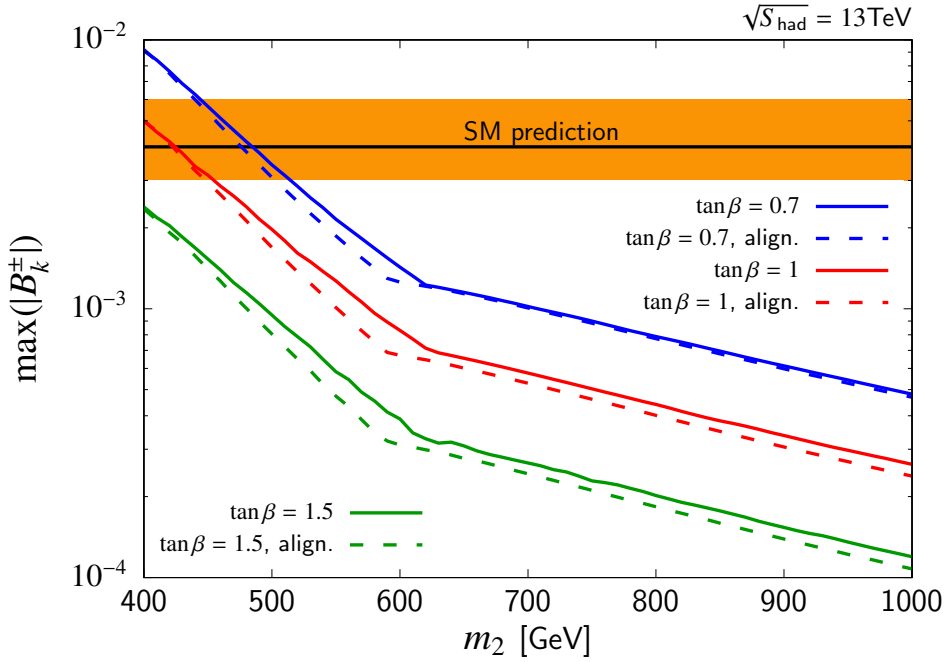


Figure 4.9.: Maximal longitudinal (anti)top-quark polarization as a function of m_2 for $\tan\beta = 0.7, 1, 1.5$ and $\sqrt{S_{\text{had}}} = 13\text{TeV}$ using the PDF set CT10nlo [100].

solid curves in Fig. 4.9 represent the maximal polarization when the mixing angles are allowed to vary as given in Eq. (4.41). The dashed curves show the maximal polarization in the alignment limit. The behaviour of the maximal polarization for $\tan\beta = 1$ at $\sqrt{S_{\text{had}}} = 13\text{TeV}$ is very similar to the 8TeV case. For $\tan\beta = 0.7$ ($\tan\beta = 1.5$) the polarization is enhanced (reduced) with respect to $\tan\beta = 1$ due to the enhanced (reduced) Yukawa coupling to top quarks. But even for $\tan\beta = 0.7$ the longitudinal top-quark polarization induced by a CP violating 2HDM remains a small effect and exceeds the SM contribution only slightly for masses $m_2 < 500\text{GeV}$.

The very small effects in the SM make the top-quark polarization a promising observable to look for new physics effects. We have seen that the 2HDM with a CP violating Higgs potential can generate top-quark polarization already at tree level. However its magnitude does not significantly exceed the SM value. In fact, for large masses of the heavy Higgs bosons this effect reduces strongly and becomes much smaller than the SM contribution.

4.2.4. Spin correlations

Besides the polarization the spin dependent matrix elements allow also the investigation of spin correlations. These correlations are, contrary to top-quark polarization, already present at LO in the SM. Top quark pairs in the SM can be up to $\approx 50\%$ spin correlated [120] at the LHC depending on the choice of reference axis. When considering only the $q\bar{q}$ channel there exists even a reference axis [121] that yields a 100% spin correlation between the produced top and antitop quark. Hence, at a proton-antiproton collider such as the Tevatron spin correlations of almost 80%⁶ [112] are achievable when using an appropriate reference axis. Contributions from BSM physics such as the 2HDM can enhance or reduce these spin correlations. In particular,

maximization over a multidimensional parameter space and are therefore not expected to be smooth.

⁶Here the result at NLO QCD is taken. At LO the correlation can be even larger: 93.7%.

no CP violation is required (otherwise the SM effects would be much smaller). In order to determine the largest effects of heavy Higgs bosons on the spin correlation of $t\bar{t}$ pairs we follow the strategy of Ref. [120] and determine the largest eigenvalue and the corresponding eigenvector of the matrix

$$C_{2\text{HDM}}^{mn} = C_{\phi_{2,3}}^{mn} + \sum_j (C_{\phi_j}^{mn} + C_{\text{int},j}^{mn}), \quad m, n = 1, 2, 3 \quad (4.56)$$

in the spin dependent matrix elements in Eqs. (4.4), (4.15) and (4.24). $C_{2\text{HDM}}$ receives only contributions from c_0 , c_2 and c_5 such that the general structure is given by

$$C_{2\text{HDM}}^{mn} = c_{2\text{HDM},0} \delta_{mn} + c_{2\text{HDM},2} \epsilon_{mnl} \hat{k}_l + c_{2\text{HDM},5} \hat{k}_m \hat{k}_n. \quad (4.57)$$

Due to this very simple structure which depends only on $\hat{\mathbf{k}}$ we can identify, without loss of generality, the z -axis with the direction of the top-quark three-momentum $\hat{\mathbf{k}}$

$$\hat{\mathbf{k}} = \begin{pmatrix} 0 \\ 0 \\ 1 \end{pmatrix} \quad (4.58)$$

to obtain $C_{2\text{HDM}}$ in matrix form

$$C_{2\text{HDM}} = \begin{pmatrix} c_0 & c_2 & 0 \\ -c_2 & c_0 & 0 \\ 0 & 0 & c_0 + c_5 \end{pmatrix}, \quad (4.59)$$

where the subscript ‘‘2HDM’’ for the matrix components has been omitted. From Eq. (4.59) it is obvious that $\hat{\mathbf{k}}$ is eigenvector of $C_{2\text{HDM}}$ with eigenvalue $c_0 + c_5$. Inserting the expressions for c_0 and c_5 from Eqs. (4.8), (4.20), (4.29) and (4.10), (4.22), (4.31) yields the relation

$$A_{2\text{HDM}} = A_{\phi_{2,3}} + \sum_j (A_{\phi_j} + A_{\text{int},j}) = -(c_{2\text{HDM},0} + c_{2\text{HDM},5}). \quad (4.60)$$

From this expression one can calculate the expectation value $C_{\text{hel}} = -4\langle(\mathbf{S}_t \cdot \hat{\mathbf{k}})(\mathbf{S}_{\bar{t}} \cdot \hat{\mathbf{k}})\rangle$ which is related to the correlation:

$$\begin{aligned} C_{\text{hel}}^{2\text{HDM}} &= \frac{-4 \int d\Phi' \text{Tr}[R^{g\bar{g} \rightarrow t\bar{t}}(\mathbf{S}_t \cdot \hat{\mathbf{k}})(\mathbf{S}_{\bar{t}} \cdot \hat{\mathbf{k}})]}{\sigma_{t\bar{t}}^{2\text{HDM}}} = \frac{-4 \int d\Phi' C_{2\text{HDM}}^{mn} \hat{k}_m \hat{k}_n}{\int d\Phi' 4A_{2\text{HDM}}} \\ &= \frac{-4 \int d\Phi' (c_{2\text{HDM},0} + c_{2\text{HDM},5})}{4 \int d\Phi' A_{2\text{HDM}}} = 1, \end{aligned} \quad (4.61)$$

where $\sigma_{t\bar{t}}^{2\text{HDM}}$ is the 2HDM contribution (including the interference with the QCD contribution) to the hadronic $t\bar{t}$ cross section and

$$d\Phi' = dx_a dx_b f_{p,a}(x_a, \mu_F) f_{p,b}(x_b, \mu_F) dz \frac{\beta_t}{8\pi s}. \quad (4.62)$$

Hence, $\hat{\mathbf{k}}$ is the eigenvector to the largest⁷ eigenvalue of $C_{2\text{HDM}}$ which corresponds to a correlation of 100%⁸. It does not come as a surprise that the optimal axis for the spin

⁷It has to be the largest eigenvalue because it corresponds to a correlation of 100%, which is the largest possible correlation.

⁸As pointed out in Chap. 3 the expectation value $-4\langle(\mathbf{S}_t \cdot \hat{\mathbf{k}})(\mathbf{S}_{\bar{t}} \cdot \hat{\mathbf{k}})\rangle$ equals the correlation in the case of vanishing polarization. If the polarization is nonzero but small $-4\langle(\mathbf{S}_t \cdot \hat{\mathbf{k}})(\mathbf{S}_{\bar{t}} \cdot \hat{\mathbf{k}})\rangle$ can still be considered as correlation to good approximation.

4. Heavy Higgs effects in top-quark pair production at leading order in α_s

correlation is given in the helicity basis. When the spin-0 boson decays at rest the momenta of the top and antitop are given in the $t\bar{t}$ rest frame where the orbital angular momentum is zero. Hence, the spins of top and antitop have to compensate each other to yield a vanishing total angular momentum. In the $t\bar{t}$ rest frame the momenta of the top and antitop have opposite directions $\hat{\mathbf{k}}_t = -\hat{\mathbf{k}}_{\bar{t}}$ such that the spins compensate each other if the top spin aligns (or anti-aligns) with $\hat{\mathbf{k}}_t$ and the antitop spin aligns (or anti-aligns) with $\hat{\mathbf{k}}_{\bar{t}}$. Hence, the spins are 100% correlated in the helicity basis.

Unfortunately one has no direct access to the 2HDM contribution to C_{hel} as given in Eq. (4.61) because C_{hel} also receives contributions from QCD. These are much larger than the 2HDM contributions such that deviations of C_{hel} from the SM due to the 2HDM are difficult to detect. This shows also that in order to increase the sensitivity of the $t\bar{t}$ spin correlations to the effects of heavy Higgs bosons it is not enough to find a reference axis that maximizes the 2HDM contribution. The very same axis can in fact also yield large contributions from QCD. Hence, in the following we determine the reference axis $\hat{\mathbf{x}}_{\text{max}}$ which maximizes the ratio

$$\delta C \equiv \left| \frac{C^{\text{QCD}+2\text{HDM}} - C^{\text{QCD}}}{C^{\text{QCD}}} \right|, \quad (4.63)$$

i.e. $\hat{\mathbf{x}}_{\text{max}}$ maximizes the 2HDM contribution with respect to the QCD contribution. The ratio δC can be considered as a signal-to-background ratio. Due to the nonlocal character of δC one cannot simply determine the reference axis that maximizes δC for each phase space point⁹. Therefore we take a different approach by choosing an orthonormal basis [118] $\{\hat{\mathbf{k}}, \hat{\mathbf{n}}, \hat{\mathbf{r}}\}$ where $\hat{\mathbf{k}}$ is the direction of the top-quark momentum in the $t\bar{t}$ rest frame and

$$\hat{\mathbf{n}} = \frac{1}{r}(\hat{\mathbf{p}} \times \hat{\mathbf{k}}), \quad \hat{\mathbf{r}} = \frac{1}{r}(\hat{\mathbf{p}} - z\hat{\mathbf{k}}) \quad (4.64)$$

with

$$z = \hat{\mathbf{p}} \cdot \hat{\mathbf{k}}, \quad r = \sqrt{1 - z^2}, \quad (4.65)$$

where $\hat{\mathbf{p}}$ is the proton beam direction. Then we define the reference axis¹⁰

$$\hat{\mathbf{x}}(\theta, \varphi) = \hat{\mathbf{k}} \sin \theta \cos \varphi + \hat{\mathbf{n}} \text{sign}(z) \sin \theta \sin \varphi + \hat{\mathbf{r}} \text{sign}(z) \cos \theta \quad (4.66)$$

and determine

$$\delta C_{\theta, \varphi} = \left| \frac{C_{\theta, \varphi}^{\text{QCD}+2\text{HDM}} - C_{\theta, \varphi}^{\text{QCD}}}{C_{\theta, \varphi}^{\text{QCD}}} \right|, \quad (4.67)$$

where

$$C_{\theta, \varphi} \equiv C(\theta, \varphi) = 4\langle (\mathbf{S}_t \cdot \hat{\mathbf{x}}_{\theta, \varphi})(\mathbf{S}_{\bar{t}} \cdot \hat{\mathbf{x}}_{\theta, \varphi}) \rangle. \quad (4.68)$$

We scan over the angles θ and φ to determine the maximum of $\delta C_{\theta, \varphi}$

$$\delta C_{\text{max}} \equiv \delta C(\hat{\mathbf{x}}_{\text{max}}) = \max_{\theta, \varphi} \left| \frac{C_{\theta, \varphi}^{\text{QCD}+2\text{HDM}} - C_{\theta, \varphi}^{\text{QCD}}}{C_{\theta, \varphi}^{\text{QCD}}} \right|. \quad (4.69)$$

⁹To determine δC the expectation values $C^{\text{QCD}+2\text{HDM}}$ and C^{QCD} have to be known. These expectation values require integrations over the whole phase space. Therefore, whether a certain reference axis is maximizing δC can only be decided after the integration over the whole phase space and not on a point by point basis.

¹⁰The extra factors of $\text{sign}(z)$ are inserted because the production density matrix for the gluon channel is even under $z \rightarrow -z$ due to the Bose symmetry of the initial state. $\hat{\mathbf{n}}$ and $\hat{\mathbf{r}}$ on the other hand are odd under $z \rightarrow -z$. Hence, the expectation values C_{kn} , C_{kr} would be zero due to the phase space integration over z . However, these contributions are generated when calculating the expectation value $C_{\theta, \varphi}$ (4.67). The factors $\text{sign}(z)$ are needed to take them into account.

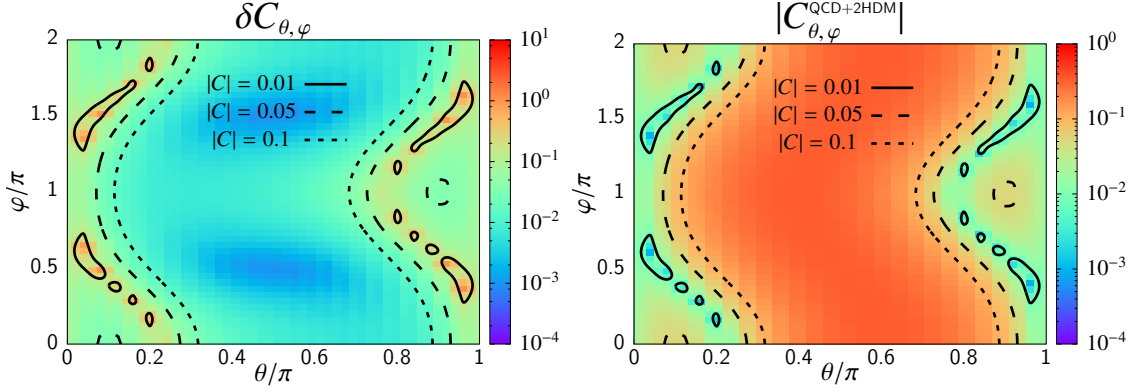


Figure 4.10.: Contour plots in θ - φ space for the signal-to-background ratio $\delta C_{\theta,\varphi}$ (lhs) and the absolute size of the spin correlation $|C_{\theta,\varphi}^{\text{QCD}+2\text{HDM}}|$ (rhs). The model parameters in this figure are given in Eq. (4.34) and by $m_2 = 500$ GeV and $m_3 = 600$ GeV. The plots show results for $\sqrt{S_{\text{had}}} = 13$ TeV using the PDF set CT10n1o [100].

In order to determine $C_{\text{max}} = 4\langle(\mathbf{S}_t \cdot \hat{\mathbf{x}}_{\text{max}})(\mathbf{S}_{\bar{t}} \cdot \hat{\mathbf{x}}_{\text{max}})\rangle$ we need to specify the parameters of the 2HDM. As an example we choose the parameters of the CP conserving scenario in the alignment limit given in Eq. (4.34). For the heavy Higgs boson masses we choose

$$m_3 = m_2 + 100\text{GeV} \quad (4.70)$$

and determine δC_{max} for different values of $m_2 \in [400, 1000]\text{GeV}$. We observe that large values of $\delta C_{\theta,\varphi}$ correspond to small spin correlations, i.e. the sensitivity to 2HDM contribution is large but the absolute values of $C^{\text{QCD}+2\text{HDM}}$ and C^{QCD} are small and therefore difficult to measure experimentally. In Fig. 4.10 this behaviour is illustrated for the case $m_2 = 500$ GeV and $m_3 = 600$ GeV. On the left hand side (lhs) the contour plot shows the ratio $\delta C_{\theta,\varphi}$ and on the rhs the absolute value of the correlation is displayed. From the color scheme one can immediately see that the two plots are quasi inverted. High signal-to-background ratios in the left plot correspond to small correlations in the right plot. That is why we apply the additional constraint

$$|C^{\text{QCD}+2\text{HDM}}| > C_{\text{min}} \quad (4.71)$$

on the maximization of $\delta C_{\theta,\varphi}$ where $C_{\text{min}} = \{0.1, 0.05, 0.01\}$, which corresponds to 10%, 5% and 1% $t\bar{t}$ spin correlation, respectively. For the case $m_2 = 500$ GeV and $m_3 = 600$ GeV the contours in θ - φ space corresponding to these constraints are shown.

The results for δC_{max} are displayed in Fig. 4.11. The upper plot shows δC_{max} as a function of m_2 for the three different constraints C_{min} and, additionally, we display δC_{hel} for the helicity axis $\hat{\mathbf{k}}$ for comparison. Note, that even though the axis $\hat{\mathbf{k}}$ yields the maximum correlation of the 2HDM contribution (Eq. (4.61)) it does not represent the axis of maximal sensitivity to the heavy Higgs bosons due to the large QCD contributions. In general δC_{max} decreases with increasing mass of the heavy Higgs bosons. For small constraints on the absolute value of the correlation, for example $C_{\text{min}} = 0.01$, the ratio δC_{max} varies between 35% and 8% in the mass range $400\text{GeV} \leq m_2 \leq 1000\text{GeV}$. For the stronger constraint $C_{\text{min}} = 0.1$ the ratio δC_{max} is about an order of magnitude smaller and varies between 2.8% and 0.9%. In the lower plot of Fig. 4.11 the absolute value of $C_{\theta,\varphi}^{\text{QCD}+2\text{HDM}}$ is shown for the maximum configuration for the three different values of C_{min} and for the helicity axis. This plot illustrates the trade-off between sensitivity (large δC_{max}) and large absolute correlations which can be seen by the reverse order of the curves in the upper and lower plots. Furthermore, the lower plot

4. Heavy Higgs effects in top-quark pair production at leading order in α_s

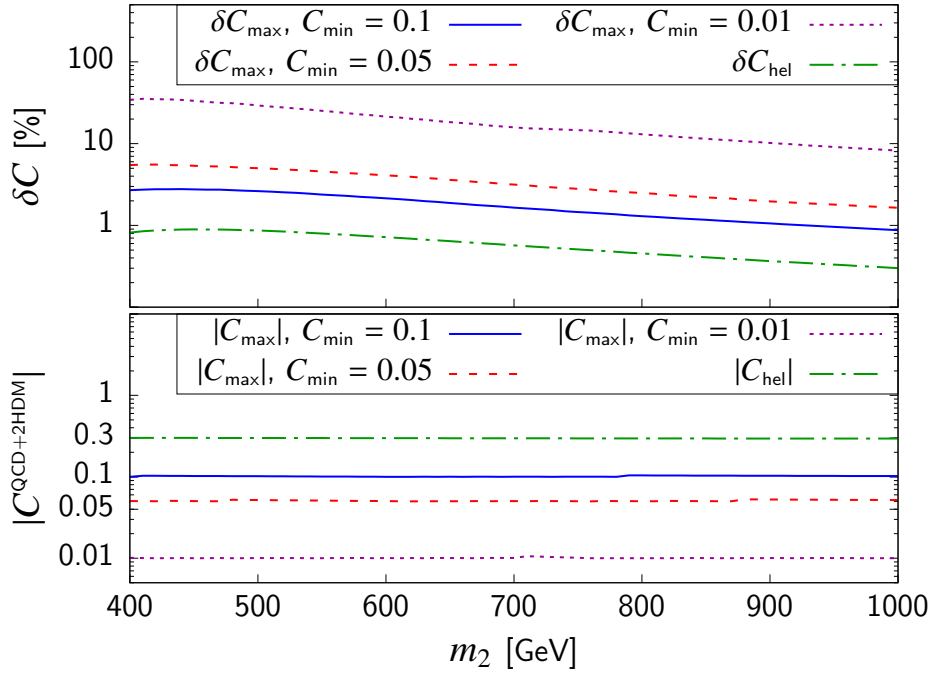


Figure 4.11.: Maximum S/B of the optimal $t\bar{t}$ spin correlation C_{\max} as a function of m_2 for the 2HDM scenario defined in Eq. (4.70). Upper plot: Maximum S/B for different constraints C_{\min} and S/B for C_{hel} . Lower plot: Absolute value of the spin correlation $|C_{\max}|$ for different constraints C_{\min} and absolute value $|C_{\text{hel}}|$. The absolute values represent the sum of QCD and 2HDM contributions. The plots show results for $\sqrt{s}_{\text{had}} = 13$ TeV using the PDF set CT10n1o [100].

shows that the maximum of $\delta C_{\theta,\varphi}$ is reached for the lowest possible absolute values of the correlation. That is why the curves deviate from C_{\min} only very little. But even C_{hel} , which is left unconstrained with respect to C_{\min} , varies only by a few percent over the mass range shown here, and is therefore almost independent of m_2 in this scenario.

This analysis shows that spin correlations present an additional handle to study effects of the 2HDM contributions in $t\bar{t}$ production. However, their measurement requires high precision because their absolute values are small when the heavy Higgs contribution is large. One possibility to circumvent this behaviour is to cut on the $t\bar{t}$ invariant mass. In Sec. 4.2.1 we have seen that the largest contributions of the heavy Higgs bosons come from the resonant region where $|m_\phi - M_{t\bar{t}}| \lesssim 100\text{GeV}$. Hence, filtering out this region by appropriate $M_{t\bar{t}}$ cuts can yield larger sensitivities. In an experimental situation it is of course not known beforehand where the resonant region is because the mass of the heavy Higgs bosons is unknown. That is why one should bin $C_{\theta,\phi}$ in $M_{t\bar{t}}$ with bin width $\Delta M_{t\bar{t}}$

$$C_{\theta,\varphi}^{M_{t\bar{t}}} = \frac{4 \int_{M_{t\bar{t}}}^{M_{t\bar{t}}+\Delta M_{t\bar{t}}} d\Phi' \text{Tr}[R^{ab \rightarrow t\bar{t}}(\mathbf{S}_t \cdot \hat{\mathbf{x}})(\mathbf{S}_{\bar{t}} \cdot \hat{\mathbf{x}})]}{\int_{M_{t\bar{t}}}^{M_{t\bar{t}}+\Delta M_{t\bar{t}}} d\sigma} \quad (4.72)$$

and search for enhancements or deficits with respect to the prediction of QCD only.

As a function of $M_{t\bar{t}}$ the observable $C_{\theta,\varphi}^{M_{t\bar{t}}}$ can have zeros. In $M_{t\bar{t}}$ bins where $C_{\theta,\varphi}^{M_{t\bar{t}},\text{QCD}} = 0$ the ratio $\delta C_{\theta,\varphi}^{M_{t\bar{t}}}$ is ill-defined. Furthermore, as we will see in the next chapter, the position of this zero can change when NLO corrections are taken into account. Consequently, predictions of the sensitivity of spin correlations in the vicinity of the zero are less robust than from $M_{t\bar{t}}$ bins in an appropriate distance from the zero. Therefore, in the following analysis we determine the zero for each observable $C_{\theta,\varphi}$ and do not consider bins that lie within $M_{t\bar{t},0} - 100\text{GeV} \leq M_{t\bar{t}} \leq M_{t\bar{t},0} + 100\text{GeV}$, where $M_{t\bar{t},0}$ is the position of the zero. As an example the result for

$$m_2 = 600\text{GeV}, \quad m_3 = 700\text{GeV}, \quad \tan\beta = 1 \quad (4.73)$$

in the alignment limit is shown in Fig. 4.12. $C_{\theta,\varphi}^{M_{t\bar{t}}}$ for $\theta = 0.88\pi$ and $\varphi = 0$ is displayed as a function of $M_{t\bar{t}}$ for $\Delta M_{t\bar{t}} = 10\text{GeV}$ (lower plot) and $\Delta M_{t\bar{t}} = 80\text{GeV}$ (upper plot). The fine binning is used to determine the zero $M_{t\bar{t},0}$. The range in $M_{t\bar{t}}$ that is excluded from the determination of $\delta C_{\text{max}}^{M_{t\bar{t}}}$ is indicated by the vertical olive green band in Fig. 4.12. All $M_{t\bar{t}}$ bins that overlap with this band are not considered when determining $\delta C_{\text{max}}^{M_{t\bar{t}}}$. As for the inclusive (in $M_{t\bar{t}}$) case we also impose the additional constraint

$$|C_{\theta,\varphi}^{M_{t\bar{t}},\text{QCD}+2\text{HDM}}| > C_{\min}. \quad (4.74)$$

In the example in Fig. 4.12 this constraint is indicated by the horizontal beige band. The $M_{t\bar{t}}$ bin $660\text{GeV} - 740\text{GeV}$ yields the largest signal-to-background ratio (S/B) which is compatible with the constraints (that lies outside the intersection of the horizontal and vertical bands): $\delta C_{\text{max}}^{M_{t\bar{t}}} = 20.3\%$.

In order to determine the maximal S/B $\delta C_{\text{max}}^{M_{t\bar{t}}}$ we maximize $\delta C_{\theta,\varphi}^{M_{t\bar{t}}}$ with respect to θ , φ and $M_{t\bar{t}}$ under the constraints described above. Here we consider different parameter sets within the scenario defined in Eq. (4.70) with $m_2 = 400, 500, 600, 700, 800, 900, 1000\text{GeV}$. The results are presented in Figs. 4.13–4.15 for $\Delta M_{t\bar{t}} = 50, 80$ and 100GeV , respectively. The solid bars represent the results for $\delta C_{\text{max}}^{M_{t\bar{t}}}$. For example, for the scenario specified in Eq. (4.70), $m_2 = 500\text{GeV}$ and $\Delta M_{t\bar{t}} = 50\text{GeV}$ the signal-to-background ratio $\delta C_{\theta,\varphi}^{M_{t\bar{t}}}$ becomes maximal for $\theta = 0.8\pi$ and $\varphi = 0.64\pi$ in the $M_{t\bar{t}}$ bin $590\text{GeV} - 640\text{GeV}$ with $\delta C_{\text{max}}^{M_{t\bar{t}}} = 37.3\%$. The values of θ and φ for which $\delta C_{\theta,\varphi}^{M_{t\bar{t}}}$ is maximized depend on the specific scenario under consideration. Hence, in a dedicated experimental search for heavy Higgs bosons of a 2HDM in the $t\bar{t}$ decay channel

4. Heavy Higgs effects in top-quark pair production at leading order in α_s

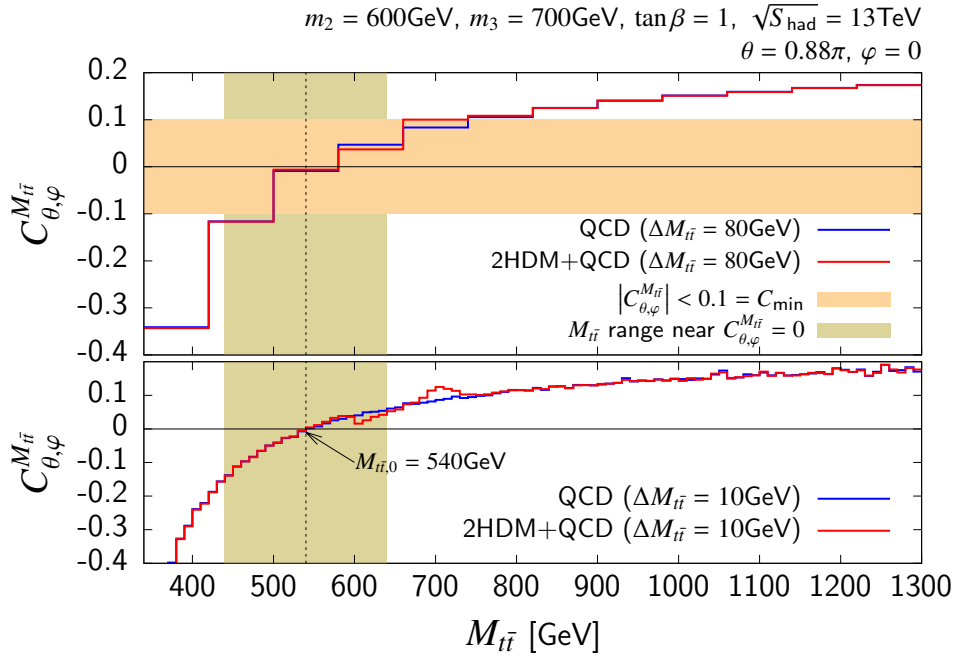


Figure 4.12.: Spin correlation $C_{\theta,\varphi}^{M_{\tilde{t}\tilde{t}}}$ as a function of $M_{\tilde{t}\tilde{t}}$. Upper plot: $M_{\tilde{t}\tilde{t}}$ binning 80GeV, lower plot: $M_{\tilde{t}\tilde{t}}$ binning 10GeV. The plots show results for $\sqrt{s}_{\text{had}} = 13$ TeV using the PDF set CT10nlo [100].

one would have to analyse a spin correlation $C_{\theta,\varphi}$ which is specific to the model (parameters) considered in the search in order to gain the optimal sensitivity. The theoretical prediction for this optimal spin correlation is given here for the scenario and parameters stated above. The numerical values for $\delta C_{\text{max}}^{M_{\tilde{t}\tilde{t}}}$ and the corresponding values for θ , φ and $M_{\tilde{t}\tilde{t}}$ can be found in Appendix E in Tabs. E.1–E.3 which correspond to Figs. 4.13–4.15, respectively.

The results for $C_{\text{min}} = 0.1, 0.05, 0.01$ are shown in orange, green and blue, respectively in Figs. 4.13–4.15. $\delta C_{\text{max}}^{M_{\tilde{t}\tilde{t}}}$ shows the same behaviour with respect to the change of C_{min} as the inclusive S/B δC_{max} : Decreasing C_{min} , i.e. allowing for smaller absolute values of spin correlations, increases $\delta C_{\text{max}}^{M_{\tilde{t}\tilde{t}}}$ and vice versa.

In an experimental analysis it is possible to use $M_{\tilde{t}\tilde{t}}$ bins as small as 40GeV in the lower $M_{\tilde{t}\tilde{t}}$ range [114, 115] but for larger values of $M_{\tilde{t}\tilde{t}}$ the bin width has to be increased to collect enough statistics per bin to obtain meaningful results. In order to assess the sensitivity of this analysis taking into account realistic $M_{\tilde{t}\tilde{t}}$ bins we present the results for $\delta C_{\text{max}}^{M_{\tilde{t}\tilde{t}}}$ for different values of $\Delta M_{\tilde{t}\tilde{t}}$. A comparison between the results displayed Figs. 4.13–4.15 shows that smaller $M_{\tilde{t}\tilde{t}}$ bin widths yield larger signal-to-background ratios. An analysis performed with small $M_{\tilde{t}\tilde{t}}$ bins therefore has a larger sensitivity to the resonant effects of heavy Higgs bosons. Peaks and dips in the distribution (see Fig. 4.12 lower plot) are better resolved by small $M_{\tilde{t}\tilde{t}}$ bins whereas large bins average over these resonant structures therefore reducing the visible effect (compare upper and lower plot in Fig. 4.12). The position of the $M_{\tilde{t}\tilde{t}}$ bins has also an effect on the maximal S/B but this is not investigated here, i.e. to generate Figs. 4.13–4.15 the $M_{\tilde{t}\tilde{t}}$ bin position is not optimized.

In Figs. 4.13–4.15 the hatched bars represent the results for the inclusive S/B δC_{max} to facilitate a direct comparison between the inclusive and binned S/B. For $C_{\text{min}} = 0.1, 0.05$ the binned analysis yields always a larger S/B ratio. The smaller the bin width the larger

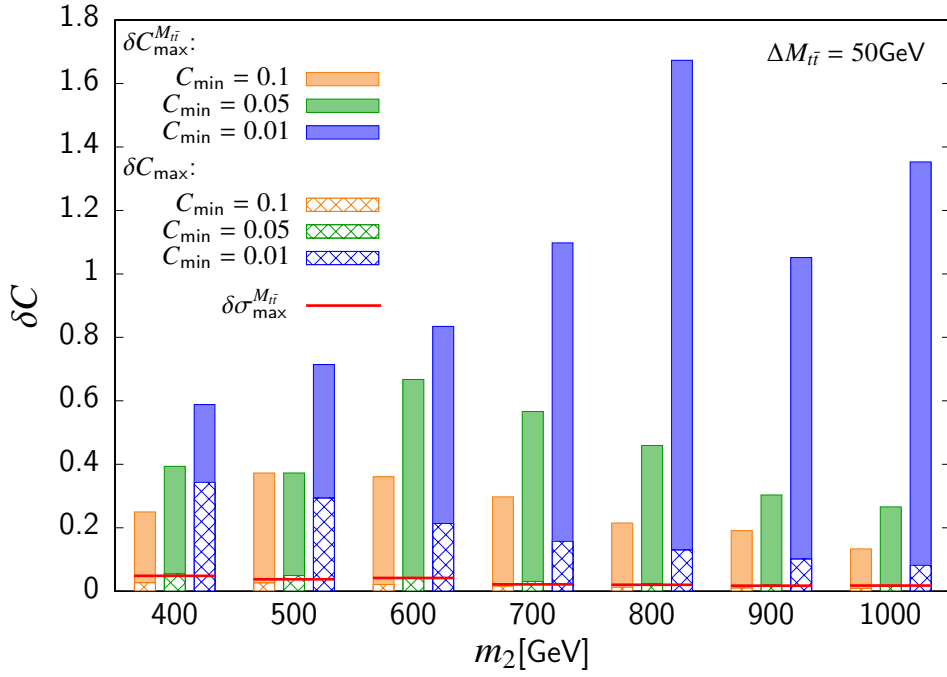


Figure 4.13.: Signal-to-background ratios for different observables and for discrete values of m_2 in the scenario defined in Eq. (4.70). $\delta C_{\max}^{M_{i\bar{i}}}$ (solid) is the maximal S/B of the binned optimal observable $C_{\theta,\varphi}^{M_{i\bar{i}}}$. δC_{\max} (hatched) is the maximal S/B of the inclusive optimal observable $C_{\theta,\varphi}$. $\delta \sigma_{\max}^{M_{i\bar{i}}}$ (red line) is the maximal S/B of the $M_{i\bar{i}}$ distribution. For the binned observables a bin width of $\Delta M_{i\bar{i}} = 50\text{GeV}$ has been used. The plot shows results for $\sqrt{s_{\text{had}}} = 13\text{ TeV}$ using the PDF set CT10n1o [100].

4. Heavy Higgs effects in top-quark pair production at leading order in α_s

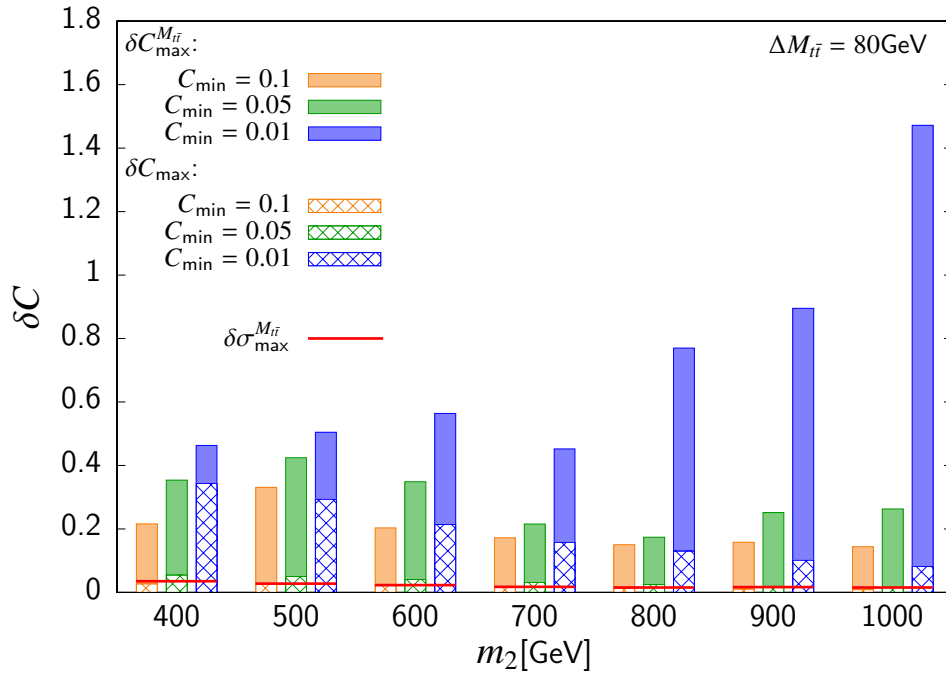


Figure 4.14.: Same as Fig. 4.13 but for $\Delta M_{\tilde{t}\tilde{t}} = 80\text{GeV}$.

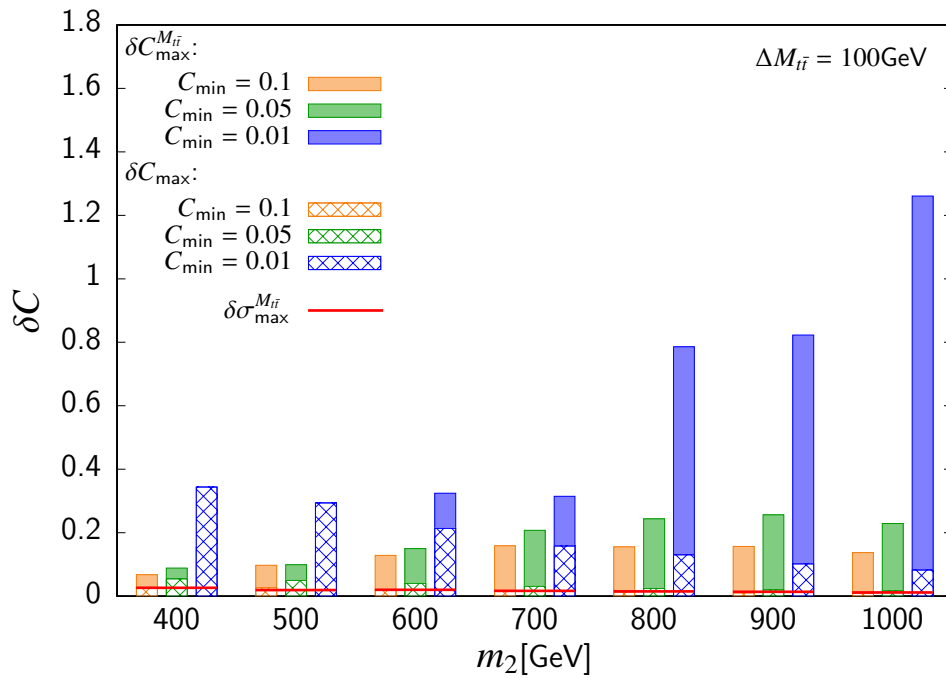


Figure 4.15.: Same as Fig. 4.13 but for $\Delta M_{\tilde{t}\tilde{t}} = 100\text{GeV}$.

the difference between δC_{\max} and $\delta C_{\max}^{M_{t\bar{t}}}$. In the results presented here there are only two cases in which the inclusive observable $C_{\theta,\phi}$ is more sensitive than the binned observable $C_{\theta,\phi}^{M_{t\bar{t}}}$ (Fig. 4.15): for $C_{\min} = 0.01$, $\Delta M_{t\bar{t}} = 100\text{GeV}$ and $m_2 = 400, 500\text{GeV}$. This happens because of the additional constraint to avoid the zero of the observable $C_{\theta,\phi}^{M_{t\bar{t}}}$. However, heavy Higgs bosons with masses $m_2 \in [400, 500]\text{GeV}$ generate peaks and/or dips in the lower $M_{t\bar{t}}$ range. Hence, in an experimental analysis it is possible to choose a small bin width such as shown in Fig. 4.13 where the binned analysis yields a much larger S/B also in the case $C_{\min} = 0.01$.

Finally, for comparison and to illustrate the gain in sensitivity, Figs. 4.13–4.15 also show the maximal S/B $\delta\sigma_{\max}^{M_{t\bar{t}}}$ of the $M_{t\bar{t}}$ distribution (red line), i.e. the maximal sensitivity of the cross section binned in $M_{t\bar{t}}$. In many (but not all) cases the inclusive spin correlation $C_{\theta,\phi}$ is already more sensitive to heavy Higgs effect than the $M_{t\bar{t}}$ distribution. The binned spin correlation $C_{\theta,\phi}^{M_{t\bar{t}}}$ is always more sensitive than the $M_{t\bar{t}}$ distribution and in most cases significantly more sensitive.

In conclusion, we observe that $t\bar{t}$ spin correlations can increase the sensitive to the heavy Higgs effects with respect to the $M_{t\bar{t}}$ distribution of the cross section. However, there is a trade-off between sensitivity and size of the correlation: the larger the sensitivity the smaller the size (absolute value) of the spin correlation which poses a challenge for the experiment. Because spin correlations are defined with respect to a certain reference axis not all spin correlations yield maximal sensitivity. A dedicated analysis needs to consider model specific optimized spin correlations. This is no problem because for the experimental search a model and parameters have to be specified anyway. With this information it is then possible to determine the optimal spin correlation (θ and φ) as it was shown in this section and perform the analysis. To access the full potential of the spin correlations the optimal correlation has to be binned in $M_{t\bar{t}}$. As can be seen from Figs. 4.13–4.15 the maximal S/B $\delta C_{\max}^{M_{t\bar{t}}}$ of the binned observable is always larger than of the inclusive one for relevant $M_{t\bar{t}}$ bin widths.

Heavy Higgs effects in top-quark pair production at next-to-leading order in α_s

In this chapter the main results of this work are presented. Many of these results have been published in Refs. [77] and [78]. At first we discuss the theoretical aspects and the computational methods used for the calculation of heavy Higgs production and decay into $t\bar{t}$ at NLO. Then we present the analytical results followed by a phenomenological discussion studying several spin independent as well as spin dependent observables.

5.1. Introduction

As we have seen in Chap. 4 the LO heavy Higgs contribution (Fig. 4.1 c) to $t\bar{t}$ production is already a one-loop process. Hence, calculating the NLO corrections would involve two-loop contributions of which an example is depicted in Fig. 5.1. Two-loop computations and in particular the calculation of unknown master integrals are highly complex in general. The fact that the contributions of the kind displayed in Fig. 5.1 involve multiscale (Higgs mass, top mass, kinematic invariants) two-loop integrals introduces another level of complexity to the problem. The investigation of NLO correction to 2HDM contributions to $t\bar{t}$ production does not justify such an endeavor until actual experimental evidence has been found. However, in this work we attempt a first step in the direction of the full NLO calculation by computing the 2HDM contributions in the so-called *large top mass limit*. In this limit which is described in detail in Sec. 5.2.1 the two-loop calculation is effectively reduced to a one-loop calculation.

In Chap. 4 it was also pointed out that the dominant contributions of heavy Higgs bosons to $t\bar{t}$ production emanate from the kinematical phase space region close to the resonance.

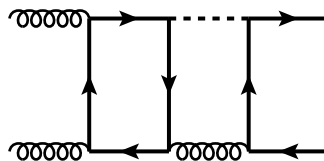


Figure 5.1.: Example Feynman diagram for an NLO two-loop contribution to $t\bar{t}$ production involving heavy Higgs bosons.

5. Heavy Higgs effects in top-quark pair production at next-to-leading order in α_s

Furthermore, at leading order we have already restricted ourselves to resonant contributions because the nonresonant amplitudes are subdominant as explained in Chap. 4. At NLO we are also interested in the *resonant* production of heavy Higgs bosons and their decay into $t\bar{t}$. Hence, we restrict the NLO calculation to the resonant regime by applying the so-called *soft gluon approximation* which is explained in Sec. 5.2.3.

Apart from these two approximations (large top mass limit and soft gluon approximation) we apply standard techniques to calculate the NLO corrections. In the following section these methods are described in detail.

5.2. Computational methods

This section is dedicated to the calculational tools and methods that have been applied to obtain the analytical and phenomenological results presented in Secs. 5.3 and 5.4.

5.2.1. Large top mass limit

The top mass dependence of the coupling between gluons and the heavy Higgs bosons ϕ_j mediated by the top loop (see for example Fig. 4.1 c) is given by the form factors

$$F_{Sj} = \frac{\alpha_s a_{tj}}{8\pi v} \tau [1 - (1 - \tau)f(\tau)], \quad F_{Pj} = \frac{\alpha_s b_{tj}}{16\pi v} \tau f(\tau), \quad \tau = 4m_t^2/s \quad (5.1)$$

where s is the partonic center of mass energy squared. If we were to consider Higgs production only then s would be fixed to $s = m_{\phi_j}^2$. The ratio τ then reads

$$\tau = \left(\frac{2m_t}{m_{\phi_j}} \right)^2. \quad (5.2)$$

For the SM Higgs with $m_{\phi_1} = m_h = 125\text{GeV}$ the inverse ratio

$$\eta \equiv \frac{1}{\tau} = \left(\frac{m_{\phi_j}}{2m_t} \right)^2 \quad (5.3)$$

is small such that an expansion of the form factors in powers of η is possible

$$F_{Sj} = \frac{\alpha_s a_{tj}}{8\pi v} \eta^{-1} [1 + (1 - \eta^{-1}) \arcsin^2(\sqrt{\eta})] = \frac{\alpha_s a_{tj}}{8\pi v} \left\{ \frac{2}{3} + \frac{7}{45} \eta + \mathcal{O}(\eta^2) \right\}, \quad (5.4)$$

$$F_{Pj} = -\frac{\alpha_s b_{tj}}{16\pi v} \eta^{-1} \arcsin^2(\sqrt{\eta}) = -\frac{\alpha_s b_{tj}}{16\pi v} \left\{ 1 + \frac{1}{3} \eta + \mathcal{O}(\eta^2) \right\}. \quad (5.5)$$

The large top mass limit

$$F_j^{S,\infty} = \lim_{m_t \rightarrow \infty} F_{Sj} = \frac{\alpha_s a_{tj}}{12\pi v}, \quad F_j^{P,\infty} = \lim_{m_t \rightarrow \infty} F_{Pj} = -\frac{\alpha_s b_{tj}}{16\pi v} \quad (5.6)$$

is equivalent to keeping only the leading order in the η -expansion and neglecting terms of order $\mathcal{O}(\eta)$. It is often said that in this approximation the top quark in the loop which mediates the coupling between gluons and Higgs bosons (see Fig. 4.1 c) is “integrated out” because the large top mass limit resembles an effective field theory with $N_F = 5$ active flavours and with an effective coupling between gluons and Higgs bosons. This effective coupling can be parametrized by the following Lagrangian

$$\mathcal{L}_{\text{eff}} = \sum_{j=2}^3 [f_{Sj} G_{\mu\nu}^a G_a^{\mu\nu} + f_{Pj} \tilde{G}_{\mu\nu}^a G_a^{\mu\nu}] \phi_j, \quad (5.7)$$

where $G_{\mu\nu}^a = \partial_\mu G_\nu^a - \partial_\nu G_\mu^a - g_s f^{abc} G_\mu^b G_\nu^c$ is the field strength tensor of the gluon field G_μ^a and $\widetilde{G}_{\mu\nu}^a = \epsilon_{\alpha\beta\mu\nu} G^{a,\alpha\beta}$ is its dual. f_{Sj} and f_{Pj} are the effective scalar and pseudoscalar couplings, respectively, of ϕ_j to gluons. The Lagrangian in Eq. (5.7) generates the couplings $gg\phi_j$, $ggg\phi_j$ and $gggg\phi_j$. Up to NLO QCD only the first two couplings contribute to heavy Higgs boson production and decay into top quarks. Their Feynman rules are given by

$$\begin{aligned}
 & \text{Diagram 1: } \phi_j \text{ (dashed) } \rightarrow \text{gluon}(a, \mu, p_1) + \text{gluon}(b, \nu, p_2) \\
 & = -4i\delta^{ab} \left[f_{Sj} (g_{\mu\nu}(p_1 \cdot p_2) - p_{2\mu} p_{1\nu}) - 2f_{Pj} \epsilon_{\mu\nu\rho\sigma} p_1^\rho p_2^\sigma \right], \quad (5.8) \\
 & \text{Diagram 2: } \phi_j \text{ (dashed) } \rightarrow \text{gluon}(a, \mu, p_1) + \text{gluon}(b, \nu, p_2) + \text{gluon}(c, \rho, p_3) \\
 & = 4g_s f^{abc} \left\{ f_{Sj} \left[g_{\mu\nu}(p_1 - p_2)_\rho + g_{\nu\rho}(p_2 - p_3)_\mu + g_{\rho\mu}(p_3 - p_1)_\nu \right] \right. \\
 & \quad \left. - 2f_{Pj} (p_1 + p_2 + p_3)^\alpha \epsilon_{\alpha\mu\nu\rho} \right\}, \quad (5.9)
 \end{aligned}$$

where the convention $\epsilon_{0123} = +1$ is used. The coefficients f_{Sj} and f_{Pj} in the effective Lagrangian describe the low energy behaviour of the coupling between heavy Higgs bosons and gluons. They can be expanded in powers of α_s as follows

$$f_{Sj} = \frac{\alpha_s}{\pi} \left(f_{Sj}^{(0)} + \frac{\alpha_s}{\pi} f_{Sj}^{(1)} + \dots \right), \quad f_{Pj} = \frac{\alpha_s}{\pi} \left(f_{Pj}^{(0)} + \frac{\alpha_s}{\pi} f_{Pj}^{(1)} + \dots \right). \quad (5.10)$$

By comparing the leading order of the η expansion of Green's functions in the full theory with Green's functions in the effective field theory the effective couplings can be determined

$$\frac{\alpha_s}{\pi} f_{Sj}^{(0)} = F_j^{S,\infty}, \quad \frac{\alpha_s}{\pi} f_{Pj}^{(0)} = F_j^{P,\infty}. \quad (5.11)$$

To obtain the coefficients of higher powers of α_s one has to calculate Green's functions in the full and effective theory up to the respective order in α_s . In Ref. [122–125] the Wilson coefficients have been calculated for up to three loops and the operator renormalization was performed accordingly. Here we need only the coefficients up to $f_{Sj}^{(1)}$, $f_{Pj}^{(1)}$

$$f_{Sj}^{(1)} = \frac{(4\pi)^\epsilon}{\Gamma(1-\epsilon)} \frac{a_{tj}}{12v} \left(\frac{11}{4} - \frac{\beta_0}{\epsilon} \right) = \frac{(4\pi)^\epsilon}{\Gamma(1-\epsilon)} f_{Sj}^{(0)} \left(\frac{11}{4} - \frac{\beta_0}{\epsilon} \right), \quad (5.12)$$

$$f_{Pj}^{(1)} = \frac{(4\pi)^\epsilon}{\Gamma(1-\epsilon)} \frac{b_{tj}}{16v} \frac{\beta_0}{\epsilon} = -\frac{(4\pi)^\epsilon}{\Gamma(1-\epsilon)} f_{Pj}^{(0)} \frac{\beta_0}{\epsilon}, \quad (5.13)$$

where $\epsilon = (4-d)/2$ is the dimensional regulator working in d space-time dimensions, and

$$\beta_0 = \frac{1}{2} \left(\frac{11}{6} C_A - \frac{2}{3} T_R N_F \right) \quad (5.14)$$

denotes the leading coefficient of the QCD β -function with N_F being the number of massless quark flavors and $T_R = 1/2$.

The expansion in η has been performed under the assumption that $m_{\phi_j} < 2m_t$. While this is true for the SM the relation does not hold for the heavy Higgs bosons studied here because we are interested in $m_{\phi_j} > 2m_t$. However, as pointed out in Sec. 2.6 (Fig. 2.3) it was shown in

5. Heavy Higgs effects in top-quark pair production at next-to-leading order in α_s



Figure 5.2.: Dyson summation for the Higgs propagator (dashed line). The gray circles are one-particle irreducible two-point functions inserted into the propagator.

Ref. [104] that the range of validity of the heavy top mass limit can be extended by applying an appropriate K -factor (Eq. (2.127)) such that the Higgs production cross section remains accurate within about 10% uncertainty up to masses $m_\phi = 1\text{TeV}$.

This method was applied in Ref. [104] to Higgs production. Here we apply the K -factor to the process $pp \rightarrow \phi \rightarrow t\bar{t}$ for resonantly produced heavy Higgs bosons ϕ with $m_\phi \in [2m_t, 1\text{TeV}]$. Since we consider the resonant region the heavy Higgs bosons are produced (almost) on-shell similar to the Higgs production process and then decay into $t\bar{t}$. Hence, the K -factor prescription captures the behaviour of the full m_t dependence to the accuracy given above. This argument holds for the heavy Higgs amplitude squared $|\mathcal{M}_{\phi_j}^{gg}|^2$ but not necessarily for the interference term $\mathcal{M}_{\text{QCD},\phi}^{gg}$. Therefore, in this work, we choose to apply the K -factor only to the signal amplitude squared.

As a final remark of this subsection it shall be pointed out that the heavy top mass limit is only applied to the gluon-Higgs interaction. Although the resulting effective interaction can be described by the effective Lagrangian given in Eq. (5.7) we are not working in an effective field theory because the top quark is not completely integrated out. In fact the top quark appears as a final state. The use of the notation and methods of effective field theory should rather be seen as equivalent to performing the η expansion and keeping only the leading term. It has been shown that for the gluon-Higgs interaction this approximation has an acceptable accuracy (10%) up to Higgs masses of about 1TeV when using an appropriate K -factor.

5.2.2. Treatment of unstable particles

The consistent gauge invariant treatment of unstable particles in perturbative quantum field theory is nontrivial. The problem is that in processes involving the production and decay of unstable particles a nonintegrable singularity arises from the propagator

$$\frac{1}{p^2 - m_\phi^2} \quad (5.15)$$

of the unstable particle ϕ at $p^2 = m_\phi^2$, where m_ϕ is the (real) mass of ϕ . Without further treatment the cross section for processes of this kind cannot be calculated. However, the resummation of insertions of one-particle irreducible self energy diagrams into the propagator (Dyson summation, see Fig. 5.2) yields

$$\frac{1}{p^2 - m_\phi^2 + \hat{\Sigma}(p^2)}, \quad (5.16)$$

where $\hat{\Sigma}(p^2)$ is the renormalized self energy of ϕ . The pole of this modified propagator is shifted off the real axis into the complex plain because for unstable particles the self energy acquires an imaginary part. Hence, there is no singularity at $p^2 = m_\phi^2$ anymore. Unfortunately, the Dyson summation mixes different orders of perturbation theory. This is problematic because gauge invariance is only guaranteed order by order. The mixture of (incomplete) contributions from different orders jeopardizes gauge invariance.

A consistent framework of describing resonances in perturbation theory is given by the so-called *complex mass scheme* [126–128]. This scheme introduces complex masses μ_ϕ for unstable particles such that the propagator can be written as

$$\frac{1}{p^2 - \mu_\phi^2} \quad (5.17)$$

with $\mu_\phi^2 \in \mathbb{C}$ but $p^2 \in \mathbb{R}$ for physical processes. Again, the singularity is avoided but this scheme also preserves gauge invariance [126–128]. The complex mass can be parametrized by

$$\mu_\phi^2 = m_\phi^2 - i\Gamma_\phi m_\phi. \quad (5.18)$$

The physical interpretation of m_ϕ and Γ_ϕ becomes clear when μ_ϕ is renormalized. The full propagator of the complex mass scheme has the form

$$\frac{1}{p^2 - \mu_\phi^2 + \hat{\Sigma}(p^2)}, \quad (5.19)$$

where μ_ϕ is the renormalized complex mass. The renormalization condition [127] in the complex mass scheme is the generalization of the on-shell renormalization condition, i.e. the position of the pole in the complex p^2 -plane in Eq. (5.19) is at $p^2 = \mu_\phi^2$:

$$\hat{\Sigma}(\mu_\phi^2) = 0. \quad (5.20)$$

To obtain an expression for the renormalized mass m_ϕ we express the renormalized self energy $\hat{\Sigma}$ in terms of the unrenormalized self energy Σ_0 , the complex-mass counter term $\delta\mu_\phi^2$ and the wave function counter term δZ_ϕ

$$\hat{\Sigma}(p^2) = \Sigma_0(p^2) + (p^2 - \mu_\phi^2)\delta Z_\phi - \delta\mu_\phi^2. \quad (5.21)$$

From the renormalization condition Eq. (5.20) then follows

$$\Sigma_0(\mu_\phi^2) = \delta\mu_\phi^2. \quad (5.22)$$

In the on-shell renormalization scheme the mass renormalization of on-shell mass $m_{\phi,OS}$ is given by $m_{\phi,0}^2 = m_{\phi,OS}^2 + \delta m_{\phi,OS}^2$ where $m_{\phi,0}$ is the bare mass and $\delta m_{\phi,OS}^2$ is the on-shell mass renormalization counter term. In analogy, the renormalization of the complex mass μ_ϕ is given by

$$m_{\phi,0}^2 = \mu_\phi^2 + \delta\mu_\phi^2, \quad (5.23)$$

where $m_{\phi,0}$ is of course the same real bare mass as in the on-shell case. Combining Eqs. (5.18), (5.22) and (5.23) gives

$$\Sigma_0(\mu_\phi^2) = m_{\phi,0}^2 - m_\phi^2 + i\Gamma_\phi m_\phi. \quad (5.24)$$

For $\Gamma_\phi \ll m_\phi$ the unrenormalized self energy $\Sigma_0(\mu_\phi^2)$ can be expanded around $\mu_\phi^2 = m_\phi^2$ [127]

$$\begin{aligned} \Sigma_0(\mu_\phi^2) &= \Sigma_0(m_\phi^2) + (\mu_\phi^2 - m_\phi^2) \left. \frac{\partial \Sigma_0(p^2)}{\partial p^2} \right|_{p^2=m_\phi^2} + \mathcal{O}((\mu_\phi^2 - m_\phi^2)^2) \\ &= \Sigma_0(m_\phi^2) - i\Gamma_\phi m_\phi \Sigma_0'(m_\phi^2) + \mathcal{O}((\mu_\phi^2 - m_\phi^2)^2), \end{aligned} \quad (5.25)$$

where Σ_0' denotes the derivative with respect to p^2 . Inserting Eq. (5.25) into Eq. (5.24) and taking the real part yields

$$m_\phi^2 = m_{\phi,0}^2 - \text{Re} [\Sigma_0(m_\phi^2)] + \Gamma_\phi m_\phi \text{Im} [\Sigma_0'(m_\phi^2)]. \quad (5.26)$$

5. Heavy Higgs effects in top-quark pair production at next-to-leading order in α_s

The second term on the rhs of Eq. (5.25) is of one order higher than the first term [127] in the weak and Yukawa couplings. The same holds for the third term on the rhs of Eq. (5.26). Since we are working only in the first order of weak and Yukawa couplings the third term on the rhs of Eq. (5.26) can be neglected

$$m_\phi^2 = m_{\phi,0}^2 - \text{Re} \left[\Sigma_0(m_\phi^2) \right] + \mathcal{O}(\alpha^2, y^4), \quad (5.27)$$

where α is the coupling constant of the weak interaction and y is the Yukawa coupling. Using the on-shell scheme relation $\delta m_{\phi,OS}^2 = \text{Re} \left[\Sigma_0(m_\phi^2) \right]$ [129] one finds

$$m_\phi^2 = m_{\phi,0}^2 - \delta m_{\phi,OS}^2 = m_{\phi,OS}^2 \quad (5.28)$$

in the order of perturbation theory considered here. Hence, the mass m_ϕ in the parametrization of μ_ϕ in Eq. (5.18) is the on-shell mass up to order $\mathcal{O}(\alpha^2, y^4)$.

Taking the imaginary part of Eq. (5.24) (after expansion) gives the following relation

$$\Gamma_\phi m_\phi = \text{Im} \left[\Sigma_0(m_\phi^2) \right] - \Gamma_\phi m_\phi \text{Re} \left[\Sigma'_0(m_\phi^2) \right]. \quad (5.29)$$

Only the first term on the rhs is kept in the order of perturbation theory considered here. Thus Eq. (5.29) yields

$$\Gamma_\phi = \frac{1}{m_\phi} \text{Im} \left[\Sigma_0(m_\phi^2) \right] \quad (5.30)$$

which is the usual definition of the on-shell width in the approximation that $\Gamma_\phi \ll m_\phi$. This approximation is introduced by the expansion in Eq. (5.25) and keeping only the first term.

In summary, in the lowest order in the weak and Yukawa coupling constants the complex mass scheme is equivalent to using the Higgs on-shell mass m_ϕ and introducing a constant width Γ_ϕ in the propagator

$$\frac{1}{p^2 - m_\phi^2 + i\Gamma_\phi m_\phi}. \quad (5.31)$$

5.2.3. Soft gluon approximation

As already mentioned in the introduction to this chapter the aim of this work is to calculate the NLO QCD corrections to the *resonant* production of heavy Higgs bosons and the subsequent decay into $t\bar{t}$. At LO this was realized by taking only the resonant heavy Higgs contributions (Fig. 4.1 c) into account. At NLO this is done by formally expanding the amplitude around the pole

$$\frac{1}{s - m_\phi^2 + i\Gamma_\phi m_\phi} \quad (5.32)$$

and keeping only the leading order. This is also called the *leading pole approximation* [130,131]. In Eq. (5.32) s denotes the partonic center of mass energy squared and is equal to the four-momentum squared p^2 of the Higgs propagator, m_ϕ is the heavy Higgs boson mass and Γ_ϕ the decay width. In general the amplitude can be written as follows [130–133]

$$\mathcal{A} = \frac{\mathcal{W}(s)}{s - m_\phi^2 + \hat{\Sigma}(s)} + \mathcal{N}(s). \quad (5.33)$$

The first term is the part of the amplitude that contains resonant contributions and the second term is the nonresonant part. The position of the pole μ_ϕ is defined by the following equation

$$\mu_\phi^2 - m_\phi^2 + \hat{\Sigma}(\mu_\phi^2) = 0 \quad \Rightarrow \quad m_\phi^2 = \mu_\phi^2 + \hat{\Sigma}(\mu_\phi^2). \quad (5.34)$$

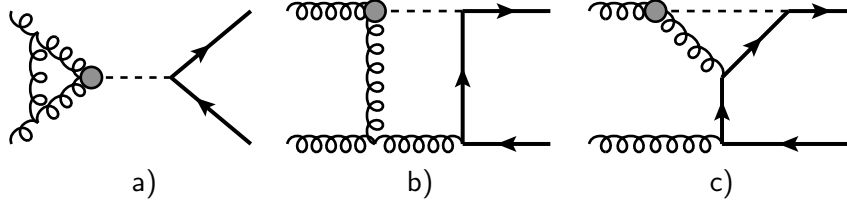


Figure 5.3.: Example Feynman diagrams for different types of amplitudes being part of the heavy Higgs boson contribution to $t\bar{t}$ production. a) factorizable, b) nonfactorizable resonant, c) nonfactorizable nonresonant.

By inserting the expression in Eq. (5.34) for m_ϕ into Eq. (5.33) and expanding the self energy around the pole

$$\hat{\Sigma}(s) = \hat{\Sigma}(\mu_\phi^2) + (s - \mu_\phi^2)\hat{\Sigma}'(\mu_\phi^2) + \mathcal{O}((s - \mu_\phi^2)^2) \quad (5.35)$$

one can isolate the pole contribution in \mathcal{A} as follows [130–133]

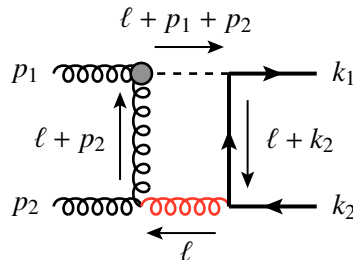
$$\mathcal{A} = \frac{\mathcal{W}(\mu_\phi^2)}{s - \mu_\phi^2} \frac{1}{1 + \hat{\Sigma}'(\mu_\phi^2)} + \left[\frac{\mathcal{W}(s)}{s - m_\phi^2 + \hat{\Sigma}(s)} - \frac{\mathcal{W}(\mu_\phi^2)}{s - \mu_\phi^2} \frac{1}{1 + \hat{\Sigma}'(\mu_\phi^2)} \right] + \mathcal{N}(s), \quad (5.36)$$

where also the numerator of the first term was expanded around μ_ϕ^2 and only the leading term was kept. The three terms on the rhs of Eq. (5.36) can be classified as follows

- I) factorizable (manifestly resonant), first term on the rhs of Eq. (5.36), Fig. 5.3a
- II) nonfactorizable resonant, second term on the rhs of Eq. (5.36) in square bracket, Fig. 5.3b
- III) nonfactorizable nonresonant, third term on the rhs of Eq. (5.36), Fig. 5.3c

The factorizable amplitudes consist of Higgs boson production and decay connected by a resonant Higgs propagator of the form given in Eq. (5.32). In particular, the Higgs boson propagator is not part of a loop. The second category comprises of contributions which are nonfactorizable, i.e. where Higgs boson production and decay can not be distinguished. In this category the Higgs boson propagator is part of the loop. However, for this class of radiative corrections the Higgs boson propagator can become resonant when the additional (with respect to the Born configuration) gluon in the loop becomes soft. The third category contains contributions that are nonfactorizable and where the Higgs boson propagator cannot become resonant. These amplitudes do not contribute to the pole and are therefore neglected in the pole approximation.

In order to isolate the resonant part of amplitudes in category II the so-called soft gluon approximation (SGA) is applied. When the additional gluon connecting Higgs production and decay is soft the Higgs propagator can become resonant. As an example consider the diagram shown in Fig. 5.3b with the following momentum flow



5. Heavy Higgs effects in top-quark pair production at next-to-leading order in α_s

where ℓ denotes the loop momentum and the additional gluon is shown in red. In the limit $\ell \rightarrow 0$ the Higgs propagator

$$\frac{1}{(\ell + p_1 + p_2)^2 - m_\phi^2 + i\Gamma_\phi m_\phi} \xrightarrow{\ell \rightarrow 0} \frac{1}{s - m_\phi^2 + i\Gamma_\phi m_\phi} \quad (5.37)$$

with $s = (p_1 + p_2)^2$. Hence, we apply the SGA to the nonfactorizable resonant contribution to extract the leading pole contribution. Technically, the SGA is performed by neglecting the additional gluon momentum q in the numerators of virtual and real corrections. In the denominator q^2 is neglected wherever possible. However, in the loop and phase space integrations, respectively, the gluon momentum q is not restricted to small values but integrated as usual up to infinity. This procedure simplifies the loop and phase space integrals considerably but introduces an uncertainty of the order of $\mathcal{O}(\Gamma_\phi/m_\phi)$ [134, 135].

To cancel the IR divergences of the virtual diagrams they have to be combined with the appropriate real contributions. Virtual diagrams of category II that are treated in the SGA then have to be added to the corresponding real corrections treated in the same approximation. It turns out and it is well known [134–137] that in the SGA the nonfactorizable resonant (category II) virtual contributions cancel exactly the corresponding real corrections. An example of the cancellation is given in Appendix F. Due to the SGA the validity of this approach to calculate heavy Higgs boson production and decay to $t\bar{t}$ is restricted to the resonance region. The uncertainties are of the order of $\mathcal{O}(\Gamma_\phi/m_\phi)$.

Schematically, the cancellation is performed as follows. First let us write the resonant NLO correction $\mathcal{M}_{\text{NLO}}^{\text{res}}$ (at the level of the matrix element squared) to the process $pp \rightarrow \phi \rightarrow t\bar{t}$ as

$$\mathcal{M}_{\text{NLO}}^{\text{res}} = \mathcal{M}_V^{\text{res}} + \int d\Phi_g \mathcal{M}_R^{\text{res}}, \quad (5.38)$$

where $\mathcal{M}_V^{\text{res}}$ represents the resonant contributions to the renormalized virtual corrections which live in the two particle final state phase space. $\mathcal{M}_R^{\text{res}}$ denotes the resonant contributions to the real corrections which involve the emission of an additional gluon in the final state. The integration is performed over the phase space of this additional gluon. The second term on the rhs of Eq. (5.38) cancels the IR divergences of the virtual corrections. The virtual and real corrections can be rewritten as

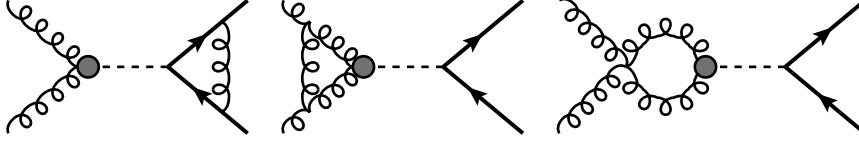
$$\mathcal{M}_V^{\text{res}} = \mathcal{M}_V^{\text{fact}} + \mathcal{M}_{V,\text{SGA}}^{\text{nf}}, \quad (5.39)$$

$$\mathcal{M}_R^{\text{res}} = \mathcal{M}_R^{\text{res}} + \mathcal{M}_{R,\text{SGA}}^{\text{nf}} - \mathcal{M}_{R,\text{SGA}}^{\text{nf}}. \quad (5.40)$$

$\mathcal{M}_V^{\text{fact}}$ is the factorizable contribution of the virtual corrections, $\mathcal{M}_{V,\text{SGA}}^{\text{nf}}$ is the nonfactorizable contribution of the virtual correction in the SGA, i.e. the resonant contribution of the nonfactorizable virtual corrections and $\mathcal{M}_{R,\text{SGA}}^{\text{nf}}$ denotes the real corrections in the SGA corresponding to the nonfactorizable virtual corrections. Using Eqs. (5.39) and (5.40) Eq. (5.38) can be written as

$$\begin{aligned} \mathcal{M}_{\text{NLO}}^{\text{res}} &= \mathcal{M}_V^{\text{fact}} + \underbrace{\mathcal{M}_{V,\text{SGA}}^{\text{nf}} + \int d\Phi_g \mathcal{M}_{R,\text{SGA}}^{\text{nf}}}_{=0} + \int d\Phi_g (\mathcal{M}_R^{\text{res}} - \mathcal{M}_{R,\text{SGA}}^{\text{nf}}) \\ &= \mathcal{M}_V^{\text{fact}} + \int d\Phi_g (\mathcal{M}_R^{\text{res}} - \mathcal{M}_{R,\text{SGA}}^{\text{nf}}). \end{aligned} \quad (5.41)$$

Hence, the ingredients for the calculation of the resonant NLO corrections are $\mathcal{M}_V^{\text{fact}}$, $\mathcal{M}_R^{\text{res}}$ and $\mathcal{M}_{R,\text{SGA}}^{\text{nf}}$. Note, that the numerical computation of the NLO corrections requires the application

Figure 5.4.: Factorizable contributions in the gg channel.

of an IR-subtraction scheme which is not included above. However, the subtraction scheme which is chosen to facilitate the numerical evaluation of the NLO corrections is described in Sec. 5.2.5. Furthermore, the SGA is in fact only needed for the Higgs-QCD interference contribution to the process but not for the signal amplitude squared. At NLO the signal amplitude squared does not involve nonfactorizable resonant contributions. This will be illustrated in Sec. 5.2.4.

The decomposition of the amplitude into factorizable and nonfactorizable resonant contribution as given in Eq. (5.36) is gauge invariant. The first term (factorizable contributions) is in general only gauge invariant if the amplitudes of production and decay are evaluated on-shell as indicated by $\mathcal{W}(s = \mu_\phi^2)^1$ in Eq. (5.36). However, in the case at hand the amplitudes for off-shell production and decay of a Higgs boson are gauge invariant. In our approach we evaluate the numerator of the first term in Eq. (5.36) off-shell which includes also nonresonant contributions. These are, however, gauge invariant and suppressed in the resonant region.

5.2.4. Virtual corrections

In this subsection a detailed account is given of the virtual corrections contributing to the resonant production of heavy Higgs bosons and their decay into $t\bar{t}$. Furthermore methods and tools to derive the virtual corrections are presented.

The virtual corrections contributing at $\mathcal{O}(\alpha_s^3)$ to the gluon fusion process $gg \rightarrow t\bar{t}$ involving a heavy Higgs boson in the large top mass limit are shown in Figs. 5.4 and 5.5. While Fig. 5.4 presents the factorizable contributions Fig. 5.5a shows example Feynman diagrams for the nonfactorizable resonant contributions and Fig. 5.5b for nonfactorizable nonresonant contributions. In the quark annihilation channel $q\bar{q} \rightarrow t\bar{t}$ the only kind of Feynman diagram contributing at $\mathcal{O}(\alpha_s^3)$ is depicted in Fig. 5.6. It is a nonfactorizable nonresonant contribution. At a first glance one would expect the diagram in Fig. 5.6 to have resonant contributions when the gluon in the loop becomes soft. However, for $\ell \rightarrow 0$, where ℓ is the gluon momentum flowing into the $gg\phi$ vertex, the whole vertex vanishes too (cf. Eq. (5.8)). In the approximation considered here only resonant contributions are taken into account, such that the $q\bar{q}$ channel does not contribute at $\mathcal{O}(\alpha_s^3)$. For the calculation of observables such as the cross section the scattering amplitude has to be squared. Schematically, up to one-loop order this can be written as

$$|\mathcal{M}|^2 = \left| \text{tree} + \text{one-loop} \right|^2 = \left| \text{tree} \right|^2 + 2\text{Re} \left[\text{one-loop} \times \left(\text{tree} \right)^* \right] + \dots \quad (5.42)$$

where diagrams with a single-lined circle represent tree-level processes and with double-lined circles one-loop processes. The dots stand for one-loop contributions squared which are of higher order in α_s . The first term on the rhs of the second equal sign in Eq. (5.42) is the LO

¹ Since we work in the lowest order in the weak and Yukawa couplings the on-shell amplitudes are evaluated at $s = m_\phi^2$ instead of the complex value μ_ϕ^2 .

5. Heavy Higgs effects in top-quark pair production at next-to-leading order in α_s

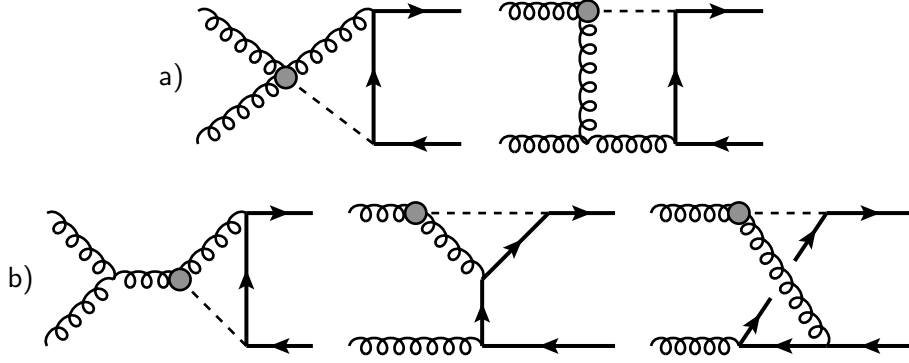


Figure 5.5.: Example Feynman diagrams for nonfactorizable contributions in the gg channel: a) resonant, b) nonresonant.

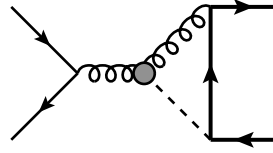


Figure 5.6.: Example Feynman diagram for nonfactorizable nonresonant contribution in the $q\bar{q}$ channel.

contribution which is discussed in Chap. 4 and is of $\mathcal{O}(\alpha_s^2)$ for the case at hand. In Eq. (5.42) this contribution is represented by a generic tree-level diagram. However, for the leading order contribution we work with the full m_t dependence in the $gg\phi$ vertex. Therefore, the leading order is a one-loop process. The second term on the rhs of the second equal sign in Eq. (5.42) is the interference of the LO contribution with the NLO one-loop contribution which is of $\mathcal{O}(\alpha_s^3)$. In this order we work in the heavy top limit such that the single-lined circle contribution in Eq. (5.42) is indeed a tree-level process (Fig. 5.8) and the double-lined circle contribution a one-loop process. The tree-loop interference ($\mathcal{O}(\alpha_s^3)$ correction) can be further decomposed as follows

$$\begin{aligned}
 & \left(\text{circle} \right) \times \left(\text{circle} \right)^* = \left(\text{QCDW} + \text{Higgs} \right) \times \left(\text{QCD} + \text{Higgs} \right)^* \\
 & = \left(\text{Higgs} \right) \times \left(\text{Higgs} \right)^* + \left(\text{Higgs} \right) \times \left(\text{QCD} \right)^* + \left(\text{QCD} \right) \times \left(\text{Higgs} \right)^* \\
 & + \left(\text{QCDW} \right) \times \left(\text{QCD} \right)^* , \tag{5.43}
 \end{aligned}$$

where “QCD” denotes pure QCD diagrams, “QCDW” denotes QCD and weak corrections and “Higgs” denotes diagrams involving a heavy Higgs boson. As for the LO contribution discussed in Chap. 4 one can split up the NLO correction into

1. signal amplitude squared (first term in the second line of Eq. (5.43))
2. Higgs-QCD interference (second and third term in the second line of Eq. (5.43))

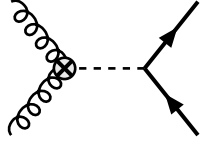


Figure 5.7.: Born-like heavy Higgs contribution from the $O(\alpha_s^2)$ term $f_{S,P}^{(1)}$ of the effective $gg\phi$ coupling.

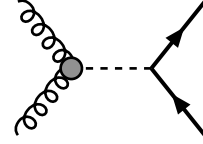


Figure 5.8.: Leading order heavy Higgs exchange diagram in the heavy top mass limit.

3. QCDW contribution (third line in Eq. (5.43)).

The virtual QCDW contribution including the $q\bar{q}$ channel is known from Ref. [111, 112, 138–141]. It is taken into account in all numerical NLO results presented in Sec. 5.4 but is not discussed further here. The contribution from the interference of weak corrections with LO Higgs diagrams (Fig. 4.1 c)

$$\left(\text{weak} \right) \times \left(\text{Higgs} \right)^* \quad (5.44)$$

is formally of higher order and not taken into account. This work focuses on the contributions in the second line of Eq. (5.43).

Let us first consider the signal amplitude squared $\mathcal{M}_\phi^{(1)}$. It is given by the sum of the factorizable loop-contribution $\mathcal{A}_\phi^{(1),\text{fact}}$ (Fig. 5.4), the nonfactorizable resonant contribution $\mathcal{A}_\phi^{(1),\text{nf,res}}$ (Fig. 5.5a) and the Born-like $O(\alpha_s^2)$ contribution $\mathcal{A}_{\phi,B}^{(1)}$ (Fig. 5.7) from $f_{S,P}^{(1)}$ in Eqs. (5.12) and (5.13) interfered with the tree-level contribution for the heavy Higgs exchange in the large top mass limit $\mathcal{A}_\phi^{(0),\infty}$ (Fig. 5.8)

$$\begin{aligned} \mathcal{M}_\phi^{(1)} &\equiv \frac{1}{N_{gg}} \sum_{\text{spin,col.}} \left\{ 2\text{Re} \left[\left(\text{Higgs} \right) \times \left(\text{Higgs} \right)^* \right] + 2\text{Re} \left[\left(\text{Higgs} \right) \times \left(\text{Higgs} \right)^* \right] \right\} \\ &= \frac{1}{N_{gg}} \sum_{\text{spin,col.}} \left\{ 2\text{Re} \left[\left(\mathcal{A}_\phi^{(1),\text{fact}} + \mathcal{A}_\phi^{(1),\text{nf,res}} \right) \times \left(\mathcal{A}_\phi^{(0),\infty} \right)^* \right] + 2\text{Re} \left[\mathcal{A}_{\phi,B}^{(1)} \times \left(\mathcal{A}_\phi^{(0),\infty} \right)^* \right] \right\}. \end{aligned} \quad (5.45)$$

However, the interference of nonfactorizable resonant contributions $\mathcal{A}_\phi^{(1),\text{nf,res}}$ (Fig. 5.5a) with the LO contribution $\mathcal{A}_\phi^{(0),\infty}$ (Fig. 5.8) vanishes due to the QCD color structure

$$\mathcal{A}_\phi^{(1),\text{nf,res}} \times \left(\mathcal{A}_\phi^{(0),\infty} \right)^* \sim f^{abc} t_{ij}^c \times \delta^{ab} \delta_{ij} = 0, \quad (5.46)$$

where f^{abc} are the structure functions of $SU(3)_c$ and t_{ij}^c are the generators of $SU(3)_c$ in the fundamental representation. a, b, c denote color indices in the adjoint representation and i, j in the fundamental representation. Hence, only the interference of $\mathcal{A}_\phi^{(1),\text{fact}}$ and $\mathcal{A}_{\phi,B}^{(1)}$ with $\mathcal{A}_\phi^{(0),\infty}$ contributes to the resonant signal amplitude squared

$$\mathcal{M}_\phi^{(1)} = \frac{1}{N_{gg}} \sum_{\text{spin,col.}} 2\text{Re} \left[\left(\mathcal{A}_\phi^{(1),\text{fact}} + \mathcal{A}_{\phi,B}^{(1)} \right) \times \left(\mathcal{A}_\phi^{(0),\infty} \right)^* \right]. \quad (5.47)$$

5. Heavy Higgs effects in top-quark pair production at next-to-leading order in α_s

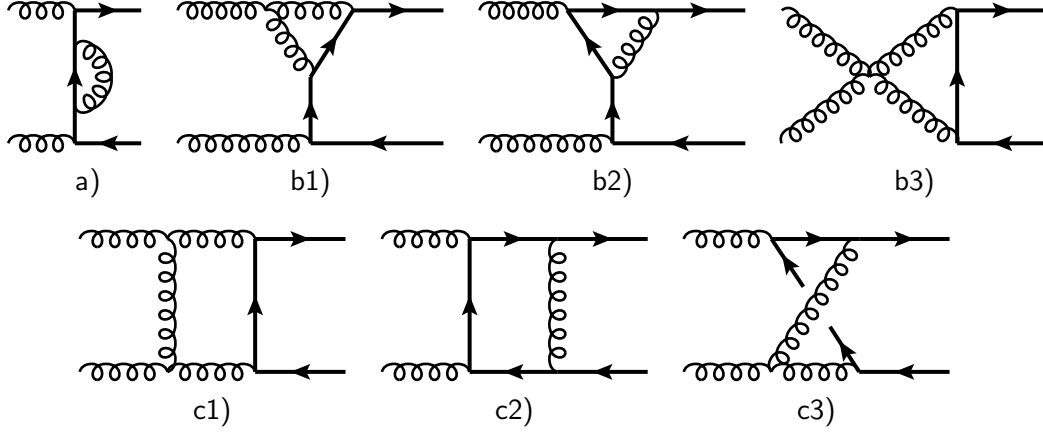


Figure 5.9.: Example QCD Feynman diagrams contributing to the interference term $\mathcal{M}_{\phi, \text{QCD}}^{(0,1)}$.

The second contribution is the interference

$$\begin{aligned}
 \mathcal{M}_{\phi, \text{QCD}}^{(1,0)} &\equiv \frac{1}{N_{gg}^{\text{spin, col.}}} \sum 2\text{Re} \left[\text{Higgs} \times \left(\text{QCD} \right)^* \right] \\
 &= \frac{1}{N_{gg}^{\text{spin, col.}}} \sum 2\text{Re} \left[\left(\mathcal{A}_{\phi}^{(1, \text{fact})} + \mathcal{A}_{\phi, \text{SGA}}^{(1, \text{nf, res})} \right) \times \left(\mathcal{A}_{\text{QCD}}^{(0)} \right)^* \right] \\
 &= \mathcal{M}_{\phi, \text{QCD}}^{(1,0, \text{fact})} + \mathcal{M}_{\phi, \text{QCD, SGA}}^{(1,0, \text{nf})}, \tag{5.48}
 \end{aligned}$$

where $\mathcal{A}_{\text{QCD}}^{(0)}$ is the LO QCD contribution (cf. Chap. 4). The nonfactorizable resonant amplitude $\mathcal{A}_{\phi}^{(1, \text{nf, res})}$ is evaluated in the SGA to extract only the resonant contribution denoted by $\mathcal{A}_{\phi, \text{SGA}}^{(1, \text{nf, res})}$. The factorizable and nonfactorizable interference terms are defined as

$$\mathcal{M}_{\phi, \text{QCD}}^{(1,0, \text{fact})} = \frac{1}{N_{gg}^{\text{spin, col.}}} \sum 2\text{Re} \left[\mathcal{A}_{\phi}^{(1, \text{fact})} \times \left(\mathcal{A}_{\text{QCD}}^{(0)} \right)^* \right], \tag{5.49}$$

$$\mathcal{M}_{\phi, \text{QCD, SGA}}^{(1,0, \text{nf})} = \frac{1}{N_{gg}^{\text{spin, col.}}} \sum 2\text{Re} \left[\mathcal{A}_{\phi, \text{SGA}}^{(1, \text{nf, res})} \times \left(\mathcal{A}_{\text{QCD}}^{(0)} \right)^* \right]. \tag{5.50}$$

Finally, the third contribution in the second line of Eq. (5.43) is given by

$$\begin{aligned}
 \mathcal{M}_{\phi, \text{QCD}}^{(0,1)} &\equiv \frac{1}{N_{gg}^{\text{spin, col.}}} \sum 2\text{Re} \left[\text{QCD} \times \left(\text{Higgs} \right)^* \right] \\
 &= \frac{1}{N_{gg}^{\text{spin, col.}}} \sum 2\text{Re} \left[\mathcal{A}_{\text{QCD}}^{(1)} \times \left(\mathcal{A}_{\phi}^{(0)} \right)^* \right], \tag{5.51}
 \end{aligned}$$

where $\mathcal{A}_{\text{QCD}}^{(1)}$ is the pure QCD one-loop correction to $t\bar{t}$ production in the gg channel. Due to the QCD color structure only a subclass of one-loop QCD diagrams contributes to the interference $\mathcal{M}_{\phi, \text{QCD}}^{(0,1)}$. Example diagrams are shown in Fig. 5.9.

This concludes the list of contributions to the virtual NLO QCD corrections to $t\bar{t}$ production involving heavy Higgs boson. The calculation of these corrections has been performed by making use of the computer algebra programs FORM [142] and Mathematica [143]. In the following some aspects of the calculation of the one-loop corrections will be discussed.

Dimensional Regularization

In quantum field theoretical (e.g. in QCD) calculations of observable quantities beyond LO divergences occur in intermediate steps. One source of these divergences are the point-like interactions of particles in the theory. These kind of divergences are often referred to as *UV-divergences* because they are related to the divergences of loop-integrals in the limit where the loop momentum $\ell \rightarrow \infty$. Another source of divergences are soft and/or collinear massless particles. These divergences are often collectively called *IR-divergences* because they are related to loop integral divergences in the limit where $\ell \rightarrow 0$. In order to perform calculations at one-loop order and beyond it is necessary to parametrize the divergences occurring in loop integrals (and ultimately also in real radiation corrections). This parametrization is also called *regularization* because a parameter is introduced that regularizes the divergences for certain values of the regulator. The final result of the physical theory is then obtained in a some limit of this regulator and, in particular, is independent of the chosen regularization procedure. One requirement for the regularization procedure is to be unitary [144] but that still leaves a variety of regulators to be chosen from, e.g. cut-off regularization, Pauli-Villars regularization, dimensional regularization. The kind of regularization that has become the most common tool in calculating observables in high energy physics is *dimensional regularization* [145–149] (DimReg). Here the idea is to calculate Feynman diagrams, in particular, loop integrals as an analytic function of the dimensionality $d = 4 - 2\epsilon$ of space-time. The singularities for example of one-loop integrals then appear as $1/\epsilon$ -poles (UV and IR-divergences) and $1/\epsilon^2$ -poles (IR-divergences). In the full physical observable these divergences cancel such that the limit $\epsilon \rightarrow 0$ ($d \rightarrow 4$) can safely be performed. Dimensional regularization has some advantageous features [150] which have made it so popular in loop-calculations

1. Often the calculational effort in DimReg is less than in other regularization procedures.
2. DimReg preserves Poincaré and gauge invariance.
3. As already mentioned DimReg cannot only regularize UV-divergences but also IR-divergences [151–153]. In this context it also can be used to dimensionally regularize IR-divergent phase space integrals in the real corrections.

There exist different prescriptions of dimensional regularization called *schemes* (see e.g. [144]). They all have in common that momenta of *internal*² particles are defined in d dimensions. However, the regularization schemes differ in the treatment of the number of polarizations and helicities of internal particles and whether momenta of *external*³ particles and their polarizations/helicities are treated in d or 4 dimensions. Here two examples for dimensional regularization schemes are given. In *conventional dimensional regularization* all momenta (internal and external) are defined in d dimensions and there are $d - 2$ gluon polarizations for internal as well as external gluons. The second example is the *'t Hooft-Veltman* scheme where only internal momenta and gluon polarizations are treated in d dimensions while external ones are treated in 4 dimensions. In this work the 't Hooft-Veltman scheme is used for dimensional regularization.

Extending the theory from four space-time dimensions to d space-time dimensions also changes the *mass dimension* of the fields and couplings in the theory. In natural units a physical quantity can be expressed in powers of mass which is called the mass dimension. For example, the SI units s, m, kg have the mass dimensions $[s] = -1$, $[m] = -1$, $[kg] = 1$, where the

²For virtual diagrams internal particles are defined [154] as part of a one-particle irreducible loop diagram. For real diagrams they are defined as soft and/or collinear particles in the initial or final state.

³All particles that are not internal (see definition above) are external.

5. Heavy Higgs effects in top-quark pair production at next-to-leading order in α_s

square bracket denotes the mass dimension. Consequently, energy has the mass dimension $[J] = [\text{kg m}^2/\text{s}^2] = 1 - 2 - (-2) = 1$ and the action $[Js] = 1 - 1 = 0$. Since

$$0 = [S] = \left[\int d^d x \mathcal{L} \right] = [d^d x] + [\mathcal{L}] = -d + [\mathcal{L}] \quad (5.52)$$

the Lagrangian \mathcal{L} must have mass dimension $[\mathcal{L}] = d$. The kinetic term for the gluons involves terms like

$$[\partial_\mu A_\nu \partial^\mu A^\nu] = 2 \left[\frac{\partial}{\partial x} \right] + 2[A] = 2 + 2[A] \stackrel{!}{=} d. \quad (5.53)$$

Hence, the mass dimension of the gluon field is $[A] = (d - 2)/2$. The gluon three-vertex has mass dimension

$$\left[g_s^{\text{dim}} \frac{\partial}{\partial x} AAA \right] = [g_s^{\text{dim}}] + 3[A] + 1 = [g_s^{\text{dim}}] + \frac{3}{2}(d - 2) + 1 \stackrel{!}{=} d \quad (5.54)$$

such that the QCD coupling constant in d dimensions has mass dimension $[g_s^{\text{dim}}] = \frac{4-d}{2} = \epsilon$. In order to keep g_s dimensionless an arbitrary mass scale μ is introduced

$$g_s^{\text{dim}} = \mu^\epsilon g_s \quad (5.55)$$

with $[\mu] = 1$. This mass scale is called *renormalization scale* because it parametrizes the dependence of the renormalized coupling constant on the energy scale.

The extension of γ_5 to d dimensions is problematic. In particular, simultaneously assuming a d dimensional anticommuting $(\{\gamma_5, \gamma_\mu\} = 0)$ γ_5 and cyclicity of the trace ("naive" γ_5) leads to inconsistencies. For example, starting from $\text{Tr}[\gamma_5 \gamma_\alpha \gamma_\mu \gamma_\nu \gamma_\rho \gamma_\sigma \gamma^\alpha]$ and using a naive γ_5 one can derive the relation

$$d \text{Tr}[\gamma_5 \gamma_\mu \gamma_\nu \gamma_\rho \gamma_\sigma] = (8 - d) \text{Tr}[\gamma_5 \gamma_\mu \gamma_\nu \gamma_\rho \gamma_\sigma]. \quad (5.56)$$

Equation (5.56) is true for $d = 4$ where $\text{Tr}[\gamma_5 \gamma_\mu \gamma_\nu \gamma_\rho \gamma_\sigma] \neq 0$ but in $d \neq 4$ dimensions Eq. (5.56) is fulfilled only for $\text{Tr}[\gamma_5 \gamma_\mu \gamma_\nu \gamma_\rho \gamma_\sigma] = 0$. Hence, the limit $d \rightarrow 4$ is not continuous. This is related to the axial anomaly [155, 156], the nonconservation of the axial current $j_5^\mu = \bar{\psi} \gamma^\mu \gamma_5 \psi$ for massless fermions. This result has been derived by using the Pauli-Villars regularization which does not suffer from inconsistencies in the treatment of γ_5 . However, when using the naive γ_5 in DimReg one would be able to derive [150] the wrong result $\partial_\mu j_5^\mu = 0$. Methods to remedy this situation have been devised e.g. in Ref. [157], where a finite counter term is used to restore the Adler-Bell-Jackiw anomaly. However, in the calculations performed in this work this kind of renormalization is not required [158] because here at NLO only diagrams containing open fermion lines contribute. The LO contribution with the full m_t dependence where the gluons couple to the heavy Higgs bosons via a top-quark loop (Fig. 4.1 c) is UV and IR finite. Hence, this contribution can be evaluated in four space-time dimensions where γ_5 is well-defined.

Passarino–Veltman reduction

A general one-loop Feynman diagram gives rise to so-called *tensor integrals* of the following form

$$I_N^{\mu_1 \mu_2 \dots \mu_r} = \int \frac{d^d \ell}{(2\pi)^d} \frac{\ell^{\mu_1} \ell^{\mu_2} \dots \ell^{\mu_r}}{P_1 P_2 \dots P_N}, \quad (5.57)$$

where N is the number of propagators in the loop, μ_1, \dots, μ_r are Lorentz indices and r is the rank of the tensor integral. P_1, \dots, P_N denote inverse propagators which are functions of the

masses m_i of the particles in the loop, the external (with respect to the loop) momenta p_i and the loop momentum ℓ

$$P_j = P_j(m_j, \{p_i\}, \ell), \quad i = 1, \dots, N-1, \quad j = 1, \dots, N. \quad (5.58)$$

In Eq. (5.57) the loop integral is dimensionally regularized by extending the integration to $d = 4 - 2\epsilon$ space-time dimensions. The integral I_N is conventionally denoted by $I_1 = A$, $I_2 = B$, $I_3 = C$, etc. Passarino and Veltman [159] introduced a method to reduce tensor one-loop integrals of the form in Eq. (5.57) to scalar integrals of the form

$$I_N = \int \frac{d^d \ell}{(2\pi)^d} \frac{1}{P_1 P_2 \dots P_N}, \quad (5.59)$$

where the numerator does not contain the loop momentum. In the following this method, often referred to as *Passarino–Veltman reduction*, is described briefly.

Since $I_N^{\mu_1 \mu_2 \dots \mu_r}$ is indeed a rank- r Lorentz tensor which depends only on the external momenta p_i it is possible to decompose $I_N^{\mu_1 \mu_2 \dots \mu_r}$ into the most general rank- r Lorentz tensor structure that can be constructed out of p_i^μ and $g^{\mu\nu}$. As an example consider the rank-one two-point function

$$B^\mu = \int \frac{d^d \ell}{(2\pi)^d} \frac{\ell^\mu}{[\ell^2 - m_1^2][(\ell + p_1)^2 - m_2^2]} = p_1^\mu B_1. \quad (5.60)$$

The coefficient B_1 can be determined by contracting Eq. (5.60) with $p_{1\mu}$

$$\int \frac{d^d \ell}{(2\pi)^d} \frac{\ell \cdot p_1}{[\ell^2 - m_1^2][(\ell + p_1)^2 - m_2^2]} = p_1^2 B_1. \quad (5.61)$$

The numerator of the integrand can be written as

$$\ell \cdot p_1 = \frac{1}{2} \left([(\ell + p_1)^2 - m_2^2] - [\ell^2 - m_1^2] - p_1^2 - m_1^2 + m_2^2 \right). \quad (5.62)$$

Inserting Eq. (5.62) into Eq. (5.61) yields

$$B_1 = \frac{1}{2p_1^2} \left(A(m_1) - A(m_2) - (p_1^2 + m_1^2 - m_2^2) B_0(p_1^2, m_1^2, m_2^2) \right), \quad (5.63)$$

where

$$A(m) = \int \frac{d^d \ell}{(2\pi)^d} \frac{1}{\ell^2 - m^2}, \quad (5.64)$$

$$B_0(p^2, m_1^2, m_2^2) = \int \frac{d^d \ell}{(2\pi)^d} \frac{1}{[\ell^2 - m_1^2][(\ell + p)^2 - m_2^2]} \quad (5.65)$$

are scalar integrals. The key point of this method which restricts it to one-loop tensor integrals is Eq. (5.62). At one-loop it is always possible to rewrite scalar products of the loop momentum with itself or external momenta in terms of the inverse propagators that occur in the loop integral, propagator masses and external momenta squared. Thus the cancellation of the inverse propagators in the numerator with the propagators of the loop always leads to scalar integrals where loop momenta are absent in the numerator. So far only the most simple example has been presented for illustration. In general the determination of the Passarino–Veltman coefficients involves solving systems of equations. Even though for high-rank tensor

5. Heavy Higgs effects in top-quark pair production at next-to-leading order in α_s

integrals there are many tensor coefficients the system of equations can be broken down to smaller ones each containing not more than three equations. The most economical way of deriving the Passarino–Veltman coefficients is iteratively, i.e. expressing the coefficients of higher rank tensor integrals in terms of the coefficients of lower rank integrals. Again, a simple example shall illustrate this procedure. Consider the rank-two two-point function

$$B^{\mu\nu} = \int \frac{d^d \ell}{(2\pi)^d} \frac{\ell^\mu \ell^\nu}{[\ell^2 - m_1^2][(\ell + p_1)^2 - m_2^2]} = g^{\mu\nu} B_{00} + p_1^\mu p_1^\nu B_{11}. \quad (5.66)$$

The idea is to reduce the rank of $B^{\mu\nu}$ by one by contracting with $p_{1\mu}$

$$p_{1\mu} B^{\mu\nu} = \frac{1}{2} (p_1^\nu A(m_2) + f_1 B^\nu) = p_1^\nu \frac{1}{2} (A(m_2) + f_1 B_1) = p_1^\nu B_{00} + p_1^\nu p_1^2 B_{11}, \quad (5.67)$$

where $f_1 = p_1^2 + m_1^2 - m_2^2$. From Eq. (5.67) follows

$$B_{11} = \frac{1}{2p_1^2} (A(m_2) + f_1 B_1 - 2B_{00}), \quad (5.68)$$

where B_1 is the coefficient of the rank-one two-point function derived above in Eq. (5.63). The coefficient B_{00} can be calculated by contracting Eq. (5.66) with $g_{\mu\nu}$

$$g_{\mu\nu} B^{\mu\nu} = A(m_2) + m_1^2 B_0 = dB_{00} + p_1^2 B_{11}. \quad (5.69)$$

Inserting Eq. (5.68) into Eq. (5.69) gives

$$B_{00} = \frac{1}{2(d-1)} (A(m_2) + 2m_1 B_0 - f_1 B_1). \quad (5.70)$$

A direct general expression for the coefficients is usually only given for the two-point function. The coefficients of three and four-point functions are given in the form of systems of equations. They can be obtained from the original publication [159] or for example from Ref. [160] where some typographical errors in Ref. [159] have been corrected.

In renormalizable quantum field theories the maximal rank of an N -point tensor integral is $r = N$. Since the NLO calculation in this work makes use of effective $gg\phi$ and $ggg\phi$ couplings (see Sec. 5.2.1) the rank could in principle be larger. However, as it turns out Passarino–Veltman coefficients for up to rank-three four-point functions are needed in this calculation.

Renormalization

In general quantum field theories can contain free parameters. For example, in the SM couplings and masses of particles are not determined by the theory itself and therefore have to be measured by experiment. Usually these free parameters appear in the Lagrangian description of the theory. In quantum field theory *renormalization* is a method to express physical observable quantities in terms of the measurement results for the unknown parameters instead of expressing them in terms of the parameters in the Lagrangian. In this way any kind of observable that can be calculated in a quantum field theory is directly related to a set of experimental measurement results. When this set of required measurements is finite to all perturbative orders the theory is called *renormalizable*. If infinitely many measurements are required to determine all free parameters of the full (all orders) theory then this theory is called *nonrenormalizable*.

A consequence of renormalization is the fact that UV-divergences are absorbed into the parameters of the Lagrangian such as masses and couplings. In the NLO calculation discussed

here UV-divergences occur in the loop integrals of the contribution $\mathcal{M}_{\phi, \text{QCD}}^{(0,1)}$ (Fig. 5.9a,b1,b2). The renormalization is performed by rewriting the so-called *bare* (unrenormalized) parameters and fields in the Lagrangian as

$$\alpha_s^B = Z_{\alpha_s} \alpha_s, \quad A_\mu^B = \sqrt{Z_3} A_\mu, \quad \psi_t^B = \sqrt{Z_2} \psi_t, \quad m_t^B = Z_m m_t, \quad (5.71)$$

where the superscript B denotes bare quantities and the coefficients Z_{α_s} , Z_2 , Z_3 and Z_m are called *renormalization constants*. α_s , A_μ , ψ_t and m_t denote the renormalized coupling constant of QCD, gluon field, top-quark field and top-quark mass, respectively. As an example of the renormalization procedure consider the gluon-top-quark interaction term $\mathcal{L}_{g\bar{t}t}$ in the Lagrangian. Using the relations in Eq. (5.71) $\mathcal{L}_{g\bar{t}t}$ can be rewritten as follows

$$\begin{aligned} \mathcal{L}_{g\bar{t}t} &= -g_s^B \bar{\psi}_t^B \gamma^\mu t^a \psi_t^B A_\mu^{a,B} = -Z_2 \sqrt{Z_3} \sqrt{Z_{\alpha_s}} g_s \bar{\psi}_t \gamma^\mu t^a \psi_t A_\mu^a \\ &= -g_s \bar{\psi}_t \gamma^\mu t^a \psi_t A_\mu^a - \underbrace{(Z_2 \sqrt{Z_3} \sqrt{Z_{\alpha_s}} - 1)}_{\equiv \delta Z_1} g_s \bar{\psi}_t \gamma^\mu t^a \psi_t A_\mu^a. \end{aligned} \quad (5.72)$$

The gluon-top-quark interaction term is now written only in terms of renormalized quantities. Furthermore, a second term, the so-called *counterterm*, appears. This additional term in the Lagrangian in Eq. (5.72) corresponds to a new Feynman rule

$$a, \mu \text{ (loop)} \text{ (vertex)} = -ig_s \delta Z_1 t^a \gamma^\mu. \quad (5.73)$$

When calculating matrix elements not only the standard interaction term has to be taken into account but also the additional counterterm in Eq. (5.73).

The renormalization constants are defined with respect to a certain *renormalization scheme*. All schemes have in common that the counter term cancels the UV-divergences. However, the subtraction of additional finite parts depends on the scheme. The simplest scheme subtracts only the UV-pole and is therefore termed *minimal subtraction* (MS) [161]. In this scheme for example δZ_1 is defined by [162]

$$\begin{aligned} \mu \text{ (loop)} \text{ (vertex)} + \mu \text{ (loop)} \text{ (vertex)} + \mu \text{ (loop)} \text{ (vertex)} &= -ig_s \gamma_\mu t^a \left[\frac{\alpha_s}{4\pi} (C_A + C_F) \frac{1}{\epsilon} + \delta Z_1^{\text{MS}} \right] + \text{finite terms} \end{aligned} \quad (5.74)$$

such that the term in square brackets vanishes. It is immediately clear that first δZ_1 is of $\mathcal{O}(\alpha_s)$ and therefore does not contribute at LO and second that by taking into account higher-loop diagrams in Eq. (5.74) δZ_1 can be determined to higher orders in α_s . Hence, in perturbation theory δZ_1 and renormalization constants in general are power series in α_s and therefore often parametrized as

$$Z = 1 + \delta Z. \quad (5.75)$$

In a related scheme which is frequently used and called the “ $\overline{\text{MS}}$ scheme” [163] in addition to the pole a finite contribution which always accompanies the pole is subtracted such that

$$\frac{\alpha_s}{4\pi} (C_A + C_F) \left[\frac{1}{\epsilon} - \gamma_E + \ln(4\pi) \right] + \delta Z_1^{\overline{\text{MS}}} = 0, \quad (5.76)$$

where $\gamma_E = 0.577216\dots$ is Euler’s constant.

Another example of a renormalization scheme is the so-called *on-shell scheme* (e.g. in [129, 164]) which is widely used for the renormalization of the mass. There are two defining renormalization conditions:

5. Heavy Higgs effects in top-quark pair production at next-to-leading order in α_s

1. The full renormalized propagator has its pole at the so-called *on-shell mass* m_{OS} .
2. The residue of the full renormalized propagator is one.

For example in QCD the full renormalized top-quark propagator is given by

$$S(p) = \frac{1}{\not{p} - m_{OS} + \hat{\Sigma}(p)}, \quad (5.77)$$

where

$$\hat{\Sigma}(p) = (\not{p} - m_{OS})\hat{\Sigma}_2(p^2) + m_{OS}\hat{\Sigma}_1(p^2) \quad (5.78)$$

is the renormalized self energy. The first renormalization condition in the on-shell scheme gives

$$\hat{\Sigma}_1(m_{OS}^2) \stackrel{!}{=} 0. \quad (5.79)$$

Expanding the self energy around the pole $p^2 = m_{OS}^2$

$$\hat{\Sigma}(p) \approx [\hat{\Sigma}_2(m_{OS}^2) + 2m_{OS}^2\hat{\Sigma}'_1(m_{OS}^2)](\not{p} - m_{OS}) \quad (5.80)$$

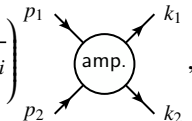
gives

$$S(p^2) = \frac{1}{\not{p} - m_{OS}} \frac{1}{[1 + \hat{\Sigma}_2(m_{OS}^2) + 2m_{OS}^2\hat{\Sigma}'_1(m_{OS}^2)]}. \quad (5.81)$$

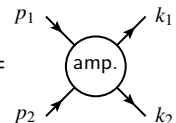
Hence, the second renormalization condition in the on-shell scheme can be expressed as

$$\hat{\Sigma}_2(m_{OS}^2) + 2m_{OS}^2\hat{\Sigma}'_1(m_{OS}^2) = 0. \quad (5.82)$$

One advantage of the on-shell scheme is that it is not necessary to calculate self energy corrections of the external legs. This is due to the second renormalization condition and the Lehmann-Symanzik-Zimmermann (LSZ) reduction formula [165] which relates Green's functions with S -matrix elements. For example, for a $2 \rightarrow 2$ process the LSZ formula can be cast in the following form [23]

$$\langle k_1, k_2 | S | p_1, p_2 \rangle = \left(\prod_{i=1}^4 \sqrt{R_i} \right) \text{amp.}, \quad (5.83)$$


where the left hand side represents the S -matrix element for the scattering of two incoming particles with momenta p_1 and p_2 into two outgoing particles with momenta k_1 and k_2 . On the rhs R_i denotes the residue of the full propagator of particle⁴ i and the Feynman diagram represents an amputated Green's function without external propagators. Since in the on-shell scheme the residue R is set to one (second renormalization condition) Eq. (5.83) simplifies to

$$\langle k_1, k_2 | S | p_1, p_2 \rangle = \text{amp.}, \quad (5.84)$$


such that indeed only amputated Green's functions have to be calculated without external self energy corrections.

The renormalization of the QCD corrections shown in Fig. 5.9 is performed in the $\overline{\text{MS}}$ scheme with the top-quark mass defined on-shell. The wavefunction renormalization of the

⁴For simplicity scalar particles are considered in this example.

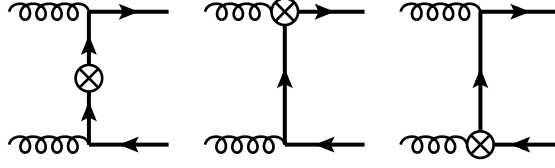


Figure 5.10.: Example counterterm Feynman diagrams.

gluon and top-quark fields is performed in the on-shell scheme. The renormalization constants are provided in Ref. [166]:

$$\delta Z_{\alpha_s} = \frac{\alpha_s}{2\pi} \frac{1}{\epsilon_{UV}} C(\epsilon) \left\{ \left(\frac{N_f}{3} - \frac{11}{2} \right) + \frac{1}{3} \left(\frac{\mu^2}{m_t^2} \right)^\epsilon \right\}, \quad (5.85)$$

$$\delta Z_2 = -\frac{\alpha_s}{3\pi} C(\epsilon) \left\{ \left(\frac{\mu^2}{m_t^2} \right)^\epsilon \left(\frac{1}{\epsilon_{UV}} + \frac{2}{\epsilon_{IR}} \right) + 4 \right\}, \quad (5.86)$$

$$\delta Z_3 = -\frac{\alpha_s}{2\pi} \left(\frac{\mu^2}{m_t^2} \right)^\epsilon C(\epsilon) \left\{ \left(\frac{N_f}{3} - \frac{5}{2} \right) \left(\frac{1}{\epsilon_{UV}} - \frac{1}{\epsilon_{IR}} \right) - \frac{1}{3} \frac{1}{\epsilon_{UV}} \right\}, \quad (5.87)$$

$$\delta Z_m = -\frac{\alpha_s}{3\pi} \left(\frac{3}{\epsilon_{UV}} C(\epsilon) \left(\frac{\mu^2}{m_t^2} \right)^\epsilon + 4 \right), \quad (5.88)$$

with

$$C(\epsilon) = (4\pi)^\epsilon \Gamma(1 + \epsilon) \quad (5.89)$$

and $N_f = 5$, the number of light quark flavors. The subscripts UV and IR indicate the kind of singularity. The renormalization constants are used to construct the counterterms. As an example consider the gluon-top-quark counterterm (5.73) which involves the renormalization constant

$$\begin{aligned} \delta Z_1 &= \sqrt{Z_{\alpha_s}} Z_2 \sqrt{Z_3} - 1 = \left(1 + \frac{1}{2} \delta Z_{\alpha_s} \right) \left(1 + \delta Z_2 \right) \left(1 + \frac{1}{2} \delta Z_3 \right) - 1 + \mathcal{O}(\alpha_s^2) \\ &= \frac{1}{2} \delta Z_{\alpha_s} + \delta Z_2 + \frac{1}{2} \delta Z_3 + \mathcal{O}(\alpha_s^2). \end{aligned} \quad (5.90)$$

Inserting Eqs. (5.85), (5.86) and (5.87) gives

$$\delta Z_1 = -\frac{\alpha_s}{\pi} \left[\frac{13}{12} C(\epsilon) \frac{1}{\epsilon_{UV}} - \frac{2N_f - 31}{24} C(\epsilon) \frac{1}{\epsilon_{IR}} + \frac{4}{3} + \ln \left(\frac{\mu^2}{m_t^2} \right) \right] + \mathcal{O}(\alpha_s^2). \quad (5.91)$$

The one-loop contributions of the type shown in Fig. 5.9 b3, c1–c3 are UV-finite. The contributions of the type shown in Fig. 5.9a,b1,b2 have UV-divergences which are cancelled by counterterm contributions of the type shown in Fig. 5.10. Since the vertex counterterm is proportional to the vertex itself all counterterm amplitudes which involve only vertex counterterms are proportional to the LO amplitude (with the proportionality constant δZ_1). This is also true for the spin dependent part of the amplitude, i.e. the UV-divergences in the spin dependent part of the vertex corrections are proportional to the LO spin structures. Schematically, the cancellation of the divergences in the vertex corrections is given by

$$\mathcal{M}_{\phi, \text{QCD}}^{(0,1), \text{vertex}} + 2\delta Z_1 \mathcal{M}_{\phi, \text{QCD}}^{(0,0)} = \text{UV-finite}, \quad (5.92)$$

where $\mathcal{M}_{\phi, \text{QCD}}^{(0,1), \text{vertex}}$ is the vertex contribution of the NLO QCD corrections shown in Fig. 5.9 and $\mathcal{M}_{\phi, \text{QCD}}^{(0,0)}$ is the LO contribution to the QCD-Higgs interference.

5. Heavy Higgs effects in top-quark pair production at next-to-leading order in α_s

The structure of the divergence in the top-quark self energy diagram (Fig. 5.9a) is more complicated. However, also the cancellation of this UV-divergences has been performed and checked for the spin independent as well as spin dependent part using the counterterm

$$\rightarrow \otimes \rightarrow = i[(\not{p} - m)\delta Z_2 - m\delta Z_m] \quad (5.93)$$

and the renormalization constants given in Eqs. (5.86) and (5.88). The complete counterterm amplitude can be expressed as

$$\begin{aligned} \mathcal{M}_{\phi, \text{QCD}}^{\text{CT}} &= (2\delta Z_1 - \delta Z_2)\mathcal{M}_{\phi, \text{QCD}}^{(0,0)} + \delta Z_m \mathcal{M}_{\phi, \text{QCD}}^m \\ &= (\delta Z_{\alpha_s} + \delta Z_2 + \delta Z_3)\mathcal{M}_{\phi, \text{QCD}}^{(0,0)} + \delta Z_m \mathcal{M}_{\phi, \text{QCD}}^m, \end{aligned} \quad (5.94)$$

where $\mathcal{M}_{\phi, \text{QCD}}^m$ is the part of the counterterm amplitude associated with the mass renormalization. Note that without the top-quark mass counterterm the renormalization can simply be performed by multiplying the bare matrix element, e.g. $\mathcal{M}_{gg \rightarrow q\bar{q}}^B$, by the field renormalization constants of the external fields and the coupling renormalization constant

$$\mathcal{M}_{gg \rightarrow q\bar{q}}^B \rightarrow \sqrt{Z_2} \sqrt{Z_2} \sqrt{Z_3} \sqrt{Z_3} Z_{\alpha_s} \mathcal{M}_{gg \rightarrow q\bar{q}} = [1 + \delta Z_{\alpha_s} + \delta Z_2 + \delta Z_3 + \mathcal{O}(\alpha_s^2)] \mathcal{M}_{gg \rightarrow q\bar{q}}. \quad (5.95)$$

The QCD coupling constant renormalization as given by Eq. (5.85) is performed in the so-called *five-flavour scheme*. This is an effective theory where the top quark has been integrated out. The bare coupling constant $g_s = \sqrt{4\pi\alpha_s}$ in the full theory (including the top quark) and in the effective theory are related by the so-called *decoupling relation* [167–172] (using the notation of [173])

$$g_s^{B'} = \zeta_g^B g_s^B. \quad (5.96)$$

The bare and renormalized quantities are related by

$$g_s^B = Z_g g_s \quad \text{and} \quad g_s^{B'} = Z'_g g'_s. \quad (5.97)$$

Inserting Eq. (5.97) into Eq. (5.96) gives the decoupling relation for the renormalized quantities

$$g'_s = \zeta_g g_s, \quad (5.98)$$

where

$$\zeta_g = \frac{Z_g}{Z'_g} \zeta_g^B. \quad (5.99)$$

The explicit decoupling relation for α_s is given by [167, 170, 174]

$$\alpha_s^{(N_f)} = \zeta_g^2 \alpha_s^{(N_f+1)} = \alpha_s^{(N_f+1)} \left[1 - \frac{\alpha_s^{(N_f+1)}}{\pi} \frac{1}{6} \ln \frac{\mu^2}{m_t^2} + \mathcal{O}(\alpha_s^2) \right]. \quad (5.100)$$

The renormalization constant δZ_{α_s} in the pure $\overline{\text{MS}}$ scheme is give by [162]

$$\delta Z_{\alpha_s}^{(N_f+1), \overline{\text{MS}}} = \frac{\alpha_s^{(N_f+1)}}{2\pi} \left(\frac{N_f + 1}{3} - \frac{11}{2} \right) \frac{C(\epsilon)}{\epsilon}. \quad (5.101)$$

To express the renormalization constant in terms of $\alpha_s^{(N_f)}$ one has to invert Eq. (5.100)

$$\alpha_s^{(N_f+1)} = \alpha_s^{(N_f)} \left[1 + \frac{\alpha_s^{(N_f)}}{\pi} \frac{1}{6} \ln \frac{\mu^2}{m_t^2} \right]. \quad (5.102)$$

From the definition of Z_{α_s} (5.71) we obtain

$$\begin{aligned}
 \alpha_s^B &= \alpha_s^{(N_f+1)} \left[1 + \delta Z_{\alpha_s^{(N_f+1)}, \overline{\text{MS}}} \right] \\
 &= \alpha_s^{(N_f)} \left(1 + \frac{\alpha_s^{(N_f)}}{\pi} \frac{1}{6} \ln \frac{\mu^2}{m_t^2} \right) \left[1 + \frac{\alpha_s^{(N_f)}}{2\pi} \left(\frac{N_f+1}{3} - \frac{11}{2} \right) \frac{C(\epsilon)}{\epsilon} \right] \\
 &= \alpha_s^{(N_f)} \left(1 + \frac{\alpha_s^{(N_f)}}{2\pi} \left(\frac{N_f+1}{3} - \frac{11}{2} \right) \frac{C(\epsilon)}{\epsilon} + \frac{\alpha_s^{(N_f)}}{\pi} \frac{1}{6} \ln \frac{\mu^2}{m_t^2} + \mathcal{O}(\alpha_s^2) \right) \\
 &= \alpha_s^{(N_f)} \left(1 + \delta Z_{\alpha_s^{(N_f)}, \overline{\text{MS}}} \right)
 \end{aligned} \tag{5.103}$$

with

$$\delta Z_{\alpha_s^{(N_f)}, \overline{\text{MS}}} = \frac{\alpha_s^{(N_f)} C(\epsilon)}{2\pi \epsilon} \left[\left(\frac{N_f}{3} - \frac{11}{2} \right) + \frac{1}{3} \left(\frac{\mu^2}{m_t^2} \right)^\epsilon \right], \tag{5.104}$$

where $N_f = 5$ and which agrees with Eq. (5.85).

5.2.5. Real corrections

In this subsection an overview is given over the real corrections contributing to the resonant production of heavy Higgs bosons and their subsequent decay into $t\bar{t}$.

The contribution from the virtual corrections discussed in Sec. 5.2.4 still contains infrared divergences after UV renormalization. These are cancelled by the respective real corrections as stated by the Kinoshita-Lee-Nauenberg theorem [175, 176]. A manifestation of this theorem is the cancellation of virtual and real correction in the SGA as demonstrated in Appendix F. The physical reason for this cancellation is that additional (with respect to the LO scattering process) radiation of partons that are soft or collinear is not observable. Hence, processes with soft and/or collinear radiation are indistinguishable from a process without such radiation. For a complete description of (finite) physical scattering processes with a defined number of initial and final state particles all indistinguishable contributions must be taken into account. Hence, even though we are interested only in the production of a top-quark pair at NLO QCD we must take processes with the emission of an additional soft/collinear parton into account. Schematically, the process under consideration beyond LO is therefore denoted by

$$pp \rightarrow \phi \rightarrow t\bar{t}X \tag{5.105}$$

where X stands for additional partons.

Besides additional partons in the final state the real corrections also involve different channels in the initial state. While only the gg channel contributes to the virtual corrections to heavy Higgs boson exchange the real corrections contribute to gg , gq and $q\bar{q}$ channels. The amplitudes can be divided into those involving a heavy Higgs boson $\mathcal{A}_\phi^{R,gg}$ (Fig. 5.11a1,a2), $\mathcal{A}_\phi^{R,gq}$ (Fig. 5.11b)) and $\mathcal{A}_\phi^{R,q\bar{q}}$ (Fig. 5.11c) and those of pure QCD nature $\mathcal{A}_{\text{QCD}}^{R,gg}$ (Fig. 5.12a), $\mathcal{A}_{\text{QCD}}^{R,gq}$ (Fig. 5.12b) and $\mathcal{A}_{\text{QCD}}^{R,q\bar{q}}$ (Fig. 5.12c).

The pure QCD amplitudes squared $|\mathcal{M}_{\text{QCD}}^{R,gg}|^2$, $|\mathcal{M}_{\text{QCD}}^{R,gq}|^2$, $|\mathcal{M}_{\text{QCD}}^{R,q\bar{q}}|^2$ are taken into account in the NLO calculation and the phenomenological results presented in this chapter but are not further discussed here (see Ref. [111, 112, 138–141]). The signal amplitude squared in the gg channel is denoted by

$$|\mathcal{M}_\phi^{R,gg}|^2 = \frac{1}{N_{gg}} \sum_{\text{spin, col.}} \mathcal{A}_\phi^{R,gg} (\mathcal{A}_\phi^{R,gg})^* \tag{5.106}$$

5. Heavy Higgs effects in top-quark pair production at next-to-leading order in α_s

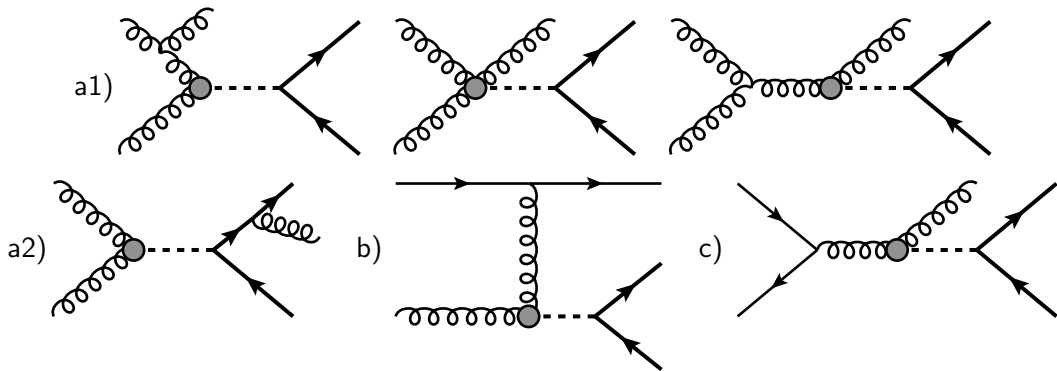


Figure 5.11.: Example Feynman diagrams for real corrections to $t\bar{t}$ production involving heavy Higgs bosons: a1) initial state radiation in the gg channel, a2) final state radiation in the gg channel, b) gq channel c) $q\bar{q}$ channel.

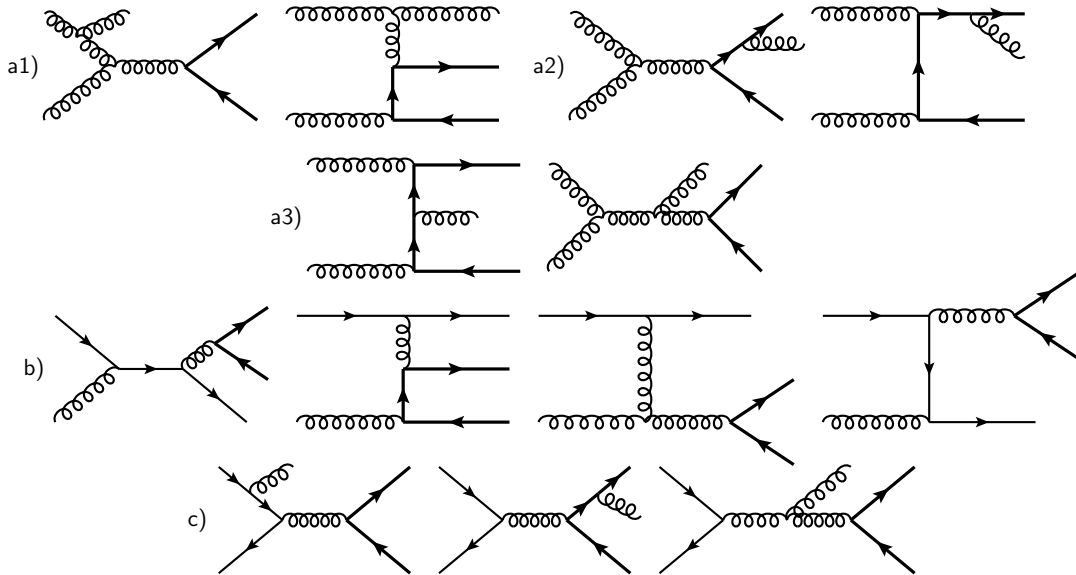


Figure 5.12.: Example Feynman diagrams for the pure QCD real corrections to $t\bar{t}$ production: a1) initial state radiation in the gg channel, a2) final state radiation in the gg channel, a3) intermediate state radiation in the gg channel, b) gq channel, c) $q\bar{q}$ channel.

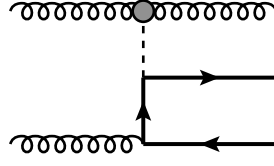
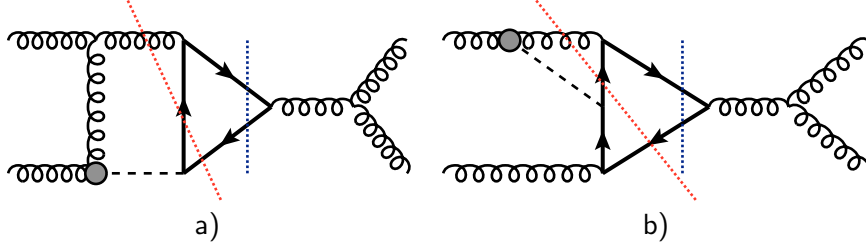

 Figure 5.13.: Example Feynman diagram for nonresonant real corrections in the gg channel.


Figure 5.14.: Interference Feynman diagrams: the blue dotted cut corresponds to virtual correction and the red dotted cut corresponds to a real correction. a) nonfactorizable resonant, b) nonfactorizable nonresonant.

and can be divided into initial state radiation (Fig. 5.11a1) and final state radiation (Fig. 5.11a2)

$$|\mathcal{M}_\phi^{R,gg}|^2 = |\mathcal{M}_{\phi,ISR}^{R,gg}|^2 + |\mathcal{M}_{\phi,FSR}^{R,gg}|^2 \quad (5.107)$$

because there are no interference terms between initial and final state radiation due to the color structure. The signal amplitudes squared for the gq and $q\bar{q}$ channels are denoted by

$$|\mathcal{M}_\phi^{R,gq}|^2 = \frac{1}{N_{gq}} \sum_{\text{spin,col.}} \mathcal{A}_\phi^{R,gq} (\mathcal{A}_\phi^{R,gq})^*, \quad (5.108)$$

$$|\mathcal{M}_\phi^{R,q\bar{q}}|^2 = \frac{1}{N_{q\bar{q}}} \sum_{\text{spin,col.}} \mathcal{A}_\phi^{R,q\bar{q}} (\mathcal{A}_\phi^{R,q\bar{q}})^*, \quad (5.109)$$

with $N_{gq} = 4N_c(N_c^2 - 1)$ and $N_{q\bar{q}} = 4N_c^2$.

Now we turn to the contribution of the real corrections to the interference between signal and QCD background. As explained in Sec. 5.2.3 we apply the SGA to the interference between the amplitudes $\mathcal{A}_\phi^{R,gg}$ and $\mathcal{A}_{\text{QCD}}^{R,gg}$. After cancellation of the nonfactorizable resonant virtual and real corrections the remaining contributions to the real correction in the gg channel can be written as (cf. Eq. (5.41))

$$\mathcal{M}_{\phi,\text{QCD}}^{R,gg} \simeq \mathcal{M}_{\phi,\text{QCD}}^{R,gg,\text{res}} - \mathcal{M}_{\phi,\text{QCD,SGA}}^{R,gg,\text{nf}}, \quad (5.110)$$

where

$$\mathcal{M}_{\phi,\text{QCD}}^{R,gg,\text{res}} = \frac{1}{N_{gg}} \sum_{\text{spin,col.}} 2\text{Re} \left[\mathcal{A}_\phi^{R,gg} (\mathcal{A}_{\text{QCD}}^{R,gg})^* \right]. \quad (5.111)$$

Note that in $\mathcal{M}_{\phi,\text{QCD}}^{R,gg,\text{res}}$ manifestly nonresonant contributions of the kind shown in Fig. 5.13 have been omitted. The second term on the rhs in Eq. (5.110), $\mathcal{M}_{\phi,\text{QCD,SGA}}^{R,gg,\text{nf}}$, denotes the nonfactorizable resonant part of the real corrections in the SGA. In order to identify this contribution we proceed with the following method. Since it is easier to identify resonant (factorizable

5. Heavy Higgs effects in top-quark pair production at next-to-leading order in α_s

and nonfactorizable) contributions in the virtual corrections by inspecting Feynman diagrams we consider Feynman diagrams of the interference between one-loop amplitudes and tree-level amplitudes. In Fig. 5.14 two examples of such interference diagrams are shown. The blue dotted lines indicate cuts that correspond to virtual corrections. In Figure 5.14a the blue cut represents a nonfactorizable resonant virtual correction whereas in Fig. 5.14b the blue cut gives rise to a nonfactorizable nonresonant virtual correction. Cutting through three propagators in the interference diagram as shown by the red dotted lines in Fig. 5.14 generates real corrections. Those real corrections generated from resonant interference diagrams (e.g. Fig. 5.14a) are attributed to the resonant part while those real corrections generated from nonresonant interference diagrams (e.g. Fig. 5.14b) are attributed to the nonresonant part.

The virtual nonfactorizable resonant contributions $\mathcal{M}_{\phi,\text{QCD}}^{(1,0),\text{nf}}$ are given by the interference of diagrams depicted in Fig. 5.5a and Fig. 4.1a. The corresponding real corrections $\mathcal{M}_{\phi,\text{QCD}}^{R,gg,\text{nf}}$, as determined by the method described above, are given by the interference of diagrams shown in Fig. 5.11a (initial state radiation in the signal amplitude, $\mathcal{A}_{\phi,\text{ISR}}^{R,gg}$) and diagrams shown in Fig. 5.12a2 (final state radiation in the QCD amplitude, $\mathcal{A}_{\text{QCD,FSR}}^{R,gg}$)

$$\mathcal{M}_{\phi,\text{QCD}}^{R,gg,\text{nf}} = \frac{1}{N_{gg}} \sum_{\text{spin,col.}} 2\text{Re} \left[\mathcal{A}_{\phi,\text{ISR}}^{R,gg} \left(\mathcal{A}_{\text{QCD,FSR}}^{R,gg} \right)^* \right]. \quad (5.112)$$

After the nonfactorizable contributions in the real corrections have been identified the SGA is applied as discussed in Sec. 5.2.3 to obtain $\mathcal{M}_{\phi,\text{QCD,SGA}}^{R,gg,\text{nf}}$ in Eq. (5.110). While $\mathcal{M}_{\phi,\text{QCD}}^{R,gg,\text{res}}$ is gauge invariant the contribution $\mathcal{M}_{\phi,\text{QCD,SGA}}^{R,gg,\text{nf}}$ is gauge invariant only in the exact soft limit, i.e. at the resonance. The gauge dependence away from the resonance is of order $\mathcal{O}(\Gamma/m)$ which is the order of uncertainty of this approach.

All contributions from the virtual and real corrections at NLO contributing to the resonant production of heavy Higgs bosons and their decay to $t\bar{t}$ have been worked out in Secs. 5.2.4 and 5.2.5. As mentioned above the IR divergences of the virtual corrections are cancelled by the real corrections. The method used to perform this cancellation in the numerical calculation is described in Sec. 5.2.6.

5.2.6. Catani–Seymour dipole subtraction

The NLO QCD correction σ^{NLO} to the partonic cross section can be written as

$$\sigma^{\text{NLO}} = \int_m d\sigma^V + \int_{m+1} d\sigma^R, \quad (5.113)$$

where m and $m+1$ indicate the number of final state particles. $d\sigma^V$ and $d\sigma^R$ denote virtual and real corrections, respectively. Both contributions are separately IR divergent but in the sum IR divergences in the virtual corrections are cancelled by IR divergences in the real corrections. Equation (5.113) illustrates that this cancellation is nontrivial because virtual and real corrections have different numbers of final state particles and are therefore integrated over different phase space regions. Hence, in a numerical calculation these two contributions have to be integrated separately preventing the cancellation of IR divergences in intermediate stages of the calculation.

In principle there exist two kinds of methods to handle the IR divergences in numerical calculations. The first method, so-called *phase space slicing*, divides the phase space into singular and nonsingular regions. The singular part can be calculated analytically extracting the IR divergences explicitly, e.g. as poles in ϵ in dimensional regularization. These divergences are cancelled analytically with the IR divergences from the virtual corrections. The integration

over the phase space where the real corrections do not give rise to IR divergences is performed numerically. The second kind of method is based on implementing subtraction terms that render virtual and real corrections separately IR finite but do not change the cross section. In this work a subtraction method called *Catani–Seymour dipole subtraction* [177, 178] is chosen to handle the occurring IR divergences.

This method introduces universal subtraction terms, so-called *dipoles*, that reproduce the singular behaviour of the real corrections pointwise in the soft/collinear phase space regions. The subtraction terms are constructed such that they can be analytically integrated over the additionally emitted soft/collinear parton. This integration yields the so-called *integrated dipoles* which contain the dimensionally regularized IR divergences as explicit $1/\epsilon$ and $1/\epsilon^2$ poles. The integrated dipoles live in the same phase space as the virtual corrections since the additional parton is integrated out. By subtracting the dipoles from the real corrections the singularities are cancelled pointwise such that a numerical Monte Carlo integration over the real phase space can be performed. In order not to change the result for the cross section the integrated dipoles have to be added to the integration over the virtual corrections where they cancel the IR divergences from the loop amplitudes explicitly. Hence, the integration in the virtual phase space can also be performed numerically as well. Schematically, this subtraction procedure can be written as [177]

$$\sigma^{\text{NLO}} = \int_{m+1} \left[(d\sigma^R)_{\epsilon=0} - (d\sigma^A)_{\epsilon=0} \right] + \int_m \left[d\sigma^V + \int_1 d\sigma^A \right]_{\epsilon=0}, \quad (5.114)$$

where $d\sigma^A$ denotes the dipoles and $\int_1 d\sigma^A$ denotes the integrated dipoles. The real corrections and the dipoles are evaluated in $d = 4$ dimensions. The virtual corrections and integrated dipoles are evaluated in $d = 4 - 2\epsilon$ dimensions and after the cancellation of the ϵ poles the limit $\epsilon \rightarrow 0$ can safely be performed in the integrand of the second integral in Eq. (5.114).

In the presence of initial state partons the real corrections give rise to collinear initial state singularities which are not cancelled by the virtual correction. Instead they have to be factorized and absorbed into the PDFs by a kind of IR renormalization procedure that introduces the so-called *factorization scale* μ_F . Since we study proton-proton collisions there are partons in the initial state which involve additional terms in the subtraction formula [177]

$$\begin{aligned} \sigma^{\text{NLO}} &= \sigma^{\text{NLO}\{m+1\}}(p) + \sigma^{\text{NLO}\{m\}}(p) + \int_0^1 dx d\hat{\sigma}^{\text{NLO}\{m\}}(x; xp) \\ &= \int_{m+1} \left[(\sigma^R(p))_{\epsilon=0} - \left(\sum_{\text{dipoles}} d\sigma^B(p) \otimes (dV_{\text{dipole}} + dV'_{\text{dipole}}) \right)_{\epsilon=0} \right] \\ &+ \int_m \left[d\sigma^V(p) + d\sigma^B(p) \otimes \mathbf{I} \right]_{\epsilon=0} + \int_0^1 dx \int_m \left[d\sigma^B(xp) \otimes (\mathbf{K} + \mathbf{P})(x) \right]. \end{aligned} \quad (5.115)$$

The dipole terms are written in factorized form where $d\sigma^B$ denotes the process-dependent Born-like differential cross section and dV_{dipole} denotes the universal dipole term without initial state partons and dV'_{dipole} denotes the contribution to the dipole terms that cancels singularities from partons that are collinear to the initial state partons. The symbol \otimes represents color and spin correlations. The term $d\sigma^B(p) \otimes \mathbf{I}$ denotes the integrated dipoles cancelling all IR divergences in the virtual contribution $d\sigma^V$. The last term in Eq. (5.115) is a finite remainder of the factorization procedure of the collinear singularities in the initial state. For a thorough description of all terms in Eq. (5.115) and further details on the subtraction procedure the reader is referred to Refs. [177] and [178].

In this work we implement the Catani–Seymour dipole subtraction in a straightforward way. The top-quark polarization and $t\bar{t}$ spin correlations in the subtraction terms can be calculated

5. Heavy Higgs effects in top-quark pair production at next-to-leading order in α_s

in the same way as for the LO process because the subtraction terms are constructed from the Born matrix elements. There is only one subtlety related to the application of the SGA. The contribution $\mathcal{M}_{\phi,\text{QCD,SGA}}^{R,gg,nf}$ in Eq. (5.110) effectively functions as a subtraction terms for divergences from initial-final-state correlations. However, only the combination $\mathcal{A}_{\phi,\text{ISR}}^{R,gg} \left(\mathcal{A}_{\text{QCD,FSR}}^{R,gg} \right)^*$ is subtracted while the combination $\mathcal{A}_{\phi,\text{FSR}}^{R,gg} \left(\mathcal{A}_{\text{QCD,ISR}}^{R,gg} \right)^*$ is still present in $\mathcal{M}_{\phi,\text{QCD}}^{R,gg}$ and contains IR divergences. The corresponding dipole subtraction term for initial-final-state correlations does not distinguish between these two contributions. As it turns out one has to multiply the dipole term by 1/2 to cancel the remaining divergences. To retain the balance between dipoles and integrated dipoles such that the cross section is not changed the integrated dipoles corresponding to initial-final-correlations also have to be multiplied by 1/2. That this is the correct procedure is verified by the explicit cancellation of the IR divergences in the virtual corrections. Since the contribution $\mathcal{M}_{\phi,\text{QCD,SGA}}^{(1,0),nf}$ is cancelled by $\mathcal{M}_{\phi,\text{QCD,SGA}}^{R,gg,nf}$ the corresponding divergences are absent in the virtual corrections. The factor of 1/2 takes care that only the remaining divergences are cancelled.

5.3. Analytical results

The calculation of the virtual and real corrections has been performed analytically up to the phase space integration and convolution with the PDFs which were implemented via numerical Monte Carlo methods [179]. Since the full analytical result is rather lengthy only the signal amplitude squared is presented because it can be written in a compact form [77]. The renormalized virtual correction to the signal amplitude squared is given by

$$\begin{aligned} \mathcal{M}_{\phi}^{(1)} &= \frac{\alpha_s}{\pi} \left\{ -\frac{(4\pi)^\epsilon}{\Gamma(1-\epsilon)} \left\{ \text{Re} \left[\left(\frac{\mu^2}{-s-i0} \right)^\epsilon \right] \frac{C_A}{\epsilon^2} + \frac{2\beta_0}{\epsilon} \right\} |\mathcal{M}_{\phi}^{(0),\infty}|^2 \right. \\ &+ \left(\frac{4\pi\mu^2}{m_t^2} \right)^\epsilon \Gamma(1+\epsilon) C_F \frac{1}{\epsilon} \text{Re}(a_{-1}) |\mathcal{M}_{\phi}^{(0),\infty}|^2 \\ &+ \frac{11}{2} [|\mathcal{M}_{\phi}^{(0),\infty}|^2]_{f_p=0} + 2C_A [|\mathcal{M}_{\phi}^{(0),\infty}|^2]_{f_s=0} \\ &\left. + C_F \left[\text{Re}(a_0) [|\mathcal{M}_{\phi}^{(0),\infty}|^2]_{b_i=0} + \text{Re}(\bar{a}_0) [|\mathcal{M}_{\phi}^{(0),\infty}|^2]_{a_i=0} \right] + \mathcal{O}(\epsilon) \right\}, \quad (5.116) \end{aligned}$$

where $|\mathcal{M}_{\phi}^{(0),\infty}|^2$ is the spin dependent LO signal amplitude squared where the $gg\phi$ coupling is implemented in the heavy top mass limit. $|\mathcal{M}_{\phi}^{(0),\infty}|^2$ is obtained from $|\mathcal{M}_{\phi}^{(0)}|^2$ by the following replacement (Sec. 5.2.1)

$$F_j^S \rightarrow F_j^{S,\infty} = \frac{\alpha_s}{\pi} f_{Sj}^{(0)}, \quad F_j^P \rightarrow F_j^{P,\infty} = \frac{\alpha_s}{\pi} f_{Pj}^{(0)}. \quad (5.117)$$

The matrix elements $[|\mathcal{M}_{\phi}^{(0),\infty}|^2]_{f_s=0}$ and $[|\mathcal{M}_{\phi}^{(0),\infty}|^2]_{f_p=0}$ are obtained from $|\mathcal{M}_{\phi}^{(0),\infty}|^2$ by setting $f_{Sj}^{(0)} = 0$ and $f_{Pj}^{(0)} = 0$, respectively. Similarly, the matrix elements $[|\mathcal{M}_{\phi}^{(0),\infty}|^2]_{a_i=0}$ and $[|\mathcal{M}_{\phi}^{(0),\infty}|^2]_{b_i=0}$ are obtained by setting $a_{ij} = 0$ and $b_{ij} = 0$, respectively, everywhere in $|\mathcal{M}_{\phi}^{(0),\infty}|^2$ except in the coefficients $f_{Sj}^{(0)}$ and $f_{Pj}^{(0)}$. The coefficients a_{-1} , a_0 and \bar{a}_0 are related to the one-loop $\phi_j \rightarrow t\bar{t}$ form factor and are given for example in Ref. [158]. They are reproduced

here for convenience

$$\text{Re}(a_{-1}) = -1 - \frac{(1+y^2)H(0; y)}{1-y^2}, \quad (5.118)$$

$$\begin{aligned} \text{Re}(a_0) &= -\left(\frac{1-y^2-4\zeta_2-4y^2\zeta_2}{1-y^2}\right) - \frac{4yH(0; y)}{1-y^2} - \frac{(1+y^2)H(0, 0; y)}{1-y^2} \\ &\quad - \frac{2(1+y^2)H(1, 0; y)}{1-y^2}, \end{aligned} \quad (5.119)$$

$$\text{Re}(\bar{a}_0) = -\frac{(1+y^2)H(0, 0; y)}{1-y^2} - \frac{2(1+y^2)H(1, 0; y)}{1-y^2} - \frac{1-y^2-4\zeta_2-4y^2\zeta_2}{1-y^2}, \quad (5.120)$$

where $\zeta_2 = \pi^2/6$ represents the value of the Riemann zeta function $\zeta(s)$ for $s = 2$ and

$$y = \frac{1-\beta_t}{1+\beta_t}. \quad (5.121)$$

In Eqs. (5.118)–(5.120) H denotes harmonic polylogarithms [180]. Explicitly⁵,

$$H(0; y) = \ln y, \quad (5.122)$$

$$H(0, 0; y) = \frac{1}{2!} \ln^2 y, \quad (5.123)$$

$$H(1, 0; y) = -\ln y \ln(1-y) - \text{Li}_2(y), \quad (5.124)$$

where $\text{Li}_2(y)$ is the dilogarithm defined in Eq. (2.100). The virtual correction in Eq. (5.116) contains IR divergences in the form of ϵ poles. As explained in Sec. 5.2.6 we apply the Catani–Seymour dipole subtraction to subtract the IR divergences from real and virtual corrections in order to be able to integrate them numerically over the phase space. The finite IR-subtracted virtual correction is obtained by adding the integrated dipole term denoted by $d\sigma_{\mathbf{I}} \equiv d\sigma^B \otimes \mathbf{I}$ in Eq. (5.115)

$$\begin{aligned} d\sigma_V + d\sigma_{\mathbf{I}} &= \frac{1}{32\pi} \frac{\alpha_s \beta_t}{\pi^s} \left\{ \left[2\beta_0 + \frac{67}{18} C_A - \frac{10}{9} N_F T_R \right. \right. \\ &\quad + C_F \left(3 - \frac{\beta_t^2 + 6\beta_t + 1}{12\beta_t} \pi^2 - \frac{1+\beta_t^2}{4\beta_t} \ln^2 y - \frac{1+\beta_t^2}{2\beta_t} \ln \left(\frac{1+\beta_t^2}{2} \right) \ln(y) \right. \\ &\quad + \left. \left. \left(\frac{1+\beta_t^2}{2\beta_t} \ln(y) + \frac{3}{2} \right) \ln \left(\frac{1-\beta_t^2}{2(1+\beta_t^2)} \right) + \mathcal{V}_q^{(\text{NS})} \right) + 2\beta_0 \ln \left(\frac{\mu^2}{s} \right) \right] |\mathcal{M}_\phi^{(0, \infty)}|^2 \\ &\quad + 2C_A [|\mathcal{M}_\phi^{(0, \infty)}|^2]_{f_s=0} + \frac{11}{2} [|\mathcal{M}_\phi^{(0, \infty)}|^2]_{f_p=0} \\ &\quad + \left. C_F \left[\text{Re}(a_0) [|\mathcal{M}_\phi^{(0, \infty)}|^2]_{b_t=0} + \text{Re}(\bar{a}_0) [|\mathcal{M}_\phi^{(0, \infty)}|^2]_{a_t=0} \right] \right\} d \cos(\theta) \quad (5.125) \end{aligned}$$

⁵Note that in the preprint version of [180] in Eq. (11) there is a typo in the expression for $H(1, 0; y)$. The correct expression is given in Eq. (5.124).

5. Heavy Higgs effects in top-quark pair production at next-to-leading order in α_s

with

$$\begin{aligned}
\mathcal{V}_q^{(\text{NS})} &= \frac{3}{2} \ln\left(\frac{1}{2}(1 + \beta_t^2)\right) \\
&+ \frac{1 + \beta_t^2}{2\beta_t} \left(2 \ln(y) \ln\left(\frac{2(1 + \beta_t^2)}{(1 + \beta_t)^2}\right) + 2\text{Li}_2(y^2) - 2\text{Li}_2\left(\frac{2\beta_t}{1 + \beta_t}\right) - \frac{\pi^2}{6} \right) \\
&+ \ln\left(1 - \frac{1}{2}\sqrt{1 - \beta_t^2}\right) - 2 \ln\left(1 - \sqrt{1 - \beta_t^2}\right) - \frac{1 - \beta_t^2}{1 + \beta_t^2} \ln\left(\frac{\sqrt{1 - \beta_t^2}}{2 - \sqrt{1 - \beta_t^2}}\right) \\
&- \frac{\sqrt{1 - \beta_t^2}}{2 - \sqrt{1 - \beta_t^2}} + 2 \frac{(1 - \sqrt{1 - \beta_t^2} - \beta_t^2)}{1 + \beta_t^2} + \frac{\pi^2}{2}. \tag{5.126}
\end{aligned}$$

The analytical cancellation of IR divergences between the virtual correction and the integrated dipoles serves as an important check. The contribution from the $\mathbf{K-P}$ term in Eq. (5.115) in the $\overline{\text{MS}}$ factorization scheme for the signal amplitude squared is given by

$$\begin{aligned}
\sigma_{\mathbf{K-P}}(s) &= \int_0^1 dx \int_m \left[d\sigma^{\text{B}}(xp) \otimes (\mathbf{K} + \mathbf{P})(x) \right] \\
&= \frac{\alpha_s}{\pi} \int_0^1 dx \int d\Pi_2 \left\{ \overline{K}^{gg}(x) + \widetilde{K}^{gg}(x) - P^{gg}(x) \ln\left(\frac{\mu_F^2}{xs}\right) \right\} |\mathcal{M}_\phi^{(0,\infty)}(xs)|^2. \tag{5.127}
\end{aligned}$$

$|\mathcal{M}_\phi^{(0,\infty)}(xs)|^2$ denotes the LO spin dependent signal amplitude squared in the heavy top mass limit evaluated at the partonic center-of-mass energy squared xs and $d\Pi_2$ is the Lorentz invariant two-particle phase space measure. The remaining contributions in Eq. (5.127) are defined in [177].

The contribution to the virtual corrections from the interference between the signal amplitude and the QCD background is rather lengthy. The analytical result is not reproduced here but taken into account in the numerical results in Sec. 5.4.

In the following the spin dependent matrix elements for the real corrections to the signal amplitude squared are presented. They can be written in a uniform notation

$$\begin{aligned}
|\mathcal{M}_\phi^{R,X}|^2 &= \frac{4\alpha_s^3 m_t^2}{\pi v^2} \mathcal{N}_X \\
&\times \left\{ \sum_{j=2,3} \left[(f_{Sj}^{(0)})^2 + 4(f_{Pj}^{(0)})^2 \right] (a_{ij}^2 K_a^X + a_{ij} b_{ji} K_{ab}^X + b_{ij}^2 K_b^X) |P_j(s_X)|^2 \right. \\
&+ \left[f_{S2}^{(0)} f_{S3}^{(0)} + 4f_{P2}^{(0)} f_{P3}^{(0)} \right] \left[(a_{12} b_{13} + a_{13} b_{12}) K_{ab}^X + 2(a_{12} a_{13} K_a^X + b_{12} b_{13} K_b^X) \right] \text{Re}[P_{23}(s_X)] \\
&+ \left. \left[f_{S2}^{(0)} f_{S3}^{(0)} + 4f_{P2}^{(0)} f_{P3}^{(0)} \right] (a_{12} b_{13} - a_{13} b_{12}) \widetilde{K}_{ab}^X \text{Im}[P_{23}(s_X)] \right\}, \tag{5.128}
\end{aligned}$$

where \mathcal{N}_X , K_a^X , K_b^X , K_{ab}^X and \widetilde{K}_{ab}^X are coefficients that depend on the production channel $X = gg, gq, q\bar{q}$. s_X is a kinematic variable that also depends on the channel. Furthermore, we have defined the Higgs boson propagator as

$$P_j(s) = \frac{1}{s - m_j^2 + i\Gamma_j m_j}, \quad P_{23}(s) = P_2(s) [P_3(s)]^*. \tag{5.129}$$

The second line in Eq. (5.128) represents the individual contribution from each of the two heavy neutral Higgs bosons ϕ_2 and ϕ_3 . The third and fourth line represent the contribution

from the interference between ϕ_2 and ϕ_3 which is only present in the case of CPV. The interference term in the fourth line gives rise to top and antitop-quark spin polarization while all other terms in Eq. (5.128) contribute to spin correlation and the spin independent part of the matrix element.

In the gg channel

$$g(p_1) + g(p_2) \rightarrow t(k_1) + \bar{t}(k_2) + g(q) \quad (5.130)$$

the matrix element can be divided into initial state radiation and final state radiation without an interference between the two. In the case of initial state radiation the $t\bar{t}$ pair is produced in the color singlet state. However, in the case of final state radiation the $t\bar{t}$ pair is produced in the color octet state. Hence, these two contributions cannot interfere. The coefficients defined in Eq. (5.128) of the spin dependent matrix element for initial state radiation in the gg channel of the signal amplitude squared are given by

$$\mathcal{N}_{gg,ISR} = \frac{C_A}{C_F} \frac{(s+t+u)^4 + s^4 + t^4 + u^4}{stu}, \quad (5.131)$$

$$K_a^{gg,ISR} = 2(k_1 \cdot s_2)(k_2 \cdot s_1) + (s_1 \cdot s_2)t_{12} - t_{12}, \quad (5.132)$$

$$K_b^{gg,ISR} = -2(k_1 \cdot s_2)(k_2 \cdot s_1) + s_{12}(s_1 \cdot s_2) + s_{12}, \quad (5.133)$$

$$K_{ab}^{gg,ISR} = -4\epsilon(k_1, k_2, s_1, s_2), \quad (5.134)$$

$$\widetilde{K}_{ab}^{gg,ISR} = -4m_t [(k_1 \cdot s_2) + (k_2 \cdot s_1)] \quad (5.135)$$

and $s_X = s_{gg,ISR} = s_{12}$. In Eq. (5.134) the ϵ tensor is contracted with the four-vectors k_1 , k_2 , s_1 and s_2

$$\epsilon(k_1, k_2, s_1, s_2) \equiv \epsilon_{\mu\nu\rho\sigma} k_1^\mu k_2^\nu s_1^\rho s_2^\sigma \quad (5.136)$$

with the convention $\epsilon_{0123} = 1$. k_1 and k_2 are the four-momenta of top and antitop quark (5.130). The spin four-vectors of top and antitop quark are denoted by s_1 and s_2 , respectively. The kinematical variables in Eqs. (5.131)–(5.135) are defined as follows

$$s = (p_1 + p_2)^2, \quad t = (p_1 - q)^2, \quad u = (p_2 - q)^2, \quad s_{12} = (k_1 + k_2)^2, \quad t_{12} = (k_1 - k_2)^2. \quad (5.137)$$

The coefficients of the real matrix element for final state radiation in the gg channel are given by

$$\mathcal{N}_{gg,FSR} = \frac{s^2}{s_{13}^2 s_{23}^2}, \quad (5.138)$$

$$\begin{aligned} K_a^{gg,FSR} &= 8m_t^4 (s - s_{12})^2 - 2m_t^2 (s(s_{13} + s_{23})^2 + 4s_{12}s_{13}s_{23}) + s_{13}s_{23} (s^2 + s_{12}^2) \\ &+ 4m_t^2 (s_{13} - s_{23})(s_{13} + s_{23}) [(k_2 \cdot s_1)(q \cdot s_2) - (k_1 \cdot s_2)(q \cdot s_1)] \\ &+ 4 (s_{13}s_{23}s - m_t^2 (s - s_{12})^2) (k_1 \cdot s_2)(k_2 \cdot s_1) \\ &+ 4m_t^2 (s - s_{12})^2 (q \cdot s_1)(q \cdot s_2) \\ &+ 2 [-4m_t^4 (s - s_{12})^2 + m_t^2 (s(s_{13} + s_{23})^2 + 4s_{12}s_{13}s_{23}) - s_{12}s_{13}s_{23}s] (s_1 \cdot s_2), \end{aligned} \quad (5.139)$$

$$\begin{aligned} K_b^{gg,FSR} &= -2m_t^2 s (s - s_{12})^2 + s_{13}s_{23} (s^2 + s_{12}^2) \\ &+ 4m_t^2 (s - s_{12})^2 [(k_1 \cdot s_2)(q \cdot s_1) + (k_2 \cdot s_1)(q \cdot s_2) + (q \cdot s_1)(q \cdot s_2)] \\ &+ 4 (m_t^2 (s - s_{12})^2 - s_{13}s_{23}s) (k_1 \cdot s_2)(k_2 \cdot s_1) \\ &+ 2s (s_{12}s_{13}s_{23} - m_t^2 (s - s_{12})^2) (s_1 \cdot s_2), \end{aligned} \quad (5.140)$$

5. Heavy Higgs effects in top-quark pair production at next-to-leading order in α_s

$$\begin{aligned}
K_{ab}^{gg,FSR} &= \frac{2}{t} \left\{ \left[2s_{13}s_{23}^2 \right] \epsilon(k_1 \cdot s_2) \epsilon(k_1, k_2, p_1, s_1) \right. \\
&+ \left[2s_{23}(s_{23}t_1 - 2s_{13}t_2) \right] \epsilon(k_1 \cdot s_2) \epsilon(k_1, k_2, q, s_1) \\
&+ 4m_t^2 s_{23}^2 \left[- (q \cdot s_1) \epsilon(k_1, k_2, p_1, s_2) + (q \cdot s_2) \epsilon(k_1, k_2, p_1, s_1) \right. \\
&\quad \left. - (p_1 \cdot s_1) \epsilon(k_1, k_2, q, s_2) + (p_1 \cdot s_2) \epsilon(k_1, k_2, q, s_1) \right] \\
&+ \left[4m_t^2 s_{13}t(s_{13} + 2s_{23}) - 2s_{13}s_{23}(2st + s_{13}t_2) \right] \epsilon(k_1, k_2, s_1, s_2) \\
&- s_{23}^2 \left[2m_t^2(s_{23} - s_{13}) + s_{12}s_{13} \right] \epsilon(k_1, p_1, s_1, s_2) \\
&+ \left[2m_t^2(2s s_{13}t - 2s_{12}s_{13}t + s_{23}(s_{23}(t_1 + t_2) - 2s_{13}t_2)) \right. \\
&\quad \left. + s_{12}s_{23}(2s_{13}t_2 - s_{23}t_1) \right] \epsilon(k_1, q, s_1, s_2) \\
&+ \left[4m_t^2 s_{13}s_{23}^2 \right] \epsilon(k_2, p_1, s_1, s_2) \\
&\left. - \left[4m_t^2 s_{23}(st - s_{12}t + s_{13}t_2) \right] \epsilon(k_2, q, s_1, s_2) \right\}, \tag{5.141}
\end{aligned}$$

$$\begin{aligned}
\tilde{K}_{ab}^{gg,FSR} &= 4m_t \left\{ \left(2m_t^2(s - s_{12})^2 - s_{13}s_{23}(s + s_{12}) \right) [(k_1 \cdot s_2) + (k_2 \cdot s_1)] \right. \\
&- (s - s_{12}) (s_{23}s - 2m_t^2(s - s_{12})) (q \cdot s_1) \\
&\left. - (s - s_{12}) (s_{13}s - 2m_t^2(s - s_{12})) (q \cdot s_2) \right\} \tag{5.142}
\end{aligned}$$

and $s_{gg,FSR} = s$. The kinematical variables introduced in Eqs. (5.138)–(5.142) are defined as

$$s_{13} = 2(k_1 \cdot q), \quad s_{23} = 2(k_2 \cdot q), \quad t_1 = -2(k_1 \cdot p_1), \quad t_2 = -2(k_2 \cdot p_1). \tag{5.143}$$

The coefficients for the spin dependent matrix element of the signal amplitude squared in the gq and $q\bar{q}$ channels

$$g(p_1) + q(p_2) \rightarrow t(k_1) + \bar{t}(k_2) + q(q) \tag{5.144}$$

and

$$q(p_1) + \bar{q}(p_2) \rightarrow t(k_1) + \bar{t}(k_2) + g(q) \tag{5.145}$$

are given by

$$\mathcal{N}_{gq} = \frac{s^2 + u^2}{-t}, \tag{5.146}$$

$$\mathcal{N}_{q\bar{q}} = \frac{2C_F(t^2 + u^2)}{s}, \tag{5.147}$$

$$K_a^{gq} = K_a^{q\bar{q}} = K_a^{gg,ISR}, \tag{5.148}$$

$$K_b^{gq} = K_b^{q\bar{q}} = K_b^{gg,ISR}, \tag{5.149}$$

$$K_{ab}^{gq} = K_{ab}^{q\bar{q}} = K_{ab}^{gg,ISR}, \tag{5.150}$$

$$\tilde{K}_{ab}^{gq} = \tilde{K}_{ab}^{q\bar{q}} = \tilde{K}_{ab}^{gg,ISR} \tag{5.151}$$

and $s_{gq} = s_{q\bar{q}} = s_{gg,ISR} = s_{12}$.

The analytical result for the real correction contribution to the interference of the signal amplitude and the QCD background is lengthy and not reproduced here. However, it is taken into account in the numerical results presented in Sec. 5.4.

5.4. Phenomenological results

In this section the phenomenological results of this work are presented by studying collider observables. They are divided into two groups. On the one side we consider observables that are insensitive to the spin properties of the produced $t\bar{t}$ pair but are widely used in phenomenological studies and experimental analyses. On the other side we study spin dependent observables that take into account the spin information of the $t\bar{t}$ pair. Making use of this additional information studying spin dependent observables such as polarization and spin correlation can result in a higher sensitivity to new physics effects (Sec. 4.2.4).

As explained in Sec. 5.2.1 the heavy top mass approximation in Higgs production via gluon fusion can be improved by applying a correction factor (K -factor) introduced in Ref. [104]. We apply this factor to the signal amplitude squared which in the resonance region is very similar to Higgs production. However, the interference between the signal and the QCD background is an effect that does not occur in Higgs production. Hence, an estimate of the applicability of the K -factor to the interference is rather ambiguous. Therefore we choose not to apply the K -factor to the interference contribution. Specifically, the K -factor is introduced as follows. The total cross section at NLO can be decomposed into

$$\sigma_{\text{NLO}}^{\text{approx.}} = \sigma_{\text{NLO}}^{\text{QCDW}} + \sigma_{\text{NLO}}^{\phi, \text{approx.}}, \quad (5.152)$$

where $\sigma_{\text{NLO}}^{\text{QCDW}}$ denotes the nonresonant $t\bar{t}$ cross section including the NLO QCD and weak corrections and $\sigma_{\text{NLO}}^{\phi, \text{approx.}}$ is the contribution of the heavy Higgs bosons including the interference with the QCD background at NLO in the heavy to mass limit. $\sigma_{\text{NLO}}^{\text{QCDW}}$ is known from Ref. [111, 112, 138–141] and $\sigma_{\phi, \text{NLO}}^{\text{approx.}}$ is calculated as follows

$$\sigma_{\text{NLO}}^{\phi, \text{approx.}} = \sum_{j=2,3} \left(\sigma_{\text{full},j}^{(0)} + \sigma_{\text{full},j,\text{QCD}}^{(0)} + K_j \sigma_{\text{eff},j}^{(1)} + \sigma_{\text{eff},j,\text{QCD}}^{(1)} \right) \quad (5.153)$$

with

$$K_j = \frac{\sigma_{\text{full},j}^{(0)}}{\sigma_{\text{eff},j}^{(0)}}. \quad (5.154)$$

In Eq. (5.153) the superscript (0) and (1) denote LO and NLO contribution, respectively. The subscript “full” indicates a contribution with full top mass dependence whereas “eff” denotes an effective gluon-Higgs coupling. Terms with “QCD” as subscript indicate the interference contribution and those without “QCD” the signal amplitude squared. Thus, K_j is the ratio between the signal cross section at LO with full m_t dependence with respect to the signal cross section with an effective $gg\phi$ coupling also at LO. Note, that in Eq. (5.153) the contribution from the Higgs-Higgs interference is neglected. It has been checked that for the parameter scenarios considered in this work the Higgs-Higgs interference contribution is tiny and therefore phenomenologically irrelevant.

In Eq. (5.153) the K -factor methods applied in this work are defined for the total cross section but these formulas can be applied to the individual bins of differential cross sections as well.

5.4.1. Spin independent observables

This section is mainly based on Ref. [77]. We study spin independent observables within three phenomenologically viable parameter sets (scenarios) for the type-II 2HDM, two for the CPC and one for the CPV case. There are some common features of these parameter sets. First,

5. Heavy Higgs effects in top-quark pair production at next-to-leading order in α_s

the 125 GeV Higgs boson is identified with ϕ_1 and the parameters are chosen such that its couplings to fermions and gauge bosons are SM-like. For scenarios 1–3 (see below) the total decay width Γ_1 of ϕ_1 is of the order of 4 MeV and plays no role for the numerical evaluation of the observables in $t\bar{t}$ production studied in this work. As mentioned before the contribution of ϕ_1 is attributed to the corrections of the weak interaction to $t\bar{t}$ production which are taken into account in the numerical results. Second, the masses of the other two heavy neutral Higgs bosons are chosen such that $m_2, m_3 > 2m_t$. Third, we set $\tan\beta = 0.7$ to enhance the Yukawa coupling to top quarks in order to obtain a stronger signal. Due to experimental constraints [181–183] from B physics for values of $\tan\beta < 1$ we choose the mass of the charged Higgs boson $m_+ > 720$ GeV. Hence, the decay mode $\phi_{2,3} \rightarrow W^\pm H^\mp$ cannot occur.

The total decay widths of the heavy Higgs bosons ϕ_2, ϕ_3 are fixed by the model parameters (Sec. 2.4) and have to be calculated accordingly (Sec. 2.6) for a consistent treatment of the model. In this work we determine the total decay widths by summing the largest two body decay rates. The computer programs HDECAY [184] and 2HDMC [96] can perform this task while taking into account QCD corrections to the decays $\phi_j \rightarrow q\bar{q}$ and $\phi_j \rightarrow gg$. Both codes apply only to the CPC case but it is possible to adapt them to the CPV case. However, both programs use the fixed renormalization scale $\mu_R = m_\phi$ which is not suitable for our application since we vary μ_R (see below). Hence, we use the formulas given in Sec. 2.6 to calculate the partial widths of the heavy Higgs bosons using the parameter sets of the three scenarios defined below. The results were cross checked with 2HDMC for $\mu = m_\phi$. Electroweak corrections to the decay widths Γ_2, Γ_3 are not taken into account because we consider the process $pp \rightarrow \phi_{2,3} \rightarrow t\bar{t}$ only up to lowest order in non-QCD couplings.

Scenario 1

We consider the type-II 2HDM with a CPC Higgs potential in the alignment limit with the following set of parameters

$$\begin{aligned} \tan\beta = 0.7, \quad \alpha_1 = \beta = 0.61, \quad \alpha_2 = \alpha_3 = 0, \\ m_1 = 125\text{GeV}, \quad m_2 = 550\text{GeV}, \quad m_3 = 510\text{GeV}, \quad m_+ > 720\text{GeV}. \end{aligned} \quad (5.155)$$

This choice of parameters implies that ϕ_1 and ϕ_2 are pure scalars while ϕ_3 is a pseudoscalar Higgs boson, cf. Tab. 5.1. The reduced Yukawa couplings (cf. Tab. 2.2) and couplings to the weak gauge bosons (cf. Sec. 2.2) which result from (5.155) are given in Tab. 5.1.

Table 5.1.: Values of the reduced Yukawa couplings to the third-generation fermions and couplings to gauge bosons $V = W^\pm, Z$ of the neutral Higgs bosons ϕ_j in scenarios 1 and 2.

	a_{jt}	$a_{jb} = a_{j\tau}$	b_{jt}	$b_{jb} = b_{j\tau}$	f_{jVV}
ϕ_1	1	1	0	0	1
ϕ_2	1.429	-0.700	0	0	0
ϕ_3	0	0	1.429	0.700	0

The largest two-body decay rates of the scalar ϕ_2 and the pseudoscalar ϕ_3 are given in Tab. 5.2. According to Tab. 2.1 there are in general many coupling configurations to gauge bosons in a CPC 2HDM. However, due to the alignment limit $\alpha_1 = \beta$ the decay rates for $\phi_{2,3} \rightarrow VV$, $\phi_3 \rightarrow Z\phi_1$ and $\phi_2 \rightarrow \phi_1\phi_1$ are zero to the lowest order in the non-QCD couplings.

Table 5.2.: Dominant partial decay widths and the total widths of the two heavy, neutral Higgs bosons ϕ_2 and ϕ_3 in scenario 1. The super- and subscripts denote the shift due to the scale variations according to Eq. (5.156).

	Γ_2 [GeV]	Γ_3 [GeV]
$\phi_i \rightarrow t\bar{t}$	$34.48^{+0.33}_{-0.28}$	$49.15^{+0.38}_{-0.32}$
$\phi_i \rightarrow gg$	$0.08^{+0.01}_{-0.01}$	$0.13^{+0.02}_{-0.02}$
Total	$34.56^{+0.34}_{-0.28}$	$49.28^{+0.40}_{-0.34}$

The partial decay widths for $\phi_j \rightarrow f\bar{f}$ ($f \neq t$), $\phi_j \rightarrow \gamma\gamma$ and $\phi_j \rightarrow Z\gamma$ are very small ($\lesssim 10^{-3}\text{GeV}$) and are therefore neglected in the total decay width. The decay width to $b\bar{b}$ is suppressed due to the choice $\tan\beta = 0.7$. Hence, there are only two decay channels remaining. The corresponding partial decay widths are presented in Tab. 5.2. We see that the total decay width is dominated by the decay into $t\bar{t}$. The uncertainties result from the variation of the renormalization scale μ_R

$$\frac{\mu_0}{2} \leq \mu_R \leq 2\mu_0, \quad \mu_0 = \frac{m_2 + m_3}{4}. \quad (5.156)$$

Scenario 2

The values of the mixing angles and $\tan\beta$ in scenario 2 are the same as for scenario 1 (5.155). Hence, the values of the reduced Yukawa couplings and couplings to gauge bosons of the neutral Higgs bosons given in Tab. 5.1 also apply to scenario 2. However, the choice of masses differs from scenario 1

$$m_1 = 125\text{GeV}, \quad m_2 = 550\text{GeV}, \quad m_3 = 700\text{GeV}, \quad m_+ > 720\text{GeV}. \quad (5.157)$$

While the masses of the heavy neutral Higgs bosons in scenario 1 are nearly degenerate the pseudoscalar ϕ_3 in scenario 2 is considerably heavier than the scalar ϕ_2 . The decay rates for $\phi_{2,3} \rightarrow VV$, $\phi_3 \rightarrow \phi_1 Z$ and $\phi_2 \rightarrow \phi_1 \phi_1$ are zero to lowest order in the non-QCD couplings due to the alignment limit. The decays $\phi_3 \rightarrow \phi_1 \phi_1$ and $\phi_3 \rightarrow \phi_1 \phi_2$ are not possible in the CPC 2HDM. However, due to the larger mass separation of ϕ_2 and ϕ_3 with respect to scenario 1 the decay channel $\phi_3 \rightarrow Z\phi_2$ opens up and contributes to the total decay width of ϕ_3 (cf. Tab. 5.3). Also in scenario 2 the total decay width is dominated by the decay into $t\bar{t}$.

Table 5.3.: Dominant partial decay widths and total widths of the two heavy, neutral Higgs bosons ϕ_2 and ϕ_3 in scenario 2. The super- and subscripts denote the shift due to the scale variations according to Eq. (5.156).

	Γ_2 [GeV]	Γ_3 [GeV]
$\phi_i \rightarrow t\bar{t}$	$34.41^{+0.32}_{-0.26}$	$71.97^{+0.15}_{-0.13}$
$\phi_i \rightarrow \phi_2 Z$	0	3.14
$\phi_i \rightarrow gg$	$0.08^{+0.01}_{-0.01}$	$0.17^{+0.01}_{-0.01}$
Total	$34.49^{+0.33}_{-0.27}$	$75.28^{+0.14}_{-0.11}$

5. Heavy Higgs effects in top-quark pair production at next-to-leading order in α_s

Scenario 3

We consider a type-II 2HDM with a CPV Higgs potential (without approximate Z_2 symmetry) such that (2.81) forms a set of independent parameters. The set of model parameters defining scenario 3 is given by

$$\tan\beta = 0.7, \quad \alpha_1 = \beta, \quad \alpha_2 = \frac{\pi}{15}, \quad \alpha_3 = \frac{\pi}{4}, \quad (5.158)$$

$$m_1 = 125\text{GeV}, \quad m_2 = 500\text{GeV}, \quad m_3 = 800\text{GeV}, \quad m_+ > 720\text{GeV}. \quad (5.159)$$

For this choice of parameters the reduced Yukawa couplings and the couplings to gauge bosons are listed in Tab. 5.4. As this table shows, in this scenario the three neutral Higgs bosons $\phi_{1,2,3}$ are CP mixtures. All of the three neutral Higgs bosons including ϕ_1 have scalar as well as pseudoscalar couplings to fermions. Hence, in this model we move away from the strict alignment limit. However, the mixing angles are chosen such that the reduced Yukawa couplings and the couplings to gauge bosons of ϕ_1 are SM-like. The results for the most

Table 5.4.: Values of the reduced Yukawa couplings and couplings to gauge bosons $V = W^\pm, Z$ of the neutral Higgs bosons ϕ_j for scenario 3.

	a_{jt}	$a_{jb} = a_{j\tau}$	b_{jt}	$b_{jb} = b_{j\tau}$	f_{jVV}
ϕ_1	0.978	0.978	0.297	0.146	0.978
ϕ_2	0.863	-0.642	0.988	0.484	-0.147
ϕ_3	-1.157	0.348	0.988	0.484	-0.147

Table 5.5.: Dominant partial decay widths and total widths of the two heavy, neutral Higgs bosons ϕ_2 and ϕ_3 in scenario 3, defined in (5.158)–(5.160). The super- and subscripts denote the shift due to the scale variations according to Eq. (5.156).

	Γ_2 [GeV]	Γ_3 [GeV]
$\phi_i \rightarrow t\bar{t}$	$32.31^{+0.31}_{-0.26}$	$85.05^{+0.30}_{-0.25}$
$\phi_i \rightarrow VV$	1.12	5.11
$\phi_i \rightarrow \phi_1 Z$	0.65	3.24
$\phi_i \rightarrow \phi_2 Z$	0	31.28
$\phi_i \rightarrow \phi_1 \phi_1$	2.38	3.00
$\phi_i \rightarrow \phi_1 \phi_2$	0	0.31
$\phi_i \rightarrow gg$	$0.08^{+0.01}_{-0.01}$	$0.17^{+0.01}_{-0.01}$
Total	$36.55^{+0.32}_{-0.27}$	$128.16^{+0.29}_{-0.24}$

important two-body decay widths and the total widths of ϕ_2, ϕ_3 are given in Tab. 5.5. In this scenario without approximate Z_2 symmetry we have to specify also the values of the complex parameters λ_6 and λ_7 in the 2HDM potential. Here we choose

$$\text{Re}\lambda_6 = 0, \quad \text{Im}\lambda_6 = -3.677 \quad \text{and} \quad \lambda_7 = 0. \quad (5.160)$$

These parameters are only relevant for the calculation of the decay widths which involve trilinear Higgs couplings, i.e. only the decays $\phi_i \rightarrow \phi_1\phi_1$ and $\phi_i \rightarrow \phi_1\phi_2$ listed in Tab. 5.5. Due to the large mass separation between ϕ_2 and ϕ_3 , the deviation from the alignment limit and the fact that all neutral Higgs bosons are CP mixtures there are more decay channels that contribute to the total decay widths than in scenarios 1 and 2.

Experimental constraints

The parameters of scenarios 1–3 are chosen such as to comply with experimental constraints. We consider several of these constraints derived from experimental measurements.

1. Measurements of the couplings of the 125 GeV boson by the CMS [8] and ATLAS [9] experiments constrain the allowed deviation of the Yukawa couplings and couplings to gauge bosons of ϕ_1 from their respective SM values to about 20%–30%. Hence, even for scenario 3 where ϕ_1 contains a pseudoscalar component the respective couplings given in Tab. 5.4 fall into the allowed range.
2. Searches for heavy BSM resonances decaying into W^+W^- [185], ZZ [185, 186], $Z\phi_1$ [187, 188], $\phi_1\phi_1$ [189, 190], $\tau^-\tau^+$ [191, 192], $b\bar{b}$ [193] can constrain the 2HDM parameter space. Since the partial decay widths of ϕ_2 and ϕ_3 into these final states are very small or even zero in scenarios 1–3 (cf. Tabs. 5.1 and 5.4) these measurements do not exclude scenarios 1–3.
3. An ATLAS search for heavy resonances decaying into $t\bar{t}$ which was recently published [114, 115] has excluded scenario 1 with a confidence of 95%. According to their results scenario 1 lies just outside the allowed parameter space. The boundaries of this allowed region are however subject to systematic uncertainties both experimental and theoretical. An analysis with more statistics might be able to exclude scenario 1 more firmly.
4. B-physics observables such as rare decays $B \rightarrow X_s + \gamma$ and neutral $B_d^0-\bar{B}_d^0$ mixing are sensitive to contributions of the charged Higgs boson H^\pm in the loop and give constraints on the $\tan\beta-m_+$ parameter space. As mentioned above for the choice of $\tan\beta = 0.7$ the constraints derived in [181–183] demand $m_+ > 720$ GeV for the scenarios to stay within the allowed parameter region.
5. Measurements of the electroweak oblique parameters S , T and U also constrain the allowed 2HDM parameter space. Scenarios 1–3 are compatible with these constraints [79, 194–196] mainly because ϕ_1 is SM-like, ϕ_2 , ϕ_3 and H^\pm are heavy and the couplings of ϕ_2 and ϕ_3 to gauge bosons of the weak interaction are suppressed or even zero.
6. Experimental results on the electric dipole moments of the neutron [197] and the electron [198] are relevant for constraining the CPV scenario 3. The choice of mixing angles and masses in scenario 3 (5.158), (5.159) is made in accordance with the constraints derived in Ref. [117].

Results

The numerical evaluation of the (differential) cross section for the resonant production of heavy Higgs bosons and decay into $t\bar{t}$ is performed using the following input values for the SM parameters. The on-shell top-quark mass and the masses of the gauge bosons are set to

$$m_t = 173.34 \text{ GeV}, \quad m_W = 80.385 \text{ GeV}, \quad m_Z = 91.1876 \text{ GeV}. \quad (5.161)$$

5. Heavy Higgs effects in top-quark pair production at next-to-leading order in α_s

For the electromagnetic fine structure constant the following value is used

$$\alpha = \frac{1}{129}. \quad (5.162)$$

Via the LHAPDF library [101, 102] we employ the PDF set CT10nlo [100] which provides also the value for the coupling constant of the strong force, $\alpha_s(\mu)$ at a scale μ . As a common practice we use the residual scale dependence of the results to estimate the uncertainty due to missing higher orders. Here this is done by setting the renormalization scale μ_R equal to the factorization scale μ_F ($\mu_F = \mu_R \equiv \mu$) and varying the scale μ around the central value

$$\mu_0 = \frac{m_2 + m_3}{4} \quad (5.163)$$

according to Eq. (5.156). The choice for this central scale is motivated by the choice $\mu_0 = m_h/2$ in the SM case (e.g. see [199]).

The numerical results for the pure QCD contribution including the weak corrections have been provided by the authors of [111, 112]. The analytical results (Sec. 5.3) as well as numerical results for the signal amplitude squared and the interference between the signal and the nonresonant QCD background including the spin dependent part were derived in this work and published in Refs. [77, 78].

In the following results for proton-proton collisions at a hadronic center-of-mass energy of $\sqrt{s} = 13$ TeV are presented. The inclusive hadronic cross section at NLO for the three type-II 2HDM scenarios defined above is given in Tab. 5.6. σ_{QCDW} denotes the inclusive cross section of $t\bar{t}$ production including NLO QCD and weak corrections but without the contribution from the heavy Higgs bosons ϕ_2 and ϕ_3 . However, due to the choice of the renormalization and factorization scale $\mu = \mu_0 = (m_2 + m_3)/4$ the cross section σ_{QCDW} depends on the scenario. $\sigma_{2\text{HDM}}$ denotes the inclusive hadronic cross sections of the resonant production of the neutral heavy Higgs bosons of the 2HDM and their decay into $t\bar{t}$ at NLO QCD. This cross section also includes the contribution from the interference between the resonant signal process and the nonresonant QCD background at NLO QCD. From Tab. 5.6 it becomes clear, that the inclusive $t\bar{t}$ cross section is not an adequate observable to study the effects of heavy Higgs bosons. The S/B (last row in Tab. 5.6) for scenarios 1–3 are roughly between 1% and 2%. Hence, it is necessary to study more sensitive observables such as differential cross sections. Since these observables contain more information about the collision process they are potentially more sensitive to new physics effects.

Table 5.6.: Inclusive $t\bar{t}$ production cross sections in different type-II 2HDM scenarios at NLO. The superscripts (subscripts) correspond to $\mu = \mu_0/2$ ($\mu = 2\mu_0$). The scale variation changes the ratio by less than ± 0.001 and is not displayed in the table.

	Scenario 1	Scenario 2	Scenario 3
σ_{QCDW} [pb]	$643.22^{+81.23}_{-77.71}$	$624.25^{+80.98}_{-76.19}$	$619.56^{+81.05}_{-75.72}$
$\sigma_{2\text{HDM}}$ [pb]	$13.59^{+1.85}_{-1.64}$	$7.4^{+0.77}_{-0.78}$	$7.21^{+0.81}_{-0.77}$
$\sigma_{2\text{HDM}}/\sigma_{\text{QCDW}}$	0.021	0.012	0.012

One kind of differential cross section already studied at LO is the $t\bar{t}$ invariant mass distribution. The results for scenario 1–3 at NLO QCD are presented in Figs. 5.15–5.17, respectively. The upper plots show the $M_{t\bar{t}}$ distribution in black for the SM including NLO QCD and weak corrections. The red histogram represents the sum of the SM contribution and the contribution from the 2HDM including the interference between signal and background at NLO QCD. The

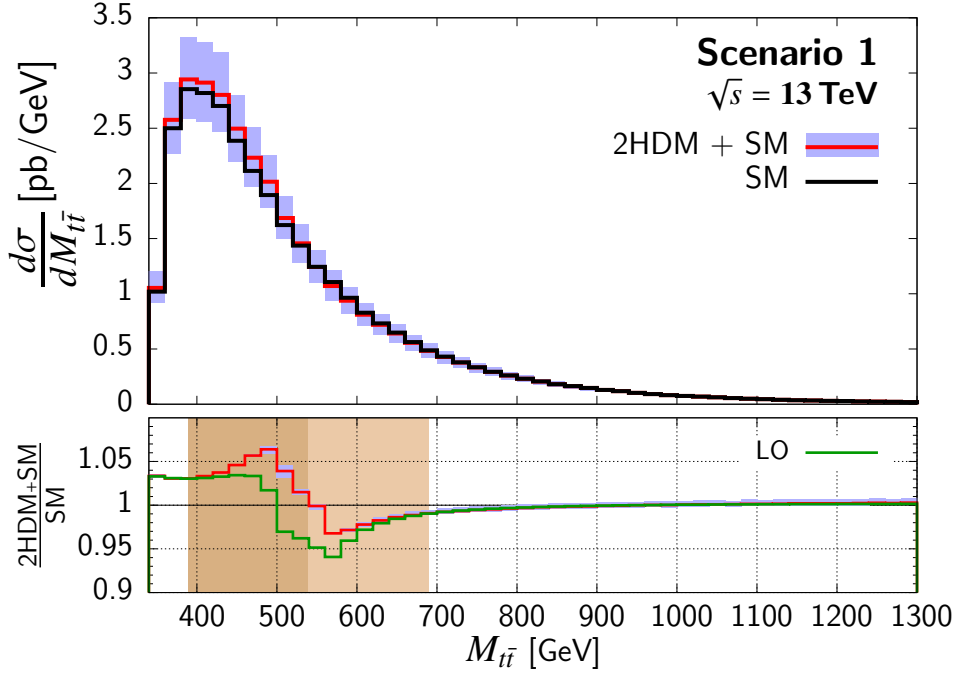


Figure 5.15.: Distribution of the $t\bar{t}$ invariant mass for scenario 1 at NLO. Upper panel: $M_{t\bar{t}}$ distribution for the SM including NLO QCD and weak corrections (black). $M_{t\bar{t}}$ distribution for the sum of SM contribution and the contribution involving the neutral heavy Higgs bosons including the Higgs-QCD interference at NLO QCD (red). Lower panel: signal-to-background ratio at NLO (red) and LO (green).

blue shaded area indicates the uncertainty of the prediction due to the residual scale dependence estimated by varying the scale according to Eq. (5.156). The lower plots in Figs. 5.15–5.17 display in red the S/B ($(\text{SM}+2\text{HDM})/\text{SM}$) at NLO QCD. The scale uncertainty is strongly reduced in this ratio due to cancellations between numerator and denominator. Hence, the blue shaded area is invisible for most of the bins. The green curve shows the LO prediction of the S/B for comparison. While the NLO corrections to the S/B are sizeable with respect to the LO prediction the overall contribution from ϕ_2 and ϕ_3 in scenarios 1–3 is rather small, 5%–7%, due to the large QCD background. In scenario 1 where the two resonances overlap a peak value of the S/B of approximately 7% is observed. In scenarios 2 and 3 the maximal S/B is smaller. Even though this can be considered a small effect it is larger than for the inclusive cross section (Tab. 5.6). This can be understood from the S/B plots in Figs. 5.15–5.17 which clearly show that the contribution from ϕ_2 , ϕ_3 induces a peak-dip structure in the $M_{t\bar{t}}$ distribution with respect to the SM background. In the inclusive case, when integrating over $M_{t\bar{t}}$, the peak and dip contributions partially cancel which reduces the overall effect. Hence, the inclusive cross section shows only very little sensitivity to the effects of the 2HDM in $t\bar{t}$ production.

Since the validity of the calculation of the NLO corrections to the heavy Higgs contribution in the approach used in this work is restricted to the resonance region we apply $M_{t\bar{t}}$ cuts around this region. These cuts are indicated as orange shaded regions in the S/B (lower) plots in Figs. 5.15–5.17. As described above the peak-dip feature is located in this region. To avoid the (partial) cancellation between peak and dip and therefore enhance the signal we divide the $M_{t\bar{t}}$ cut into two regions as listed in Tab. 5.7. These cuts are chosen such that the lower $M_{t\bar{t}}$ window contains the peak and the upper one the dip. As an illustrative example of how

5. Heavy Higgs effects in top-quark pair production at next-to-leading order in α_s

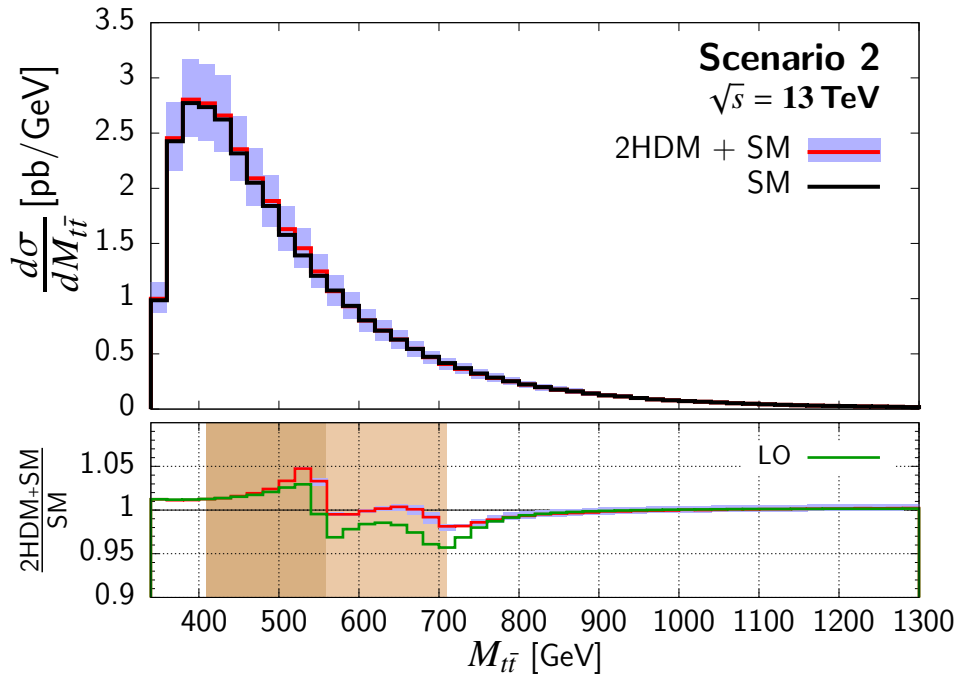


Figure 5.16.: Same as Fig. 5.15 but for scenario 2.

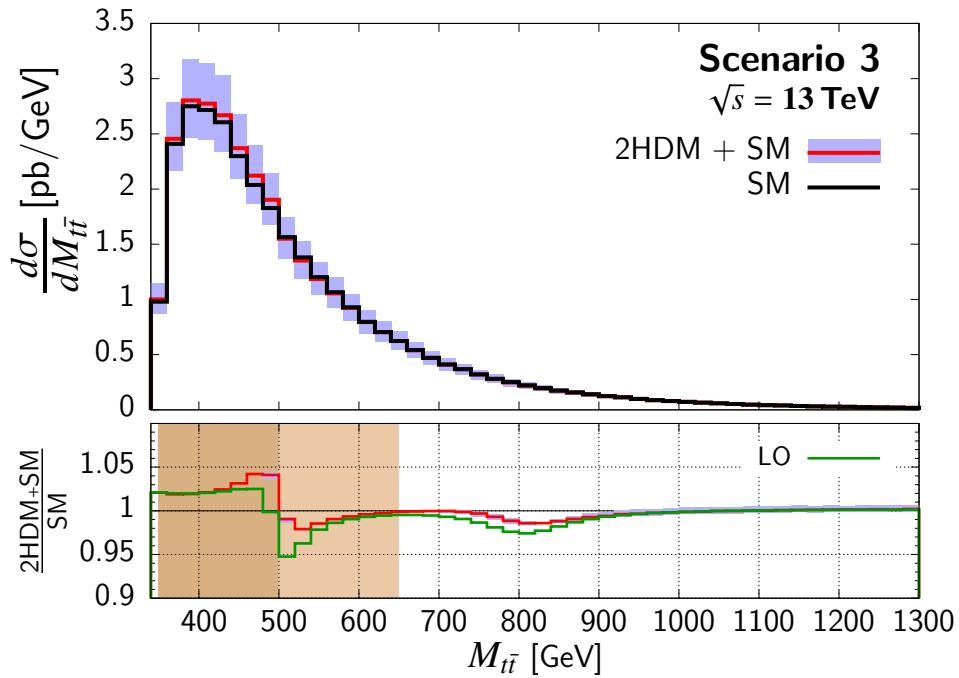


Figure 5.17.: Same as Fig. 5.15 but for scenario 3.

Table 5.7.: $M_{\tilde{t}\tilde{t}}$ windows used in the computation of the y_t and $\cos\theta_{CS}$ distributions.

	Lower $M_{\tilde{t}\tilde{t}}$ window	Upper $M_{\tilde{t}\tilde{t}}$ window
Scenario 1	$390 \text{ GeV} \leq M_{\tilde{t}\tilde{t}} \leq 540 \text{ GeV}$	$540 \text{ GeV} \leq M_{\tilde{t}\tilde{t}} \leq 690 \text{ GeV}$
Scenario 2	$410 \text{ GeV} \leq M_{\tilde{t}\tilde{t}} \leq 560 \text{ GeV}$	$560 \text{ GeV} \leq M_{\tilde{t}\tilde{t}} \leq 710 \text{ GeV}$
Scenario 3	$350 \text{ GeV} \leq M_{\tilde{t}\tilde{t}} \leq 500 \text{ GeV}$	$500 \text{ GeV} \leq M_{\tilde{t}\tilde{t}} \leq 650 \text{ GeV}$

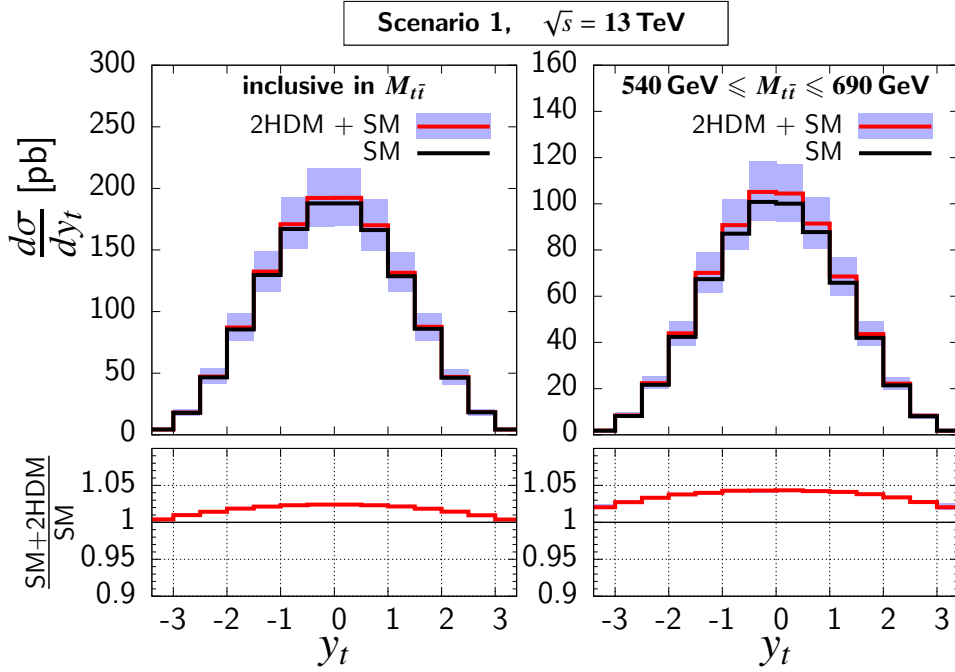


Figure 5.18.: Comparison between the top-quark rapidity distribution in scenario 1 with (right plot) and without (left plot) $M_{\tilde{t}\tilde{t}}$ cut at NLO. Upper panels: top-quark rapidity distribution for the SM (QCD and weak corrections) at NLO (black) and sum of SM and 2HDM heavy Higgs contribution including Higg-QCD interference at NLO (red). Lower panels: signal-to-background ratio.

this kind of cut can enhance the sensitivity of an observable we compare in Fig. 5.18 the distribution of the top-quark rapidity y_t and the corresponding S/B with and without a cut on $M_{\tilde{t}\tilde{t}}$. The top-quark rapidity is defined as

$$y_t = \frac{1}{2} \ln \frac{E_t + k_t^z}{E_t - k_t^z}, \quad (5.164)$$

where E_t and k_t^z are the energy and the z component of the momentum (along the beam axis), respectively, of the top quark in the laboratory frame. In the upper plots of Fig. 5.18 the distribution for the SM (black) and including the 2HDM contribution (red) is shown. From the lower plots it can be seen that the S/B is enhanced (right plot) when imposing an appropriate $M_{\tilde{t}\tilde{t}}$ cut with respect to the case when $d\sigma/dy_t$ is evaluated inclusively in $M_{\tilde{t}\tilde{t}}$ (left plot).

In an experimental analysis where the mass of the resonance(s) is not known beforehand one could use a sliding $M_{\tilde{t}\tilde{t}}$ window and scan the relevant $M_{\tilde{t}\tilde{t}}$ range for enhancements in observables such as y_t . A simple binning in $M_{\tilde{t}\tilde{t}}$ as it was done for example for the forward-backward asymmetry of $t\bar{t}$ (e.g. [200]) might not be enough to detect the resonance. If the

5. Heavy Higgs effects in top-quark pair production at next-to-leading order in α_s

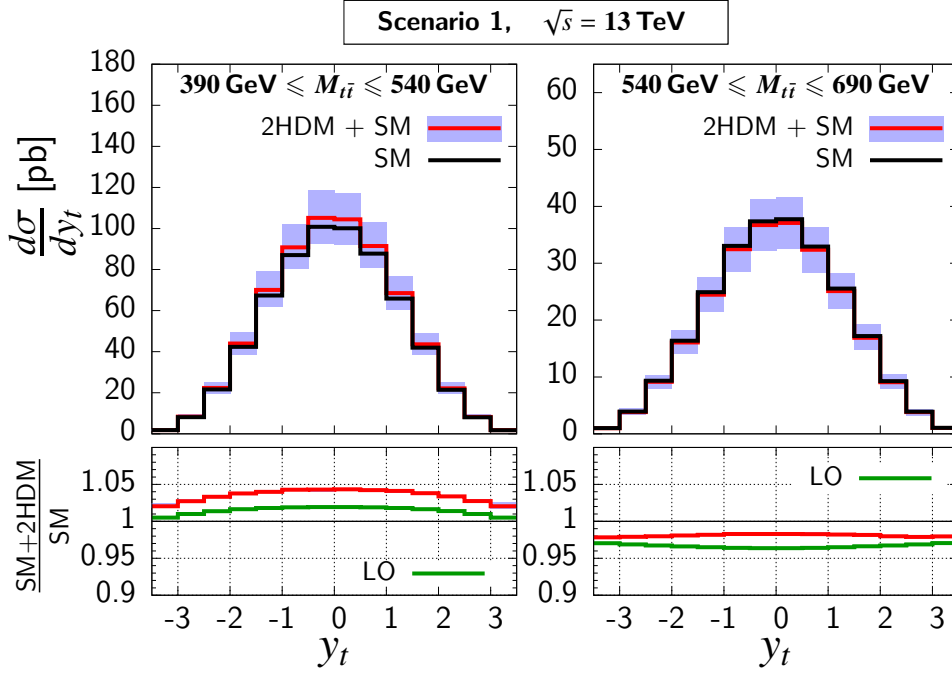


Figure 5.19.: Top quark rapidity distribution for scenario 1 at NLO evaluated for selected $M_{t\bar{t}}$ windows (Tab. 5.7). Upper panels: y_t distribution for the SM only (black) including NLO QCD and weak corrections and for the sum of SM and 2HDM contributions (red) including the Higgs-QCD interference at NLO QCD. Lower panels: signal-to-background ratio at LO (green) and NLO (red).

$M_{t\bar{t}}$ bin is large the peak and dip might still (partially) cancel if they fall into the same bin. In the presence of a peak-dip structure by shifting the $M_{t\bar{t}}$ window in small steps one will arrive at a setting where the window contains either the peak or the dip. These are the configurations specified in Tab. 5.7 for scenario 1–3.

The results for the top-quark rapidity distribution are presented in Figs. 5.19–5.21 for the $M_{t\bar{t}}$ cuts listed in Tab. 5.7 for scenario 1–3. The left plots show the $d\sigma/dy_t$ in the lower $M_{t\bar{t}}$ window (first column in Tab. 5.7) indicated by the dark orange shaded region in the S/B plots in Figs. 5.15–5.17 and the right plots show the rapidity distribution in the upper $M_{t\bar{t}}$ window (second column in Tab. 5.7) indicated by the light orange shaded region in the S/B plots in Figs. 5.15–5.17. The layout of the left and right plots and the color code of the curves is analogous to the $M_{t\bar{t}}$ distribution plots in Figs. 5.15–5.17. In all three scenarios the QCD correction is positive. For the lower $M_{t\bar{t}}$ window containing the peak this leads to an enhancement of the S/B with respect to the LO prediction. In scenario 1 the S/B is enhanced by roughly a factor of two while in scenario 2 and 3 the enhancement is very small. In the upper $M_{t\bar{t}}$ window containing the dip the positive NLO QCD corrections lead to a reduction of the S/B.

The strongest effects of heavy Higgs bosons in the y_t distribution occur in scenario 1 (Fig. 5.19). In the lower $M_{t\bar{t}}$ window in the central region $|y_t| \leq 1$ the S/B is about 4%. For the other scenarios the S/B is smaller. Hence, the sensitivity of the top-quark rapidity distribution to heavy Higgs contributions in $t\bar{t}$ production is slightly smaller than for the $M_{t\bar{t}}$ distribution in the scenarios under consideration. The distribution of the antitop-quark rapidity $y_{\bar{t}}$ is very similar to the one of the top quark and does not bear any significant new insights with respect to the 2HDM contribution. The inclusive $t\bar{t}$ charge asymmetry $A_C = [N(\delta|y| > 0) - N(\delta|y| < 0)]/N_{\text{tot}}$

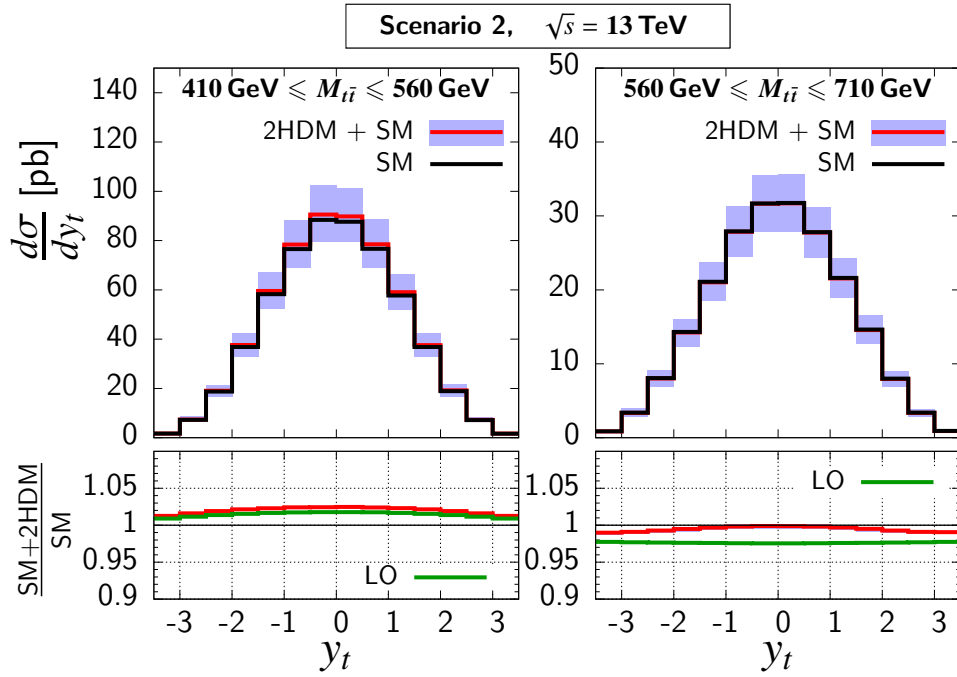


Figure 5.20.: Same as Fig. 5.19 but for scenario 2.

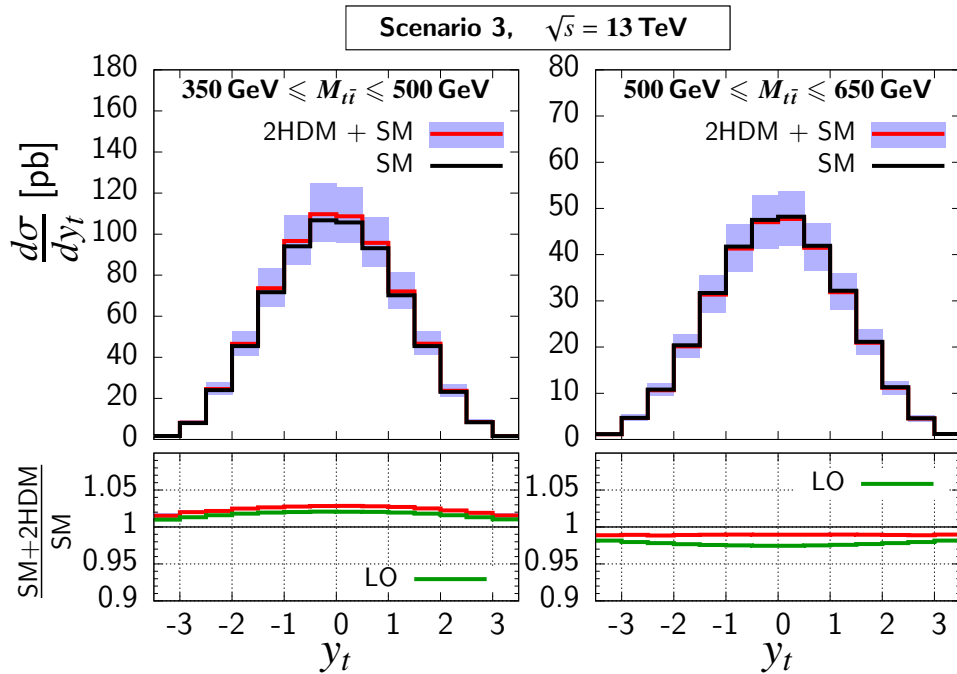


Figure 5.21.: Same as Fig. 5.19 but for scenario 3.

5. Heavy Higgs effects in top-quark pair production at next-to-leading order in α_s

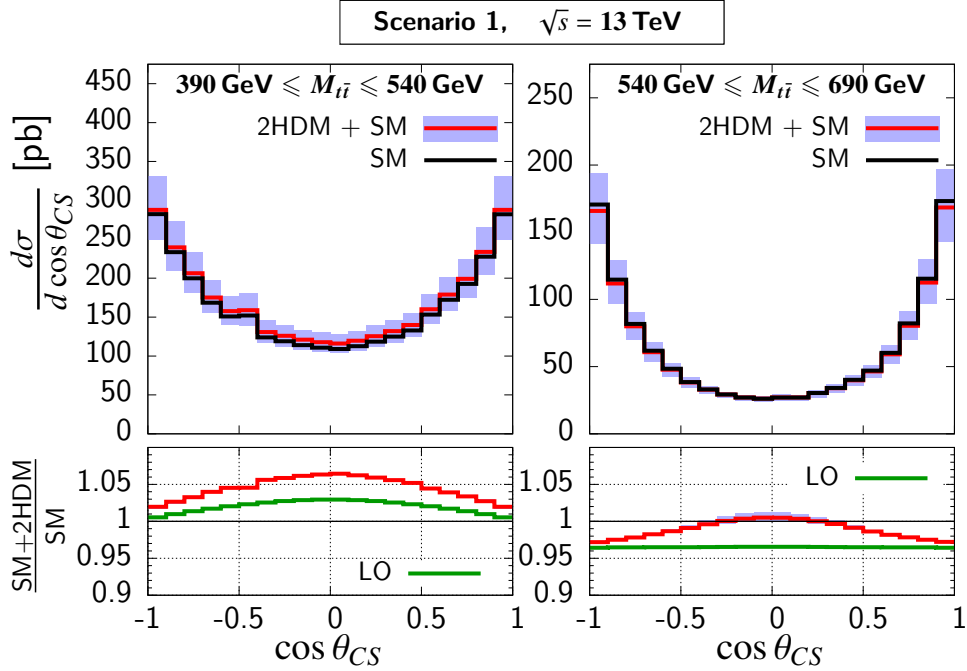


Figure 5.22.: Distribution of the cosine of the Collins–Soper angle for scenario 1 at NLO evaluated for selected $M_{t\bar{t}}$ windows (Tab. 5.7). Upper panels: $\cos \theta_{CS}$ distribution for the SM only (black) including NLO QCD and weak corrections and for the sum of SM and 2HDM contributions (red) including the Higgs–QCD interference at NLO QCD. Lower panels: signal-to-background ratio at LO (green) and NLO (red).

with $\delta|y| = |y_t| - |y_{\bar{t}}|$ which is nonzero in the SM is not affected by the heavy Higgs contribution.

Besides $M_{t\bar{t}}$ and y_t we also study the sensitivity of the Collins–Soper angle [201] θ_{CS} to the effects of the heavy neutral Higgs bosons of the 2HDM on $t\bar{t}$ production. The Collins–Soper angle θ_{CS} is defined as the angle between the top-quark direction in the $t\bar{t}$ rest frame and the bisecting line between \mathbf{p}_1 and $-\mathbf{p}_2$. Where \mathbf{p}_1 and \mathbf{p}_2 denote the three-momenta of the two incoming partons in the $t\bar{t}$ rest frame. If the $t\bar{t}$ pair does not have any transverse momentum (e.g. for LO $t\bar{t}$ production) the Collins–Soper angle is identical to the scattering angle between the top quark and the beam axis in the $t\bar{t}$ rest frame. The results for the distribution of the cosine of the Collins–Soper angle $\cos \theta_{CS}$ for scenarios 1–3 are presented in Figs. 5.22–5.24. The layout of the plot and the color code of the curves is the same as for the Figs. 5.19–5.21. The qualitative behavior of the S/B of the Collins–Soper angle distributions is similar to y_t : positive NLO QCD corrections enhance the signal in lower $M_{t\bar{t}}$ window and reduce it in the upper $M_{t\bar{t}}$ window. The strongest effects are seen in the lower $M_{t\bar{t}}$ window in scenario 1 where the S/B rises up to 7% in the central region $\cos \theta_{CS} \approx 0$.

The transverse momentum of the top quarks has also been investigated in [77] but the sensitivity to heavy Higgs bosons in $t\bar{t}$ production is less than the sensitivity of the observables discussed here. All three differential cross sections can achieve a S/B of a few percent in scenario 1. From these results it seems that the $M_{t\bar{t}}$ distribution performs comparatively well with respect to the S/B which confirms its adequacy as an observable to search for such resonances. The achievable S/B in the $M_{t\bar{t}}$ distribution depends on the bin size. In the results presented here a bin width of 20 GeV is used. For a larger bin size the maximum S/B in the $M_{t\bar{t}}$ distribution is reduced.

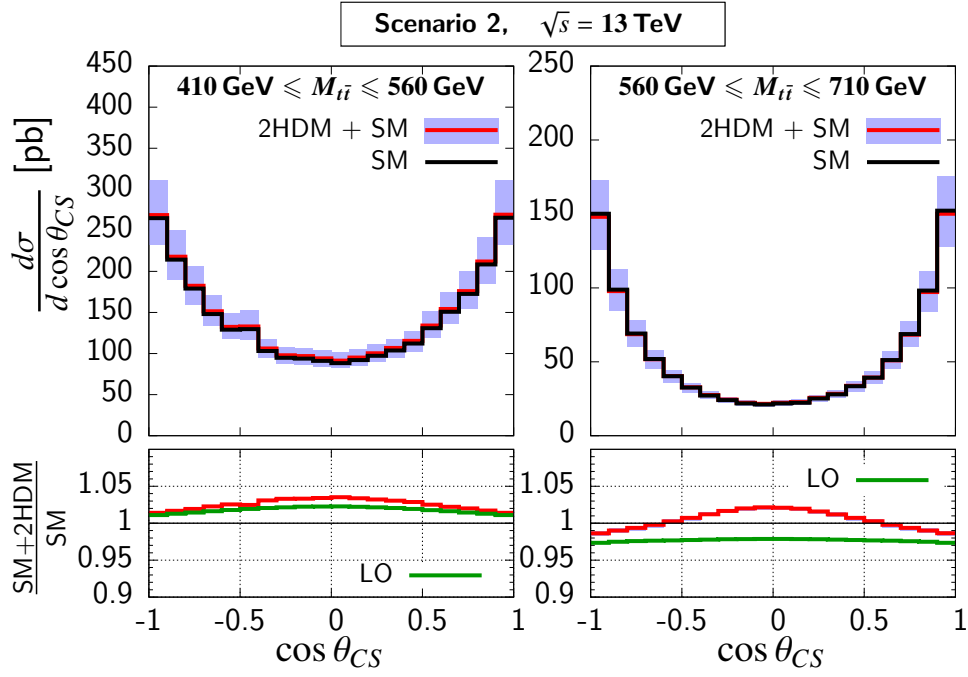


Figure 5.23.: Same as Fig. 5.22 but for scenario 2.

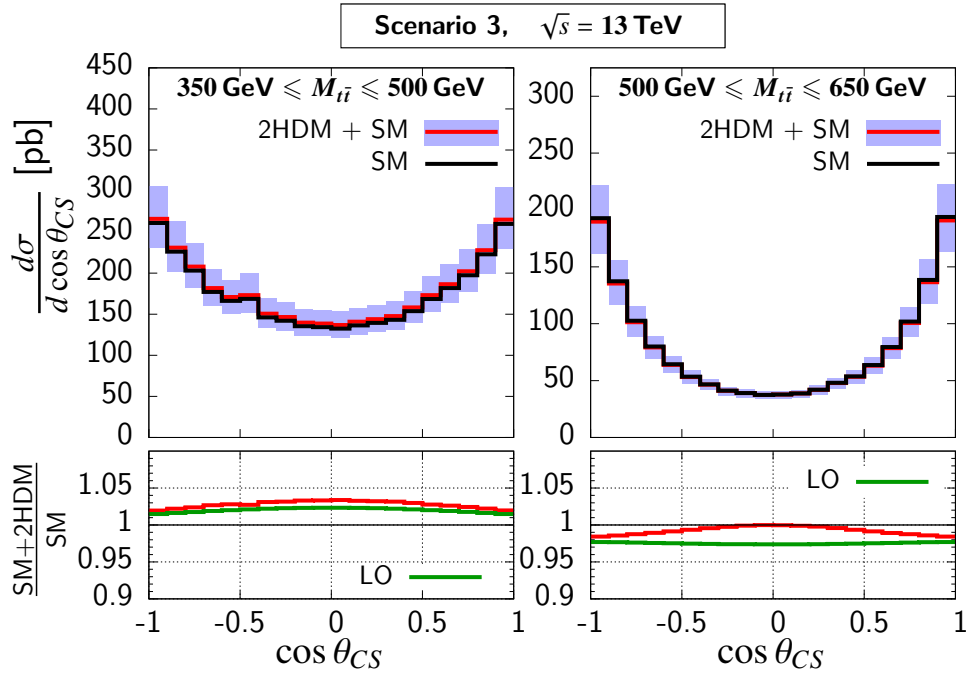


Figure 5.24.: Same as Fig. 5.22 but for scenario 3.

5.4.2. Spin dependent observables

In Sec. 4.2.4 it was shown that spin dependent observables have the potential to increase the sensitivity to the effects of heavy Higgs bosons in $t\bar{t}$ production significantly. In this section we study at NLO QCD several spin dependent observables that are sensitive to top-quark polarization and $t\bar{t}$ spin correlations. As described in Sec. 3.3 these kinds of spin effects in $t\bar{t}$ production are experimentally accessible by studying angular distributions of the decay products of the $t\bar{t}$ pair. Here the dileptonic decay of the $t\bar{t}$ pair is considered

$$pp \rightarrow t + \bar{t} + X \rightarrow \ell^+ \ell'^- + \text{jets} + E_T^{\text{miss}}, \quad \ell, \ell' = e, \mu. \quad (5.165)$$

We calculate four P - and CP -even $t\bar{t}$ spin correlations at the level of the intermediate t and \bar{t} states and present them in terms of the angular correlations of the two leptons. Furthermore, we investigate the P - and CP -odd triple correlation as well as the top-quark longitudinal polarization. Additionally, we investigate the correlation of the leptonic azimuthal angles and study its sensitivity to the CP nature of the heavy Higgs bosons in the 2HDM. The results presented in this section are mainly based on Ref. [78].

Type-II 2HDM scenarios

In order to study whether suitable observables allow to discriminate between a scalar, pseudoscalar, and a CP mixture we introduce three scenarios, Ia, Ib and Ic that represent these three cases and allow for a direct comparison. The masses of the two heavy neutral Higgs bosons in these three scenarios are set to 400 GeV and 900 GeV. In the CPC scenarios Ia and Ib the Higgs bosons are CP eigenstates. In scenario Ia the scalar ϕ_2 has a mass of 400 GeV and the pseudoscalar ϕ_3 a mass of 900 GeV. In scenario Ib the situation is reversed such that the scalar has a mass of 900 GeV and the pseudoscalar a mass of 400 GeV. Scenario Ic represents the case of a CPV 2HDM Higgs potential where the two heavy Higgs bosons are CP mixtures. Focusing, for example, on the lighter Higgs boson scenarios Ia–Ic facilitate the comparison between 400 GeV resonances of different CP nature. Besides this comparative study we also analyse these scenarios by investigating the sensitivity of several spin dependent observables to heavy Higgs effects in $t\bar{t}$ production. As will be shown below the sensitivity can be increased with respect to the $M_{t\bar{t}}$ distribution by using spin dependent observables. However, for scenarios Ia–Ic the effects seen in the $M_{t\bar{t}}$ distribution are already quite large for the 400 GeV resonance (see Appendix G). That is why from an experimental point of view these scenarios are excluded at a confidence of at least 95% by a recent ATLAS analysis [114, 115]. Hence, a fourth scenario labeled “scenario II” is introduced which shows only small effects in the $M_{t\bar{t}}$ distribution and is therefore experimentally not excluded yet. We investigate if spin dependent observables can provide a sensitivity which is enhanced with respect to the $M_{t\bar{t}}$ distribution also in the case of scenario II. The CPC scenario II features a heavy scalar ϕ_2 with a mass of 600 GeV and a pseudoscalar with a mass of 900 GeV.

The list of values of model parameters for scenarios Ia–Ic and II is given in Tab. 5.8 and the resulting Yukawa couplings and couplings to vector bosons are listed in Tab. 5.9. The dominant two-body decay rates and the total decay width of ϕ_2 and ϕ_3 in scenarios Ia–Ic and II are presented in Tabs. 5.10 and 5.11.

Observables

In the following we define and summarize the spin dependent observables used to analyse scenarios Ia–Ic and II. As mentioned above we consider the dileptonic decay of the $t\bar{t}$ pair

Table 5.8.: Input values for the type-II 2HDM parameters for scenarios Ia–Ic and II.

	Scenario Ia	Scenario Ib	Scenario Ic	Scenario II
$\tan\beta$	1	1	1	1
α_1	β	β	β	β
α_2	0	0	$\pi/15$	0
α_3	0	0	$\pi/4$	0
m_1 [GeV]	125	125	125	125
m_2 [GeV]	400	900	400	600
m_3 [GeV]	900	400	900	900
m_+ [GeV]	> 820	> 820	> 820	> 820

Table 5.9.: Reduced scalar (a_{jf}) and pseudoscalar (b_{jf}) Yukawa couplings and couplings to weak gauge bosons (f_{jVV}) for scenarios Ia–Ic and II.

	a_{jt}	$a_{jb} = a_{j\tau}$	b_{jt}	$b_{jb} = b_{j\tau}$	f_{jVV}
Scenarios Ia, Ib, II					
ϕ_1	1	1	0	0	1
ϕ_2	1	-1	0	0	0
ϕ_3	0	0	1	1	0
Scenario Ic					
ϕ_1	0.978	0.978	0.208	0.208	0.978
ϕ_2	0.560	-0.854	0.692	0.692	-0.147
ϕ_3	-0.854	0.560	0.692	0.692	-0.147

Table 5.10.: Dominant two-body partial widths and total decay width of ϕ_2 and ϕ_3 in scenarios Ia–Ic. The subscripts and superscripts denote the shift due to scale variations according to Eq. (5.156). Partial decay widths that show these shifts are calculated at NLO QCD.

	Scenario Ia		Scenario Ib		Scenario Ic	
	Γ_2	Γ_3	Γ_2	Γ_3	Γ_2	Γ_3
$\phi_i \rightarrow t\bar{t}$	$3.97^{+0.10}_{-0.08}$	$45.43^{+0.36}_{-0.30}$	$39.85^{+0.20}_{-0.17}$	$15.09^{+0.31}_{-0.26}$	$8.47^{+0.18}_{-0.15}$	$50.80^{+0.32}_{-0.27}$
$\phi_i \rightarrow VV$	0	0	0	0	0.52	7.37
$\phi_i \rightarrow \phi_1 Z$	0	0	0	0	0.27	4.73
$\phi_i \rightarrow \phi_2 Z$	0	116.85	0	0	0	111.80
$\phi_i \rightarrow \phi_3 Z$	0	0	116.85	0	0	0
$\phi_i \rightarrow \phi_1 \phi_1$	0	0	0	0	3.20	6.14
$\phi_i \rightarrow \phi_1 \phi_2$	0	0	0	0	0	4.00
$\phi_i \rightarrow \phi_2 \phi_2$	0	0	0	0	0	11.81
$\phi_i \rightarrow gg$	$0.017^{+0.003}_{-0.002}$	$0.107^{+0.0003}_{-0.0036}$	$0.068^{+0.004}_{-0.005}$	$0.051^{+0.009}_{-0.007}$	$0.030^{+0.005}_{-0.004}$	$0.100^{+0.003}_{-0.005}$
Total	$3.99^{+0.10}_{-0.08}$	$162.39^{+0.36}_{-0.30}$	$156.76^{+0.19}_{-0.16}$	$15.14^{+0.32}_{-0.27}$	$12.49^{+0.19}_{-0.15}$	$184.95^{+0.32}_{-0.26}$

5. Heavy Higgs effects in top-quark pair production at next-to-leading order in α_s

Table 5.11.: Dominant two-body partial width and total decay width of ϕ_2 and ϕ_3 in scenario II. The subscripts and superscripts denote the shift due to scale variations according to Eq. (5.156). Partial decay widths that show these shifts are calculated at NLO QCD.

	Γ_2	Γ_3
$\phi_i \rightarrow t\bar{t}$	$20.65^{+0.12}_{-0.10}$	$45.50^{-0.35}_{+0.29}$
$\phi_i \rightarrow \phi_2 Z$	0	35.34
$\phi_i \rightarrow gg$	$0.040^{+0.005}_{-0.005}$	$0.106^{+0.001}_{-0.004}$
Total	$20.69^{+0.13}_{-0.11}$	$80.94^{-0.35}_{+0.29}$

(5.165). For the two final state charged leptons the normalized double differential distribution is defined as (see also Appendix C.3)

$$\frac{1}{\sigma} \frac{d^2\sigma}{d\cos\theta_+ d\cos\theta_-} = \frac{1}{4} \left(1 + B_1(\hat{\mathbf{a}}_1) \cos(\theta_+) + B_2(\hat{\mathbf{a}}_2) \cos(\theta_-) - C(\hat{\mathbf{a}}_1, \hat{\mathbf{a}}_2) \cos(\theta_+) \cos(\theta_-) \right), \quad (5.166)$$

where θ_+ (θ_-) is the angle between the direction of the three-momentum $\hat{\mathbf{q}}_{\ell^+}$ ($\hat{\mathbf{q}}_{\ell^-}$) of the positively (negatively) charged lepton in the top (antitop) rest frame and an arbitrary reference axis $\hat{\mathbf{a}}_1$ ($\hat{\mathbf{a}}_2$). The coefficient C is sensitive to $t\bar{t}$ spin correlations and is given by

$$C = -9 \langle \cos\theta_+ \cos\theta_- \rangle_{\ell\ell}, \quad (5.167)$$

where the expectation value is evaluated with respect to the dileptonic phase space. According to Eq. (C.35) C can also be determined at the level the intermediate $t\bar{t}$ pair

$$C(\hat{\mathbf{a}}_1, \hat{\mathbf{a}}_2) = \kappa_\ell^2 \langle 4(\mathbf{S}_t \cdot \hat{\mathbf{a}}_1)(\mathbf{S}_{\bar{t}} \cdot \hat{\mathbf{a}}_2) \rangle_{t\bar{t}}, \quad (5.168)$$

where the expectation value is evaluated with respect to the $t\bar{t}$ phase space. From Eqs. (5.167) and (5.168) follows

$$\langle \cos\theta_+ \cos\theta_- \rangle_{\ell\ell} = -\kappa_\ell^2 \frac{4}{9} \langle (\mathbf{S}_t \cdot \hat{\mathbf{a}}_1)(\mathbf{S}_{\bar{t}} \cdot \hat{\mathbf{a}}_2) \rangle_{t\bar{t}}. \quad (5.169)$$

This relation is also derived for $\hat{\mathbf{a}}_1 = \hat{\mathbf{k}}_t = \hat{\mathbf{k}}$ and $\hat{\mathbf{a}}_2 = \hat{\mathbf{k}}_{\bar{t}} = -\hat{\mathbf{k}}$ in Sec. 3.3 and holds only if no acceptance cuts are applied to the dileptonic final state. The coefficient κ_ℓ is the spin analyzing power of the lepton where the following convention is used

$$\kappa_\ell = \kappa_{\ell^+} = \kappa_{\ell^-}. \quad (5.170)$$

The value of κ_ℓ including NLO QCD corrections is given in Ref. [202]

$$\kappa_\ell = 1 - 0.015\alpha_s. \quad (5.171)$$

We calculate the expectation values $\langle (\mathbf{S}_t \cdot \hat{\mathbf{a}}_1)(\mathbf{S}_{\bar{t}} \cdot \hat{\mathbf{a}}_2) \rangle_{t\bar{t}}$ and use Eq. (5.168) to obtain the coefficient $C(\hat{\mathbf{a}}_1, \hat{\mathbf{a}}_2)$ in the double differential distribution (5.166). In particular, we use the orthogonal basis $\{\hat{\mathbf{k}}, \hat{\mathbf{n}}, \hat{\mathbf{r}}\}$ introduced in Ref. [118] and used in Sec. 4.2.4 to construct three observables

$$C_{\text{hel}} \equiv C(\hat{\mathbf{k}}, -\hat{\mathbf{k}}), \quad C_{\text{nn}} \equiv C(\hat{\mathbf{n}}, -\hat{\mathbf{n}}), \quad C_{\text{rr}} \equiv C(\hat{\mathbf{r}}, -\hat{\mathbf{r}}), \quad (5.172)$$

that are sensitive to $t\bar{t}$ spin correlations.

Another spin correlation that is considered here is related to the opening angle distribution (see Appendix C.4)

$$\frac{1}{\sigma} \frac{d\sigma}{d \cos \varphi} = \frac{1}{2} (1 - D \cos \varphi), \quad (5.173)$$

where $\cos \varphi = \hat{\mathbf{q}}_{\ell^+} \cdot \hat{\mathbf{q}}_{\ell^-}$. The coefficient D is given by

$$D = -3 \langle \cos \varphi \rangle_{\ell\ell}, \quad (5.174)$$

where the expectation value is evaluated in the dileptonic phase space. As for the other spin correlations above there exists a spin operator that corresponds to the angular correlation $\hat{\mathbf{q}}_{\ell^+} \cdot \hat{\mathbf{q}}_{\ell^-}$. It is obtained by the replacement

$$\hat{\mathbf{q}}_{\ell^+} \rightarrow \mathbf{S}_t, \quad \hat{\mathbf{q}}_{\ell^-} \rightarrow \mathbf{S}_{\bar{t}}. \quad (5.175)$$

Therefore, alternatively, D can be expressed in term of this operator according to Eq. (C.43)

$$D = \kappa_\ell^2 \frac{4}{3} \langle (\mathbf{S}_t \cdot \mathbf{S}_{\bar{t}}) \rangle_{t\bar{t}}, \quad (5.176)$$

where the expectation value is evaluated in the $t\bar{t}$ phase space. Again, we can derive a relation between the $t\bar{t}$ spin correlation and the experimentally accessible opening angle φ if no acceptance cut are applied to the leptons

$$\langle \cos \varphi \rangle_{\ell\ell} = -\kappa_\ell^2 \frac{4}{9} \langle (\mathbf{S}_t \cdot \mathbf{S}_{\bar{t}}) \rangle_{t\bar{t}}. \quad (5.177)$$

Since $\{\hat{\mathbf{k}}, \hat{\mathbf{n}}, \hat{\mathbf{r}}\}$ is an orthonormal basis the following relation holds

$$D = -\frac{1}{3} (C_{\text{hel}} + C_{\text{nn}} + C_{\text{rr}}) \quad (5.178)$$

and D is therefore not independent of C_{hel} , C_{nn} and C_{rr} . However, Eq. (5.178) can be used as a cross check of the results. Furthermore, even though D is not independent of the other three observables D could be more sensitive to the heavy Higgs effects than those other observables.

We also investigate the longitudinal top-quark polarization

$$B_k^+ = \langle 2\mathbf{S}_t \cdot \hat{\mathbf{k}} \rangle \quad (5.179)$$

within the three scenarios Ia–Ic at NLO QCD. Instead of presenting the results for B_k^+ as it was done in Sec. 4.2.3 we calculate the coefficient $B_1(\hat{\mathbf{a}}_1)$ of the double differential distribution (5.166). Performing the integration over θ_- in Eq. (5.166) results in the following angular distribution

$$\frac{1}{\sigma} \frac{d\sigma}{d \cos \theta_+} = \frac{1}{2} (1 + B_1(\hat{\mathbf{a}}_1) \cos \theta_+). \quad (5.180)$$

The coefficient B_1 can be extracted calculating the expectation value

$$B_1(\hat{\mathbf{a}}_1) = 3 \langle \cos \theta_+ \rangle_{\ell\ell}. \quad (5.181)$$

The corresponding spin operator is obtained by the replacement (5.175) in $\cos \theta_+ = \hat{\mathbf{q}}_{\ell^+} \cdot \hat{\mathbf{a}}_1$. Hence, B_1 can also be obtained from (C.33)

$$B_1(\hat{\mathbf{k}}) = \kappa_\ell \langle 2\mathbf{S}_t \cdot \hat{\mathbf{k}} \rangle_{t\bar{t}} = \kappa_\ell B_k^+, \quad (5.182)$$

where the reference axis $\hat{\mathbf{a}}_1$ has been set to $\hat{\mathbf{k}}$, the direction of the momentum of the top quark in the $t\bar{t}$ rest frame. The longitudinal polarization of the antitop quark B_k^- does not give any additional information. Hence, the results are not presented here.

5. Heavy Higgs effects in top-quark pair production at next-to-leading order in α_s

A nonvanishing polarization indicates P violation but not necessarily CPV . In other words, B_1 can have CPC as well as CPV contributions. In order to study CPV we analyze the P - and CP -odd triple correlation

$$O_{CP} = (\hat{\mathbf{q}}_{\ell^+} \times \hat{\mathbf{q}}_{\ell^-}) \cdot \hat{\mathbf{k}}. \quad (5.183)$$

The expectation value of O_{CP} is related to the expectation value of the corresponding spin operator as follows

$$\langle O_{CP} \rangle = -\kappa_\ell^2 \frac{4}{9} \langle (\mathbf{S}_t \times \mathbf{S}_{\bar{t}}) \cdot \hat{\mathbf{k}} \rangle. \quad (5.184)$$

This relation can be obtained by a similar calculation as outlined in Sec. 3.3 for $\langle \cos \theta_+ \cos \theta_- \rangle$. Note, that $\langle O_{CP} \rangle$ can also be expressed through the ‘‘off-diagonal’’ expectation values $C(\hat{\mathbf{n}}, \hat{\mathbf{r}})$ and $C(\hat{\mathbf{r}}, \hat{\mathbf{n}})$ [118]

$$C(\hat{\mathbf{n}}, \hat{\mathbf{r}}) - C(\hat{\mathbf{r}}, \hat{\mathbf{n}}) = 9 \langle O_{CP} \rangle. \quad (5.185)$$

Furthermore, we construct a CP -sensitive angular observable ϕ_{CP}^* similar to what has been done in Ref. [203]. In order to define ϕ_{CP}^* we identify the z -axes in the top and antitop rest frames with the direction of the top-quark momentum $\hat{\mathbf{k}}$ in the $t\bar{t}$ rest frame. The azimuthal angle ϕ^* between the two charged leptons of (5.165) is defined with respect to this z axis

$$\phi^* = \arccos(\hat{\mathbf{q}}_{\ell^+}^\perp \cdot \hat{\mathbf{q}}_{\ell^-}^\perp), \quad \phi^* \in [0, \pi]. \quad (5.186)$$

The unit three-vector $\hat{\mathbf{q}}_{\ell^\pm}^\perp$ ($\hat{\mathbf{q}}_{\ell^\pm}^\perp$) defines the direction of of the positively (negatively) charged lepton perpendicular to $\hat{\mathbf{k}}$ in the (anti)top-quark rest frame

$$\hat{\mathbf{q}}_{\ell^\pm}^\perp = \frac{\hat{\mathbf{q}}_{\ell^\pm} - (\hat{\mathbf{q}}_{\ell^\pm} \cdot \hat{\mathbf{k}})\hat{\mathbf{k}}}{|\hat{\mathbf{q}}_{\ell^\pm} - (\hat{\mathbf{q}}_{\ell^\pm} \cdot \hat{\mathbf{k}})\hat{\mathbf{k}}|}. \quad (5.187)$$

In order to probe the CP properties of the heavy Higgs bosons in scenarios la–lc we make use of the CP -odd triple product O_{CP} (5.184) to construct a CP -sensitive observable from ϕ^* similar to Ref. [203]. This observable is defined as

$$\phi_{CP}^* = \begin{cases} \phi^* & \text{if } (\hat{\mathbf{q}}_{\ell^+} \times \hat{\mathbf{q}}_{\ell^-}) \cdot \hat{\mathbf{k}} \geq 0 \\ 2\pi - \phi^* & \text{if } (\hat{\mathbf{q}}_{\ell^+} \times \hat{\mathbf{q}}_{\ell^-}) \cdot \hat{\mathbf{k}} < 0 \end{cases}, \quad \phi_{CP}^* \in [0, 2\pi]. \quad (5.188)$$

We study the normalized distribution $\sigma^{-1} d\sigma/d\phi_{CP}^*$ and investigate its discriminating power to distinguish between scalars, pseudoscalar and CP -mixed Higgs bosons. The observable ϕ_{CP}^* is defined at the level of the $t\bar{t}$ decay products, namely the charged leptons. It does not have a corresponding spin operator defined at the level of the intermediate $t\bar{t}$ state. Hence, for the calculation of ϕ_{CP}^* the inclusion of the decay of the $t\bar{t}$ pair is required. Here the on-shell decay of the top and antitop at LO is considered. The procedure how to take the on-shell decay into account given the spin dependent matrix element of $t\bar{t}$ production is described in Sec. 3.4.

All spin dependent observables summarized here are ratios of some kind. For $\sigma^{-1} d\sigma/d\phi_{CP}^*$ this is most obvious because the distribution is normalized to the inclusive cross section. For the expectation values of spin operators considered here the same normalization is performed because schematically

$$\langle O \rangle = \frac{1}{\sigma} \int d\sigma O. \quad (5.189)$$

Since the results are presented within fixed order perturbation theory we expand all ratios and normalized cross sections up to NLO in α_s . As an example take Eq. (5.189). Let us denote

$$\int d\sigma O = c^{(0)} + c^{(1)} + O(\alpha_s^4), \quad (5.190)$$

$$\sigma = \sigma^{(0)} + \sigma^{(1)} + O(\alpha_s^4), \quad (5.191)$$

where the superscript denotes the perturbative order: (0) stands for LO or $\mathcal{O}(\alpha_s^2)$ in this case and (1) stands for NLO or $\mathcal{O}(\alpha_s^3)$. The expansion of Eq. (5.189) including a factor of κ_ℓ^n from the definition of the observables C_{hel} , C_{nn} , C_{rr} , D , O_{CP} ($n = 2$) and B_1 ($n = 1$) up to NLO is then given by

$$\kappa_\ell^n \langle \mathcal{O} \rangle = \frac{c^{(0)}}{\sigma^{(0)}} \left[1 + n\kappa_\ell^{(1)} - \frac{\sigma^{(1)}}{\sigma^{(0)}} + \frac{c^{(1)}}{c^{(0)}} + \mathcal{O}(\alpha_s^2) \right], \quad (5.192)$$

with $\kappa_\ell^{(1)} = -0.015\alpha_s$ (cf. Eq. (5.171)).

In this subsection we adopted the line of thought were we start from the experimentally accessible observable, e.g. the double differential distribution (5.166), and identify the corresponding spin property of the $t\bar{t}$ pair, e.g. spin correlations with respect to a certain reference axis. This has the advantage that we can determine the observables at the level of $t\bar{t}$ and then map them onto the corresponding observables defined at the level of the $t\bar{t}$ decay products when no acceptance cuts are applied. When studying models of new physics phenomenologically the opposite direction can become more relevant. One aims to study a certain spin property of the $t\bar{t}$ system defined by the respective spin operator because analytical results suggest a strong dependence on new physics effects. Starting from this operator defined at the intermediate $t\bar{t}$ state the corresponding angular correlation with respect to the $t\bar{t}$ decay products is determined. Predictions for this observable within the new physics model can be compared with experimental results.

In the case where acceptance cuts are taken into account, thus generating predictions for the so-called *fiducial* phase space region, the observable has to be calculated at the level of the $t\bar{t}$ decay products. However, in this work the detector acceptance is not taken into account but results presented here can be compared to fiducial results that are extrapolated to the full phase space as for example in Ref. [119].

Results

Most of the results presented in the following were published in Ref. [78]. The numerical setup and SM input parameters are the same as those used to generate the results of the spin independent observables (cf. Eqs. (5.161), (5.162) and (5.163)).

In Appendix G the $M_{t\bar{t}}$ distributions for scenarios la–lc are presented in Figs. G.1–G.3. These figures show that the 400 GeV Higgs boson in scenarios la–lc generates a peak-dip structure in the $M_{t\bar{t}}$ spectra. Using these distributions we determine the locations of the peak and dip and define regions of $M_{t\bar{t}}$ which contain only the peak (dark ocher shaded areas in the lower panels of Figs. G.1–G.3) and only the dip (light ocher shaded areas in the lower panels of Figs. G.1–G.3). This is the same procedure implemented for the spin independent observables y_t and $\cos\theta_{CS}$ in Sec. 5.4.1 to avoid the (partial) cancellation of peak and dip and therefore enhance the signal.

The parameters of scenarios la–lc (Tab. 5.8), were chosen to facilitate a direct comparison between Higgs bosons of different CP nature. The CP -sensitive observable ϕ_{CP}^* is used to investigate this aspect of scenarios la–lc. In Fig. 5.25 the normalized distribution $\sigma^{-1}d\sigma/d\phi_{CP}^*$ is shown for scenarios la–lc within the $M_{t\bar{t}}$ windows containing either the peak (plots on the lhs) or the dip (plots on the rhs) generated by the 400 GeV resonance. In the upper panels of the plots shown in Fig. 5.25 the contribution from the SM including NLO QCD and weak corrections is shown in black. The red histogram represents the sum of SM and 2HDM contribution to the ϕ_{CP}^* distribution including the Higgs-QCD interference. In the lower panels the signal-to-background ratio (SM+2HDM)/SM at NLO is shown in red and at LO in green. In the upper $M_{t\bar{t}}$ window ($400 \text{ GeV} \leq M_{t\bar{t}} \leq 460 \text{ GeV}$) the effects on the ϕ_{CP}^* distribution are very small ($S/B \lesssim 1\%$) irrespective of the CP nature of the 400 GeV Higgs

5. Heavy Higgs effects in top-quark pair production at next-to-leading order in α_s

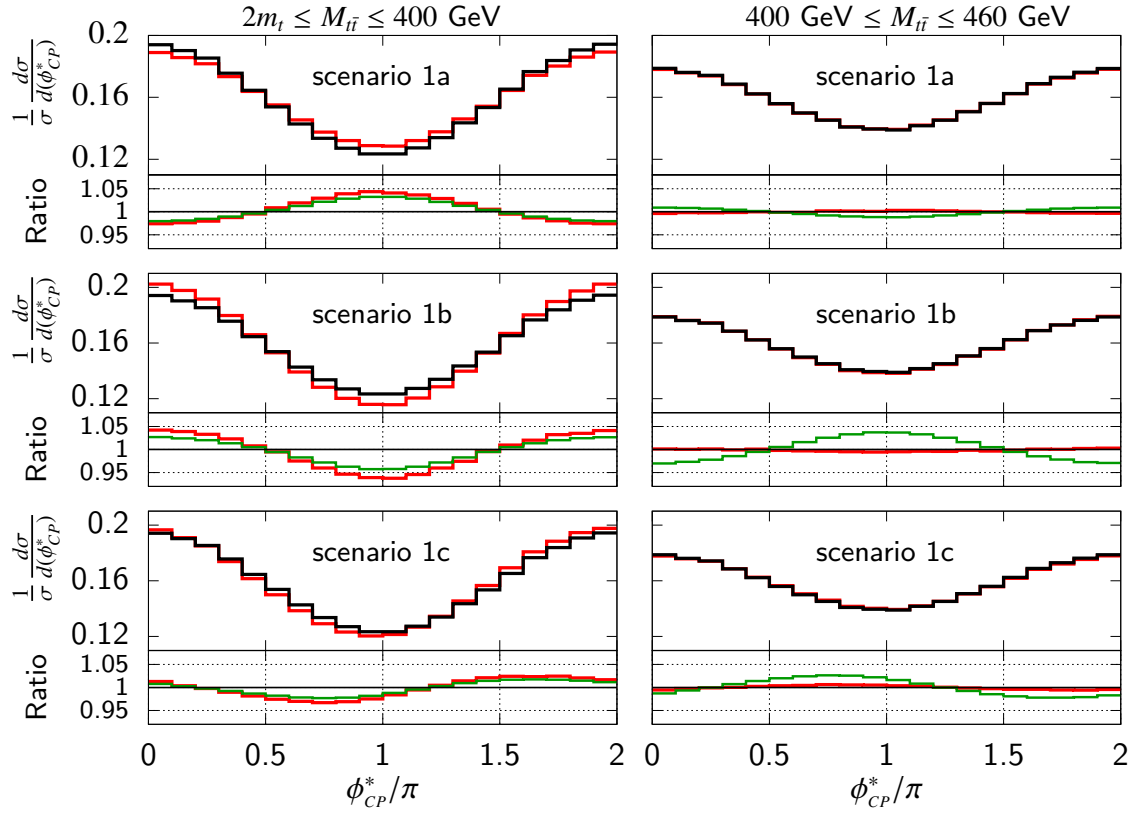


Figure 5.25.: Normalized distribution of the CP -sensitive observable ϕ_{CP}^* for scenarios 1a–1c in selected regions of $M_{H\bar{i}}$. Upper panels show the distribution for the SM including NLO QCD and weak corrections (black) and the sum of SM and 2HDM contributions including the Higgs-QCD interference at NLO QCD (red). In the lower panels the ratio (SM+2HDM)/SM is presented at NLO (red) and LO (green).

boson. However, in the peak region ($2m_t \leq M_{t\bar{t}} \leq 400$ GeV) the S/B rises up to approximately 6%. Furthermore, the ϕ_{CP}^* distributions show different behaviour for the scalar (scenario Ia), pseudoscalar (scenario Ib) and the CP mixture (scenario Ic) at 400 GeV which is most visible in the S/B plots. The S/B resembles a trigonometric function with its maximum (minimum) at $\phi_{CP}^* = \pi$ ($\phi_{CP}^* = 0, 2\pi$) if the 400 GeV Higgs boson is a scalar. In the case of a pseudoscalar the positions of minimum and maximum are interchanged with the maximum at $\phi_{CP}^* = 0, 2\pi$ and the minimum at $\phi_{CP}^* = \pi$. In scenario Ic, where the 400 GeV Higgs boson is a CP -mixed state maximum and minimum of the S/B are located at $\phi_{CP}^* \neq 0, \pi, 2\pi$. In Ref. [203] where a similar observable was studied in the case of Higgs boson decay to $\tau^+\tau^-$ the differential cross section of the respective observable is in fact a cosine with a phase shift that is determined by the ratio between the scalar and pseudoscalar reduced Yukawa couplings. In contrast to the tau-pair decay channel of a Higgs boson the background in the $t\bar{t}$ decay channel is not flat in ϕ_{CP}^* and the Higgs-QCD interference is strong. Therefore the S/B in the $t\bar{t}$ channel is not exactly a trigonometric function and the relation between the CP dependent shift of maxima and minima and the Yukawa couplings is more complicated. Furthermore, the nonresonant QCD background contribution is large and leads to small signal-to-background ratios. Figures G.1–G.3 illustrate that scenarios Ia–Ic present realizations of the type-II 2HDM with strong signals in the $M_{t\bar{t}}$ distribution. Actually they are so strong, that these scenarios are now excluded by a recent ATLAS analysis [114, 115] performed with the 8 TeV LHC data. Hence, for scenarios that are not excluded yet and where the signal is therefore even weaker one can expect even lower S/B in the ϕ_{CP}^* distribution than for scenarios Ia–Ic. This shows that ϕ_{CP}^* , while in principle capable of discriminating between different CP eigenstates or CP mixture, is probably not sensitive enough to determine the CP properties of a heavy Higgs boson that has not been discovered yet. The NLO corrections do not change this picture even though they slightly increase the S/B in the lower $M_{t\bar{t}}$ bin.

In Sec. 4.2.4 it was shown that in SM $t\bar{t}$ production (via the processes shown in Figs. 4.1a and 4.1b) the spins of t and \bar{t} are correlated to a certain degree and that the contribution from heavy Higgs bosons can change this correlation. In the following we study the effects of heavy Higgs bosons in scenarios Ia–Ic on $t\bar{t}$ spin correlations at NLO QCD. For this purpose we investigate the observables C_{hel} , C_{nn} , C_{rr} and D introduced above and assess their sensitivity to the contributions from heavy Higgs bosons. Again, we evaluate these observables in the $M_{t\bar{t}}$ windows

$$2m_t \leq M_{t\bar{t}} \leq 400\text{GeV} \quad \text{and} \quad 400\text{GeV} \leq M_{t\bar{t}} \leq 460\text{GeV}. \quad (5.193)$$

The results for scenarios Ia–Ic are presented in Figs. 5.26–5.28. The figures are divided into two plots: The upper plot displays the result for the lower $M_{t\bar{t}}$ window and the lower plot for the upper $M_{t\bar{t}}$ window. Each plot shows the results for all four observables C_{hel} , C_{nn} , C_{rr} and D and is divided into two parts. The upper part shows the value of the respective observable for the SM only (coarse hatched) and for the sum of SM and 2HDM contribution (fine hatched) including the Higgs-QCD interference at LO (red) and NLO (blue). The solid filled regions of the bars indicate the shift in the observable due to scale variations according to Eq. (5.156). The lower parts of the plots show the S/B in percent for each observable at LO (red) and NLO (blue). The darker area in the bars illustrates the shift due to scale variations. For comparison the green band indicates the S/B of the cross section at NLO within the respective $M_{t\bar{t}}$ window. This is obtained from the $M_{t\bar{t}}$ distributions shown in Figs. G.1–G.3. In scenario Ia (Fig. 5.26) the S/B of the cross section is very small in the upper $M_{t\bar{t}}$ bin such that the green band is not visible there.

The S/B is mostly larger in the lower $M_{t\bar{t}}$ window which contains the peak than in the upper $M_{t\bar{t}}$ window which constrains the dip. A common observation for all three scenarios is that least one of the spin correlation observables reaches beyond the green band and is

5. Heavy Higgs effects in top-quark pair production at next-to-leading order in α_s

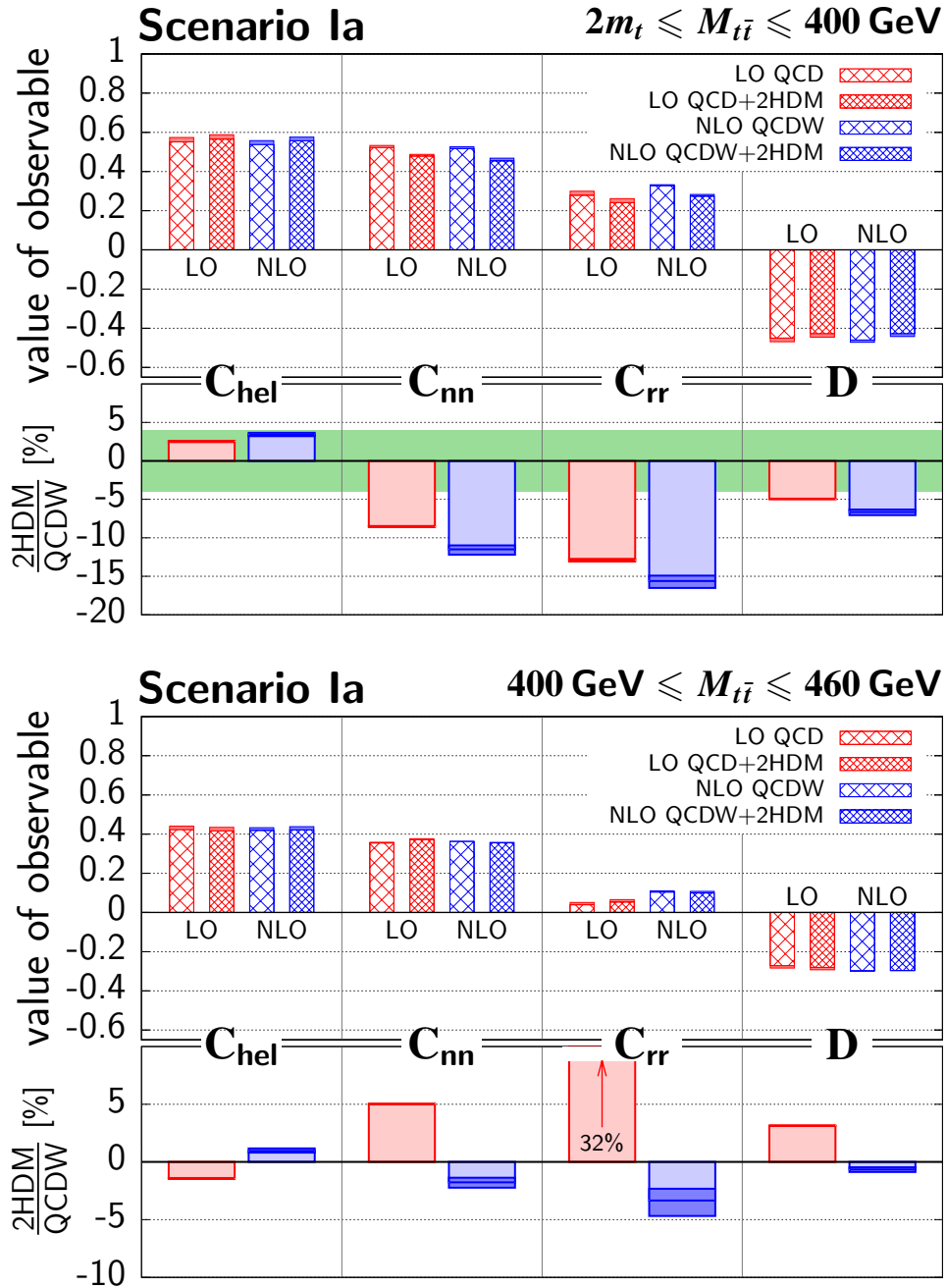


Figure 5.26.: Results for the spin correlation observables C_{hel} , C_{nn} , C_{rr} and D evaluated in the lower $M_{\tilde{t}\tilde{t}}$ bin (upper plot) and the upper $M_{\tilde{t}\tilde{t}}$ bin (lower plot) (5.193) for scenario Ia.

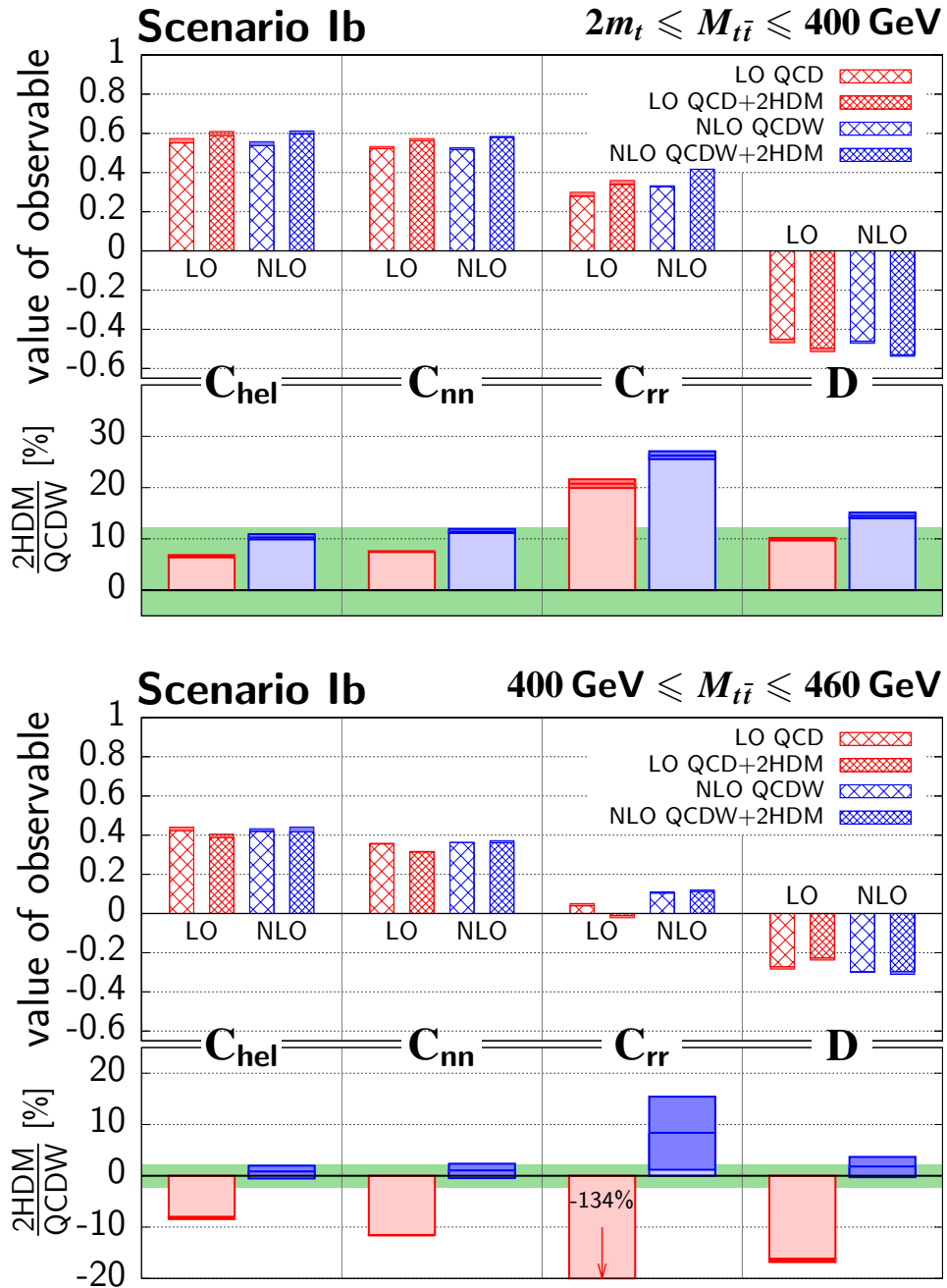


Figure 5.27.: Same as Fig. 5.26 but for scenario Ib.

5. Heavy Higgs effects in top-quark pair production at next-to-leading order in α_s

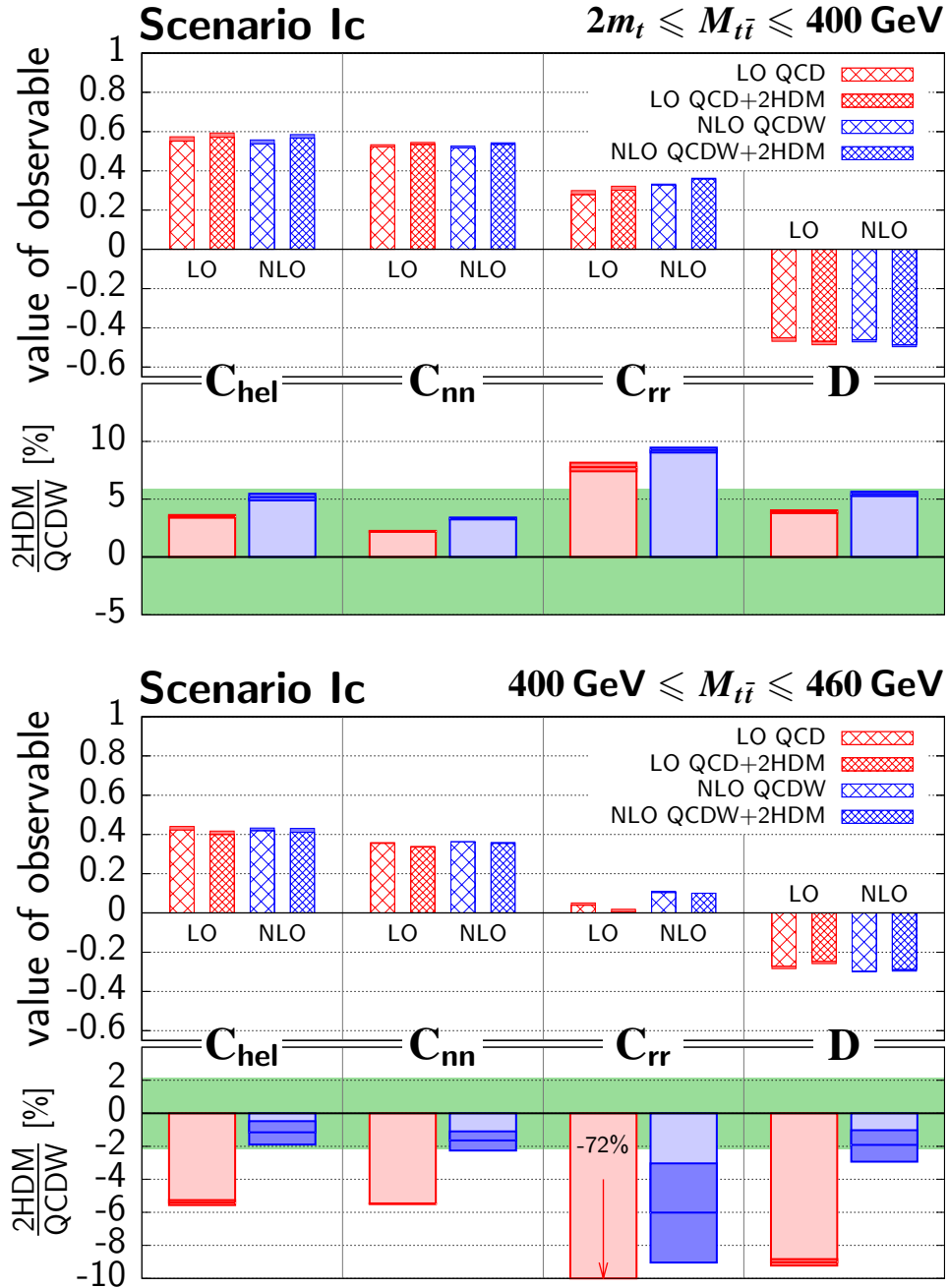


Figure 5.28.: Same as Fig. 5.26 but for scenario 1c.

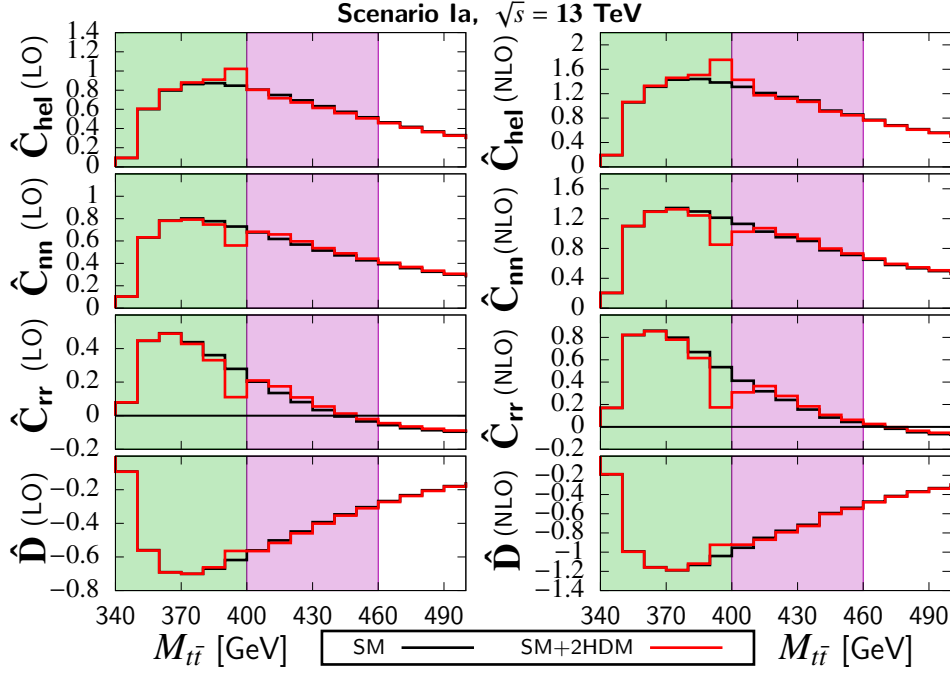


Figure 5.29.: Unnormalized spin correlation observables binned in $M_{\tilde{t}\tilde{t}^*}$ for scenario Ia. The labels of the ordinates of the plots are short notations, e.g. \hat{C}_{hel} stands for $d\hat{C}_{\text{hel}}/dM_{\tilde{t}\tilde{t}^*}$. The units are pb/GeV. The black histograms represent the SM contribution. The sum of SM and 2HDM contributions including the Higgs-QCD interference is shown in red. The plots on the lhs display the results at LO and on the rhs at NLO. The green and purple shaded regions indicate the lower and upper $M_{\tilde{t}\tilde{t}^*}$ bins (5.193), respectively.

therefore more sensitive than the $M_{\tilde{t}\tilde{t}^*}$ distribution in the respective $M_{\tilde{t}\tilde{t}^*}$ window. This confirms at NLO what has been observed already at LO in Sec. 4.2.4: spin dependent observables can increase the sensitivity to heavy Higgs effects in $\tilde{t}\tilde{t}^*$ production with respect to spin independent observables such as $d\sigma/dM_{\tilde{t}\tilde{t}^*}$. This effect is largest for the observable C_{rr} in scenario Ia where its S/B is almost a factor of four larger than the S/B of the $M_{\tilde{t}\tilde{t}^*}$ distribution.

In the upper $M_{\tilde{t}\tilde{t}^*}$ window the S/B of the LO prediction of C_{rr} takes on rather large values (indicated by arrows in the plots) which deviate strongly from the prediction at NLO. The reason for this large difference is the fact that the observable C_{rr} as a function of $M_{\tilde{t}\tilde{t}^*}$ has a zero in the upper $M_{\tilde{t}\tilde{t}^*}$ bin at LO. Taking NLO corrections into account the position of this zero is shifted to the boundary or even outside the $M_{\tilde{t}\tilde{t}^*}$ window. As an example this behavior is illustrated in Fig. 5.29 for scenario Ia. The plots in Fig. 5.29 show the numerators of the spin correlation observables

$$\hat{C}(\hat{\mathbf{a}}_1, \hat{\mathbf{a}}_2) = \sigma C(\hat{\mathbf{a}}_1, \hat{\mathbf{a}}_2), \quad (5.194)$$

i.e. without normalization with respect to the cross section, binned in $M_{\tilde{t}\tilde{t}^*}$. The lower (upper) $M_{\tilde{t}\tilde{t}^*}$ window is indicated as green (purple) shaded area. The plots on the lhs represent the LO results and on the rhs the NLO results. The SM predictions are shown in black and the sum of SM and 2HDM contributions including the Higgs-QCD interference in red. The described behavior of C_{rr} in the upper $M_{\tilde{t}\tilde{t}^*}$ bin when comparing LO with NLO results can be seen in Fig. 5.29 (third plot from the top). Due to cancellations between positive and negative contributions the observable C_{rr} becomes very sensitive to NLO corrections in the upper $M_{\tilde{t}\tilde{t}^*}$

5. Heavy Higgs effects in top-quark pair production at next-to-leading order in α_s

Table 5.12.: R -ratios and K -factors for C_{hel} , C_{nn} , C_{rr} and D in the lower and upper $M_{t\bar{t}}$ bin for scenarios la–lc.

$M_{t\bar{t}}$ bin [GeV]	C_{hel}		C_{nn}		C_{rr}		D	
	lower	upper	lower	upper	lower	upper	lower	upper
Scenario la								
R	0.99	1.01	0.98	0.98	1.04	1.21	1.00	1.01
K	0.99	1.01	0.96	0.95	1.11	1.73	1.00	1.04
Scenario lb								
R	1.01	1.03	1.01	1.06	1.08	1.91	1.03	1.11
K	1.01	1.09	1.03	1.16	1.20	-7.40	1.06	1.31
Scenario lc								
R	1.00	1.01	1.00	1.02	1.06	1.55	1.01	1.06
K	0.99	1.03	1.00	1.06	1.16	7.84	1.03	1.16

bin. The large difference between LO and NLO prediction is therefore not an indication for the breakdown of the perturbative expansion but rather an artefact of this specific observable. Figure 5.29 also illustrates that the other observables C_{hel} , C_{nn} and D do not have zeros in the $M_{t\bar{t}}$ region under consideration. Hence, they are not as sensitive to higher order correction as C_{rr} (Fig. 5.26).

It is also possible to quantify the behavior of C_{rr} to a certain extend. First consider the ratio between the NLO and LO predictions, the K -factor. In scenario la the K -factor for C_{rr} is given by $K = 1.7$ and for scenarios lb and lc $|K| > 7$. Additionally, we consider the ratio R between the observable in its expanded form (5.192) with respect to the unexpanded version. This ratio can be interpreted as an estimate of the contribution of missing higher order corrections to the observable. For C_{rr} in the upper $M_{t\bar{t}}$ bin the ratio evaluates to $R = 1.2$, $R = 1.9$ and $R = 1.5$ for scenarios la, lb and lc, respectively. The other observables have lower values for R . In Tab. 5.4.2 the K -factor and the R -ratio of the SM+2HDM contribution are listed for C_{hel} , C_{nn} , C_{rr} and D in scenarios la–lc in the lower and upper $M_{t\bar{t}}$ bin. As can be seen from this table the high values for K and R of C_{rr} in the upper $M_{t\bar{t}}$ bin ($400 \text{ GeV} \leq M_{t\bar{t}} \leq 460 \text{ GeV}$) stand out with respect to the mostly low values of the other observables. Comparing K and R between different observables is not to be seen as a rigorous procedure to determine the perturbative convergence of the observables but rather as a method to identify potential problems. The fact that there is a coherent tendency of K and R to be (considerably) larger for C_{rr} in the upper $M_{t\bar{t}}$ window gives a strong hint that the predictions for this observable in this particular $M_{t\bar{t}}$ range is less robust and subject to large corrections as higher orders are taken into account. However, the predictions for C_{rr} in the lower $M_{t\bar{t}}$ bin are robust and even show large enhancements of the S/B with respect to the distribution $d\sigma/dM_{t\bar{t}}$.

The case studied here is only one example. In general spin correlation observables can receive positive and negative contributions from different regions of $M_{t\bar{t}}$. Hence, when binning such observables in $M_{t\bar{t}}$ some bins might contain a zero (in the sense discussed above). As the example has shown the predictions of spin correlations in the $M_{t\bar{t}}$ -vicinity of such zeros are less robust with respect to higher order corrections. Therefore, one should choose $M_{t\bar{t}}$ bins that are sufficiently far from the zero of the observable. This is also the reason why in Sec. 4.2.4 we have excluded the region in $M_{t\bar{t}}$ around the zero of the spin correlation observable $C_{\theta,\varphi}^{M_{t\bar{t}}}$ (Fig. 4.12). The question might be raised if the binning in $M_{t\bar{t}}$ is necessary at all. The fact that the restriction of the observable to a certain $M_{t\bar{t}}$ range can enhance the S/B has been shown in Sec. 4.2.4 at LO. For NLO this statement is confirmed by Tabs. H.1–H.3 in

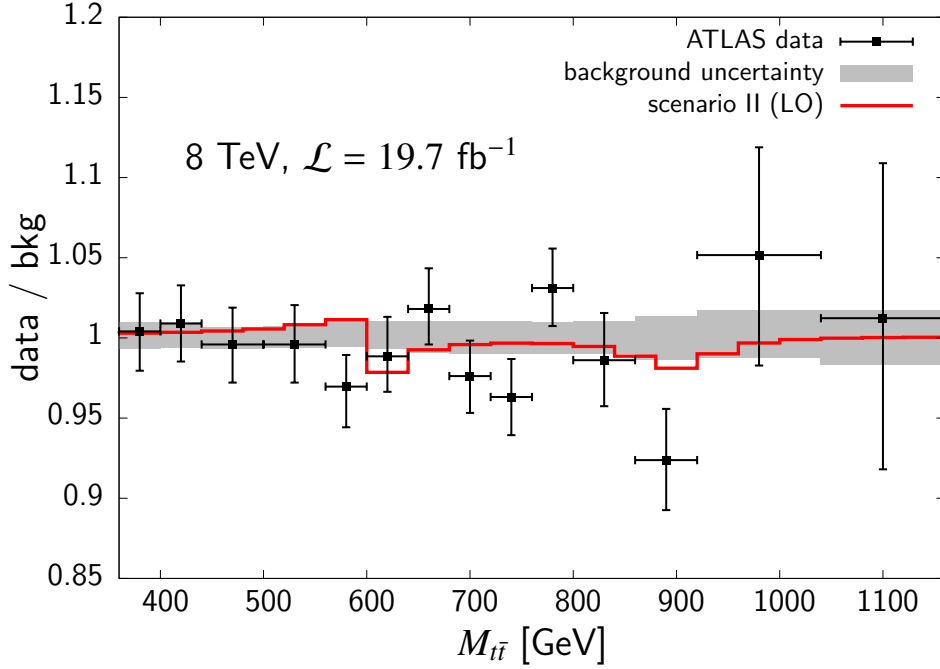


Figure 5.30.: Data-to-background ratio of the $M_{t\bar{t}}$ distribution as determined by the ATLAS analysis in Ref. [114]. The data of this plot was extracted from Ref. [114] Fig. 7a by using the tool EasyNData [105]. The background uncertainty is shown in gray, the ATLAS data is presented in black and the result for the signal-to-background ratio of the $M_{t\bar{t}}$ distribution for scenario II at LO is superimposed in red.

Appendix H where the numerical values for the results shown in Figs. 5.26–5.28 are presented. In addition these tables also list the results for the observables and S/B without applying any $M_{t\bar{t}}$ cuts. The $M_{t\bar{t}}$ cuts mostly enhance the S/B and therefore increase the sensitivity of the spin dependent observables to the effects of heavy Higgs boson in $t\bar{t}$ production.

Figures 5.26–5.28 show that the uncertainty bands of the LO and NLO in most cases do not overlap. Since the observables C_{hel} , C_{nn} , C_{rr} and D are ratios as in Eq. (5.189) at LO the dependence on α_s and therefore on μ_R cancels exactly. Hence, the variation of $\mu = \mu_R = \mu_F$ does not give a reliable estimate of the uncertainty of the LO prediction.

As mentioned above scenarios Ia–Ic show quite strong signals in the $M_{t\bar{t}}$ distribution (Figs. G.1–G.3) and can therefore be experimentally constrained. The reason that spin dependent observables can enhance the S/B, e.g. by a factor of four in scenario Ia, might be connected to the fact that the signal is already strong in the spin independent $M_{t\bar{t}}$ distribution. In the following we study scenario II to find out if this assumption is correct. This scenario shows a much weaker signal in the $M_{t\bar{t}}$ distribution and is therefore experimentally not excluded yet. This is illustrated in Fig. 5.30 by superimposing the results for the $M_{t\bar{t}}$ signal-to-background ratio in scenario II with the data/background plot from the experimental analysis in Ref. [114]. In Fig. 5.31 the results for the observable $C_{\text{hel}}^{M_{t\bar{t}}}$ are presented for scenario II. $C_{\text{hel}}^{M_{t\bar{t}}}$ is defined by

$$C_{\text{hel}}^{M_{t\bar{t}}} = -\kappa_\ell^2 C_{\theta,\varphi}^{M_{t\bar{t}}}, \quad \theta = \frac{\pi}{2}, \varphi = 0 \quad (5.195)$$

and $C_{\theta,\varphi}^{M_{t\bar{t}}}$ is defined in Eq. (4.72). Hence, the observable $C_{\text{hel}}^{M_{t\bar{t}}}$ contains the expectation value C_{hel} for a range of $M_{t\bar{t}}$ bins. The upper panel in Fig. 5.31 displays the observable in the SM including

5. Heavy Higgs effects in top-quark pair production at next-to-leading order in α_s

NLO QCD and weak corrections (black), the sum of SM and 2HDM contribution including the Higgs-QCD interference also at NLO QCD (red) and the LO prediction for SM+2HDM (green). In the lower panel the signal-to-background ratio of $C_{\text{hel}}^{M_{\bar{t}\bar{t}}}$ (red) and $d\sigma/dM_{\bar{t}\bar{t}}$ (purple) are shown. In the region $750 \text{ GeV} \leq M_{\bar{t}\bar{t}} \leq 1050 \text{ GeV}$ there is a peculiar peak structure visible in the S/B plot. This results from an interplay between the wide ($\Gamma_3 = 81 \text{ GeV}$, cf. Tab. 5.11) resonance and the fact that $C_{\text{hel}}^{M_{\bar{t}\bar{t}}}$ crosses the zero at $\approx 900 \text{ GeV}$. Comparing the result for LO and NLO we see that the position of the zero of $C_{\text{hel}}^{M_{\bar{t}\bar{t}}}$ receives a large shift from $M_{\bar{t}\bar{t}} \approx 750 \text{ GeV}$ to $M_{\bar{t}\bar{t}} \approx 900 \text{ GeV}$ when going from LO to NLO. The prediction for $C_{\text{hel}}^{M_{\bar{t}\bar{t}}}$ in this region is therefore very sensitive to higher order corrections which affects the robustness of the results in this $M_{\bar{t}\bar{t}}$ region. Here, two solutions to this problem are suggested. As has been mentioned above one possibility to obtain results that are robust with respect to higher order corrections is to restrict the $M_{\bar{t}\bar{t}}$ range to an appropriate region that is sufficiently far from the zero of $C_{\text{hel}}^{M_{\bar{t}\bar{t}}}$. Fortunately, the 600 GeV Higgs boson in scenario II can be studied with $C_{\text{hel}}^{M_{\bar{t}\bar{t}}}$ because its resonance region is far from the zero. Fig. 5.31 shows that the S/B of $C_{\text{hel}}^{M_{\bar{t}\bar{t}}}$ in the $M_{\bar{t}\bar{t}}$ bin 550 – 600 GeV is much larger than the S/B seen in the $M_{\bar{t}\bar{t}}$ distribution of the cross section shown in purple. Hence, even for a scenario that shows only small effects in the $d\sigma/dM_{\bar{t}\bar{t}}$ distribution the spin dependent observable C_{hel} can produce a considerable gain in sensitivity when compared to the same $M_{\bar{t}\bar{t}}$ bins used in $d\sigma/dM_{\bar{t}\bar{t}}$. If we were interested in studying the 900 GeV Higgs boson in scenario II we encounter the problem of the zero of $C_{\text{hel}}^{M_{\bar{t}\bar{t}}}$ which is located at 900 GeV. To avoid this problem one can study other observables which do not have zeros or zeros that are located far from the interesting $M_{\bar{t}\bar{t}}$ region (resonance region). This is illustrated in Fig. 5.32 where the results for

$$C_{\text{nn}}^{M_{\bar{t}\bar{t}}} = -\kappa_t^2 C_{\theta,\varphi}^{M_{\bar{t}\bar{t}}}, \quad \theta = \pi/2, \varphi = \pi/2 \quad (5.196)$$

are presented. The observable $C_{\text{nn}}^{M_{\bar{t}\bar{t}}}$ has no zero in the considered $M_{\bar{t}\bar{t}}$ range. For both resonances at $M_{\bar{t}\bar{t}} = 600 \text{ GeV}$ and $M_{\bar{t}\bar{t}} = 900 \text{ GeV}$ $C_{\text{nn}}^{M_{\bar{t}\bar{t}}}$ gives larger S/B than the $d\sigma/dM_{\bar{t}\bar{t}}$ distribution. The gain in sensitivity is particularly pronounced for the 600 GeV Higgs boson where the S/B for $C_{\text{nn}}^{M_{\bar{t}\bar{t}}}$ is $\approx 12\%$ while in the $M_{\bar{t}\bar{t}}$ distribution S/B is only 2-3%. For the 900 GeV Higgs boson the S/B of $C_{\text{nn}}^{M_{\bar{t}\bar{t}}}$ is also increased with respect to the $M_{\bar{t}\bar{t}}$ distribution but here the effect is less pronounced.

In principle we could apply the procedure described in Sec. 4.2.4 and scan over the directions of reference axes or equivalently the angles θ and φ to obtain the optimal observable with the largest S/B in an $M_{\bar{t}\bar{t}}$ bin sufficiently far from the zero of that observable at NLO. But this goes beyond the scope of this work.

The results for C_{hel} , C_{nn} and C_{rr} within the SM including NLO QCD and weak corrections were already calculated in Ref. [118] and agree with those presented in Figs. 5.26–5.28 and Tabs. H.1–H.3 when the different scale choices are taken into account. As mentioned in the beginning of this section the numerical results for the pure QCD and weak corrections to the SM contribution in this work have been provided by the authors of [111, 112]. The spin correlations C_{hel} , C_{nn} and C_{rr} have also been measured [119] inclusively in $M_{\bar{t}\bar{t}}$ in dileptonic $t\bar{t}$ events at the LHC with a hadronic center of mass energy of 8 TeV. The experimental results corrected to the parton level and to the full phase space agree with the respective SM predictions. It was checked that at 8 TeV the spin correlations C_{hel} , C_{nn} and C_{rr} including the contributions from heavy Higgs bosons in scenarios Ia–Ic and II agree with the results of [119] within the experimental uncertainties. At this point the question might be raised how scenarios Ia–Ic can be constrained by the $M_{\bar{t}\bar{t}}$ distribution and not by the spin correlation measurement given that spin dependent observables are more sensitive than spin independent ones. There are two reasons. First, the spin correlation measurement was performed inclusively in $M_{\bar{t}\bar{t}}$. As can be seen from Tabs. H.1–H.3 the restriction to relevant $M_{\bar{t}\bar{t}}$ regions is crucial to reach large

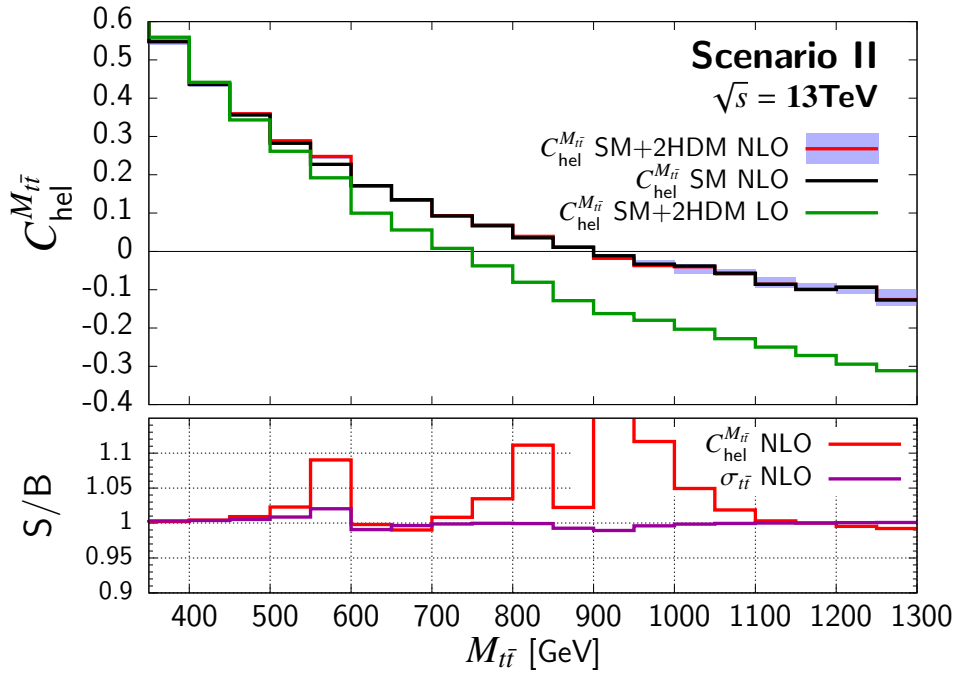


Figure 5.31.: Results for $C_{\text{hel}}^{M_{\tilde{t}\tilde{t}}}$ in scenario II. Upper panel: SM contribution including NLO QCD and weak corrections (black) and sum of SM and 2HDM contribution including the Higgs-QCD interference at NLO QCD (red). The blue shaded regions represent the uncertainty due to scale variations according to Eq. (5.156). The result at LO for SM+2HDM is shown in green. Lower plot: S/B of $C_{\text{hel}}^{M_{\tilde{t}\tilde{t}}}$ and of the $M_{\tilde{t}\tilde{t}}$ distribution with 50-GeV binning (purple) both at NLO QCD.

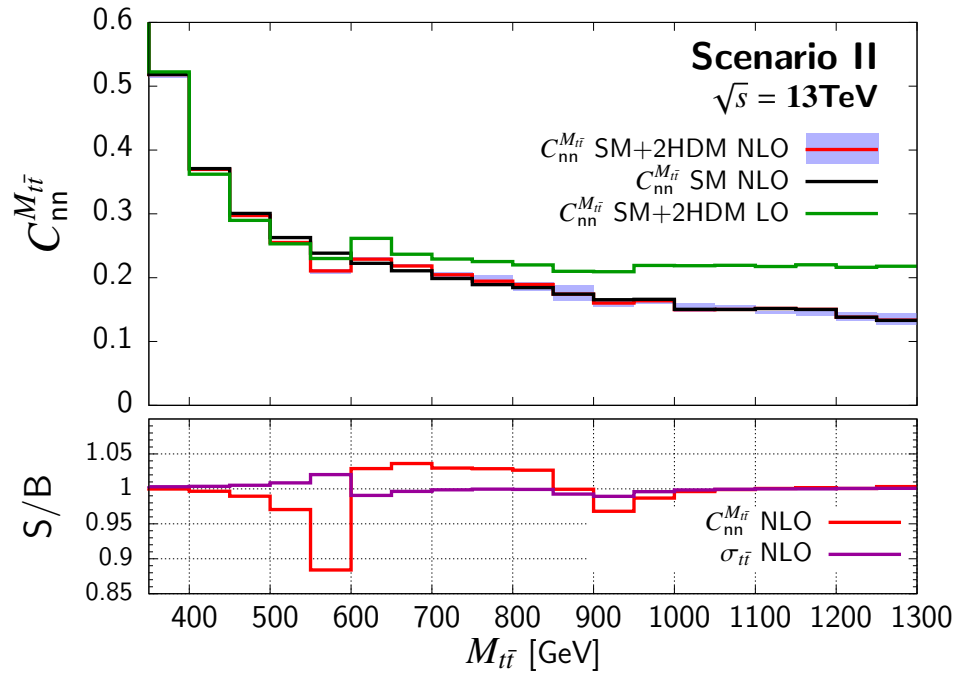


Figure 5.32.: Same as Fig. 5.31 but for $C_{\text{nn}}^{M_{\tilde{t}\tilde{t}}}$.

5. Heavy Higgs effects in top-quark pair production at next-to-leading order in α_s

Table 5.13.: Results for the expectation value of the triple correlation $\langle O_{CP} \rangle$ for scenario 1c within the lower and upper $M_{t\bar{t}}$ bins (5.193) and inclusively in $M_{t\bar{t}}$. The first column lists the results at LO and the second column including NLO QCD corrections. Subscripts and Superscripts indicate the shift of the observable induced by scale variations according to Eq. (5.156).

$M_{t\bar{t}}$ [GeV]	LO 2HDM	NLO 2HDM
$[2m_t, 400]$	$-0.549^{+0.007}_{-0.007} \times 10^{-2}$	$-0.824^{+0.024}_{-0.029} \times 10^{-2}$
$[400, 460]$	$0.587^{+0.005}_{-0.005} \times 10^{-2}$	$0.127^{+0.062}_{-0.054} \times 10^{-2}$
incl.	$0.666^{+0.005}_{-0.005} \times 10^{-3}$	$-0.814^{+0.008}_{-0.020} \times 10^{-3}$

signal-to-background ratios. Second, the experimental statistical uncertainties of the 8-TeV data and the systematic uncertainties are comparatively large such that the gain in sensitivity is lost by the dominating uncertainties.

The spin correlations C_{hel} , C_{nn} , C_{rr} and D do not provide any information about the CP nature of the Higgs bosons. In the following we investigate the P - and CP -odd triple product O_{CP} defined above. This observable cannot distinguish between a scalar and a pseudoscalar but it can detect CPV. If there are no other sources of CPV than the 2HDM a nonvanishing expectation value $\langle O_{CP} \rangle$ indicates CPV in the Higgs potential and therefore the presence of CP -mixed Higgs bosons. There is no CP -violating contribution from the SM to $t\bar{t}$ production. Hence, we obtain $\langle O_{CP} \rangle \neq 0$ only in the CPV scenario 1c. The results for $\langle O_{CP} \rangle$ for dileptonic $t\bar{t}$ events at 13 TeV are presented in Tab. 5.13. The results are shown for the $M_{t\bar{t}}$ bins defined in Eq. (5.193) and inclusively in $M_{t\bar{t}}$. The effects of CPV are very small in scenario 1c. Even in the $M_{t\bar{t}}$ bins around the 400 GeV resonance where the largest effects are expected $\langle O_{CP} \rangle$ is below the percent level. Due to (partial) peak-dip cancellation the inclusive expectation value of the triple correlation is one order of magnitude lower. Using the relation [118]

$$C(\hat{\mathbf{n}}, -\hat{\mathbf{r}}) - C(\hat{\mathbf{r}}, -\hat{\mathbf{n}}) = 9\langle O_{CP} \rangle \quad (5.197)$$

the expectation value of the triple correlation can also be determined by measuring the off-diagonal spin correlations $C(\hat{\mathbf{n}}, -\hat{\mathbf{r}})$ and $C(\hat{\mathbf{r}}, -\hat{\mathbf{n}})$. This measurement was performed by ATLAS at 8 TeV in Ref. [119] with the result

$$C(\hat{\mathbf{n}}, -\hat{\mathbf{r}}) - C(\hat{\mathbf{r}}, -\hat{\mathbf{n}}) = -0.006 \pm 0.108. \quad (5.198)$$

Due to the comparatively large uncertainty of the experimental value and the small effects of CPV scenario 1c is not constrained by this measurement. In principle the 2HDM could generate larger CPV effects but not without violating indirect constraints from low-energy experiments [95, 117, 204, 205]. In particular, upper limits on the electric dipole moments of the neutron [197] and electron [198] provide constraints on CPV 2HDM scenarios. The dominant contribution to the electric dipole moments results from ϕ_1 exchange. The contribution from the heavy Higgs bosons ϕ_2 and ϕ_3 is subdominant. The parameters of scenario 1c lie within the allowed range derived in [117, 205]. The fact that the parameters of scenario 1c (Tab. 5.8) were chosen not to deviate too much from the SM alignment limit and to be in agreement with experimental constraints is mainly responsible for these small values of $\langle O_{CP} \rangle$. The NLO corrections do not significantly increase this expectation value.

Table 5.14.: The coefficient $B_1(\hat{\mathbf{k}})$ in the double differential distribution (5.166) that is proportional to the longitudinal polarization of the top quark. The results are presented for the lower and upper $M_{t\bar{t}}$ bin (5.193) and inclusively in $M_{t\bar{t}}$. The SM contribution to scenarios la–lc is presented in the third column. In scenario lc there is, in addition, the contribution from the heavy Higgs bosons denoted by “2HDM”.

$M_{t\bar{t}}$ [GeV]	LO	NLO		
	2HDM	2HDM+QCDW	QCDW	$\frac{2\text{HDM}}{\text{QCDW}}$
$[2m_t, 400]$	$0.110^{+0.001}_{-0.001} \times 10^{-1}$	$0.492^{+0.020}_{+0.014} \times 10^{-2}$	$0.169^{+0.120}_{-0.098} \times 10^{-2}$	$1.91^{+4.30}_{-1.20}$
$[400, 460]$	$-0.769^{+0.007}_{-0.007} \times 10^{-2}$	$0.403^{+0.313}_{-0.293} \times 10^{-2}$	$0.316^{+0.174}_{-0.139} \times 10^{-2}$	$0.275^{+0.187}_{-0.655}$
incl.	$-0.600^{+0.024}_{-0.026} \times 10^{-3}$	$0.617^{+0.227}_{-0.185} \times 10^{-2}$	$0.553^{+0.209}_{-0.164} \times 10^{-2}$	$0.114^{+0.006}_{-0.007}$

Finally, we consider the longitudinal top-quark polarization at NLO for the scenarios la–lc. The P -violating weak interaction in the SM generates longitudinally polarized top quarks which is a small effect. We include weak corrections into the nonresonant $t\bar{t}$ background denoted by “QCDW” in Tab. 5.4.2. This contribution agrees with the results of Ref. [118] when taking different scale choices into account and is present in all three scenarios. However, only in the CPV scenario lc there is an additional contribution from the 2HDM to B_1 . The results for this contribution are presented at LO and NLO in Tab. 5.4.2. The cuts applied to $M_{t\bar{t}}$ (5.193) increase the S/B as can be seen from the last column of Tab. 5.4.2. However, the results for the longitudinal polarization of the top quark are all below the percent level even including the contribution from the 2HDM and exhibit large scale uncertainties. This confirms what is also observed at LO: The effects of longitudinal top-quark polarization are very small in 2HDM scenarios that are not excluded by CP -sensitive measurements. The ATLAS and CMS experiments [119, 206] also measured the longitudinal top-quark polarization inclusively in $M_{t\bar{t}}$ at 8 TeV. These measurements are in agreement with the SM predictions of Ref. [118] but due to the relatively large uncertainties they cannot constrain scenario lc.

Summary and Conclusions

In this thesis $t\bar{t}$ production at the LHC is considered under the assumption of an extended Higgs sector featuring heavy neutral Higgs bosons that couple to top quarks. As a specific realization of a SM extension of the Higgs sector the type-II 2HDM is considered. This model gives rise to five physical Higgs bosons: two are electrically charged and three are neutral. One of the neutral Higgs bosons is associated with the 125 GeV Higgs boson while the other two are considered heavy enough to decay into a $t\bar{t}$ pair and therefore represent the actual object of interest in this work.

A particular emphasis in this thesis is placed on the phenomenological study of spin dependent observables which are accessible at the LHC through angular correlations of the $t\bar{t}$ decay products. These observables can be calculated by using the spin dependent matrix element as has been explicitly shown in Chap. 3. This facilitates the numerical computation of top-quark polarization and $t\bar{t}$ spin correlation observables especially in the case of NLO corrections. Furthermore, through the spin dependent matrix element the on-shell decay of the $t\bar{t}$ pair can be realized in a simple manner. As a byproduct of introducing the spin dependent matrix element via the spin density matrix formalism in Chap. 3 it is also briefly pointed out how this is related to the spinor helicity formalism which is widely used in the literature.

Heavy Higgs production and decay into $t\bar{t}$ is studied at LO in α_s in Chap. 4. The $M_{t\bar{t}}$ distribution is presented for two example scenarios to illustrate the main features of the spin independent contribution to this process. In particular, the size of the Higgs-QCD interference which is at least as large as the signal amplitude squared and can lead to distortions of the resonance peak resulting, for example, in a peak-dip structure. Furthermore, the $M_{t\bar{t}}$ distribution shows that heavy Higgs contributions outside the resonance region are negligible. The Higgs-Higgs interference between the two heavy Higgs bosons which is present in CPV 2HDM scenarios is investigated by estimating its maximum with respect to the single Higgs contribution. This interference is found to be a nonnegligible effect in cases where $m_2 \approx m_3$ and for low masses.

Spin dependent observables are also investigated at LO. The longitudinal top-quark polarization is studied as an observable that is potentially sensitive to CPV effects in the 2HDM because, in particular, it is zero at LO in the SM. It turns out that the maximum of the longitudinal top-quark polarization generated by CPV in the 2HDM is comparable in size to the SM value $B_{k,SM}^\pm \sim O(10^{-3})$ for heavy Higgs masses $m_2 < 600$ GeV and $\tan\beta = 1$. For masses $m_2 > 600$ GeV it is more than one order of magnitude smaller than the SM value. The fact that $|B_k^\pm|$ is so small can be attributed to the constraints on the parameter space of the mixing angles that strongly restrict the CPV effects necessary for longitudinal top-quark

6. Summary and Conclusions

polarization.

As a second kind of spin dependent observable $t\bar{t}$ spin correlations are investigated at LO in Chap. 4. The maximal S/B is determined by scanning over the directions of correlation reference axes and binning the spin correlation in $M_{t\bar{t}}$. Hence, this method determines the reference axis and $M_{t\bar{t}}$ bin with the largest sensitivity to heavy Higgs effect in $t\bar{t}$ spin correlations. We observe a trade-off between sensitivity and size of the correlation. However, a significant enhancement of the S/B is achieved with respect to the $M_{t\bar{t}}$ distribution of the cross section such that it might not be necessary to go to very small correlations in order to be more sensitive than the $M_{t\bar{t}}$ distribution.

The results at NLO are presented in Chap. 5 and the computational methods used for this calculation are discussed. In particular, two approximations are applied in the NLO calculation. The large top mass limit leads to an effective coupling between gluons and heavy Higgs bosons reducing the two-loop calculation to one loop. To extend the validity of this approximation an additional rescaling is applied which has been used also in the case of Higgs production. Taking the results of the $M_{t\bar{t}}$ distribution at LO as a guidance the NLO calculation is restricted to the resonant region which contains the dominant contributions from heavy Higgs bosons. This is done by performing the leading pole approximation in the resonant Higgs propagator and applying the soft gluon approximation to extract the resonant contribution from the non-factorizable part of the amplitude. In total this gives the NLO corrections for the *resonant* contribution of heavy Higgs bosons to $t\bar{t}$ production. The analytical results for the NLO corrections are presented in terms of virtual and real corrections in Chap. 5 with an emphasis on the signal amplitude squared. Phenomenological results at NLO QCD are presented for spin independent as well as spin dependent observables for a set of representative 2HDM scenarios. Comparing the sensitivity of $M_{t\bar{t}}$, y_t and $\cos\theta_{CS}$ distributions shows that the $M_{t\bar{t}}$ distribution performs comparatively well among the spin independent observables. The NLO corrections are sizeable compared to the signal contribution but the overall effect remains small due to the large QCD background. Compared to spin correlations the $M_{t\bar{t}}$ distribution is in general less sensitive to heavy Higgs effects. Concerning the NLO corrections to spin dependent observables it is pointed out that zeros in the $M_{t\bar{t}}$ distribution of the spin correlations are very sensitive to radiative corrections. When considering $t\bar{t}$ spin correlation binned in $M_{t\bar{t}}$ it is important to take this effect into account in order to obtain robust predictions. This also shows the importance of NLO QCD corrections to $t\bar{t}$ spin correlations. Effects of CPV are also investigated in terms of the longitudinal top-quark polarization and the CP -odd triple product. The NLO corrections do not change the fact that the longitudinal top-quark polarization is very small. The effect of CPV heavy Higgs bosons on the CP -odd triple product are very small as well. Finally, the possibility to distinguish between Higgs bosons of different CP nature using an observable based on the azimuthal angle between the charged leptons in the dileptonic decay channel of $t\bar{t}$ is studied as well. While it is shown that this observable can in principle distinguish between scalar, pseudoscalar or CP mixture, the large QCD background and interference result in a low sensitivity of this observable with a S/B of a few percent.

As an outlook we consider two of the main aspects of this thesis: spin dependent observables and NLO corrections. In this work the sensitivity of spin dependent observables has been studied at the parton level. It would be interesting to extend this analysis to include effects at particle level, e.g. reconstruction, detector effects, fiducial phase space regions, and study how these effects change the sensitivity of spin observables. Furthermore, instead of considering the $M_{t\bar{t}}$ distribution of expectation values (spin correlations) an extension to double differential distributions, e.g. $d\sigma/[d(\cos\theta_+ \cos\theta_-)dM_{t\bar{t}}]$, could be interesting. Quite generally, the analysis of the optimal spin correlation performed in Chap. 4 could also be beneficial for the study of

other new physics models that involve the top quark. With respect to the NLO corrections a next step towards the full calculation could be made by removing either the large top mass approximation or the SGA. With the results of these two calculations one could approach the full result from two directions and obtain more information about the involved uncertainties. The ultimate goal, if feasible, would be the full two-loop calculation.

Concluding remark: This thesis gives a detailed account of the effects of heavy Higgs bosons in $t\bar{t}$ production within the type-II 2HDM both at LO and NLO QCD. The results presented here suggest that spin dependent observables can increase the sensitivity to these effects significantly in particular when binned in $M_{t\bar{t}}$. In order to obtain robust results NLO corrections should be taken into account. The experimental situation concerning the measurement of $t\bar{t}$ spin correlations at the moment of writing this thesis is such that these observables have been measured but the uncertainties are still too large to constrain the 2HDM. However, with much more statistics to be produced at the LHC, a top-quark factory, resulting in smaller experimental uncertainties spin dependent observables may become an important tool in BSM searches in the top-quark sector.

Trilinear couplings among the Higgs bosons of the 2HDM

In the following the trilinear couplings among the Higgs bosons of the 2HDM that arise from the scalar potential (2.3) are presented. A general expression for all trilinear couplings among the neutral Higgs bosons is given here. However, only the following subset of couplings is relevant for the two-body decays considered in Sec. 2.6

$$\phi_1^2\phi_2, \quad \phi_1^2\phi_3, \quad \phi_1\phi_2\phi_3, \quad \phi_2^2\phi_3, \quad \phi_2\phi_3^2. \quad (\text{A.1})$$

The couplings ϕ_j^3 , $j = 1, 2, 3$ do not play any role in the decays. The couplings $\phi_1\phi_2^2$ and $\phi_1\phi_3^2$ are also not considered here because $m_1 < m_2, m_3$ is assumed.

The Lagrangian corresponding to the trilinear couplings is given by

$$\mathcal{L}_{\phi^3} = v \sum_{j \leq k \leq l=1}^3 \frac{f_{jkl}}{c_{jkl}} \phi_j \phi_k \phi_l \quad (\text{A.2})$$

with

$$c_{jkl} = 2(\delta_{jk} + \delta_{jl} + \delta_{kl}) + |\epsilon_{jkl}| = n! \quad (\text{A.3})$$

where n is the number of identical indices. In the expressions for the coupling functions f_{jkl} the following short notation is used

$$\lambda_{345} = \lambda_3 + \lambda_4 + \text{Re}(\lambda_5), \quad (\text{A.4})$$

$$\lambda_{345}^- = \lambda_3 + \lambda_4 - \text{Re}(\lambda_5). \quad (\text{A.5})$$

A. Trilinear couplings among the Higgs bosons of the 2HDM

$$\begin{aligned}
f_{jkl} = & +3\mathcal{R}_{111}^{jkl} \left[\lambda_1 \cos \beta + \text{Re}(\lambda_6) \sin \beta \right] \\
& +\mathcal{R}_{112}^{jkl} \left[\lambda_{345} \sin \beta + 3\text{Re}(\lambda_6) \cos \beta \right] \\
& -\mathcal{R}_{113}^{jkl} \left[\text{Im}(\lambda_5) \sin \beta \cos \beta + \text{Im}(\lambda_6) (\cos(2\beta) + 2) \right] \\
& +\mathcal{R}_{122}^{jkl} \left[\lambda_{345} \cos \beta + 3\text{Re}(\lambda_7) \sin \beta \right] \\
& -\mathcal{R}_{123}^{jkl} \left[\text{Im}(\lambda_5) + (\text{Im}(\lambda_6) + \text{Im}(\lambda_7)) \sin \beta \cos \beta \right] \\
& +\mathcal{R}_{133}^{jkl} \left[(\lambda_1 - 2\text{Re}(\lambda_5)) \sin^2 \beta \cos \beta + \lambda_{345}^- \cos^3 \beta \right. \\
& \quad \left. + \text{Re}(\lambda_6) \sin^3 \beta + (\text{Re}(\lambda_7) - 2\text{Re}(\lambda_6)) \sin \beta \cos^2 \beta \right] \\
& +3\mathcal{R}_{222}^{jkl} \left[\lambda_2 \sin \beta + \text{Re}(\lambda_7) \cos \beta \right] \\
& +\mathcal{R}_{223}^{jkl} \left[\text{Im}(\lambda_7) (\cos(2\beta) - 2) - \text{Im}(\lambda_5) \sin \beta \cos \beta \right] \\
& +\mathcal{R}_{233}^{jkl} \left[(\lambda_2 - 2\text{Re}(\lambda_5)) \sin \beta \cos^2 \beta + \lambda_{345}^- \sin^3 \beta \right. \\
& \quad \left. + (\text{Re}(\lambda_6) - 2\text{Re}(\lambda_7)) \sin^2 \beta \cos \beta + \text{Re}(\lambda_7) \cos^3 \beta \right] \\
& +3\mathcal{R}_{333}^{jkl} \left[\text{Im}(\lambda_5) \sin \beta \cos \beta - \text{Im}(\lambda_6) \sin^2 \beta - \text{Im}(\lambda_7) \cos^2 \beta \right]
\end{aligned} \tag{A.6}$$

with

$$\mathcal{R}_{n_1 n_2 n_3}^{jkl} = \sum_{\sigma \in S_3(\{n_1, n_2, n_3\})} R_{j\sigma_1} R_{k\sigma_2} R_{l\sigma_3}, \tag{A.7}$$

where $S_3(\{n_1, n_2, n_3\})$ denotes all permutation of numbers n_1 , n_2 and n_3 . For example

$$\mathcal{R}_{113}^{112} = R_{11} R_{11} R_{23} + R_{11} R_{13} R_{21} + R_{13} R_{11} R_{21} = R_{11}^2 R_{23} + 2R_{11} R_{13} R_{21}. \tag{A.8}$$

These results agree with those in Refs. [88, 207, 208].

Theoretical constraints on the 2HDM from stability, unitarity and perturbativity

In this appendix the theoretical constraints that are imposed on the 2HDM by stability, unitarity and perturbativity are briefly discussed. We restrict the discussion to LO. In particular, the running of couplings is not considered.

B.1. Boundedness of the potential from below

In order to determine if the Higgs potential V_Φ is bounded from below one has to inspect the sign of V_Φ asymptotically for large field values. Demanding that the potential does not become negative in any direction gives constraints on the parameters of the potential. Often the stronger requirement of strict positivity is imposed on the potential. However, this constraint can exclude viable and interesting potentials such as tree-level potentials of SUSY where flat directions exist for large field values in the part of the potential containing the quartic terms (V_4). The following serves as a simple example of how constraints on the potential parameters can be derived from the requirement that the potential is strictly positive.

In the case of strict positivity the quartic terms (V_4) dominate over the bilinear terms in the potential such that it is sufficient to consider V_4 only. The positivity conditions on the parameters of the most general potential have been studied in Refs. [81, 92, 209]. Restricting the parameter space, e.g. by imposing Z_2^{SB} symmetry ($\lambda_6 = \lambda_7 = 0$) yields simple conditions [91, 210, 211] on the parameters of V_4 . To derive these constraints one can rewrite the potential

$$V_4(\lambda_6 = 0, \lambda_7 = 0) = +\frac{\lambda_1}{2} (\Phi_1^\dagger \Phi_1)^2 + \frac{\lambda_2}{2} (\Phi_2^\dagger \Phi_2)^2 + \lambda_3 (\Phi_1^\dagger \Phi_1) (\Phi_2^\dagger \Phi_2) + \lambda_4 (\Phi_1^\dagger \Phi_2) (\Phi_2^\dagger \Phi_1) + \frac{\lambda_5}{2} (\Phi_1^\dagger \Phi_2)^2 + \frac{\lambda_5^*}{2} (\Phi_2^\dagger \Phi_1)^2 \quad (\text{B.1})$$

by using [88]

$$\begin{aligned} \Phi_1^\dagger \Phi_1 &= |\Phi_1|^2 = x_1 \geq 0, & \Phi_2^\dagger \Phi_2 &= |\Phi_2|^2 = x_2 \geq 0, \\ \Phi_1^\dagger \Phi_2 &= \sqrt{x_1 x_2} \rho e^{i\theta}, & \Phi_2^\dagger \Phi_1 &= \sqrt{x_1 x_2} \rho e^{-i\theta}, \end{aligned} \quad (\text{B.2})$$

where $|\rho| \leq 1$ and $\theta \in [0, 2\pi)$. Substituting Eq. (B.2) in Eq. (B.1) yields

$$V_4 = \frac{\lambda_1}{2} x_1^2 + \frac{\lambda_2}{2} x_2^2 + \left[\lambda_3 + \rho^2 (\lambda_4 + |\lambda_5| \cos \delta) \right] x_1 x_2. \quad (\text{B.3})$$

B. Theoretical constraints on the 2HDM from stability, unitarity and perturbativity

where $\lambda_5 = |\lambda_5|e^{i\gamma}$ and $\delta = \gamma + 2\theta$. The potential in Eq. (B.3) has to be strictly positive for large x_1, x_2 irrespective of the direction in x_1 - x_2 space and for any allowed values of ρ and δ . Probing positivity in the direction where x_1 is large and $x_2 = 0$ or vice versa gives the following conditions:

$$\lambda_1 > 0, \quad \lambda_2 > 0. \quad (\text{B.4})$$

The direction where x_1 and x_2 are simultaneously large can be studied by rewriting the potential as

$$V_4 = \frac{1}{2} \left(\sqrt{\lambda_1}x_1 - \sqrt{\lambda_2}x_2 \right)^2 + \left[\sqrt{\lambda_1\lambda_2} + \lambda_3 + \rho^2 (\lambda_4 + |\lambda_5| \cos \delta) \right] x_1 x_2. \quad (\text{B.5})$$

The first term in Eq. (B.5) is either zero (e.g. in the direction where $x_2 = \sqrt{\lambda_1/\lambda_2}x_1$) or greater than zero. Thus V_4 can only be strictly positive if the term in square brackets is strictly positive

$$\sqrt{\lambda_1\lambda_2} + \lambda_3 + \rho^2 (\lambda_4 + |\lambda_5| \cos \delta) > 0 \quad (\text{B.6})$$

for all allowed values of ρ and δ . Rewriting condition (B.6)

$$\lambda_3 + \rho^2 (\lambda_4 + |\lambda_5| \cos \delta) > -\sqrt{\lambda_1\lambda_2} \quad (\text{B.7})$$

shows that strongest constraints for $\rho^2 = 1$ arise from the situation where all terms on the left-hand side of (B.7) are negative ($\lambda_3, \lambda_4 < 0$ and $\cos \delta = -1$) which yields the constraint

$$\sqrt{\lambda_1\lambda_2} + \lambda_3 + \lambda_4 - |\lambda_5| > 0. \quad (\text{B.8})$$

In a situation where e.g. $\lambda_3 \leq -\sqrt{\lambda_1\lambda_2}$ and $\lambda_4 - |\lambda_5| > 0$ compensate each other such that condition (B.8) is fulfilled would in fact violate condition (B.6) for $\rho = 0$. This observation puts another constraint on λ_3

$$\sqrt{\lambda_1\lambda_2} + \lambda_3 > 0. \quad (\text{B.9})$$

In summary the parameters of the Z_2^{SB} constrained potential have to fulfill the following conditions to generate a potential that is bounded from below

$$\lambda_1 > 0, \quad \lambda_2 > 0, \quad \lambda_3 + \sqrt{\lambda_1\lambda_2} > 0, \quad \lambda_3 + \lambda_4 - |\lambda_5| + \sqrt{\lambda_1\lambda_2} > 0. \quad (\text{B.10})$$

Note that these conditions ensure positivity of the tree-level potential. However, the renormalization group running of the parameters of the Higgs potential can restrict the allowed parameter range even further if one demands that the potential is bounded from below over the range of scales $M_Z \leq \mu \leq \Lambda$ where Λ is some large scale where the 2HDM is expected to lose its validity. For example, the conditions (B.10) may hold for a particular scale $\mu = \mu_1$ but can be violated at another scale $\mu = \mu_2$. This analysis goes beyond the scope of this work but can be found in the literature, e.g. in Refs. [211–217].

The boundedness of the potential from below is a necessary condition for the stability of the vacuum. However, even in the case of the SM where only one Higgs boson is present the scalar potential including quantum corrections can have more than one minimum. This opens the possibility that the vacuum state of the universe today is only a local minimum and can tunnel into another minimum which lies deeper. This situation is even more pronounced for the 2HDM where several Higgs bosons generate a multidimensional Higgs potential. Fortunately, it has been shown [218–220] that minima of different natures (CPV, charge breaking, neutral and CPC) cannot coexist in the 2HDM. However, this still leaves open the possibility that for example a neutral vacuum state decays into another neutral vacuum state (as possibly in the SM). This situation was also investigated (see Ref. [221] and reference therein) with the conclusion that there exist parameter regions of such unstable neutral vacua which should be excluded from the viable parameter space of the 2HDM. The analysis in Ref. [221] was also done at tree-level and the conclusions might change as one includes radiative corrections by calculating the effective potential of the 2HDM.

B.2. Unitarity

Besides the stability of the vacuum another constraint on the Higgs potential comes from the requirement that the interaction of the Higgs bosons have to obey perturbative unitarity. What this means in particular will be briefly discussed in this section.

If the interaction potential is symmetric under rotations in three dimensions angular momentum is conserved and it is possible to expand the $2 \rightarrow 2$ scattering amplitude \mathcal{A} in terms of eigenstates of the angular momentum operator, e.g. spherical harmonics $Y_l^m(\theta, \varphi)$. The incident wave in the scattering process can be asymptotically described by a plane wave which has a cylindrical symmetry around the direction of propagation, i.e. it is symmetric in φ . Thus in the expansion of the plane wave only spherical harmonics with $m = 0$ appear. Since $Y_l^0(\theta) = \sqrt{(2l+1)/(4\pi)}P_l(\cos\theta)$ the expansion of the scattering amplitude [20] is realized in terms of the Legendre polynomials $P_l(\cos\theta)$

$$\mathcal{A}(\theta) = 16\pi \sum_l a_l (2l+1) P_l(\cos\theta), \quad (\text{B.11})$$

where a_l is called the partial amplitude of the angular momentum l , $P_l(\cos\theta)$ are the Legendre polynomials and θ is the scattering angle. In order to conserve probability (and unitarity) the partial amplitudes have to fulfill the following condition

$$|a_l| \leq 1. \quad (\text{B.12})$$

a_l is defined as the amplitude of a scattered partial wave of angular momentum l with respect to the corresponding incoming wave. Since the intensity of the scattered wave can not exceed the intensity of the incoming wave $|a_l|$ has to fulfill (B.12).

The unitarity constraint (B.12) was first used in Ref. [222] to set a theoretical bound on the SM Higgs boson mass. The authors of Ref. [222] determined the partial wave amplitudes a_0 of all $2 \rightarrow 2$ scattering processes involving longitudinally polarized gauge bosons (W_L^\pm, Z_L) and the Higgs boson h in the initial and final state at tree-level. From this collection of a_0 amplitudes they constructed the T -matrix¹ of the partial waves with $l = 0$

$$T = \begin{pmatrix} a_0(W_L^+ W_L^- \rightarrow W_L^+ W_L^-) & a_0(W_L^+ W_L^- \rightarrow Z_L Z_L) & a_0(W_L^+ W_L^- \rightarrow hh) & \dots & \dots \\ a_0(Z_L Z_L \rightarrow W_L^+ W_L^-) & a_0(Z_L Z_L \rightarrow Z_L Z_L) & \dots & \dots & \dots \\ a_0(hh \rightarrow W_L^+ W_L^-) & \dots & \dots & \dots & \dots \\ \vdots & & & & \vdots \\ \vdots & & & & \vdots \end{pmatrix} \quad (\text{B.13})$$

in the limit $s \gg m_h^2$ where a unitarity violating behaviour would cause problems². Then the T -matrix was diagonalized and the constraint on the largest eigenvalue ω_{\max}

$$|\omega_{\max}| \leq 1 \quad (\text{B.14})$$

was used to derive an upper bound on the SM Higgs mass. In Ref. [222] it was also shown that because of the Goldstone equivalence theorem the scattering amplitudes involving W_L^\pm and Z_L are equivalent to those involving the respective Goldstone bosons G^\pm and G^0 in the high energy limit. For the unitarity analysis of the 2HDM [223–227] one can therefore study the scattering

¹In the usual notation the T -matrix denotes the nontrivial part of the S -matrix $S = 1 + iT$.

²The partial wave amplitudes a_l with $l > 0$ vanish for $s \gg m_h^2$. So they do not play a role for tree-level unitarity bounds.

B. Theoretical constraints on the 2HDM from stability, unitarity and perturbativity

amplitudes between the unphysical Higgs states $\xi_{1,2}^\pm$, $\varphi_{1,2}$ and $\chi_{1,2}$ (see Eq. (2.4)) which already include the scattering amplitudes of longitudinally polarized gauge bosons in the high energy limit. It turns out that it is sufficient to study only scattering amplitudes involving four-point vertices. All other contributions are negligible in the high energy limit. The amplitudes \mathcal{A}_{ijkl} with four-point vertices are in fact dimensionless functions of the parameters in the quartic interaction part of the Higgs potential

$$\mathcal{A}_{ijkl} = \mathcal{A}_{ijkl}(\lambda_1, \dots, \lambda_7), \quad i, j, k, l = \xi_{1,2}^\pm, \varphi_{1,2}, \chi_{1,2}. \quad (\text{B.15})$$

In particular, there is no $\cos \theta$ dependence. Hence, for this specific contribution all partial waves except a_0 are zero such that the scattering amplitude $\mathcal{A}_{ijkl} = 16\pi a_0^{ijkl}$. From the partial wave amplitudes a_0^{ijkl} the eigenvalues ω_n of the T -matrix can be determined where $n = 1, \dots, \dim(T)$. The ω_n are then functions of the parameters λ_k , $k = 1, \dots, 7$ and have to obey the unitarity condition³

$$|\omega_j(\lambda_1, \dots, \lambda_7)| \leq 1. \quad (\text{B.16})$$

Unfortunately, Eq. (B.16) does not give constraints as simple as Eq. (B.10). However, the described method was used to derive bounds on the parameters of the general 2HDM potential and upper bounds on the masses of the physical Higgs bosons. The results can be found for example in Ref. [223–227]. Besides the unitarity limit originally used in Ref. [222] tighter bounds can be found in the literature [228, 229] based on

$$|\text{Re}(a_0)| \leq \frac{1}{2}. \quad (\text{B.17})$$

The unitarity analysis of the 2HDM can and has been extended to include NLO corrections of the scattering amplitudes [230, 231] but this aspect is not discussed here.

B.3. Perturbativity

Perturbation theory can in principle only be applied whenever the respective expansion parameter is small enough, i.e. smaller than one. In quantum field theories this parameter is the coupling constant of the respective theory, e.g. α_s in QCD⁴. Hence if the coupling constant assumes values that are too large perturbativity is jeopardized. This is for example observed for QCD where α_s becomes large for smaller energy scales and the theory enters the so-called *nonperturbative* regime involving for example mesonic and hadronic bound states. This also shows that perturbativity is not a requirement for a consistent theory. It is, however, a requirement for the consistent application of perturbation theory. A rigorous analysis of the applicability of perturbation theory to the 2HDM would involve the calculation of higher order corrections. However, a rough estimate of the perturbative bound can be found by considering that at each order the scattering amplitudes receive a loop-factor of $1/(16\pi^2)$ and two more factors of the Higgs coupling constants λ_j , $j = 1, \dots, 7$ such that the actual expansion parameters are $\lambda_j/(4\pi)$. In this naive estimate the limit on the coupling constants is given by

$$|\lambda_j| < 4\pi. \quad (\text{B.18})$$

³In the SM the eigenvalues of the T -matrix of all scalar scattering amplitudes are pure numbers because there is only one Higgs self-coupling. Hence in the SM it is sufficient that the largest eigenvalue obeys the unitarity constraint. This ensures that all scattering amplitudes are unitary. In the 2HDM there are many self-couplings in the Higgs potential and the eigenvalues are functions of these coupling parameters. Therefore in general all eigenvalues ω_n have to fulfill the unitarity bound.

⁴For simplicity the effect of large logarithms that can appear in perturbation theory and which then have to be resummed by effectively considering $\alpha_s \times \log(M/\mu)$ as an expansion parameter is not considered here.

On the other hand higher order calculation in the Higgs sector of the SM suggest a tighter bound [232]

$$|\lambda_j| < 2\pi. \tag{B.19}$$

While it can be interesting to study the impact of these bounds on observables that are sensitive to the 2HDM one has to keep in mind that they are merely rough estimates and should be applied as such. In this work the tree-level perturbativity as outlined above and often used in the literature will therefore play no significant role.

On-shell decay of the top-quark pair system

In this part of the appendix we discuss various aspects of $t\bar{t}$ on-shell production and the subsequent dileptonic decay. In Sec. C.1 we illustrate that the factorization of $t\bar{t}$ production and decay in the narrow width approximation, i.e. on-shell decay, can be written in terms of production and decay density matrices. A master formula for the differential cross section of $t\bar{t}$ production and dileptonic decay is derived in Sec. C.2. This result is used to obtain the expression for the double differential distribution. The coefficients B and C in this distribution are expressed in terms of expectation values of spin operators. Furthermore, in Sec. C.4 the opening angle distribution is derived from the master formula of Sec. C.2.

C.1. Factorization of top-quark pair production and decay

The factorization of on-shell production and subsequent decay of the $t\bar{t}$ pair can be written in a compact form in terms of the production and decay density matrices introduced in Sec. 3.2 and Sec. 3.3, respectively. In order to derive the relation used in Eq. (3.44) consider the decay of the $t\bar{t}$ pair as schematically shown in Fig. C.1. \mathcal{D}_t and $\mathcal{D}_{\bar{t}}$ denote the decay vertices of the top and antitop, respectively, and $\mathcal{P}_{t\bar{t}}$ represents the amplitude for the production of a $t\bar{t}$ pair. The amplitude of the process shown in Fig. C.1 is given by

$$\mathcal{A} = P_t(k_t, m_t, \Gamma_t) P_{\bar{t}}(k_{\bar{t}}, m_t, \Gamma_t) \bar{u}_b \mathcal{D}_t(k_t + m_t) \mathcal{P}_{t\bar{t}}(-k_{\bar{t}} + m_t) \mathcal{D}_{\bar{t}} v_b \quad (\text{C.1})$$

with

$$P(k, m, \Gamma) = \frac{i}{k^2 - m^2 + i\Gamma m}. \quad (\text{C.2})$$

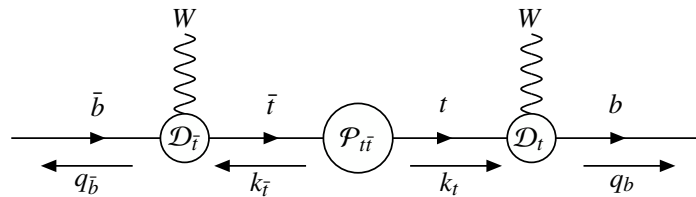


Figure C.1.: Schematic Feynman amplitude for $t\bar{t}$ production with subsequent decay of the (anti)top into W^+b ($W^-\bar{b}$).

C. On-shell decay of the top-quark pair system

Using the completeness relations

$$\sum_s u_s(k, m) \bar{u}_s(k, m) = \not{k} + m, \quad \sum_s v_s(k, m) \bar{v}_s(k, m) = \not{k} - m \quad (\text{C.3})$$

gives

$$\mathcal{A} = -P_t(k_t, m_t, \Gamma_t) P_{\bar{t}}(k_{\bar{t}}, m_t, \Gamma_t) \sum_{s, r} \bar{u}_b \mathcal{D}_t u_t^s \bar{u}_t^s \mathcal{P}_{\bar{t}} v_t^r \bar{v}_t^r \mathcal{D}_{\bar{t}} v_b. \quad (\text{C.4})$$

The squared matrix element is obtained by multiplying \mathcal{A} with its hermitian conjugate \mathcal{A}^\dagger

$$|\mathcal{M}|^2 = \mathcal{A} \mathcal{A}^\dagger = \text{BW}(k_t, m_t, \Gamma_t) \text{BW}(k_{\bar{t}}, m_t, \Gamma_t) \times \sum_{s, s', r, r'} \left[\bar{u}_b \mathcal{D}_t u_t^s \bar{u}_t^s \mathcal{P}_{\bar{t}} v_t^r \bar{v}_t^r \mathcal{D}_{\bar{t}} v_b \right] \left[\bar{v}_b \mathcal{D}_{\bar{t}} v_t^{r'} \bar{v}_t^{r'} \mathcal{P}_{\bar{t}} u_t^{s'} \bar{u}_t^{s'} \mathcal{D}_t u_b \right] \quad (\text{C.5})$$

with the Breit-Wigner function

$$\text{BW}(k, m, \Gamma) = \frac{1}{(k^2 - m^2)^2 + \Gamma^2 m^2}. \quad (\text{C.6})$$

In the limit where $m_t \gg \Gamma_t$ (narrow width approximation) the Breit-Wigner function can be approximated by a delta function

$$\lim_{\Gamma_t/m_t \rightarrow 0} \text{BW}(k, m, \Gamma) = \frac{\pi}{\Gamma m} \delta(k^2 - m^2). \quad (\text{C.7})$$

Rearranging the terms in square brackets in Eq. (C.5) and applying the narrow width approximation yields

$$\begin{aligned} |\mathcal{M}(ab \rightarrow t\bar{t} \rightarrow b\bar{b}\ell^+\ell^-v\bar{v})|^2 &= \frac{\pi^2}{\Gamma_t^2 m_t^2} \delta(k_t^2 - m_t^2) \delta(k_{\bar{t}}^2 - m_t^2) \\ &\times \sum_{s, s', r, r'} \underbrace{\bar{u}_t^s \mathcal{P}_{\bar{t}} v_t^r \bar{v}_t^{r'} \mathcal{P}_{\bar{t}} u_t^{s'}}_{R_{ss', rr'}^{ab \rightarrow t\bar{t}}} \underbrace{\bar{u}_t^{s'} \mathcal{D}_t u_b \bar{u}_b \mathcal{D}_t u_t^s}_{D_{ss'}^{t \rightarrow b\ell^+v}} \underbrace{\bar{v}_t^{r'} \mathcal{D}_{\bar{t}} v_b \bar{v}_b \mathcal{D}_{\bar{t}} v_t^{r'}}_{D_{rr'}^{\bar{t} \rightarrow \bar{b}\ell^- \bar{v}}} \\ &= \frac{\pi^2}{\Gamma_t^2 m_t^2} \delta(k_t^2 - m_t^2) \delta(k_{\bar{t}}^2 - m_t^2) \text{Tr}[R^{ab \rightarrow t\bar{t}} D^{t \rightarrow b\ell^+v} \otimes D^{\bar{t} \rightarrow \bar{b}\ell^- \bar{v}}]. \quad (\text{C.8}) \end{aligned}$$

C.2. Leading order master formula for top-quark pair production and dileptonic decay

In this section the matrix element in Eq. (C.8) for the process

$$a(p_a) b(p_b) \rightarrow t(k_t) \bar{t}(k_{\bar{t}}) \rightarrow b(q_b) \bar{b}(q_{\bar{b}}) \ell^+(q_{\ell^+}) \ell^-(q_{\ell^-}) \nu(q_\nu) \bar{\nu}(q_{\bar{\nu}}) \quad (\text{C.9})$$

is integrated over the final state (6-particle) phase space where the narrow width approximation is applied to both top and antitop as well as the W bosons. The differential partonic cross section is given by

$$\begin{aligned} \sigma(s) &= \frac{1}{2(2\pi)^{14} s} \int \frac{d^3 q_b}{2E_b} \frac{d^3 q_{\bar{b}}}{2E_{\bar{b}}} \frac{d^3 q_{\ell^+}}{2E_{\ell^+}} \frac{d^3 q_{\ell^-}}{2E_{\ell^-}} d^4 q_\nu \delta_+(q_\nu^2) d^4 q_{\bar{\nu}} \delta_+(q_{\bar{\nu}}^2) \\ &\quad \delta^{(4)}(P - k_b - k_{\bar{b}} - q_{\ell^+} - q_{\ell^-} - q_\nu - q_{\bar{\nu}}) \\ &\quad d^4 k_t \delta^{(4)}(k_t - k_b - q_{\ell^+} - q_\nu) d^4 k_{\bar{t}} \delta^{(4)}(k_{\bar{t}} - k_{\bar{b}} - q_{\ell^-} - q_{\bar{\nu}}) \\ &\quad \delta(k_t^2 - m_t^2) \delta(k_{\bar{t}}^2 - m_t^2) \delta((q_{\ell^+} + q_\nu)^2 - m_W^2) \delta((q_{\ell^-} + q_{\bar{\nu}})^2 - m_W^2) |\widetilde{\mathcal{M}}|^2, \quad (\text{C.10}) \end{aligned}$$

C.2. Leading order master formula for top-quark pair production and dileptonic decay

where $|\widetilde{\mathcal{M}}|^2$ is the matrix element in Eq. (C.8) where all delta functions have been pulled out. At first the integrations over

$$d^4 q_\nu \delta_+(q_\nu^2) d^4 q_{\bar{\nu}} \delta_+(q_{\bar{\nu}}^2) \delta^{(4)}(k_t - k_b - q_{\ell^+} - q_\nu) \delta^{(4)}(k_{\bar{t}} - k_{\bar{b}} - q_{\ell^-} - q_{\bar{\nu}}) \quad (\text{C.11})$$

and then over

$$d^4 k_{\bar{t}} \delta^{(4)}(P - k_t - k_{\bar{t}}) \quad (\text{C.12})$$

are performed. The integration over $d^4 k_t$ gives

$$d^4 k_t \delta(k_t^2 - m_t^2) \delta((P - k_t)^2 - m_t^2) = \frac{d\Omega_t}{8} \beta_t, \quad d\Omega_t = d \cos \theta_t d\varphi_t, \quad \beta_t = \sqrt{1 - \frac{4m_t^2}{s}}. \quad (\text{C.13})$$

The delta functions from the narrow width approximation of the W propagators can be rewritten as¹

$$\begin{aligned} \delta((q_{\ell^+} + q_\nu)^2 - m_W^2) &= \frac{1}{2m_t} \delta\left(E_b - \frac{m_t^2 - m_W^2}{2m_t^2}\right), \\ \delta((q_{\ell^-} + q_{\bar{\nu}})^2 - m_W^2) &= \frac{1}{2m_t} \delta\left(E_{\bar{b}} - \frac{m_t^2 - m_W^2}{2m_t^2}\right), \end{aligned} \quad (\text{C.14})$$

where E_b is given in the top-quark rest frame and $E_{\bar{b}}$ in the antitop-quark rest frame. The delta functions from the on-shell condition of the neutrino $\delta(q_\nu^2) = \delta((k_t - q_b - k_{\ell^+})^2)$ and of the antineutrino $\delta(q_{\bar{\nu}}^2) = \delta((k_{\bar{t}} - q_{\bar{b}} - k_{\ell^-})^2)$ can be written as

$$\begin{aligned} \delta((k_t - q_b - k_{\ell^+})^2) &= \frac{2}{m_t^2 (1 - \omega)x_+} \delta\left(\hat{\mathbf{q}}_b \cdot \hat{\mathbf{q}}_{\ell^+} - \frac{2\omega - (1 + \omega)x_+}{(1 - \omega)x_+}\right), \\ \delta((k_{\bar{t}} - q_{\bar{b}} - k_{\ell^-})^2) &= \frac{2}{m_t^2 (1 - \omega)x_-} \delta\left(\hat{\mathbf{q}}_{\bar{b}} \cdot \hat{\mathbf{q}}_{\ell^-} - \frac{2\omega - (1 + \omega)x_-}{(1 - \omega)x_-}\right), \end{aligned} \quad (\text{C.15})$$

where $\omega = m_W^2/m_t^2$ and $x_\pm = 2E_{\ell^\pm}/m_t$ with the energy E_{ℓ^+} of antilepton in the top-quark rest frame and the energy E_{ℓ^-} of lepton in the antitop-quark rest frame. Rewriting the remaining phase space measures as integrations over energies and angles yields

$$\begin{aligned} \frac{d^3 q_b}{2E_b} \frac{d^3 q_{\bar{b}}}{2E_{\bar{b}}} &= \frac{1}{4} dE_b dE_{\bar{b}} d\Omega_b d\Omega_{\bar{b}} E_b E_{\bar{b}} = \frac{1}{16} dE_b dE_{\bar{b}} d\Omega_b d\Omega_{\bar{b}} m_t^2 (1 - \omega)^2, \\ \frac{d^3 q_{\ell^+}}{2E_{\ell^+}} \frac{d^3 q_{\ell^-}}{2E_{\ell^-}} &= \frac{1}{4} dE_{\ell^+} dE_{\ell^-} d\Omega_{\ell^+} d\Omega_{\ell^-} E_{\ell^+} E_{\ell^-} = \frac{m_t^4}{64} x_+ x_- d\Omega_{\ell^+} d\Omega_{\ell^-} dx_+ dx_-. \end{aligned} \quad (\text{C.16})$$

Altogether this gives

$$\begin{aligned} \sigma(s) &= \frac{\beta_t}{(4\pi)^{14} s} \int_\omega^1 dx_+ \int_\omega^1 dx_- \int d\Omega_{\ell^+} \int d\Omega_{\ell^-} \int d\Omega_t |\widetilde{\mathcal{M}}|^2 \\ &\times \int dE_b \delta\left(E_b - \frac{m_t^2 - m_W^2}{2m_t}\right) \int dE_{\bar{b}} \delta\left(E_{\bar{b}} - \frac{m_t^2 - m_W^2}{2m_t}\right) \\ &\times \int d\Omega_b \delta\left(\hat{\mathbf{q}}_b \cdot \hat{\mathbf{q}}_+ - \frac{2\omega - (1 + \omega)x_+}{(1 - \omega)x_+}\right) \int d\Omega_{\bar{b}} \delta\left(\hat{\mathbf{q}}_{\bar{b}} \cdot \hat{\mathbf{q}}_- - \frac{2\omega - (1 + \omega)x_-}{(1 - \omega)x_-}\right), \end{aligned} \quad (\text{C.17})$$

¹Using $(q_{\ell^+} - q_\nu)^2 = (k_t - q_b)^2 = m_t^2 - 2m_t E_b$ where E_b is given in the top-quark rest frame. Analogously for $q_{\ell^-} + q_{\bar{\nu}}$.

C. On-shell decay of the top-quark pair system

where the integration boundaries of the x_{\pm} integrations are given by the condition

$$-1 \leq \frac{2\omega - (1 + \omega)x_{\pm}}{(1 - \omega)x_{\pm}} \leq 1 \quad (\text{C.18})$$

and where

$$|\widetilde{\mathcal{M}}|^2 = 4G_t G_{\bar{t}} \frac{\pi^2}{m_t^2 \Gamma_t^2} \left(A + \kappa_{\ell} \hat{\mathbf{q}}_{\ell^+} \cdot \mathbf{B}^+ - \kappa_{\ell} \hat{\mathbf{q}}_{\ell^-} \cdot \mathbf{B}^- - \kappa_{\ell}^2 C_{ij} \hat{q}_{\ell^+}^i \hat{q}_{\ell^-}^j \right) \quad (\text{C.19})$$

with

$$G_t = \Gamma_t \text{BR}(t \rightarrow b\ell^+\nu) \frac{1536\pi^3 m_t}{(1 - \omega)^2 (1 + 2\omega)} (1 - x_+) x_+, \quad (\text{C.20})$$

$$G_{\bar{t}} = \Gamma_{\bar{t}} \text{BR}(\bar{t} \rightarrow \bar{b}\ell^-\bar{\nu}) \frac{1536\pi^3 m_t}{(1 - \omega)^2 (1 + 2\omega)} (1 - x_-) x_-. \quad (\text{C.21})$$

Finally, the differential partonic cross section is given by

$$\begin{aligned} \sigma(s) &= \frac{\beta_t}{16\pi^2 s} \text{BR}(t \rightarrow b\ell^+\nu) \text{BR}(\bar{t} \rightarrow \bar{b}\ell^-\bar{\nu}) \\ &\times \int_{\omega}^1 dx_+ \frac{6(1 - x_+)x_+}{(1 - \omega^2)(1 + 2\omega)} \int_{\omega}^1 dx_- \frac{6(1 - x_-)x_-}{(1 - \omega^2)(1 + 2\omega)} \int \frac{d\Omega_{\ell^+}}{4\pi} \int \frac{d\Omega_{\ell^-}}{4\pi} \int d\Omega_t \\ &\times \left(A + \kappa_{\ell} \hat{\mathbf{q}}_{\ell^+} \cdot \mathbf{B}^+ - \kappa_{\ell} \hat{\mathbf{q}}_{\ell^-} \cdot \mathbf{B}^- - \kappa_{\ell}^2 C_{ij} \hat{q}_{\ell^+}^i \hat{q}_{\ell^-}^j \right) \\ &\times \int dE_b \delta\left(E_b - \frac{m_t^2 - m_W^2}{2m_t}\right) \int dE_{\bar{b}} \delta\left(E_{\bar{b}} - \frac{m_t^2 - m_W^2}{2m_t}\right) \\ &\times \int \frac{d\Omega_b}{2\pi} \delta\left(\hat{\mathbf{q}}_b \cdot \hat{\mathbf{q}}_{\ell^+} - \frac{2\omega - (1 + \omega)x_+}{(1 - \omega)x_+}\right) \int \frac{d\Omega_{\bar{b}}}{2\pi} \delta\left(\hat{\mathbf{q}}_{\bar{b}} \cdot \hat{\mathbf{q}}_{\ell^-} - \frac{2\omega - (1 + \omega)x_-}{(1 - \omega)x_-}\right) \end{aligned} \quad (\text{C.22})$$

which is in agreement² with Ref. [108]. The numerical factors have been distributed such as to normalize the individual integrals.

C.3. Double differential distribution

From Eq. (C.22) one can derive the double differential cross section

$$\frac{1}{\sigma} \frac{d\sigma}{d\cos\theta_+ d\cos\theta_-} = \frac{1}{4} (1 + B_1 \cos\theta_+ + B_2 \cos\theta_- - C \cos\theta_+ \cos\theta_-), \quad (\text{C.23})$$

where $\cos\theta_+ = \hat{\mathbf{q}}_{\ell^+} \cdot \hat{\mathbf{a}}_1$ and $\cos\theta_- = \hat{\mathbf{q}}_{\ell^-} \cdot \hat{\mathbf{a}}_2$ with arbitrary reference axes $\hat{\mathbf{a}}_1$ and $\hat{\mathbf{a}}_2$. The directions of the lepton momenta $\hat{\mathbf{q}}_{\ell^+}$ and $\hat{\mathbf{q}}_{\ell^-}$ can be decomposed into a component parallel and perpendicular to the respective reference axes $\hat{\mathbf{a}}_1$ and $\hat{\mathbf{a}}_2$

$$\hat{\mathbf{q}}_{\ell^+} = \mathbf{q}_{\ell^+}^{\perp} + \hat{\mathbf{a}}_1 \cos\theta_+, \quad \hat{\mathbf{q}}_{\ell^-} = \mathbf{q}_{\ell^-}^{\perp} + \hat{\mathbf{a}}_2 \cos\theta_-, \quad (\text{C.24})$$

where $\mathbf{q}_{\ell^{\pm}}^{\perp}$ are the azimuthal components of $\hat{\mathbf{q}}_{\ell^+}$ and $\hat{\mathbf{q}}_{\ell^-}$. The terms \mathbf{B}^{\pm} can be decomposed analogously

$$\mathbf{B}^+ = \mathbf{B}_{\perp}^+ + \hat{\mathbf{a}}_1 (\mathbf{B}^+ \cdot \hat{\mathbf{a}}_1), \quad \mathbf{B}^- = \mathbf{B}_{\perp}^- + \hat{\mathbf{a}}_2 (\mathbf{B}^- \cdot \hat{\mathbf{a}}_2). \quad (\text{C.25})$$

²Note that in their convention $g_s^4 = 16\pi^2 \alpha_s^2$ is factored out of the production density matrix.

The \mathbf{B}^\pm terms in Eq. (C.22) can then be written as

$$\mathbf{B}^+ \cdot \hat{\mathbf{q}}_{\ell^+} = \mathbf{B}_\perp^+ \cdot \mathbf{q}_{\ell^+}^\perp + (\mathbf{B}^+ \cdot \hat{\mathbf{a}}_1) \cos \theta_+, \quad \mathbf{B}^- \cdot \hat{\mathbf{q}}_{\ell^-} = \mathbf{B}_\perp^- \cdot \mathbf{q}_{\ell^-}^\perp + (\mathbf{B}^- \cdot \hat{\mathbf{a}}_2) \cos \theta_-. \quad (\text{C.26})$$

When integrating over the azimuthal angles φ_{ℓ^+} and φ_{ℓ^-} the terms $\mathbf{B}_\perp^\pm \cdot \mathbf{q}_{\ell^\pm}^\perp$ vanish. Applying the decomposition in Eq. (C.24) to $C_{ij} \hat{q}_{\ell^+}^i \hat{q}_{\ell^-}^j$ in Eq. (C.22) gives

$$C_{ij} \hat{q}_{\ell^+}^i \hat{q}_{\ell^-}^j = C_{ij} \left[q_{\ell^+}^{\perp,i} q_{\ell^-}^{\perp,j} + q_{\ell^+}^{\perp,i} \hat{a}_2^j \cos \theta_- + \hat{a}_1^i q_{\ell^-}^{\perp,j} \cos \theta_+ + \hat{a}_1^i \hat{a}_2^j \cos \theta_+ \cos \theta_- \right]. \quad (\text{C.27})$$

When integrating over φ_{ℓ^+} and φ_{ℓ^-} only the term $C_{ij} \hat{a}_1^i \hat{a}_2^j \cos \theta_+ \cos \theta_-$ survives. After performing all trivial integrations and the integration over φ_{ℓ^+} and φ_{ℓ^-} in Eq. (C.22) the differential partonic cross section is given by

$$d\sigma = \text{BR}^2 \frac{\beta_t}{8\pi_S} d \cos \theta_+ d \cos \theta_- \frac{1}{4} \left(\bar{A} + \kappa_\ell \bar{B}^+ \cos \theta_+ - \kappa_\ell \bar{B}^- \cos \theta_- - \kappa_\ell^2 \bar{C} \cos \theta_+ \cos \theta_- \right) \quad (\text{C.28})$$

with

$$\bar{A} = \int dz A, \quad \bar{B}^+ = \int dz (\mathbf{B}^+ \cdot \hat{\mathbf{a}}_1), \quad \bar{B}^- = \int dz (\mathbf{B}^- \cdot \hat{\mathbf{a}}_2), \quad \bar{C} = \int dz C_{ij} \hat{a}_1^i \hat{a}_2^j, \quad (\text{C.29})$$

$$z = \hat{\mathbf{k}} \cdot \hat{\mathbf{p}}$$

and BR^2 is a short notation for $\text{BR}(t \rightarrow b\ell^+\nu)\text{BR}(\bar{t} \rightarrow \bar{b}\ell^-\bar{\nu})$. To obtain the hadronic differential cross section the partonic cross section has to be convoluted with the PDFs

$$d\sigma = \text{BR}^2 d \cos \theta_+ d \cos \theta_- \int dx_a dx_b f_{p,a}(x_a, \mu_F) f_{p,b}(x_b, \mu_F) \frac{\beta_t}{8\pi_S} \times \frac{1}{4} \left(\bar{A} + \kappa_\ell \bar{B}^+ \cos \theta_+ - \kappa_\ell \bar{B}^- \cos \theta_- - \kappa_\ell^2 \bar{C} \cos \theta_+ \cos \theta_- \right). \quad (\text{C.30})$$

Normalizing with respect to the total hadronic cross section

$$\sigma = \text{BR}^2 \int dx_a dx_b f_{p,a}(x_a, \mu_F) f_{p,b}(x_b, \mu_F) \frac{\beta_t}{8\pi_S} \bar{A} \quad (\text{C.31})$$

gives

$$\frac{1}{\sigma} \frac{d\sigma}{d \cos \theta_+ d \cos \theta_-} = \frac{1}{4} (1 + B_1 \cos \theta_+ + B_2 \cos \theta_- - C \cos \theta_+ \cos \theta_-) \quad (\text{C.32})$$

with³

$$B_1(\hat{\mathbf{a}}_1) = \frac{\kappa_\ell}{\sigma} \int dx_a dx_b f_{p,a}(x_a, \mu_F) f_{p,b}(x_b, \mu_F) dz \frac{\beta_t}{8\pi_S} (\mathbf{B}^+ \cdot \hat{\mathbf{a}}_1) = \kappa_\ell \langle 2\mathbf{S}_t \cdot \hat{\mathbf{a}}_1 \rangle_{t\bar{t}}, \quad (\text{C.33})$$

$$B_2(\hat{\mathbf{a}}_2) = -\frac{\kappa_\ell}{\sigma} \int dx_a dx_b f_{p,a}(x_a, \mu_F) f_{p,b}(x_b, \mu_F) dz \frac{\beta_t}{8\pi_S} (\mathbf{B}^- \cdot \hat{\mathbf{a}}_2) = \kappa_\ell \langle -2\mathbf{S}_{\bar{t}} \cdot \hat{\mathbf{a}}_2 \rangle_{t\bar{t}}, \quad (\text{C.34})$$

$$C(\hat{\mathbf{a}}_1, \hat{\mathbf{a}}_2) = \frac{\kappa_\ell^2}{\sigma} \int dx_a dx_b f_{p,a}(x_a, \mu_F) f_{p,b}(x_b, \mu_F) dz \frac{\beta_t}{8\pi_S} C_{ij} \hat{a}_1^i \hat{a}_2^j = \kappa_\ell^2 \langle 4(\mathbf{S}_t \cdot \hat{\mathbf{a}}_1)(\mathbf{S}_{\bar{t}} \cdot \hat{\mathbf{a}}_2) \rangle_{t\bar{t}}, \quad (\text{C.35})$$

where Eq. (3.27) was applied.

³The phase space measure for the $t\bar{t}$ final state is given by $d\Phi_{t\bar{t}} = \frac{\beta_t}{32\pi_S} dz$.

C.4. Opening angle distribution

In this section the master formula Eq. (C.22) is used to derive the opening angle distribution

$$\frac{1}{\sigma} \frac{d\sigma}{d\varphi} = \frac{1}{2} (1 - D \cos \varphi), \quad (\text{C.36})$$

where $\cos \varphi = \hat{\mathbf{q}}_{\ell^+} \cdot \hat{\mathbf{q}}_{\ell^-}$. The first step is to decompose the direction $\hat{\mathbf{q}}_{\ell^+}$ into a component parallel and a component perpendicular to $\hat{\mathbf{q}}_{\ell^-}$

$$\hat{\mathbf{q}}_{\ell^+} = \mathbf{q}_{\ell^+}^\perp + \hat{\mathbf{q}}_{\ell^-} \cos \varphi. \quad (\text{C.37})$$

Then the C term in Eq. (C.22) can be decomposed as follows

$$C_{ij} \hat{q}_{\ell^+}^i \hat{q}_{\ell^-}^j = C_{ij} \hat{q}_{\ell^+}^{\perp,i} \hat{q}_{\ell^-}^j + C_{ij} \hat{q}_{\ell^-}^i \hat{q}_{\ell^-}^j \cos \varphi. \quad (\text{C.38})$$

For the integration one can choose $\theta_+ = \varphi$. When integrating over the other angles θ_- , φ_- and φ_+ the \mathbf{B}^\pm terms and $C_{ij} \hat{q}_{\ell^+}^{\perp,i} \hat{q}_{\ell^-}^j$ vanish and

$$\int d \cos \theta_- d\varphi_- d\varphi_+ \hat{q}_{\ell^+}^i \hat{q}_{\ell^-}^j = \frac{8\pi^2}{3} \delta^{ij}. \quad (\text{C.39})$$

Inserting this into the master formula and performing all trivial integrations yields the hadronic differential cross section

$$d\sigma = \text{BR}^2 d\varphi \int dx_a dx_b f_{p,a}(x_a, \mu_F) f_{p,b}(x_b, \mu_F) \frac{\beta_t}{8\pi s} \frac{1}{2} (\tilde{A} - \kappa_\ell^2 \tilde{D} \cos \varphi) \quad (\text{C.40})$$

with

$$\tilde{D} = \frac{1}{3} \int dz C_{ij} \delta^{ij}. \quad (\text{C.41})$$

Normalization with the total cross section in Eq. (C.31) gives

$$\frac{1}{\sigma} \frac{d\sigma}{d \cos \varphi} = \frac{1}{2} (1 - D \cos \varphi) \quad (\text{C.42})$$

with

$$\begin{aligned} D &= \frac{\kappa_\ell^2}{\sigma} \int dx_a dx_b f_{p,a}(x_a, \mu_F) f_{p,b}(x_b, \mu_F) dz \frac{\beta_t}{8\pi s} \left(\frac{1}{3} C_{ij} \delta^{ij} \right) \\ &= \kappa_\ell^2 \left\langle \frac{4}{3} (\mathbf{S}_t \cdot \mathbf{S}_{\bar{t}}) \right\rangle. \end{aligned} \quad (\text{C.43})$$

Discrete symmetries of the production density matrix and top-quark polarization in the 2HDM

In this part of the appendix we discuss how the transformation properties (Tab. D.1) of the coefficients of the production density matrix given in Sec. 4.1 determine the polarization of top quarks within the type-II 2HDM extension of the SM. As mentioned in Sec. 4.1 the coefficients $b_1^\pm = 0$ and $b_3^\pm = 0$ due to Bose symmetry. In the following we consider the coefficients b_2^\pm which are zero for $|\mathcal{M}_{\phi_j}^{(0)}|^2$ (Eq. (4.7)) and nonzero for $\mathcal{M}_{\phi_{2,3}}^{(0)}$ (Eq. (4.18)).

This can be understood by studying the transformation properties of the production density matrix under CP , P and CPT . The initial gg state in the cms and summed over polarizations and colors is a CP -even state. The final state momentum \mathbf{k}_t in the cms transforms under CP as

$$\mathbf{k}_t \xrightarrow{P} -\mathbf{k}_t \xrightarrow{C} -\mathbf{k}_{\bar{t}} = \mathbf{k}_t. \quad (\text{D.1})$$

Hence, the effect of the CP transformation on the production density matrix is to interchange the spin indices of top and antitop

$$R_{\alpha\alpha',\beta\beta'}^{gg \rightarrow t\bar{t}}(\mathbf{p}, \mathbf{k}) \xrightarrow{CP} R_{\beta\beta',\alpha\alpha'}^{gg \rightarrow t\bar{t}}(\mathbf{p}, \mathbf{k}). \quad (\text{D.2})$$

For the b_2 term of $R^{gg \rightarrow t\bar{t}}$ this implies

$$b_2^+ \hat{k}_i (\sigma_i \otimes \mathbb{1}) + b_2^- \hat{k}_i (\mathbb{1} \otimes \sigma_i) \xrightarrow{CP} b_2^- \hat{k}_i (\sigma_i \otimes \mathbb{1}) + b_2^+ \hat{k}_i (\mathbb{1} \otimes \sigma_i). \quad (\text{D.3})$$

Hence under CP the coefficients b_2^\pm transform as

$$b_2^\pm \xrightarrow{CP} b_2^\mp. \quad (\text{D.4})$$

b_2^\pm can be decomposed into a CP -even and a CP -odd part

$$b_2^{CP\text{-even}} \hat{k}_i [(\sigma_i \otimes \mathbb{1}) + (\mathbb{1} \otimes \sigma_i)] + b_2^{CP\text{-odd}} \hat{k}_i [(\sigma_i \otimes \mathbb{1}) - (\mathbb{1} \otimes \sigma_i)] \quad (\text{D.5})$$

with

$$b_2^{CP\text{-even}} = \frac{1}{2} (b_2^+ + b_2^-) \quad \text{and} \quad b_2^{CP\text{-odd}} = \frac{1}{2} (b_2^+ - b_2^-) \quad (\text{D.6})$$

such that (using Eq. (D.4))

$$b_2^{CP\text{-even}} \xrightarrow{CP} b_2^{CP\text{-even}} \quad \text{and} \quad b_2^{CP\text{-odd}} \xrightarrow{CP} -b_2^{CP\text{-odd}}. \quad (\text{D.7})$$

Table D.1.: Transformation properties of the production density matrix coefficients in the gg channel. $\text{Im}\mathcal{T} = 0$ denotes the absence of absorptive parts in the amplitude. The table is to be read as follows: for example, $b_1^\pm(z) \xrightarrow{CP} b_1^\mp(z)$. Table taken from Ref. [107].

	CP	P	T	CPT	"Bose"
			$\text{Im}\mathcal{T} = 0$	$\text{Im}\mathcal{T} = 0$	
$A(z)$	$A(z)$	$A(z)$	$A(z)$	$A(z)$	$A(-z)$
$b_1^\pm(z)$	$b_1^\mp(z)$	$-b_1^\pm(z)$	$b_1^\pm(z)$	$b_1^\mp(z)$	$-b_1^\pm(-z)$
$b_2^\pm(z)$	$b_2^\mp(z)$	$-b_2^\pm(z)$	$b_2^\pm(z)$	$b_2^\mp(z)$	$b_2^\pm(-z)$
$b_3^\pm(z)$	$b_3^\mp(z)$	$b_3^\pm(z)$	$-b_3^\pm(z)$	$-b_3^\mp(z)$	$-b_3^\pm(-z)$
$c_0(z)$	$c_0(z)$	$c_0(z)$	$c_0(z)$	$c_0(z)$	$c_0(-z)$
$c_1(z)$	$-c_1(z)$	$-c_1(z)$	$-c_1(z)$	$c_1(z)$	$-c_1(-z)$
$c_2(z)$	$-c_2(z)$	$-c_2(z)$	$-c_2(z)$	$c_2(z)$	$c_2(-z)$
$c_3(z)$	$-c_3(z)$	$c_3(z)$	$c_3(z)$	$-c_3(z)$	$-c_3(-z)$
$c_4(z)$	$c_4(z)$	$c_4(z)$	$c_4(z)$	$c_4(z)$	$c_4(-z)$
$c_5(z)$	$c_5(z)$	$c_5(z)$	$c_5(z)$	$c_5(z)$	$c_5(-z)$
$c_6(z)$	$c_6(z)$	$c_6(z)$	$c_6(z)$	$c_6(z)$	$-c_6(-z)$
$c_7(z)$	$c_7(z)$	$-c_7(z)$	$-c_7(z)$	$-c_7(z)$	$c_7(-z)$
$c_8(z)$	$c_8(z)$	$-c_8(z)$	$-c_8(z)$	$-c_8(z)$	$-c_8(-z)$

The transformation of the production density matrix under P is given by

$$R_{\alpha\alpha',\beta\beta'}^{gg\rightarrow t\bar{t}}(\hat{\mathbf{p}}, \hat{\mathbf{k}}) = R_{\alpha\alpha',\beta\beta'}^{gg\rightarrow t\bar{t}}(-\hat{\mathbf{p}}, -\hat{\mathbf{k}}) \quad (\text{D.8})$$

and explicitly for the b_2^\pm terms

$$b_2^+ k_i (\sigma_i \otimes \mathbb{1}) + b_2^- k_i (\mathbb{1} \otimes \sigma_i) \xrightarrow{P} -b_2^+ k_i (\sigma_i \otimes \mathbb{1}) - b_2^- k_i (\mathbb{1} \otimes \sigma_i) . \quad (\text{D.9})$$

The transformation of the coefficients b_2^\pm is then given by

$$b_2^\pm \xrightarrow{P} -b_2^\pm \quad (\text{D.10})$$

or respectively

$$b_2^{CP\text{-even}} \xrightarrow{P} -b_2^{CP\text{-even}} , \quad b_2^{CP\text{-odd}} \xrightarrow{P} -b_2^{CP\text{-odd}} . \quad (\text{D.11})$$

This shows that P has to be violated to yield nonzero values for both the CP -even and the CP -odd part of b_2 . For the CP -even part this means that C has to be violated as well which is not the case in the exchange of neutral Higgs bosons. Hence the CP -even part is zero in both matrix elements $|\mathcal{M}_{\phi_j}^{(0)}|^2$ and $\mathcal{M}_{\phi_{2,3}}^{(0)}$. For the CP -odd part there is an additional requirement if CPT invariance is assumed. Then $b_2^{CP\text{-odd}}$ term must be odd under T as well. Time reversal flips the sign of spins, momenta and imaginary parts

$$\text{Re}[b_2^{CP\text{-odd}}] \hat{k}_i [(\sigma_i \otimes \mathbb{1}) - (\mathbb{1} \otimes \sigma_i)] \xrightarrow{T} \text{Re}[b_2^{CP\text{-odd}}] \hat{k}_i [(\sigma_i \otimes \mathbb{1}) - (\mathbb{1} \otimes \sigma_i)] , \quad (\text{D.12})$$

$$\text{Im}[b_2^{CP\text{-odd}}] \hat{k}_i [(\sigma_i \otimes \mathbb{1}) - (\mathbb{1} \otimes \sigma_i)] \xrightarrow{T} -\text{Im}[b_2^{CP\text{-odd}}] \hat{k}_i [(\sigma_i \otimes \mathbb{1}) - (\mathbb{1} \otimes \sigma_i)] . \quad (\text{D.13})$$

Hence only the imaginary part is odd under T such that when CPT invariance is assumed $b_2^{CP\text{-odd}}$ can only be nonzero if there are absorptive parts in the amplitude. The matrix element $|\mathcal{M}_{\phi_j}^{(0)}|^2$ factorizes into the production of a Higgs boson and its decay into $t\bar{t}$. Since the production of the scalar component of the Higgs boson and the pseudoscalar component do not interfere $|\mathcal{M}_{\phi_j}^{(0)}|^2$ contains only the terms $|\widetilde{F}_j^S|^2$ and $|\widetilde{F}_j^P|^2$ without imaginary parts. Hence also $b_2^{CP\text{-odd}}$ vanishes for $|\mathcal{M}_{\phi_j}^{(0)}|^2$. In the interference $\mathcal{M}_{\phi_{2,3}}^{(0)}$ between the two heavy Higgs bosons the scalar parts from ϕ_2 and ϕ_3 can interfere as well as the pseudoscalar parts and generate the terms $\widetilde{F}_2^S (\widetilde{F}_3^S)^*$ and $\widetilde{F}_2^P (\widetilde{F}_3^P)^*$ which have imaginary parts. Therefore the coefficient $b_2^{CP\text{-odd}} = 1/2(b_2^+ - b_2^-)$ does not vanish for $\mathcal{M}_{\phi_{2,3}}^{(0)}$ and is proportional to the imaginary parts of $\widetilde{F}_2^S (\widetilde{F}_3^S)^*$ and $\widetilde{F}_2^P (\widetilde{F}_3^P)^*$. Hence, $\mathcal{M}_{\phi_{2,3}}^{(0)}$ can contribute to the polarization of top and antitop quarks in the CPV type-II 2HDM.

Optimal spin correlations

A method to determine the $t\bar{t}$ spin correlation which yields the maximal S/B ratio for heavy Higgs effects in $t\bar{t}$ production is presented in Sec. 4.2.4. A graphical representation of the results in the scenario specified in Eq. (4.70)

$$\begin{aligned} \tan\beta &= 1, & \alpha_1 &= \beta, & \alpha_2 &= \alpha_3 = 0 \\ m_1 &= 125\text{GeV}, & m_3 &= m_2 + 100\text{GeV} \end{aligned} \quad (\text{E.1})$$

is shown in Figs. 4.13–4.15. In this appendix the numerical values corresponding to these figures are presented in Tabs. E.1–E.3. Besides the results for δC_{max} , $C_{\text{max}}^{M_{t\bar{t}}}$ and $\delta\sigma_{\text{max}}^{M_{t\bar{t}}}$ (for a definition see Sec. 4.2.4) also the values of the angles θ and φ are given in the tables presented here. These angles define the spin correlation reference axis which maximizes the S/B of the $M_{t\bar{t}}$ binned observable $C_{\text{max}}^{M_{t\bar{t}}}$. Furthermore, the tables show the $M_{t\bar{t}}$ bin for which $C_{\text{max}}^{M_{t\bar{t}}}$ becomes maximal as well as the value of $C_{\text{max}}^{M_{t\bar{t}}}$ itself. In Tables E.1, E.2 and E.3 results for an $M_{t\bar{t}}$ bin width of $\Delta M_{t\bar{t}} = 50\text{GeV}$, $\Delta M_{t\bar{t}} = 80\text{GeV}$ and $\Delta M_{t\bar{t}} = 100\text{GeV}$, respectively, are presented.

E. Optimal spin correlations

Table E.1.: Spin correlation binned in $M_{\bar{t}\bar{t}}$ with a maximal signal-to-background ratio for an $M_{\bar{t}\bar{t}}$ bin width of $\Delta M_{\bar{t}\bar{t}} = 50$ GeV. For a definition of the observables and angles see Sec. 4.2.4.

	m_2 [GeV]	m_3 [GeV]	θ/π	φ/π	$M_{\bar{t}\bar{t}}(\text{max})$ [GeV]	$\delta C_{\text{max}}^{M_{\bar{t}\bar{t}}}$ [%]	$C_{\text{max}}^{M_{\bar{t}\bar{t}}}$	δC_{max} [%]	$\delta\sigma_{\text{max}}^{M_{\bar{t}\bar{t}}}$ [%]
$C_{\text{min}} = 0.1$									
	400	500	0.64	0.72	490–540	25.0	-0.106	2.7	4.9
	500	600	0.80	0.64	590–640	37.3	0.126	2.6	3.8
	600	700	0.72	0.72	690–740	36.1	0.102	2.1	4.2
	700	800	0.60	0.84	790–840	29.7	0.104	1.6	2.2
	800	900	0.60	0.80	890–940	21.5	0.105	1.3	2.0
	900	1000	0.56	0.04	890–940	19.1	0.114	1.1	1.8
	1000	1100	0.64	0.16	1090–1140	13.4	0.102	0.9	1.8
$C_{\text{min}} = 0.05$									
	400	500	0.80	0.32	490–540	39.4	-0.054	5.5	4.9
	500	600	0.80	0.64	590–640	37.3	0.126	5.0	3.8
	600	700	0.80	0.44	690–740	66.7	0.060	4.1	4.2
	700	800	0.80	0.32	790–840	56.6	0.054	3.2	2.2
	800	900	0.72	0.52	790–840	45.9	-0.053	2.5	2.0
	900	1000	0.72	0.20	990–1040	30.3	0.057	2.0	1.8
	1000	1100	0.72	0.24	1090–1140	26.6	0.051	1.6	1.8
$C_{\text{min}} = 0.01$									
	400	500	0.76	0.52	490–540	58.8	-0.025	34.4	4.9
	500	600	0.76	0.44	590–640	71.5	-0.011	29.4	3.8
	600	700	0.76	0.48	590–640	83.5	-0.046	21.4	4.2
	700	800	0.76	0.44	690–740	109.8	-0.036	15.8	2.2
	800	900	0.76	0.48	890–940	167.3	0.024	13.0	2.0
	900	1000	0.76	0.48	990–1040	105.1	0.023	10.2	1.8
	1000	1100	0.76	0.44	1090–1140	135.3	0.017	8.2	1.8

Table E.2.: Spin correlation binned in $M_{\bar{t}\bar{t}}$ with a maximal signal-to-background ratio for an $M_{\bar{t}\bar{t}}$ bin width of $\Delta M_{\bar{t}\bar{t}} = 80$ GeV. For a definition of the observables and angles see Sec. 4.2.4.

	m_2 [GeV]	m_3 [GeV]	θ/π	φ/π	$M_{\bar{t}\bar{t}}(\text{max})$ [GeV]	$\delta C_{\text{max}}^{M_{\bar{t}\bar{t}}}$ [%]	$C_{\text{max}}^{M_{\bar{t}\bar{t}}}$	δC_{max} [%]	$\delta\sigma_{\text{max}}^{M_{\bar{t}\bar{t}}}$ [%]
$C_{\text{min}} = 0.1$									
	400	500	0.60	0.84	500–580	21.6	-0.113	2.7	3.5
	500	600	0.72	0.56	500–580	33.1	-0.101	2.6	2.8
	600	700	0.88	0.00	660–740	20.3	0.100	2.1	2.3
	700	800	0.64	0.84	740–820	17.2	0.115	1.6	1.8
	800	900	0.56	0.88	820–900	15.0	0.116	1.3	1.6
	900	1000	0.52	0.12	900–980	15.8	0.106	1.1	1.7
	1000	1100	0.52	0.80	1060–1140	14.4	0.102	0.9	1.6
$C_{\text{min}} = 0.05$									
	400	500	0.68	0.68	500–580	35.4	-0.052	5.5	3.5
	500	600	0.76	0.48	500–580	42.5	-0.085	5.0	2.8
	600	700	0.76	0.44	580–660	34.9	-0.052	4.1	2.3
	700	800	0.80	0.44	740–820	21.5	0.053	3.2	1.8
	800	900	0.72	0.64	900–980	17.4	0.053	2.5	1.6
	900	1000	0.68	0.68	980–1060	25.2	0.055	2.0	1.7
	1000	1100	0.64	0.20	1060–1140	26.3	0.058	1.6	1.6
$C_{\text{min}} = 0.01$									
	400	500	0.72	0.60	500–580	46.3	-0.033	34.4	3.5
	500	600	0.76	0.44	580–660	50.5	-0.019	29.4	2.8
	600	700	0.76	0.48	580–660	56.4	-0.038	21.4	2.3
	700	800	0.72	0.56	740–820	45.2	-0.010	15.8	1.8
	800	900	0.76	0.48	900–980	77.0	0.017	13.0	1.6
	900	1000	0.76	0.48	980–1060	89.5	0.021	10.2	1.7
	1000	1100	0.76	0.44	1060–1140	147.2	0.017	8.2	1.6

E. Optimal spin correlations

Table E.3.: Spin correlation binned in $M_{\bar{i}\bar{i}}$ with a maximal signal-to-background ratio for an $M_{\bar{i}\bar{i}}$ bin width of $\Delta M_{\bar{i}\bar{i}} = 100$ GeV. For a definition of the observables and angles see Sec. 4.2.4.

	m_2 [GeV]	m_3 [GeV]	θ/π	φ/π	$M_{\bar{i}\bar{i}}(\text{max})$ [GeV]	$\delta C_{\text{max}}^{M_{\bar{i}\bar{i}}}$ [%]	$C_{\text{max}}^{M_{\bar{i}\bar{i}}}$	δC_{max} [%]	$\delta\sigma_{\text{max}}^{M_{\bar{i}\bar{i}}}$ [%]
$C_{\text{min}} = 0.1$									
	400	500	0.56	0.84	540–640	6.8	-0.126	2.7	2.7
	500	600	0.56	0.84	540–640	9.7	-0.120	2.6	1.9
	600	700	0.72	0.80	640–740	12.9	0.127	2.1	2.0
	700	800	0.64	0.84	740–840	15.9	0.118	1.6	1.7
	800	900	0.52	0.92	840–940	15.6	0.130	1.3	1.5
	900	1000	0.68	0.08	940–1040	15.7	0.100	1.1	1.4
	1000	1100	0.60	0.16	1040–1140	13.7	0.101	0.9	1.2
$C_{\text{min}} = 0.05$									
	400	500	0.68	0.64	540–640	8.9	-0.062	5.5	2.7
	500	600	0.64	0.72	540–640	9.9	-0.073	5.0	1.9
	600	700	0.76	0.64	640–740	15.0	0.076	4.1	2.0
	700	800	0.80	0.44	740–840	20.7	0.054	3.2	1.7
	800	900	0.72	0.64	840–940	24.4	0.052	2.5	1.5
	900	1000	0.76	0.24	940–1040	25.6	0.052	2.0	1.4
	1000	1100	0.76	0.28	1040–1140	22.9	0.052	1.6	1.2
$C_{\text{min}} = 0.01$									
	400	500	0.76	0.48	540–640	15.5	-0.030	34.4	2.7
	500	600	0.76	0.44	640–740	13.0	-0.019	29.4	1.9
	600	700	0.76	0.44	640–740	32.4	-0.015	21.4	2.0
	700	800	0.64	0.68	740–840	31.5	-0.022	15.8	1.7
	800	900	0.72	0.60	840–940	78.6	0.021	13.0	1.5
	900	1000	0.76	0.48	940–1040	82.3	0.020	10.2	1.4
	1000	1100	0.76	0.44	1040–1140	126.1	0.015	8.2	1.2

Cancellation of real and virtual nonfactorizable corrections in the soft gluon approximation

This appendix follows largely along the lines of appendix B in Ref. [77].

In the following an example for the cancellation of real and virtual nonfactorizable corrections in the SGA is given. Specifically, the interference depicted in Fig. F.1 is considered. The red dotted cut corresponds to a real correction realized by the interference of a QCD diagram and a diagram involving a heavy Higgs boson each with the emission of an additional gluon. The blue dotted cut corresponds to a virtual correction, the interference of the type of diagram depicted in Fig. 5.3 b and a LO QCD diagram. At first the virtual correction is evaluated in the SGA. In this approximation the additional gluon momentum q is completely neglected in the numerator and wherever possible in the denominator. The gluon momentum is identified with the loop momentum, $q = \ell$. Hence, the corresponding loop integral reduces to the scalar integral

$$I = \int \frac{d^4\ell}{(2\pi)^4} \frac{1}{[\ell^2 + i\epsilon][-2\ell \cdot p_1 + i\epsilon][-2\ell \cdot (p_1 + p_2) + s - m_\phi^2 + i\epsilon][-2\ell \cdot k_1 + i\epsilon]}. \quad (\text{F.1})$$

The momenta of the incoming gluons are denoted p_1 and p_2 , and k_1 is the momentum of the outgoing top quark. In the denominator the ℓ^2 terms have been neglected in the last three propagators. The integration over the ℓ^0 component is performed in the complex ℓ^0 plane using the residue theorem. Closing the contour in the lower half of the plane the residue of

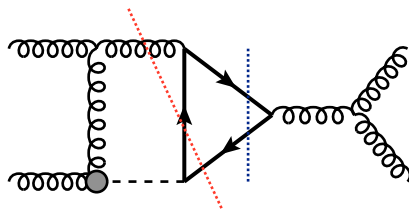


Figure F.1.: Example for the cancellation of real and virtual contributions in the SGA. The red dotted cut corresponds to the real correction and the blue dotted cut corresponds to the virtual correction.

F. Cancellation of real and virtual nonfactorizable corrections in the soft gluon approximation

the pole of the first propagator in Eq. (F.1) is picked up. The location of the poles of the other propagators is in the upper half of the ℓ^0 plane. The following result is obtained for the integral

$$\begin{aligned}
I &= -i \int \frac{d^3\ell}{(2\pi)^3} \frac{1}{2|\ell|} \frac{1}{[-2|\ell|p_1^0 + 2\ell \cdot \mathbf{p}_1 + i\varepsilon]} \\
&\times \frac{1}{[-2|\ell|(p_1^0 + p_2^0) + 2\ell(\mathbf{p}_1 + \mathbf{p}_2) + s - m_\phi^2 + i\varepsilon][-2|\ell|k_1^0 + 2\ell \cdot \mathbf{k}_1 + i\varepsilon]} \\
&= i \int \frac{d^3\ell}{(2\pi)^3} \frac{1}{2\ell^0} \frac{1}{[-2\ell \cdot p_1 + i\varepsilon][-2\ell \cdot (p_1 + p_2) + s - m_\phi^2 + i\varepsilon][2\ell \cdot k_1 - i\varepsilon]} \quad (\text{F.2})
\end{aligned}$$

with $|\ell| = \ell^0$. The integration measure $d^3\ell/[(2\pi)^3 2\ell^0]$ is identical to the Lorentz invariant phase-space measure of the gluon.

The real interference term indicated by the red dotted cut in Fig. F.1 has the following propagator structure in the SGA

$$\frac{1}{[-2q \cdot p_1 + i\varepsilon][-2q \cdot (p_1 + p_2) + s - m_\phi^2 + i\varepsilon][2q \cdot k_1 - i\varepsilon]}, \quad (\text{F.3})$$

where q is the four-momentum of the (soft) gluon. Here the propagator $[(p_1 + p_2)^2 + i\varepsilon]^{-1}$ from the QCD real radiation diagram is omitted because it does not depend on q . Taking the phase-space integration over the additional gluon momentum q into account gives

$$R = \int \frac{d^3q}{(2\pi)^3} \frac{1}{2q^0} \frac{1}{[-2q \cdot p_1 + i\varepsilon][-2q \cdot (p_1 + p_2) + s - m_\phi^2 + i\varepsilon][2q \cdot k_1 - i\varepsilon]}. \quad (\text{F.4})$$

This leads to the relation

$$I = iR. \quad (\text{F.5})$$

So far only the q, ℓ -dependent denominators were investigated and the numerators of the amplitudes (including the additional propagator) were ignored. Let us denote the virtual interference by

$$\delta\mathcal{M}_V = IN_{\text{virt}}, \quad (\text{F.6})$$

where N_{virt} includes all so far neglected terms in the numerator of the virtual interference in Fig. F.1 in the SGA and the propagator $[(p_1 + p_2)^2 + i\varepsilon]^{-1}$. The real interference is denoted by

$$\delta\mathcal{M}_R = RN_{\text{real}}, \quad (\text{F.7})$$

where N_{real} includes all so far neglected terms in the numerator of the real interference in Fig. F.1 in the SGA and the propagator $[(p_1 + p_2)^2 + i\varepsilon]^{-1}$. A straightforward explicit calculation then reveals that

$$N_{\text{virt}} = iN_{\text{real}} \quad (\text{F.8})$$

such that

$$\delta\mathcal{M}_V = IN_{\text{virt}} = iRN_{\text{virt}} = -RN_{\text{real}} = -\delta\mathcal{M}_R. \quad (\text{F.9})$$

The real and virtual corrections are equal but have opposite signs and therefore cancel each other

$$\delta\mathcal{M}_V + \delta\mathcal{M}_R = 0. \quad (\text{F.10})$$

Note that

$$\delta^{(4)}(p_1 + p_2 - k_1 - k_2 - q) \xrightarrow{\text{SGA}} \delta^{(4)}(p_1 + p_2 - k_1 - k_2) \quad (\text{F.11})$$

such that the four-momentum conservation of real and virtual contributions match in the SGA.

Top quark pair invariant mass distribution for scenarios 1a–1c

In this appendix the $M_{t\bar{t}}$ distributions in the scenarios 1a–1c are presented. They are used to

- determine the position of the $M_{t\bar{t}}$ bins containing peak and dip of resonance structure generated by the 400 GeV Higgs boson in scenarios 1a–1c and
- compare the sensitivity of heavy Higgs boson contributions to $t\bar{t}$ production with the sensitivity of spin dependent observables studied in Sec. 5.4.2.

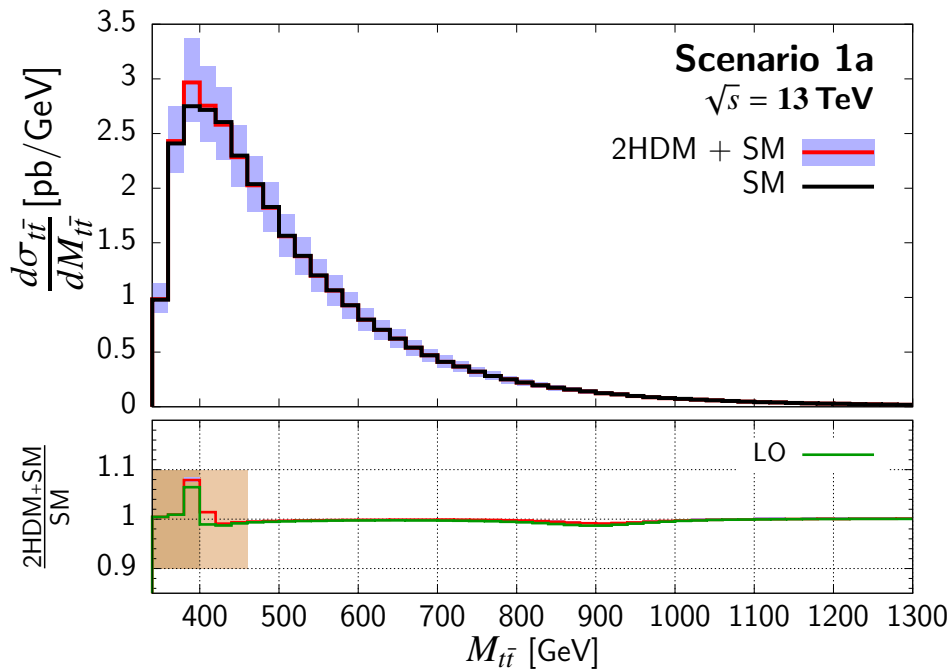


Figure G.1.: Distribution of the $t\bar{t}$ invariant mass for scenario 1a at NLO. Upper panel: $M_{t\bar{t}}$ distribution for the SM including NLO QCD and weak corrections (black). $M_{t\bar{t}}$ distribution for the sum of SM contribution and the contribution involving the neutral heavy Higgs bosons including the Higgs-QCD interference at NLO QCD (red). Lower panel: signal-to-background ratio at NLO (red) and LO (green).

G. Top quark pair invariant mass distribution for scenarios 1a–1c

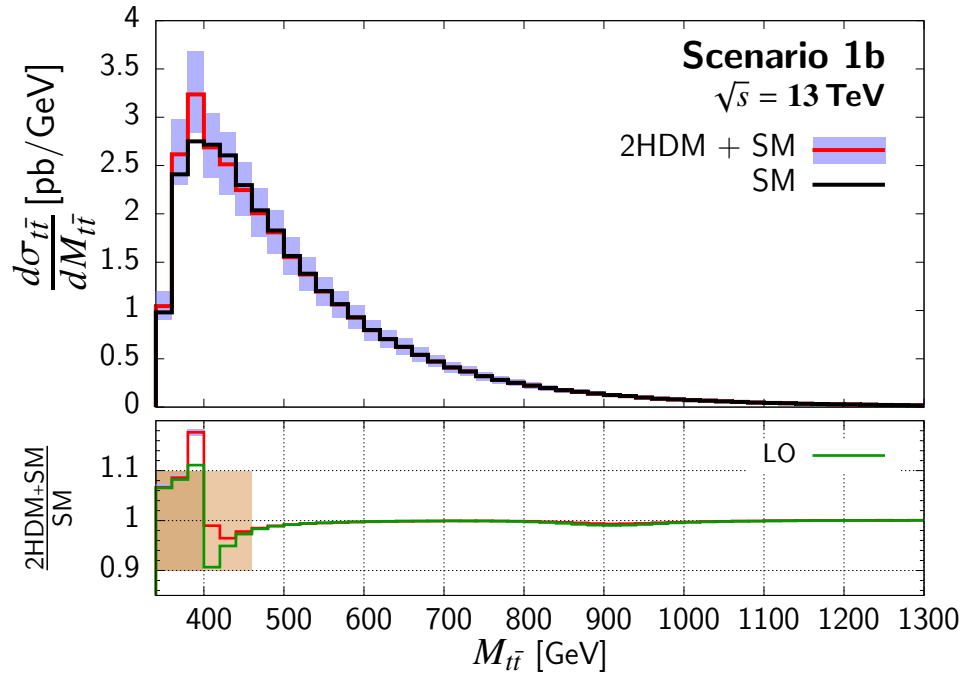


Figure G.2.: Same as Fig. G.1 but for scenario 1b.

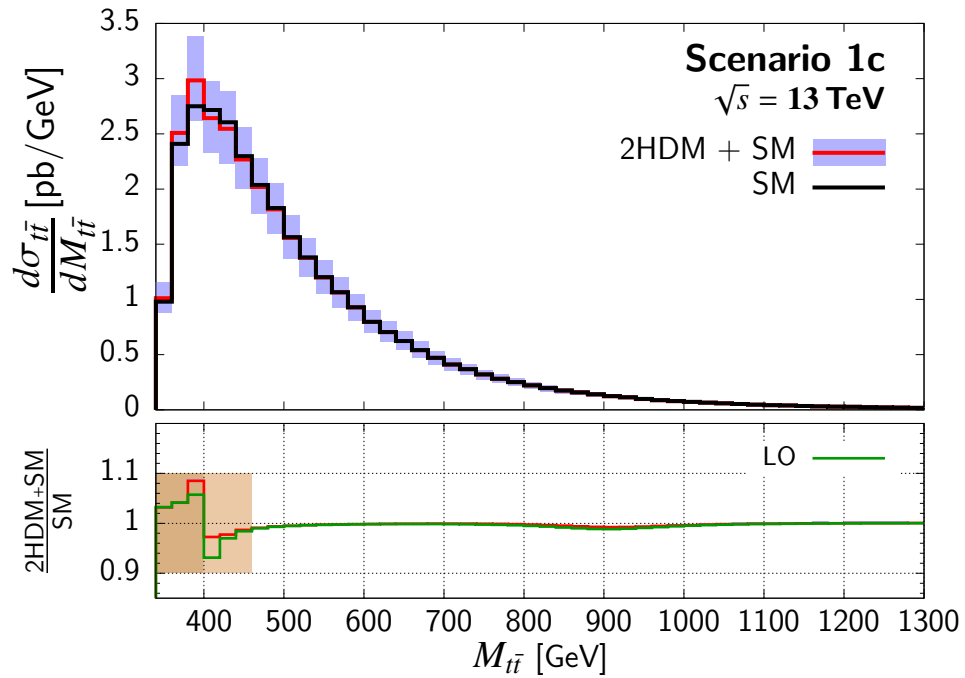


Figure G.3.: Same as Fig. G.1 but for scenario 1c.

Numerical results for C_{hel} , C_{nn} , C_{rr} and D in scenarios Ia–Ic

In the following the numerical results for the spin correlation observables C_{hel} , C_{nn} , C_{rr} and D studied at NLO QCD in Sec. 5.4.2 for the scenarios Ia–Ic are presented. The Tabs. H.1–H.3 correspond to Figs. 5.26–5.28, respectively. In addition to the results presented graphically in Sec. 5.4.2 where $M_{\bar{t}\bar{t}}$ cuts were applied the tables shown here also contain results for the observables evaluated inclusively in $M_{\bar{t}\bar{t}}$. For most of the observables an increased sensitivity is observed in the $M_{\bar{t}\bar{t}}$ bin that contains the peak in the $d\sigma/dM_{\bar{t}\bar{t}}$ distribution.

H. Numerical results for C_{hel} , C_{nn} , C_{rr} and D in scenarios Ia–Ic

Table H.1.: Spin correlations in scenario Ia.

		C_{hel}	C_{nn}	C_{rr}	D	$\sigma_{\bar{t}t} \times BR$ [pb]
$2m_t \leq M_{\bar{t}t} \leq 400$ GeV						
LO	2HDM+QCD	$0.576^{+0.011}_{-0.011}$	$0.483^{+0.005}_{-0.005}$	$0.252^{+0.010}_{-0.010}$	$-0.437^{+0.009}_{-0.009}$	$3.70^{+0.89}_{-0.68}$
	QCD	$0.562^{+0.011}_{-0.011}$	$0.528^{+0.005}_{-0.005}$	$0.289^{+0.011}_{-0.011}$	$-0.459^{+0.009}_{-0.009}$	$3.58^{+0.85}_{-0.65}$
	$\frac{2HDM}{QCD}$ [%]	$2.52^{+0.08}_{-0.08}$	$-8.52^{+0.06}_{-0.07}$	$-12.9^{+0.2}_{-0.2}$	$-4.93^{+0.03}_{-0.04}$	$3.35^{+0.05}_{-0.05}$
NLO	2HDM+QCDW	$0.567^{+0.008}_{-0.010}$	$0.462^{+0.006}_{-0.008}$	$0.278^{+0.005}_{-0.005}$	$-0.435^{+0.007}_{-0.007}$	$6.30^{+0.86}_{-0.76}$
	QCDW	$0.548^{+0.009}_{-0.011}$	$0.522^{+0.004}_{-0.005}$	$0.330^{+0.003}_{-0.002}$	$-0.466^{+0.006}_{-0.005}$	$6.06^{+0.81}_{-0.73}$
	$\frac{2HDM}{QCDW}$ [%]	$3.38^{+0.28}_{-0.17}$	$-11.5^{+0.5}_{-0.7}$	$-15.6^{+0.7}_{-0.9}$	$-6.64^{+0.33}_{-0.41}$	$3.97^{+0.24}_{-0.18}$
$400 \leq M_{\bar{t}t} \leq 460$ GeV						
LO	2HDM+QCD	$0.426^{+0.009}_{-0.009}$	$0.374^{+0.002}_{-0.002}$	$0.060^{+0.006}_{-0.006}$	$-0.286^{+0.006}_{-0.006}$	$4.49^{+1.10}_{-0.86}$
	QCD	$0.432^{+0.009}_{-0.009}$	$0.356^{+0.002}_{-0.002}$	$0.045^{+0.006}_{-0.006}$	$-0.278^{+0.006}_{-0.006}$	$4.54^{+1.10}_{-0.87}$
	$\frac{2HDM}{QCD}$ [%]	$-1.43^{+0.04}_{-0.04}$	$5.01^{+0.03}_{-0.03}$	$32.1^{+5.0}_{-3.0}$	$3.14^{+0.01}_{-0.01}$	$-1.08^{+0.01}_{-0.01}$
NLO	2HDM+QCDW	$0.430^{+0.008}_{-0.008}$	$0.356^{+0.001}_{-0.001}$	$0.103^{+0.005}_{-0.004}$	$-0.296^{+0.001}_{-0.001}$	$7.52^{+0.98}_{-0.91}$
	QCDW	$0.426^{+0.007}_{-0.007}$	$0.362^{+0.001}_{-0.000}$	$0.107^{+0.004}_{-0.003}$	$-0.298^{+0.001}_{-0.001}$	$7.53^{+0.98}_{-0.91}$
	$\frac{2HDM}{QCDW}$ [%]	$0.959^{+0.219}_{-0.150}$	$-1.76^{+0.39}_{-0.47}$	$-3.34^{+1.00}_{-1.30}$	$-0.651^{+0.194}_{-0.222}$	$-0.017^{+0.031}_{-0.012}$
incl. in $M_{\bar{t}t}$						
LO	2HDM+QCD	$0.298^{+0.003}_{-0.004}$	$0.328^{+0.000}_{-0.000}$	$-0.017^{+0.002}_{-0.003}$	$-0.203^{+0.002}_{-0.002}$	$18.7^{+5.0}_{-4.0}$
	QCD	$0.297^{+0.003}_{-0.004}$	$0.329^{+0.000}_{-0.001}$	$-0.017^{+0.002}_{-0.003}$	$-0.203^{+0.002}_{-0.002}$	$18.6^{+5.0}_{-4.0}$
	$\frac{2HDM}{QCD}$ [%]	$0.313^{+0.029}_{-0.031}$	$-0.277^{+0.022}_{-0.019}$	$2.67^{+0.19}_{-0.21}$	$-0.071^{+0.005}_{-0.004}$	$0.133^{+0.009}_{-0.011}$
NLO	2HDM+QCDW	$0.339^{+0.004}_{-0.002}$	$0.317^{+0.002}_{-0.002}$	$0.059^{+0.006}_{-0.004}$	$-0.238^{0.000}_{-0.001}$	$30.5^{+4.0}_{-4.0}$
	QCDW	$0.333^{+0.003}_{-0.002}$	$0.327^{+0.001}_{-0.001}$	$0.065^{+0.006}_{-0.004}$	$-0.242^{0.000}_{-0.001}$	$30.3^{+4.0}_{-4.0}$
	$\frac{2HDM}{QCDW}$ [%]	$1.99^{+0.03}_{-0.03}$	$-2.95^{+0.10}_{-0.13}$	$-9.98^{+0.17}_{-0.09}$	$-1.31^{+0.11}_{-0.14}$	$0.631^{+0.044}_{-0.027}$

Table H.2.: Spin correlations in scenario Ib.

		C_{hel}	C_{nn}	C_{rr}	D	$\sigma_{t\bar{t}} \times \text{BR}$ [pb]
$2m_t \leq M_{t\bar{t}} \leq 400$ GeV						
LO	2HDM+QCD	$0.599^{+0.011}_{-0.011}$	$0.567^{+0.005}_{-0.005}$	$0.349^{+0.011}_{-0.010}$	$-0.505^{+0.009}_{-0.009}$	$3.91^{+0.94}_{-0.72}$
	QCD	$0.562^{+0.011}_{-0.011}$	$0.528^{+0.005}_{-0.005}$	$0.289^{+0.011}_{-0.011}$	$-0.459^{+0.009}_{-0.009}$	$3.58^{+0.85}_{-0.65}$
	$\frac{2\text{HDM}}{\text{QCD}}$ [%]	$6.61^{+0.23}_{-0.22}$	$7.51^{+0.08}_{-0.08}$	$20.7^{+0.9}_{-0.8}$	$9.92^{+0.26}_{-0.25}$	$9.28^{+0.12}_{-0.11}$
NLO	2HDM+QCDW	$0.605^{+0.008}_{-0.009}$	$0.582^{+0.003}_{-0.003}$	$0.416^{+0.001}_{+0.000}$	$-0.534^{+0.004}_{-0.004}$	$6.81^{+0.95}_{-0.84}$
	QCDW	$0.548^{+0.009}_{-0.011}$	$0.522^{+0.004}_{-0.005}$	$0.330^{+0.003}_{-0.002}$	$-0.466^{+0.006}_{-0.005}$	$6.06^{+0.81}_{-0.73}$
	$\frac{2\text{HDM}}{\text{QCDW}}$ [%]	$10.3^{+0.6}_{-0.4}$	$11.4^{+0.5}_{-0.3}$	$26.2^{+0.9}_{-0.7}$	$14.5^{+0.7}_{-0.5}$	$12.3^{+0.5}_{-0.5}$
$400 \leq M_{t\bar{t}} \leq 460$ GeV						
LO	2HDM+QCD	$0.396^{+0.009}_{-0.009}$	$0.315^{+0.002}_{-0.002}$	$-0.016^{+0.006}_{-0.006}$	$-0.232^{+0.006}_{-0.006}$	$4.28^{+1.10}_{-0.81}$
	QCD	$0.432^{+0.009}_{-0.009}$	$0.356^{+0.002}_{-0.002}$	$0.045^{+0.006}_{-0.006}$	$-0.278^{+0.006}_{-0.006}$	$4.54^{+1.10}_{-0.87}$
	$\frac{2\text{HDM}}{\text{QCD}}$ [%]	$-8.20^{+0.22}_{-0.23}$	$-11.6^{0.0}_{-0.0}$	-134^{+16}_{-21}	$-16.5^{+0.3}_{-0.3}$	$-5.87^{+0.05}_{-0.05}$
NLO	2HDM+QCDW	$0.429^{+0.012}_{-0.013}$	$0.366^{+0.005}_{-0.005}$	$0.116^{+0.004}_{-0.004}$	$-0.304^{+0.008}_{-0.007}$	$7.36^{+0.96}_{-0.88}$
	QCDW	$0.426^{+0.007}_{-0.007}$	$0.362^{+0.001}_{-0.000}$	$0.107^{+0.004}_{-0.003}$	$-0.298^{+0.001}_{-0.001}$	$7.53^{+0.98}_{-0.91}$
	$\frac{2\text{HDM}}{\text{QCDW}}$ [%]	$0.844^{+1.150}_{-1.370}$	$1.06^{+1.30}_{-1.50}$	$8.39^{+7.00}_{-7.20}$	$1.83^{+1.90}_{-2.10}$	$-2.25^{+0.09}_{-0.04}$
incl. in $M_{t\bar{t}}$						
LO	2HDM+QCD	$0.297^{+0.003}_{-0.004}$	$0.329^{+0.000}_{-0.001}$	$-0.017^{+0.002}_{-0.002}$	$-0.203^{+0.002}_{-0.002}$	$18.7^{+5.0}_{-4.0}$
	QCD	$0.297^{+0.003}_{-0.004}$	$0.329^{+0.000}_{-0.001}$	$-0.017^{+0.002}_{-0.003}$	$-0.203^{+0.002}_{-0.002}$	$18.6^{+5.0}_{-4.0}$
	$\frac{2\text{HDM}}{\text{QCD}}$ [%]	$0.043^{+0.042}_{-0.045}$	$-0.032^{+0.026}_{-0.029}$	$0.261^{+1.140}_{-0.781}$	$-0.004^{+0.059}_{-0.064}$	$0.018^{+0.017}_{-0.019}$
NLO	2HDM+QCDW	$0.351^{+0.004}_{-0.003}$	$0.343^{+0.002}_{-0.002}$	$0.090^{+0.006}_{-0.004}$	$-0.261^{0.000}_{-0.001}$	$30.8^{+4.0}_{-4.0}$
	QCDW	$0.333^{+0.003}_{-0.002}$	$0.327^{+0.001}_{-0.001}$	$0.065^{+0.006}_{-0.004}$	$-0.242^{0.000}_{-0.001}$	$30.3^{+4.0}_{-4.0}$
	$\frac{2\text{HDM}}{\text{QCDW}}$ [%]	$5.41^{+0.17}_{-0.17}$	$4.97^{+0.10}_{-0.08}$	$38.4^{+4.0}_{-4.0}$	$8.18^{+0.26}_{-0.26}$	$1.57^{+0.12}_{-0.07}$

H. Numerical results for C_{hel} , C_{nn} , C_{rr} and D in scenarios Ia–Ic

Table H.3.: Spin correlations in scenario Ic.

		C_{hel}	C_{nn}	C_{rr}	D	$\sigma_{i\bar{i}} \times BR$ [pb]
$2m_t \leq M_{i\bar{i}} \leq 400$ GeV						
LO	2HDM+QCD	$0.582^{+0.011}_{-0.011}$	$0.539^{+0.005}_{-0.005}$	$0.311^{+0.011}_{-0.010}$	$-0.477^{+0.009}_{-0.009}$	$3.75^{+0.90}_{-0.68}$
	QCD	$0.562^{+0.011}_{-0.011}$	$0.528^{+0.005}_{-0.005}$	$0.289^{+0.011}_{-0.011}$	$-0.459^{+0.009}_{-0.009}$	$3.58^{+0.85}_{-0.65}$
	$\frac{2HDM}{QCD}$ [%]	$3.51^{+0.12}_{-0.12}$	$2.21^{+0.05}_{-0.05}$	$7.78^{+0.38}_{-0.36}$	$3.91^{+0.13}_{-0.12}$	$4.73^{+0.06}_{-0.06}$
NLO	2HDM+QCDW	$0.577^{+0.008}_{-0.010}$	$0.539^{+0.004}_{-0.005}$	$0.360^{+0.002}_{-0.002}$	$-0.492^{+0.005}_{-0.005}$	$6.42^{+0.87}_{-0.78}$
	QCDW	$0.548^{+0.009}_{-0.011}$	$0.522^{+0.004}_{-0.005}$	$0.330^{+0.003}_{-0.002}$	$-0.466^{+0.006}_{-0.005}$	$6.06^{+0.81}_{-0.73}$
	$\frac{2HDM}{QCDW}$ [%]	$5.18^{+0.29}_{-0.29}$	$3.32^{+0.10}_{-0.07}$	$9.24^{+0.22}_{-0.21}$	$5.45^{+0.21}_{-0.18}$	$5.93^{+0.27}_{-0.20}$
$400 \leq M_{i\bar{i}} \leq 460$ GeV						
LO	2HDM+QCD	$0.408^{+0.009}_{-0.009}$	$0.337^{+0.002}_{-0.002}$	$0.013^{+0.006}_{-0.006}$	$-0.253^{+0.006}_{-0.006}$	$4.36^{+1.10}_{-0.83}$
	QCD	$0.432^{+0.009}_{-0.009}$	$0.356^{+0.002}_{-0.002}$	$0.045^{+0.006}_{-0.006}$	$-0.278^{+0.006}_{-0.006}$	$4.54^{+1.10}_{-0.87}$
	$\frac{2HDM}{QCD}$ [%]	$-5.41^{+0.15}_{-0.15}$	$-5.47^{+0.01}_{-0.01}$	$-71.7^{+9.0}_{-12.0}$	$-9.02^{+0.19}_{-0.20}$	$-3.95^{+0.03}_{-0.03}$
NLO	2HDM+QCDW	$0.421^{+0.010}_{-0.010}$	$0.356^{+0.003}_{-0.002}$	$0.100^{+0.001}_{+0.000}$	$-0.293^{+0.004}_{-0.004}$	$7.36^{+0.95}_{-0.88}$
	QCDW	$0.426^{+0.007}_{-0.007}$	$0.362^{+0.001}_{-0.000}$	$0.107^{+0.004}_{-0.003}$	$-0.298^{+0.001}_{-0.001}$	$7.53^{+0.98}_{-0.91}$
	$\frac{2HDM}{QCDW}$ [%]	$-1.15^{+0.67}_{-0.74}$	$-1.65^{+0.55}_{-0.61}$	$-6.02^{+3.00}_{-3.00}$	$-1.91^{+0.88}_{-1.00}$	$-2.15^{+0.08}_{-0.09}$
incl. in $M_{i\bar{i}}$						
LO	2HDM+QCD	$0.295^{+0.003}_{-0.004}$	$0.328^{+0.000}_{-0.001}$	$-0.019^{+0.002}_{-0.003}$	$-0.201^{+0.002}_{-0.002}$	$18.6^{+5.0}_{-4.0}$
	QCD	$0.297^{+0.003}_{-0.004}$	$0.329^{+0.000}_{-0.001}$	$-0.017^{+0.002}_{-0.003}$	$-0.203^{+0.002}_{-0.002}$	$18.6^{+5.0}_{-4.0}$
	$\frac{2HDM}{QCD}$ [%]	$-0.735^{+0.009}_{-0.013}$	$-0.294^{+0.006}_{-0.007}$	$12.0^{+2.0}_{-2.0}$	$-0.853^{+0.011}_{-0.015}$	$-0.310^{+0.010}_{-0.011}$
NLO	2HDM+QCDW	$0.339^{+0.004}_{-0.003}$	$0.331^{+0.002}_{-0.001}$	$0.073^{+0.006}_{-0.004}$	$-0.248^{0.000}_{-0.001}$	$30.5^{+4.0}_{-4.0}$
	QCDW	$0.333^{+0.003}_{-0.002}$	$0.327^{+0.001}_{-0.001}$	$0.065^{+0.006}_{-0.004}$	$-0.242^{0.000}_{-0.001}$	$30.3^{+4.0}_{-4.0}$
	$\frac{2HDM}{QCDW}$ [%]	$2.01^{+0.16}_{-0.17}$	$1.21^{+0.09}_{-0.09}$	$11.4^{+2.0}_{-2.0}$	$2.49^{+0.20}_{-0.21}$	$0.442^{+0.033}_{-0.017}$

Bibliography

- [1] S. Weinberg, *A Model of Leptons*, Phys. Rev. Lett. **19** (1967) 1264–1266.
- [2] A. Salam, *Weak and Electromagnetic Interactions*, Conf. Proc. **C680519** (1968) 367–377.
- [3] D. J. Gross and F. Wilczek, *Ultraviolet Behavior of Nonabelian Gauge Theories*, Phys. Rev. Lett. **30** (1973) 1343–1346.
- [4] D. J. Gross and F. Wilczek, *Asymptotically Free Gauge Theories. 1*, Phys. Rev. **D8** (1973) 3633–3652.
- [5] D. J. Gross and F. Wilczek, *ASYMPTOTICALLY FREE GAUGE THEORIES. 2.*, Phys. Rev. **D9** (1974) 980–993.
- [6] ATLAS Collaboration, G. Aad et al., *Observation of a new particle in the search for the Standard Model Higgs boson with the ATLAS detector at the LHC*, Phys. Lett. **B716** (2012) 1–29, arXiv:1207.7214 [hep-ex].
- [7] CMS Collaboration, S. Chatrchyan et al., *Observation of a new boson at a mass of 125 GeV with the CMS experiment at the LHC*, Phys. Lett. **B716** (2012) 30–61, arXiv:1207.7235 [hep-ex].
- [8] CMS Collaboration, V. Khachatryan et al., *Precise determination of the mass of the Higgs boson and tests of compatibility of its couplings with the standard model predictions using proton collisions at 7 and 8 TeV*, Eur. Phys. J. **C75** no. 5, (2015) 212, arXiv:1412.8662 [hep-ex].
- [9] ATLAS Collaboration, G. Aad et al., *Measurements of the Higgs boson production and decay rates and coupling strengths using pp collision data at $\sqrt{s} = 7$ and 8 TeV in the ATLAS experiment*, Eur. Phys. J. **C76** no. 1, (2016) 6, arXiv:1507.04548 [hep-ex].
- [10] F. Englert and R. Brout, *Broken Symmetry and the Mass of Gauge Vector Mesons*, Phys. Rev. Lett. **13** (1964) 321–323.
- [11] P. W. Higgs, *Broken Symmetries and the Masses of Gauge Bosons*, Phys. Rev. Lett. **13** (1964) 508–509.
- [12] G. S. Guralnik, C. R. Hagen, and T. W. B. Kibble, *Global Conservation Laws and Massless Particles*, Phys. Rev. Lett. **13** (1964) 585–587.

Bibliography

- [13] G. Apollinari, O. Brüning, T. Nakamoto, and L. Rossi, *High Luminosity Large Hadron Collider HL-LHC*, CERN Yellow Report no. 5, (2015) 1–19, arXiv:1705.08830 [physics.acc-ph].
- [14] W. N. Cottingham and D. A. Greenwood, *An introduction to the standard model of particle physics*. Cambridge University Press, 2007.
- [15] M. D. Schwartz, *Quantum Field Theory and the Standard Model*. Cambridge University Press, 2014. <http://www.cambridge.org/us/academic/subjects/physics/theoretical-physics-and-mathematical-physics/quantum-field-theory-and-standard-model>.
- [16] Super-Kamiokande Collaboration, Y. Fukuda et al., *Evidence for oscillation of atmospheric neutrinos*, Phys. Rev. Lett. **81** (1998) 1562–1567, arXiv:hep-ex/9807003 [hep-ex].
- [17] SNO Collaboration, Q. R. Ahmad et al., *Measurement of the rate of $\nu_e + d \rightarrow p + p + e^-$ interactions produced by 8B solar neutrinos at the Sudbury Neutrino Observatory*, Phys. Rev. Lett. **87** (2001) 071301, arXiv:nucl-ex/0106015 [nucl-ex].
- [18] SNO Collaboration, Q. R. Ahmad et al., *Direct evidence for neutrino flavor transformation from neutral current interactions in the Sudbury Neutrino Observatory*, Phys. Rev. Lett. **89** (2002) 011301, arXiv:nucl-ex/0204008 [nucl-ex].
- [19] J. D. Bjorken and S. D. Drell, *Relativistic quantum fields*,.
- [20] C. Itzykson and J. B. Zuber, *Quantum Field Theory*. International Series In Pure and Applied Physics. McGraw-Hill, New York, 1980. <http://dx.doi.org/10.1063/1.2916419>.
- [21] S. Weinberg, *The Quantum theory of fields. Vol. 1: Foundations*. Cambridge University Press, 2005.
- [22] S. Weinberg, *The quantum theory of fields. Vol. 2: Modern applications*. Cambridge University Press, 2013.
- [23] M. E. Peskin and D. V. Schroeder, *An Introduction to quantum field theory*. Addison-Wesley, Reading, USA, 1995. <http://www.slac.stanford.edu/~mpeskin/QFT.html>.
- [24] S. Weinberg, *What is quantum field theory, and what did we think it is?*, in *Conceptual foundations of quantum field theory. Proceedings, Symposium and Workshop, Boston, USA, March 1-3, 1996*, pp. 241–251. 1996. arXiv:hep-th/9702027 [hep-th].
- [25] J. C. Romao and J. P. Silva, *A resource for signs and Feynman diagrams of the Standard Model*, Int. J. Mod. Phys. **A27** (2012) 1230025, arXiv:1209.6213 [hep-ph].
- [26] CMS Collaboration, V. Khachatryan et al., *Constraints on the spin-parity and anomalous HVV couplings of the Higgs boson in proton collisions at 7 and 8 TeV*, Phys. Rev. **D92** no. 1, (2015) 012004, arXiv:1411.3441 [hep-ex].
- [27] ATLAS Collaboration, G. Aad et al., *Study of the spin and parity of the Higgs boson in diboson decays with the ATLAS detector*, Eur. Phys. J. **C75** no. 10, (2015) 476, arXiv:1506.05669 [hep-ex]. [Erratum: Eur. Phys. J. C76, no. 3, 152 (2016)].

- [28] C.-N. Yang, *Selection Rules for the Dematerialization of a Particle Into Two Photons*, Phys. Rev. **77** (1950) 242–245.
- [29] ATLAS, CMS Collaboration, G. Aad et al., *Measurements of the Higgs boson production and decay rates and constraints on its couplings from a combined ATLAS and CMS analysis of the LHC pp collision data at $\sqrt{s} = 7$ and 8 TeV*, JHEP **08** (2016) 045, arXiv:1606.02266 [hep-ex].
- [30] ATLAS Collaboration, T. A. collaboration, *Combined measurements of Higgs boson production and decay in the $H \rightarrow ZZ \rightarrow 4\ell$ and $H \rightarrow \gamma\gamma$ channels using $\sqrt{s} = 13$ TeV pp collision data collected with the ATLAS experiment*,.
- [31] CMS Collaboration, V. Khachatryan et al., *Search for Higgs boson off-shell production in proton-proton collisions at 7 and 8 TeV and derivation of constraints on its total decay width*, JHEP **09** (2016) 051, arXiv:1605.02329 [hep-ex].
- [32] ATLAS, CMS Collaboration, G. Aad et al., *Combined Measurement of the Higgs Boson Mass in pp Collisions at $\sqrt{s} = 7$ and 8 TeV with the ATLAS and CMS Experiments*, Phys. Rev. Lett. **114** (2015) 191803, arXiv:1503.07589 [hep-ex].
- [33] DELPHI, OPAL, ALEPH, LEP Electroweak Working Group, L3 Collaboration, J. Alcaraz et al., *Precision Electroweak Measurements and Constraints on the Standard Model*, arXiv:0712.0929 [hep-ex].
- [34] M. Beneke et al., *Top quark physics, in 1999 CERN Workshop on standard model physics (and more) at the LHC, CERN, Geneva, Switzerland, 25-26 May: Proceedings*, pp. 419–529. 2000. arXiv:hep-ph/0003033 [hep-ph].
<http://weblib.cern.ch/abstract?CERN-TH-2000-100>.
- [35] A. Quadt, *Top quark physics at hadron colliders*, Eur. Phys. J. **C48** (2006) 835–1000.
- [36] W. Bernreuther, *Top quark physics at the LHC*, J. Phys. **G35** (2008) 083001, arXiv:0805.1333 [hep-ph].
- [37] W. Bernreuther and P. Uwer, *Top-quark physics at colliders*, Nucl. Part. Phys. Proc. **261-262** (2015) 414–442.
- [38] K. Kröninger, A. B. Meyer, and P. Uwer, *Top-Quark Physics at the LHC*, in *The Large Hadron Collider: Harvest of Run 1*, T. Schörner-Sadenius, ed., pp. 259–300. 2015. arXiv:1506.02800 [hep-ex].
<http://inspirehep.net/record/1375310/files/arXiv:1506.02800.pdf>.
- [39] ATLAS, CDF, CMS, D0 Collaboration, *First combination of Tevatron and LHC measurements of the top-quark mass*, arXiv:1403.4427 [hep-ex].
- [40] J. Kieseler, K. Lipka, and S.-O. Moch, *Calibration of the Top-Quark Monte Carlo Mass*, Phys. Rev. Lett. **116** no. 16, (2016) 162001, arXiv:1511.00841 [hep-ph].
- [41] A. Buckley et al., *General-purpose event generators for LHC physics*, Phys. Rept. **504** (2011) 145–233, arXiv:1101.2599 [hep-ph].
- [42] U. Langenfeld, S. Moch, and P. Uwer, *Measuring the running top-quark mass*, Phys. Rev. **D80** (2009) 054009, arXiv:0906.5273 [hep-ph].

Bibliography

- [43] S. Alioli, P. Fernandez, J. Fuster, A. Irlles, S.-O. Moch, P. Uwer, and M. Vos, *A new observable to measure the top-quark mass at hadron colliders*, Eur. Phys. J. **C73** (2013) 2438, arXiv:1303.6415 [hep-ph].
- [44] ATLAS, CMS Collaboration, M. Vos, *Top-quark mass measurements at the LHC: alternative methods*, PoS **TOP2015** (2016) 035, arXiv:1602.00428 [hep-ex].
- [45] Particle Data Group Collaboration, C. Patrignani et al., *Review of Particle Physics*, Chin. Phys. **C40** no. 10, (2016) 100001.
- [46] ATLAS Collaboration, T. A. collaboration, *Combination of cross-section measurements for associated production of a single top-quark and a W boson at $s = 8$ TeV with the ATLAS and CMS experiments*,.
- [47] CMS Collaboration, C. Collaboration, *Combination of cross-section measurements of associated production of a single top quark and a W boson at $\sqrt{s} = 8$ TeV with the ATLAS and CMS experiments*,.
- [48] K. Melnikov and M. Schulze, *NLO QCD corrections to top quark pair production and decay at hadron colliders*, JHEP **08** (2009) 049, arXiv:0907.3090 [hep-ph].
- [49] A. S. Papanastasiou, *Off-Shell Effects for Top Quark Production at Hadron Colliders*. PhD thesis, Durham U., 2012. <http://etheses.dur.ac.uk/6350/>.
- [50] ATLAS Collaboration, M. Aaboud et al., *Measurement of the $t\bar{t}$ production cross-section using $e\mu$ events with b-tagged jets in pp collisions at $\sqrt{s}=13$ TeV with the ATLAS detector*, Phys. Lett. **B761** (2016) 136–157, arXiv:1606.02699 [hep-ex]. [Erratum: Phys. Lett. B772,879(2017)].
- [51] CMS Collaboration, A. M. Sirunyan et al., *Cross section measurement of t-channel single top quark production in pp collisions at $\sqrt{s} = 13$ TeV*, Phys. Lett. **B772** (2017) 752–776, arXiv:1610.00678 [hep-ex].
- [52] M. Czakon, P. Fiedler, and A. Mitov, *Total Top-Quark Pair-Production Cross Section at Hadron Colliders Through $O(\frac{4}{s})$* , Phys. Rev. Lett. **110** (2013) 252004, arXiv:1303.6254 [hep-ph].
- [53] M. Aliev, H. Lacker, U. Langenfeld, S. Moch, P. Uwer, and M. Wiedermann, *HATHOR: HAdronic Top and Heavy quarks crOSS section calculatoR*, Comput. Phys. Commun. **182** (2011) 1034–1046, arXiv:1007.1327 [hep-ph].
- [54] P. Kant, O. M. Kind, T. Kintscher, T. Lohse, T. Martini, S. Mölbitz, P. Rieck, and P. Uwer, *HatHor for single top-quark production: Updated predictions and uncertainty estimates for single top-quark production in hadronic collisions*, Comput. Phys. Commun. **191** (2015) 74–89, arXiv:1406.4403 [hep-ph].
- [55] Planck Collaboration, P. A. R. Ade et al., *Planck 2015 results. XIII. Cosmological parameters*, Astron. Astrophys. **594** (2016) A13, arXiv:1502.01589 [astro-ph.CO].
- [56] Supernova Search Team Collaboration, A. G. Riess et al., *Observational evidence from supernovae for an accelerating universe and a cosmological constant*, Astron. J. **116** (1998) 1009–1038, arXiv:astro-ph/9805201 [astro-ph].

- [57] Supernova Cosmology Project Collaboration, S. Perlmutter et al., *Measurements of Omega and Lambda from 42 high redshift supernovae*, *Astrophys. J.* **517** (1999) 565–586, arXiv:astro-ph/9812133 [astro-ph].
- [58] S. Weinberg, *The Cosmological Constant Problem*, *Rev. Mod. Phys.* **61** (1989) 1–23.
- [59] L. Canetti, M. Drewes, and M. Shaposhnikov, *Matter and Antimatter in the Universe*, *New J. Phys.* **14** (2012) 095012, arXiv:1204.4186 [hep-ph].
- [60] A. D. Sakharov, *Violation of CP Invariance, c Asymmetry, and Baryon Asymmetry of the Universe*, *Pisma Zh. Eksp. Teor. Fiz.* **5** (1967) 32–35. [*Usp. Fiz. Nauk*161,61(1991)].
- [61] K. Kajantie, M. Laine, K. Rummukainen, and M. E. Shaposhnikov, *Is there a hot electroweak phase transition at $m(H)$ larger or equal to $m(W)$?*, *Phys. Rev. Lett.* **77** (1996) 2887–2890, arXiv:hep-ph/9605288 [hep-ph].
- [62] K. Rummukainen, M. Tsy-pin, K. Kajantie, M. Laine, and M. E. Shaposhnikov, *The Universality class of the electroweak theory*, *Nucl. Phys.* **B532** (1998) 283–314, arXiv:hep-lat/9805013 [hep-lat].
- [63] F. Csikor, Z. Fodor, and J. Heitger, *Endpoint of the hot electroweak phase transition*, *Phys. Rev. Lett.* **82** (1999) 21–24, arXiv:hep-ph/9809291 [hep-ph].
- [64] M. B. Gavela, P. Hernandez, J. Orloff, and O. Pene, *Standard model CP violation and baryon asymmetry*, *Mod. Phys. Lett.* **A9** (1994) 795–810, arXiv:hep-ph/9312215 [hep-ph].
- [65] M. B. Gavela, P. Hernandez, J. Orloff, O. Pene, and C. Quimbay, *Standard model CP violation and baryon asymmetry. Part 2: Finite temperature*, *Nucl. Phys.* **B430** (1994) 382–426, arXiv:hep-ph/9406289 [hep-ph].
- [66] P. Huet and E. Sather, *Electroweak baryogenesis and standard model CP violation*, *Phys. Rev.* **D51** (1995) 379–394, arXiv:hep-ph/9404302 [hep-ph].
- [67] J. M. Pendlebury et al., *Revised experimental upper limit on the electric dipole moment of the neutron*, *Phys. Rev.* **D92** no. 9, (2015) 092003, arXiv:1509.04411 [hep-ex].
- [68] R. J. Crewther, P. Di Vecchia, G. Veneziano, and E. Witten, *Chiral Estimate of the Electric Dipole Moment of the Neutron in Quantum Chromodynamics*, *Phys. Lett.* **88B** (1979) 123. [Erratum: *Phys. Lett.*91B,487(1980)].
- [69] M. Pospelov and A. Ritz, *Theta induced electric dipole moment of the neutron via QCD sum rules*, *Phys. Rev. Lett.* **83** (1999) 2526–2529, arXiv:hep-ph/9904483 [hep-ph].
- [70] A. Shindler, T. Luu, and J. de Vries, *Nucleon electric dipole moment with the gradient flow: The -term contribution*, *Phys. Rev.* **D92** no. 9, (2015) 094518, arXiv:1507.02343 [hep-lat].
- [71] T. Chupp, P. Fierlinger, M. Ramsey-Musolf, and J. Singh, *Electric Dipole Moments of the Atoms, Molecules, Nuclei and Particles*, arXiv:1710.02504 [physics.atom-ph].

Bibliography

- [72] D. Goncalves, P. A. N. Machado, and J. M. No, *Simplified Models for Dark Matter Face their Consistent Completions*, Phys. Rev. **D95** no. 5, (2017) 055027, arXiv:1611.04593 [hep-ph].
- [73] S. Ipek, *Perturbative analysis of the electron electric dipole moment and CP violation in two-Higgs-doublet models*, Phys. Rev. **D89** no. 7, (2014) 073012, arXiv:1310.6790 [hep-ph].
- [74] G. C. Dorsch, S. J. Huber, T. Konstandin, and J. M. No, *A Second Higgs Doublet in the Early Universe: Baryogenesis and Gravitational Waves*, JCAP **1705** no. 05, (2017) 052, arXiv:1611.05874 [hep-ph].
- [75] N. F. Bell, G. Busoni, and I. W. Sanderson, *Self-consistent Dark Matter Simplified Models with an s-channel scalar mediator*, JCAP **1703** no. 03, (2017) 015, arXiv:1612.03475 [hep-ph].
- [76] U. Husemann, *Top-Quark Physics: Status and Prospects*, Prog. Part. Nucl. Phys. **95** (2017) 48–97, arXiv:1704.01356 [hep-ex].
- [77] W. Bernreuther, P. Galler, C. Mellein, Z. G. Si, and P. Uwer, *Production of heavy Higgs bosons and decay into top quarks at the LHC*, Phys. Rev. **D93** no. 3, (2016) 034032, arXiv:1511.05584 [hep-ph].
- [78] W. Bernreuther, P. Galler, Z.-G. Si, and P. Uwer, *Production of heavy Higgs bosons and decay into top quarks at the LHC. II: Top-quark polarization and spin correlation effects*, Phys. Rev. **D95** no. 9, (2017) 095012, arXiv:1702.06063 [hep-ph].
- [79] G. C. Branco, P. M. Ferreira, L. Lavoura, M. N. Rebelo, M. Sher, and J. P. Silva, *Theory and phenomenology of two-Higgs-doublet models*, Phys. Rept. **516** (2012) 1–102, arXiv:1106.0034 [hep-ph].
- [80] Y. L. Wu and L. Wolfenstein, *Sources of CP violation in the two Higgs doublet model*, Phys. Rev. Lett. **73** (1994) 1762–1764, arXiv:hep-ph/9409421 [hep-ph].
- [81] A. W. El Kaffas, W. Khater, O. M. Ogreid, and P. Osland, *Consistency of the two Higgs doublet model and CP violation in top production at the LHC*, Nucl. Phys. **B775** (2007) 45–77, arXiv:hep-ph/0605142 [hep-ph].
- [82] A. Pich and P. Tuzon, *Yukawa Alignment in the Two-Higgs-Doublet Model*, Phys. Rev. **D80** (2009) 091702, arXiv:0908.1554 [hep-ph].
- [83] S. L. Glashow and S. Weinberg, *Natural Conservation Laws for Neutral Currents*, Phys. Rev. **D15** (1977) 1958.
- [84] E. A. Paschos, *Diagonal Neutral Currents*, Phys. Rev. **D15** (1977) 1966.
- [85] H. E. Haber, G. L. Kane, and T. Sterling, *The Fermion Mass Scale and Possible Effects of Higgs Bosons on Experimental Observables*, Nucl. Phys. **B161** (1979) 493–532.
- [86] L. J. Hall and M. B. Wise, *FLAVOR CHANGING HIGGS - BOSON COUPLINGS*, Nucl. Phys. **B187** (1981) 397–408.
- [87] P. M. Ferreira, L. Lavoura, and J. P. Silva, *Renormalization-group constraints on Yukawa alignment in multi-Higgs-doublet models*, Phys. Lett. **B688** (2010) 341–344, arXiv:1001.2561 [hep-ph].

- [88] I. F. Ginzburg and M. Krawczyk, *Symmetries of two Higgs doublet model and CP violation*, Phys. Rev. **D72** (2005) 115013, arXiv:hep-ph/0408011 [hep-ph].
- [89] I. F. Ginzburg, *On the Dynamics of the Symmetry*, Sov. J. Nucl. Phys. **25** (1977) 227. [Yad. Fiz.25,421(1977)].
- [90] C. D. Froggatt, R. G. Moorhouse, and I. G. Knowles, *Two scalar doublet models with softly broken symmetries*, Nucl. Phys. **B386** (1992) 63–114.
- [91] J. F. Gunion and H. E. Haber, *The CP conserving two Higgs doublet model: The Approach to the decoupling limit*, Phys. Rev. **D67** (2003) 075019, arXiv:hep-ph/0207010 [hep-ph].
- [92] I. P. Ivanov, *Minkowski space structure of the Higgs potential in 2HDM*, Phys. Rev. **D75** (2007) 035001, arXiv:hep-ph/0609018 [hep-ph]. [Erratum: Phys. Rev.D76,039902(2007)].
- [93] P. M. Ferreira, H. E. Haber, and J. P. Silva, *Generalized CP symmetries and special regions of parameter space in the two-Higgs-doublet model*, Phys. Rev. **D79** (2009) 116004, arXiv:0902.1537 [hep-ph].
- [94] D. Das, *New limits on $\tan \beta$ for 2HDMs with Z_2 symmetry*, Int. J. Mod. Phys. **A30** no. 26, (2015) 1550158, arXiv:1501.02610 [hep-ph].
- [95] S. Inoue, M. J. Ramsey-Musolf, and Y. Zhang, *CP-violating phenomenology of flavor conserving two Higgs doublet models*, Phys. Rev. **D89** no. 11, (2014) 115023, arXiv:1403.4257 [hep-ph].
- [96] D. Eriksson, J. Rathsman, and O. Stal, *2HDMC: Two-Higgs-Doublet Model Calculator Physics and Manual*, Comput. Phys. Commun. **181** (2010) 189–205, arXiv:0902.0851 [hep-ph].
- [97] E. Braaten and J. P. Leveille, *Higgs Boson Decay and the Running Mass*, Phys. Rev. **D22** (1980) 715.
- [98] M. Drees and K.-i. Hikasa, *NOTE ON QCD CORRECTIONS TO HADRONIC HIGGS DECAY*, Phys. Lett. **B240** (1990) 455. [Erratum: Phys. Lett.B262,497(1991)].
- [99] K. G. Chetyrkin and M. Steinhauser, *The Relation between the \overline{MS} -bar and the on-shell quark mass at order $\alpha(s)^{**3}$* , Nucl. Phys. **B573** (2000) 617–651, arXiv:hep-ph/9911434 [hep-ph].
- [100] H.-L. Lai, M. Guzzi, J. Huston, Z. Li, P. M. Nadolsky, J. Pumplin, and C. P. Yuan, *New parton distributions for collider physics*, Phys. Rev. **D82** (2010) 074024, arXiv:1007.2241 [hep-ph].
- [101] J. R. Andersen et al., *Les Houches 2013: Physics at TeV Colliders: Standard Model Working Group Report*, arXiv:1405.1067 [hep-ph].
- [102] A. Buckley, J. Ferrando, S. Lloyd, K. Nordström, B. Page, M. Rüfenacht, M. Schönherr, and G. Watt, *LHAPDF6: parton density access in the LHC precision era*, Eur. Phys. J. **C75** (2015) 132, arXiv:1412.7420 [hep-ph].
- [103] M. Spira, A. Djouadi, D. Graudenz, and P. M. Zerwas, *Higgs boson production at the LHC*, Nucl. Phys. **B453** (1995) 17–82, arXiv:hep-ph/9504378 [hep-ph].

Bibliography

- [104] M. Kramer, E. Laenen, and M. Spira, *Soft gluon radiation in Higgs boson production at the LHC*, Nucl. Phys. **B511** (1998) 523–549, arXiv:hep-ph/9611272 [hep-ph].
- [105] P. Uwer, *EasyNData: A Simple tool to extract numerical values from published plots*, arXiv:0710.2896 [physics.comp-ph].
- [106] W. Bernreuther, O. Nachtmann, P. Overmann, and T. Schröder, *Angular correlations and distributions for searches of CP violation in top quark production and decay*, Nucl. Phys. **B388** (1992) 53–80. [Erratum: Nucl. Phys.B406,516(1993)].
- [107] W. Bernreuther and A. Brandenburg, *Tracing CP violation in the production of top quark pairs by multiple TeV proton proton collisions*, Phys. Rev. **D49** (1994) 4481–4492, arXiv:hep-ph/9312210 [hep-ph].
- [108] W. Bernreuther, M. Flesch, and P. Haberl, *Signatures of Higgs bosons in the top quark decay channel at hadron colliders*, Phys. Rev. **D58** (1998) 114031, arXiv:hep-ph/9709284 [hep-ph].
- [109] R. Kleiss and W. J. Stirling, *Spinor Techniques for Calculating p anti- $p \rightarrow W^\pm / Z^0 +$ Jets*, Nucl. Phys. **B262** (1985) 235–262.
- [110] L. J. Dixon, *Calculating scattering amplitudes efficiently, in QCD and beyond. Proceedings, Theoretical Advanced Study Institute in Elementary Particle Physics, TASI-95, Boulder, USA, June 4-30, 1995*, pp. 539–584. 1996. arXiv:hep-ph/9601359 [hep-ph]. <http://www-public.slac.stanford.edu/sciDoc/docMeta.aspx?slacPubNumber=SLAC-PUB-7106>.
- [111] W. Bernreuther, A. Brandenburg, Z. G. Si, and P. Uwer, *Top quark spin correlations at hadron colliders: Predictions at next-to-leading order QCD*, Phys. Rev. Lett. **87** (2001) 242002, arXiv:hep-ph/0107086 [hep-ph].
- [112] W. Bernreuther, A. Brandenburg, Z. G. Si, and P. Uwer, *Top quark pair production and decay at hadron colliders*, Nucl. Phys. **B690** (2004) 81–137, arXiv:hep-ph/0403035 [hep-ph].
- [113] W. Bernreuther and Z.-G. Si, *Distributions and correlations for top quark pair production and decay at the Tevatron and LHC.*, Nucl. Phys. **B837** (2010) 90–121, arXiv:1003.3926 [hep-ph].
- [114] ATLAS Collaboration, T. A. collaboration, *Search for heavy Higgs bosons A/H decaying to a top-quark pair in pp collisions at $\sqrt{s} = 8$ TeV with the ATLAS detector.*,
- [115] ATLAS Collaboration, M. Aaboud et al., *Search for heavy Higgs bosons A/H decaying to a top quark pair in pp collisions at $\sqrt{s} = 8$ TeV with the ATLAS detector*, arXiv:1707.06025 [hep-ex].
- [116] S. Jung, J. Song, and Y. W. Yoon, *Dip or nothingness of a Higgs resonance from the interference with a complex phase*, Phys. Rev. **D92** no. 5, (2015) 055009, arXiv:1505.00291 [hep-ph].
- [117] C.-Y. Chen, S. Dawson, and Y. Zhang, *Complementarity of LHC and EDMs for Exploring Higgs CP Violation*, JHEP **06** (2015) 056, arXiv:1503.01114 [hep-ph].

- [118] W. Bernreuther, D. Heisler, and Z.-G. Si, *A set of top quark spin correlation and polarization observables for the LHC: Standard Model predictions and new physics contributions*, JHEP **12** (2015) 026, arXiv:1508.05271 [hep-ph].
- [119] ATLAS Collaboration, M. Aaboud et al., *Measurements of top quark spin observables in $t\bar{t}$ events using dilepton final states in $\sqrt{s} = 8$ TeV pp collisions with the ATLAS detector*, JHEP **03** (2017) 113, arXiv:1612.07004 [hep-ex].
- [120] P. Uwer, *Maximizing the spin correlation of top quark pairs produced at the Large Hadron Collider*, Phys. Lett. **B609** (2005) 271–276, arXiv:hep-ph/0412097 [hep-ph].
- [121] G. Mahlon and S. J. Parke, *Maximizing spin correlations in top quark pair production at the Tevatron*, Phys. Lett. **B411** (1997) 173–179, arXiv:hep-ph/9706304 [hep-ph].
- [122] A. Djouadi, M. Spira, and P. M. Zerwas, *Production of Higgs bosons in proton colliders: QCD corrections*, Phys. Lett. **B264** (1991) 440–446.
- [123] R. V. Harlander and W. B. Kilgore, *Soft and virtual corrections to proton proton $\rightarrow H + x$ at NNLO*, Phys. Rev. **D64** (2001) 013015, arXiv:hep-ph/0102241 [hep-ph].
- [124] K. G. Chetyrkin, B. A. Kniehl, M. Steinhauser, and W. A. Bardeen, *Effective QCD interactions of CP odd Higgs bosons at three loops*, Nucl. Phys. **B535** (1998) 3–18, arXiv:hep-ph/9807241 [hep-ph].
- [125] R. V. Harlander and W. B. Kilgore, *Production of a pseudoscalar Higgs boson at hadron colliders at next-to-next-to leading order*, JHEP **10** (2002) 017, arXiv:hep-ph/0208096 [hep-ph].
- [126] A. Denner, S. Dittmaier, M. Roth, and D. Wackerroth, *Predictions for all processes $e^+ e^- \rightarrow 4$ fermions + gamma*, Nucl. Phys. **B560** (1999) 33–65, arXiv:hep-ph/9904472 [hep-ph].
- [127] A. Denner, S. Dittmaier, M. Roth, and L. H. Wieders, *Electroweak corrections to charged-current $e^+ e^- \rightarrow 4$ fermion processes: Technical details and further results*, Nucl. Phys. **B724** (2005) 247–294, arXiv:hep-ph/0505042 [hep-ph]. [Erratum: Nucl. Phys. B854,504(2012)].
- [128] M. Nowakowski and A. Pilaftsis, *On gauge invariance of Breit-Wigner propagators*, Z. Phys. **C60** (1993) 121–126, arXiv:hep-ph/9305321 [hep-ph].
- [129] A. Denner, *Techniques for calculation of electroweak radiative corrections at the one loop level and results for W physics at LEP-200*, Fortsch. Phys. **41** (1993) 307–420, arXiv:0709.1075 [hep-ph].
- [130] R. G. Stuart, *Gauge invariance, analyticity and physical observables at the Z0 resonance*, Phys. Lett. **B262** (1991) 113–119.
- [131] A. Aepli, G. J. van Oldenborgh, and D. Wyler, *Unstable particles in one loop calculations*, Nucl. Phys. **B428** (1994) 126–146, arXiv:hep-ph/9312212 [hep-ph].
- [132] H. G. J. Veltman, *Mass and width of unstable gauge bosons*, Z. Phys. **C62** (1994) 35–52.

Bibliography

- [133] S. Dittmaier, A. Huss, and C. Schwinn, *Mixed QCD-electroweak $O(\alpha_s\alpha)$ corrections to Drell-Yan processes in the resonance region: pole approximation and non-factorizable corrections*, Nucl. Phys. **B885** (2014) 318–372, arXiv:1403.3216 [hep-ph].
- [134] V. S. Fadin, V. A. Khoze, and A. D. Martin, *How suppressed are the radiative interference effects in heavy instable particle production?*, Phys. Lett. **B320** (1994) 141–144, arXiv:hep-ph/9309234 [hep-ph].
- [135] V. S. Fadin, V. A. Khoze, and A. D. Martin, *Interference radiative phenomena in the production of heavy unstable particles*, Phys. Rev. **D49** (1994) 2247–2256.
- [136] W. Beenakker, A. P. Chapovsky, and F. A. Berends, *Nonfactorizable corrections to W pair production*, Phys. Lett. **B411** (1997) 203–210, arXiv:hep-ph/9706339 [hep-ph].
- [137] W. Beenakker, A. P. Chapovsky, and F. A. Berends, *Nonfactorizable corrections to W pair production: Methods and analytic results*, Nucl. Phys. **B508** (1997) 17–63, arXiv:hep-ph/9707326 [hep-ph].
- [138] P. Nason, S. Dawson, and R. K. Ellis, *The Total Cross-Section for the Production of Heavy Quarks in Hadronic Collisions*, Nucl. Phys. **B303** (1988) 607–633.
- [139] W. Beenakker, H. Kuijf, W. L. van Neerven, and J. Smith, *QCD Corrections to Heavy Quark Production in p anti- p Collisions*, Phys. Rev. **D40** (1989) 54–82.
- [140] P. Nason, S. Dawson, and R. K. Ellis, *The One Particle Inclusive Differential Cross-Section for Heavy Quark Production in Hadronic Collisions*, Nucl. Phys. **B327** (1989) 49–92. [Erratum: Nucl. Phys. B335,260(1990)].
- [141] W. Beenakker, W. L. van Neerven, R. Meng, G. A. Schuler, and J. Smith, *QCD corrections to heavy quark production in hadron hadron collisions*, Nucl. Phys. **B351** (1991) 507–560.
- [142] J. Kuipers, T. Ueda, J. A. M. Vermaseren, and J. Vollinga, *FORM version 4.0*, Comput. Phys. Commun. **184** (2013) 1453–1467, arXiv:1203.6543 [cs.SC].
- [143] Wolfram Research, Inc., *Mathematica 10.0*. Wolfram Research, Inc., Champaign, Illinois, 2014.
- [144] S. Catani, M. H. Seymour, and Z. Trocsanyi, *Regularization scheme independence and unitarity in QCD cross-sections*, Phys. Rev. **D55** (1997) 6819–6829, arXiv:hep-ph/9610553 [hep-ph].
- [145] G. 't Hooft and M. J. G. Veltman, *Regularization and Renormalization of Gauge Fields*, Nucl. Phys. **B44** (1972) 189–213.
- [146] C. G. Bollini and J. J. Giambiagi, *Dimensional Renormalization: The Number of Dimensions as a Regularizing Parameter*, Nuovo Cim. **B12** (1972) 20–26.
- [147] G. M. Cicuta and E. Montaldi, *Analytic renormalization via continuous space dimension*, Lett. Nuovo Cim. **4** (1972) 329–332.
- [148] J. F. Ashmore, *A Method of Gauge Invariant Regularization*, Lett. Nuovo Cim. **4** (1972) 289–290.

- [149] E. R. Speer and M. J. Westwater, *GENERIC FEYNMAN AMPLITUDES*, Ann. Inst. H. Poincaré **14** (1971) 1–55.
- [150] J. C. Collins, *Renormalization*, vol. 26 of *Cambridge Monographs on Mathematical Physics*. Cambridge University Press, Cambridge, 1986. <http://www-spires.fnal.gov/spires/find/books/www?c1=QC174.17.R46C65::1985>.
- [151] R. Gastmans and R. Meuldermans, *Dimensional regularization of the infrared problem*, Nucl. Phys. **B63** (1973) 277–284.
- [152] R. Gastmans, J. Verwaest, and R. Meuldermans, *Dimensional Regularization in Massless QED*, Nucl. Phys. **B105** (1976) 454–460.
- [153] W. J. Marciano and A. Sirlin, *Dimensional Regularization of Infrared Divergences*, Nucl. Phys. **B88** (1975) 86–98.
- [154] A. Signer and D. Stockinger, *Using Dimensional Reduction for Hadronic Collisions*, Nucl. Phys. **B808** (2009) 88–120, arXiv:0807.4424 [hep-ph].
- [155] S. L. Adler, *Axial vector vertex in spinor electrodynamics*, Phys. Rev. **177** (1969) 2426–2438.
- [156] J. S. Bell and R. Jackiw, *A PCAC puzzle: $\pi^0 \rightarrow \gamma\gamma$ in the sigma model*, Nuovo Cim. **A60** (1969) 47–61.
- [157] S. A. Larin, *The Renormalization of the axial anomaly in dimensional regularization*, Phys. Lett. **B303** (1993) 113–118, arXiv:hep-ph/9302240 [hep-ph].
- [158] W. Bernreuther, R. Bonciani, T. Gehrmann, R. Heinesch, P. Mastrolia, and E. Remiddi, *Decays of scalar and pseudoscalar Higgs bosons into fermions: Two-loop QCD corrections to the Higgs-quark-antiquark amplitude*, Phys. Rev. **D72** (2005) 096002, arXiv:hep-ph/0508254 [hep-ph].
- [159] G. Passarino and M. J. G. Veltman, *One Loop Corrections for $e^+ e^-$ Annihilation Into $\mu^+ \mu^-$ in the Weinberg Model*, Nucl. Phys. **B160** (1979) 151–207.
- [160] R. K. Ellis, Z. Kunszt, K. Melnikov, and G. Zanderighi, *One-loop calculations in quantum field theory: from Feynman diagrams to unitarity cuts*, Phys. Rept. **518** (2012) 141–250, arXiv:1105.4319 [hep-ph].
- [161] G. 't Hooft, *Dimensional regularization and the renormalization group*, Nucl. Phys. **B61** (1973) 455–468.
- [162] T. Muta, *Foundations of Quantum Chromodynamics: An Introduction to Perturbative Methods in Gauge Theories, (3rd ed.)*, vol. 78 of *World scientific Lecture Notes in Physics*. World Scientific, Hackensack, N.J., 2010. <http://www-spires.fnal.gov/spires/find/books/www?c1=QC793.3.Q35M88::2010>.
- [163] W. A. Bardeen, A. J. Buras, D. W. Duke, and T. Muta, *Deep Inelastic Scattering Beyond the Leading Order in Asymptotically Free Gauge Theories*, Phys. Rev. **D18** (1978) 3998.
- [164] A. Grozin, *Lectures on QED and QCD: Practical calculation and renormalization of one- and multi-loop Feynman diagrams*. 2007.

Bibliography

- [165] H. Lehmann, K. Symanzik, and W. Zimmermann, *On the formulation of quantized field theories*, *Nuovo Cim.* **1** (1955) 205–225.
- [166] W. Beenakker, S. Dittmaier, M. Kramer, B. Plumper, M. Spira, and P. M. Zerwas, *NLO QCD corrections to t anti- t H production in hadron collisions*, *Nucl. Phys.* **B653** (2003) 151–203, arXiv:hep-ph/0211352 [hep-ph].
- [167] S. Weinberg, *Effective Gauge Theories*, *Phys. Lett.* **91B** (1980) 51–55.
- [168] B. A. Ovrut and H. J. Schnitzer, *The Decoupling Theorem and Minimal Subtraction*, *Phys. Lett.* **100B** (1981) 403–406.
- [169] W. Wetzel, *Minimal Subtraction and the Decoupling of Heavy Quarks for Arbitrary Values of the Gauge Parameter*, *Nucl. Phys.* **B196** (1982) 259–272.
- [170] W. Bernreuther and W. Wetzel, *Decoupling of Heavy Quarks in the Minimal Subtraction Scheme*, *Nucl. Phys.* **B197** (1982) 228–236. [Erratum: *Nucl. Phys.*B513,758(1998)].
- [171] W. Bernreuther, *Decoupling of Heavy Quarks in Quantum Chromodynamics*, *Annals Phys.* **151** (1983) 127.
- [172] W. Bernreuther, *HEAVY QUARK EFFECTS ON THE PARAMETERS OF QUANTUM CHROMODYNAMICS DEFINED BY MINIMAL SUBTRACTION*, *Z. Phys.* **C20** (1983) 331–333.
- [173] K. G. Chetyrkin, B. A. Kniehl, and M. Steinhauser, *Decoupling relations to $O(\alpha_s^3)$ and their connection to low-energy theorems*, *Nucl. Phys.* **B510** (1998) 61–87, arXiv:hep-ph/9708255 [hep-ph].
- [174] B. A. Ovrut and H. J. Schnitzer, *Gauge Theories With Minimal Subtraction and the Decoupling Theorem*, *Nucl. Phys.* **B179** (1981) 381–416.
- [175] T. Kinoshita, *Mass singularities of Feynman amplitudes*, *J. Math. Phys.* **3** (1962) 650–677.
- [176] T. D. Lee and M. Nauenberg, *Degenerate Systems and Mass Singularities*, *Phys. Rev.* **133** (1964) B1549–B1562. [,25(1964)].
- [177] S. Catani and M. H. Seymour, *A General algorithm for calculating jet cross-sections in NLO QCD*, *Nucl. Phys.* **B485** (1997) 291–419, arXiv:hep-ph/9605323 [hep-ph]. [Erratum: *Nucl. Phys.*B510,503(1998)].
- [178] S. Catani, S. Dittmaier, M. H. Seymour, and Z. Trocsanyi, *The Dipole formalism for next-to-leading order QCD calculations with massive partons*, *Nucl. Phys.* **B627** (2002) 189–265, arXiv:hep-ph/0201036 [hep-ph].
- [179] G. P. Lepage, *VEGAS: AN ADAPTIVE MULTIDIMENSIONAL INTEGRATION PROGRAM*,.
- [180] E. Remiddi and J. A. M. Vermaseren, *Harmonic polylogarithms*, *Int. J. Mod. Phys.* **A15** (2000) 725–754, arXiv:hep-ph/9905237 [hep-ph].
- [181] F. Mahmoudi and O. Stal, *Flavor constraints on the two-Higgs-doublet model with general Yukawa couplings*, *Phys. Rev.* **D81** (2010) 035016, arXiv:0907.1791 [hep-ph].

- [182] T. Hermann, M. Misiak, and M. Steinhauser, $\bar{B} \rightarrow X_s \gamma$ in the Two Higgs Doublet Model up to Next-to-Next-to-Leading Order in QCD, JHEP **11** (2012) 036, arXiv:1208.2788 [hep-ph].
- [183] O. Eberhardt, U. Nierste, and M. Wiebusch, Status of the two-Higgs-doublet model of type II, JHEP **07** (2013) 118, arXiv:1305.1649 [hep-ph].
- [184] A. Djouadi, J. Kalinowski, and M. Spira, HDECAY: A Program for Higgs boson decays in the standard model and its supersymmetric extension, Comput. Phys. Commun. **108** (1998) 56–74, arXiv:hep-ph/9704448 [hep-ph].
- [185] CMS Collaboration, V. Khachatryan et al., Search for a Higgs boson in the mass range from 145 to 1000 GeV decaying to a pair of W or Z bosons, JHEP **10** (2015) 144, arXiv:1504.00936 [hep-ex].
- [186] ATLAS Collaboration, Measurements of the properties of the Higgs-like boson in the four lepton decay channel with the ATLAS detector using 25 fb¹ of proton-proton collision data,.
- [187] ATLAS Collaboration, G. Aad et al., Search for a CP-odd Higgs boson decaying to Zh in pp collisions at $\sqrt{s} = 8$ TeV with the ATLAS detector, Phys. Lett. **B744** (2015) 163–183, arXiv:1502.04478 [hep-ex].
- [188] CMS Collaboration, V. Khachatryan et al., Search for a pseudoscalar boson decaying into a Z boson and the 125 GeV Higgs boson in $^+ b\bar{b}$ final states, Phys. Lett. **B748** (2015) 221–243, arXiv:1504.04710 [hep-ex].
- [189] ATLAS Collaboration, G. Aad et al., Search For Higgs Boson Pair Production in the $\gamma\gamma b\bar{b}$ Final State using pp Collision Data at $\sqrt{s} = 8$ TeV from the ATLAS Detector, Phys. Rev. Lett. **114** no. 8, (2015) 081802, arXiv:1406.5053 [hep-ex].
- [190] CMS Collaboration, V. Khachatryan et al., Search for resonant pair production of Higgs bosons decaying to two bottom quarkantiquark pairs in protonproton collisions at 8 TeV, Phys. Lett. **B749** (2015) 560–582, arXiv:1503.04114 [hep-ex].
- [191] CMS Collaboration, V. Khachatryan et al., Search for neutral MSSM Higgs bosons decaying to a pair of tau leptons in pp collisions, JHEP **10** (2014) 160, arXiv:1408.3316 [hep-ex].
- [192] ATLAS Collaboration, G. Aad et al., Search for neutral Higgs bosons of the minimal supersymmetric standard model in pp collisions at $\sqrt{s} = 8$ TeV with the ATLAS detector, JHEP **11** (2014) 056, arXiv:1409.6064 [hep-ex].
- [193] ATLAS, CMS Collaboration, Y. Nagai, Higgs Search in $b\bar{b}$ Signatures at ATLAS and CMS, PoS **Beauty2013** (2013) 001, arXiv:1306.1784 [hep-ex].
- [194] W. Grimus, L. Lavoura, O. M. Ogreid, and P. Osland, A Precision constraint on multi-Higgs-doublet models, J. Phys. **G35** (2008) 075001, arXiv:0711.4022 [hep-ph].
- [195] W. Grimus, L. Lavoura, O. M. Ogreid, and P. Osland, The Oblique parameters in multi-Higgs-doublet models, Nucl. Phys. **B801** (2008) 81–96, arXiv:0802.4353 [hep-ph].

Bibliography

- [196] H. E. Haber and D. O'Neil, *Basis-independent methods for the two-Higgs-doublet model III: The CP-conserving limit, custodial symmetry, and the oblique parameters S, T, U*, Phys. Rev. **D83** (2011) 055017, arXiv:1011.6188 [hep-ph].
- [197] C. A. Baker et al., *An Improved experimental limit on the electric dipole moment of the neutron*, Phys. Rev. Lett. **97** (2006) 131801, arXiv:hep-ex/0602020 [hep-ex].
- [198] ACME Collaboration, J. Baron et al., *Order of Magnitude Smaller Limit on the Electric Dipole Moment of the Electron*, Science **343** (2014) 269–272, arXiv:1310.7534 [physics.atom-ph].
- [199] LHC Higgs Cross Section Working Group Collaboration, S. Dittmaier et al., *Handbook of LHC Higgs Cross Sections: 1. Inclusive Observables*, arXiv:1101.0593 [hep-ph].
- [200] CDF Collaboration, T. Aaltonen et al., *Evidence for a Mass Dependent Forward-Backward Asymmetry in Top Quark Pair Production*, Phys. Rev. **D83** (2011) 112003, arXiv:1101.0034 [hep-ex].
- [201] J. C. Collins and D. E. Soper, *Angular Distribution of Dileptons in High-Energy Hadron Collisions*, Phys. Rev. **D16** (1977) 2219.
- [202] A. Czarnecki, M. Jezabek, and J. H. Kuhn, *Lepton Spectra From Decays of Polarized Top Quarks*, Nucl. Phys. **B351** (1991) 70–80.
- [203] S. Berge, W. Bernreuther, and S. Kirchner, *Determination of the Higgs CP-mixing angle in the tau decay channels at the LHC including the DrellYan background*, Eur. Phys. J. **C74** no. 11, (2014) 3164, arXiv:1408.0798 [hep-ph].
- [204] V. Cirigliano, W. Dekens, J. de Vries, and E. Mereghetti, *Constraining the top-Higgs sector of the Standard Model Effective Field Theory*, Phys. Rev. **D94** no. 3, (2016) 034031, arXiv:1605.04311 [hep-ph].
- [205] V. Cirigliano, W. Dekens, J. de Vries, and E. Mereghetti, *Is there room for CP violation in the top-Higgs sector?*, Phys. Rev. **D94** no. 1, (2016) 016002, arXiv:1603.03049 [hep-ph].
- [206] CMS Collaboration, V. Khachatryan et al., *Measurements of t t -bar spin correlations and top quark polarization using dilepton final states in pp collisions at $\sqrt{s} = 8$ TeV*, Phys. Rev. **D93** no. 5, (2016) 052007, arXiv:1601.01107 [hep-ex].
- [207] S. Y. Choi and J. S. Lee, *Decays of the MSSM Higgs bosons with explicit CP violation*, Phys. Rev. **D61** (1999) 015003, arXiv:hep-ph/9907496 [hep-ph].
- [208] M. Carena, J. R. Ellis, S. Mrenna, A. Pilaftsis, and C. E. M. Wagner, *Collider probes of the MSSM Higgs sector with explicit CP violation*, Nucl. Phys. **B659** (2003) 145–178, arXiv:hep-ph/0211467 [hep-ph].
- [209] M. Maniatis, A. von Manteuffel, O. Nachtmann, and F. Nagel, *Stability and symmetry breaking in the general two-Higgs-doublet model*, Eur. Phys. J. **C48** (2006) 805–823, arXiv:hep-ph/0605184 [hep-ph].
- [210] N. G. Deshpande and E. Ma, *Pattern of Symmetry Breaking with Two Higgs Doublets*, Phys. Rev. **D18** (1978) 2574.

- [211] B. M. Kastening, *Bounds from stability and symmetry breaking on parameters in the two Higgs doublet potential*, arXiv:hep-ph/9307224 [hep-ph].
- [212] M. Sher, *Electroweak Higgs Potentials and Vacuum Stability*, Phys. Rept. **179** (1989) 273–418.
- [213] G. Kreyerhoff and R. Rodenberg, *Renormalization Group Analysis of Coleman-Weinberg Symmetry Breaking in Two Higgs Models*, Phys. Lett. **B226** (1989) 323–328.
- [214] J. Freund, G. Kreyerhoff, and R. Rodenberg, *Vacuum stability in a two Higgs model*, Phys. Lett. **B280** (1992) 267–270.
- [215] S. Nie and M. Sher, *Vacuum stability bounds in the two Higgs doublet model*, Phys. Lett. **B449** (1999) 89–92, arXiv:hep-ph/9811234 [hep-ph].
- [216] S. Kanemura, T. Kasai, and Y. Okada, *Mass bounds of the lightest CP even Higgs boson in the two Higgs doublet model*, Phys. Lett. **B471** (1999) 182–190, arXiv:hep-ph/9903289 [hep-ph].
- [217] P. M. Ferreira and D. R. T. Jones, *Bounds on scalar masses in two Higgs doublet models*, JHEP **08** (2009) 069, arXiv:0903.2856 [hep-ph].
- [218] P. M. Ferreira, R. Santos, and A. Barroso, *Stability of the tree-level vacuum in two Higgs doublet models against charge or CP spontaneous violation*, Phys. Lett. **B603** (2004) 219–229, arXiv:hep-ph/0406231 [hep-ph]. [Erratum: Phys. Lett. **B629**, 114(2005)].
- [219] A. Barroso, P. M. Ferreira, and R. Santos, *Charge and CP symmetry breaking in two Higgs doublet models*, Phys. Lett. **B632** (2006) 684–687, arXiv:hep-ph/0507224 [hep-ph].
- [220] A. Barroso, P. M. Ferreira, and R. Santos, *Neutral minima in two-Higgs doublet models*, Phys. Lett. **B652** (2007) 181–193, arXiv:hep-ph/0702098 [HEP-PH].
- [221] A. Barroso, P. M. Ferreira, I. P. Ivanov, and R. Santos, *Metastability bounds on the two Higgs doublet model*, JHEP **06** (2013) 045, arXiv:1303.5098 [hep-ph].
- [222] B. W. Lee, C. Quigg, and H. B. Thacker, *Weak Interactions at Very High-Energies: The Role of the Higgs Boson Mass*, Phys. Rev. **D16** (1977) 1519.
- [223] J. Maalampi, J. Sirkka, and I. Vilja, *Tree level unitarity and triviality bounds for two Higgs models*, Phys. Lett. **B265** (1991) 371–376.
- [224] S. Kanemura, T. Kubota, and E. Takasugi, *Lee-Quigg-Thacker bounds for Higgs boson masses in a two doublet model*, Phys. Lett. **B313** (1993) 155–160, arXiv:hep-ph/9303263 [hep-ph].
- [225] A. G. Akeroyd, A. Arhrib, and E.-M. Naimi, *Note on tree level unitarity in the general two Higgs doublet model*, Phys. Lett. **B490** (2000) 119–124, arXiv:hep-ph/0006035 [hep-ph].
- [226] J. Horejsi and M. Kladiva, *Tree-unitarity bounds for THDM Higgs masses revisited*, Eur. Phys. J. **C46** (2006) 81–91, arXiv:hep-ph/0510154 [hep-ph].

Bibliography

- [227] B. Świeżewska, *Yukawa independent constraints for two-Higgs-doublet models with a 125 GeV Higgs boson*, Phys. Rev. **D88** no. 5, (2013) 055027, arXiv:1209.5725 [hep-ph]. [Erratum: Phys. Rev.D88,no.11,119903(2013)].
- [228] M. Lüscher and P. Weisz, *Is There a Strong Interaction Sector in the Standard Lattice Higgs Model?*, Phys. Lett. **B212** (1988) 472–478.
- [229] W. J. Marciano, G. Valencia, and S. Willenbrock, *Renormalization Group Improved Unitarity Bounds on the Higgs Boson and Top Quark Masses*, Phys. Rev. **D40** (1989) 1725.
- [230] B. Grinstein, C. W. Murphy, and P. Uttayarat, *One-loop corrections to the perturbative unitarity bounds in the CP-conserving two-Higgs doublet model with a softly broken \mathbb{Z}_2 symmetry*, JHEP **06** (2016) 070, arXiv:1512.04567 [hep-ph].
- [231] V. Cacchio, D. Chowdhury, O. Eberhardt, and C. W. Murphy, *Next-to-leading order unitarity fits in Two-Higgs-Doublet models with soft \mathbb{Z}_2 breaking*, JHEP **11** (2016) 026, arXiv:1609.01290 [hep-ph].
- [232] U. Nierste and K. Riesselmann, *Higgs sector renormalization group in the \overline{MS} and \overline{OMS} scheme: The Breakdown of perturbation theory for a heavy Higgs*, Phys. Rev. **D53** (1996) 6638–6652, arXiv:hep-ph/9511407 [hep-ph].